



**Università  
degli Studi  
di Ferrara**

---

---

**DOCTORAL COURSE IN PHYSICS**

**IN AGREEMENT WITH THE INTERNATIONAL CENTER FOR  
RELATIVISTIC ASTROPHYSICS NETWORK (ICRANet)**

CYCLE XXXII

**COORDINATOR Prof. Eleonora LUPPI**

**BROADBAND MODELLING  
OF RELATIVISTIC EXPLOSIONS**

Scientific/Disciplinary Sector (SDS) FIS/05

**Candidate**

Dr. Marco MARONGIU

**Supervisor**

Dr. Cristiano GUIDORZI

---

---

**YEARS 2016/2019**



# Sommario

Nella nuova era dell'esplorazione del cielo transiente, i progenitori di esplosioni relativistiche – come i lampi gamma (GRB) e le supernovae relativistiche (SN) – sono tra i protagonisti più importanti della ricerca. Le osservazioni multi-frequenza del vicino GRB 170817A – le cui onde gravitazionali sono state rilevate dagli interferometri LIGO/VIRGO – e la recente scoperta alle altissime energie degli afterglow associati a due GRB brillanti (190114C e 180720B) con i telescopi Cherenkov MAGIC e HESS hanno suggellato la nascita dell'astronomia multi-messaggera. Lo studio dell'afterglow dei GRB, originato dall'interazione tra la materia espulsa e il mezzo circostante, è fondamentale per comprendere i meccanismi di emissione, la microfisica dello shock relativistico, le proprietà del mezzo circostante e del getto. Gli afterglow radio dei GRB – per quanto difficili da osservare per la loro intrinseca debolezza (dell'ordine del sub-mJy) – sono cruciali per comprendere appieno questi aspetti, e in particolare lo shock inverso, che a sua volta dipende dalle proprietà della materia espulsa e quindi dal progenitore stesso del GRB. Anche se diverse campagne osservative hanno migliorato la copertura della parte radio dello spettro di emissione, ad oggi manca un quadro esaustivo degli afterglow.

In questo contesto mi sono occupato di modellizzare l'emissione multi-frequenza degli afterglow, con particolare attenzione al radio, con la realizzazione del codice Python sAGA (Software for AfterGlow Analysis). Dopo aver testato con successo sAGA su vari afterglow di GRB (120521C, 090423 e 050904), l'ho utilizzato nel caso di GRB 160131A, i cui dati suggeriscono l'iniezione di energia da parte del progenitore, e la presenza di un getto. Inoltre, l'insolita presenza di picchi nelle curve di luce radio potrebbe essere dovuta a effetti di scintillazione interstellare. I miei risultati mostrano che i dati multi-frequenza sono difficilmente spiegabili nell'ambito del modello standard degli afterglow.

Al fine di incrementare i dati radio, ho coordinato una serie di campagne osservative con il Sardinia Radio Telescope (SRT) per gli afterglow di GRB 181201A e GRB 190114C. Nonostante queste non abbiano portato alla rivelazione degli stessi, mi hanno offerto la possibilità di confrontare tre metodi per rivelare sorgenti deboli: quick-look (il meno accurato), source extraction (tipico dell'analisi ad alte energie) e il fit con una Gaussiana bi-dimensionale. La messa a punto di una nuova metodologia per l'analisi dei dati di SRT (1) ottimizza la rivelazione di una sorgente debole ad un flusso minimo rivelabile di  $\sim 1.8$  mJy, e (2) evidenzia l'importanza di un'accurata conoscenza del fondo.

I GRB lunghi sono associati alle Ic broad-line (Ic-BL) SNe. Ad oggi il legame GRB/SN è testabile solo per i GRB a redshift  $z \lesssim 1$  per la debolezza intrinseca delle SNe. In questo contesto ho analizzato Ic-BL SN 2014ad, rivelata solo in ottico. La vicinanza di questa sorgente ( $\sim 26$  Mpc) e le osservazioni in radio e raggi-X hanno permesso di vincolare profondamente (1) il tasso di perdita di massa del progenitore, (2) l'energia totale della materia espulsa a grande velocità e (3) la geometria dell'esplosione. Ho considerato due regimi di emissione di sincrotrone (isotropa con espansione sub-relativistica, tipica delle normali SN; relativistica con getto osservato fuori asse, come nei GRB), dimostrando che i getti poco energetici osservati fuori asse in un mezzo a bassa densità non possono essere esclusi nemmeno per una BL-Ic SN così vicina.



# Abstract

In the new transient sky era, the progenitors of relativistic explosions, such as gamma-ray bursts (GRBs) and relativistic supernovae (SNe), are the focus of forefront research. Broadband observations of nearby short GRB 170817A – whose gravitational waves were detected by LIGO/VIRGO – and the recent detection at TeV energies of two bright GRB afterglows (190114C and 180720B) with the MAGIC and HESS Cherenkov telescopes heralded the birth of so-called multi-messenger astronomy. GRB afterglows, originating from the interaction between the ejecta and the circumburst medium, help constrain the radiation mechanism, the relativistic shock microphysics, the circumburst environment, the structure and geometry of the relativistic jet. Observations of radio afterglows are key to understand the reverse shock, which links directly to the nature of the outflow and, consequently, to the progenitor itself. On the other hand, they can hardly be observed with current radiotelescopes because of their faintness (mJy or sub-mJy). Recently, several radio followup campaigns improved the observational coverage of the lower part of the emission spectrum, but an exhaustive picture of GRB afterglows is still missing.

I developed an approach focused on broadband modelling (with particular attention to the radio frequencies) through the Python code called sAGA (Software for AfterGlow Analysis). After successfully testing it on various GRB afterglows (120521C, 090423, and 050904), I applied it to long GRB 160131A, whose data show evidence for energy injection and jetted emission. Radio light curves are characterised by several peaks, that could be due to either interstellar scintillation (ISS) effects or multi-component structure. My results show that the data can hardly be explained self-consistently with the standard model of GRB afterglows.

To help collect more radio data on GRB afterglows, I coordinated radio campaigns with Sardinia Radio Telescope (SRT) to observe two GRB radio afterglows (181201A and 190114C). Although they have come up with no detection, they fostered the definition and the comparative analysis of three detection methods for faint radio sources through single-dish imaging, in terms of sensitivity and robustness: quick-look (a smart but rough approach), source extraction (typical of high-energy astronomy), and fitting procedure with a 2-Dimensional Gaussian (a more sophisticated approach). The new methodology for the SRT data analysis (1) pushes down the sensitivity limits of this radiotelescope – with respect to more traditional techniques – at  $\sim 1.8$  mJy, and (2) highlights the need for accurate knowledge of the background.

L-GRBs are associated with type Ic broad-line supernovae (Ic-BL SNe). This connection can be observed only at redshift  $z \lesssim 1$  because of the intrinsic faintness of SNe. In this context, I analysed Ic-BL SN 2014ad, detected only in optical. The proximity of the source ( $\sim 26$  Mpc) and the radio/X-ray observations turned into very deep constraints on (1) the progenitor mass-loss rate, (2) the total energy of the ejecta, and (3) the explosion geometry. I considered two synchrotron emission regimes (uncollimated non-relativistic ejecta, typical of ordinary SNe); off-axis relativistic jet, such as those seen in GRBs), showing that off-axis low-energy jets expanding in a low-density medium cannot be ruled out even in the most nearby BL-Ic SNe.



# Contents

<b>Introduction</b>	<b>11</b>
<b>1 Gamma-Ray Bursts: observed properties</b>	<b>13</b>
1.1 GRB history	14
1.2 GRB Phenomenology	17
1.2.1 The burst itself: the prompt emission	17
1.2.2 The afterglow emission	20
1.3 GRB classification: progenitors and correlations	24
1.3.1 Short/hard vs. long/soft GRBs	24
1.3.2 Other GRB classifications	26
1.3.3 GRB environments and progenitors	27
1.3.4 GRB empirical correlations	28
1.4 Polarisation in the GRB emission	29
1.4.1 Afterglow emission	30
1.4.2 Prompt emission	31
1.5 The GRB-SN connection	31
1.5.1 Observational evidence	32
1.5.2 Detectability of GRB-SN	32
<b>2 Theoretical framework of GRB emission</b>	<b>35</b>
2.1 The fireball model	36
2.1.1 The compactness problem	36
2.1.2 The dynamical fireball evolution	37
2.1.3 Internal and external shocks	37
2.2 GRB synchrotron emission	39
2.2.1 Evolution of GRB synchrotron spectra and light-curves	40
2.3 Jetted emission	41
2.4 Non-relativistic transition	45
2.5 Central engines	46
2.5.1 Collapsars	46
2.5.2 Magnetars	47
2.5.3 Compact object mergers	47
2.6 Open issues on GRB science	47
<b>3 An analytical approach for broadband modelling of GRB afterglows</b>	<b>51</b>
3.1 Broadband modelling of GRBs	52
3.2 Markov Chain Monte Carlo	52
3.3 Synchrotron spectra and light-curves in sAGa	53
3.4 Jet breaks and non-relativistic transition	54
3.5 Energy injection	54

3.6	Extinction and absorption processes . . . . .	57
3.7	Radio interstellar scintillation . . . . .	57
3.8	Inverse-Compton regime . . . . .	59
3.9	Test cases for sAGa . . . . .	60
3.9.1	GRB 120521C . . . . .	60
3.9.2	GRB 090423 . . . . .	60
3.9.3	GRB 050904 . . . . .	62
3.9.4	Overview of my test results . . . . .	64
<b>4</b>	<b>Broadband modelling of the afterglow of GRB 160131A</b>	<b>67</b>
4.1	Introduction . . . . .	68
4.2	Broadband followup campaigns . . . . .	68
4.2.1	X-ray followup . . . . .	68
4.2.2	Optical followup . . . . .	69
4.2.3	Radio followup with VLA . . . . .	69
4.3	Characterisation of the afterglow . . . . .	70
4.3.1	Synchrotron ( $\nu_m$ ), cooling ( $\nu_c$ ) frequencies and circumburst density profile	70
4.3.2	Radio data analysis . . . . .	72
4.3.3	Jet break . . . . .	76
4.3.4	Self-absorption frequency ( $\nu_{sa}$ ) . . . . .	78
4.4	Broadband modelling . . . . .	78
4.4.1	Preliminary results for GRB 160131A . . . . .	78
4.5	Discussion . . . . .	81
4.5.1	Energy injection . . . . .	84
4.5.2	Multi-component SEDs in radio frequencies . . . . .	85
4.5.3	Challenges for the standard afterglow model . . . . .	85
4.5.4	Reverse shock . . . . .	86
4.5.5	Afterglow parameters obtained with sAGa . . . . .	87
4.6	Summary and conclusions . . . . .	87
<b>5</b>	<b>Constraints on the environment and energetics of BL-Ic SN2014ad from deep radio and X-ray observations</b>	<b>89</b>
<b>6</b>	<b>Optimised methods for the detection and analysis of weak radio sources with single-dish observations</b>	<b>91</b>
	<b>Conclusions</b>	<b>93</b>
	<b>Acknowledgments</b>	<b>95</b>
<b>A</b>	<b>Constraints on the Environment and Energetics of the Broad-line Ic SN2014ad from Deep Radio and X-Ray Observations</b>	<b>113</b>
<b>B</b>	<b>Methods for detection and analysis of weak radio sources with single-dish radiotelescopes</b>	<b>123</b>
	<b>Dichiarazione di conformità della tesi di Dottorato</b>	<b>146</b>





*«But I do not think it is possible really to understand the successes of Science without understanding how hard it is – how easy it is to be led astray, how difficult it is to know at any time what is the next thing to be done.».*

---

THE FIRST THREE MINUTES  
STEVEN WEINBERG

# Introduction

In this PhD Thesis I focused on the study of the broadband data modelling of relativistic explosions, in particular gamma-ray bursts (GRBs) and supernovae (SNe). I therefore aimed to develop an approach that devotes special attention to the radio band data in both the radio observations and data reduction, as well as in broadband modelling.

GRBs are the signature of cataclysmic events on stellar scale in the Universe. They consist in short and intense pulses of gamma-ray radiation, and for a few seconds they outshine the whole gamma-ray sky.

Their progenitors – either core collapsing massive stars or binary neutron star (BNS) mergers, depending on whether the GRB is classified as a long (L-GRB) or short one (S-GRB), respectively – launch relativistic jets with very high gamma-ray released isotropic equivalent energies ( $\sim 10^{51}$  erg for S-GRBs,  $\sim 10^{52}$  erg for L-GRBs), and jet opening angles of a few degrees.

The burst itself is called prompt emission, defined as the first signal of soft gamma-ray/hard X-ray emission detected by GRB detectors; the origin of this emission remains not fully understood after more than 50 years of observations. GRBs are also characterised by a long-lasting emission – days through months – at lower frequencies known as “afterglow”, originating from the interaction between the ejecta and the circumburst medium. This interaction takes place through shocks, mediated by magnetic field irregularities and resulting mainly in synchrotron radiation. The propagation of the ejecta creates two shocks: a forward shock (FS), propagating in the circumburst medium, and a reverse shock (RS), propagating back into the ejecta and radiating at lower frequencies.

GRB afterglows encode a wealth of information that links to (i) the radiation mechanism, in particular the possible presence of large-scale magnetic fields ploughing the ejecta, which is still one of the main open issues in the field; (ii) relativistic shock microphysics; (iii) energetics; (iv) jet geometry. All these issues can be addressed effectively and uniquely through observations at lower frequencies, especially the radio band. GRB radio afterglows are crucial to understand the RS component which in turn can (i) clarify the nature of the outflow and, consequently, (ii) constrain the nature of GRB progenitor stars. GRB radio afterglows are typically faint sources (mJy or sub-mJy) and can hardly be observed with the current radiotelescopes (both in interferometric and, especially, in single-dish mode). In the lastest years several dedicated radio followup campaigns improved the observational coverage of the lower part of the emission spectrum, but an exhaustive picture of GRB afterglows is still missing.

To this aim, I developed a specific Python code called sAGA (Software for AfterGlow Analysis, Chapter 3). This tool allows for the characterisation of physical properties of afterglow through broadband data analysis based on fitting procedure in Bayesian approach. The main radiative processes involved are synchrotron and inverse Compton, self-absorption, radio scintillation, optical absorption caused by dust. After successfully testing the capabilities of sAGA on various GRB afterglows (such as GRB 120521C, GRB 090423 and GRB 050904; Sect. 3.9) in the context of the standard GRB afterglow model, I analysed long GRB 160131A (Chapter 4), observed through deep follow-up campaigns from radio to high-energies. Preliminary analysis shows that the broadband data set can hardly be explained self-consistently with the standard

model of GRB afterglows.

Moreover, in the context of radio followup of GRB afterglows, I supervised a request of observational time of the INAF proposal 23-18, and two other radio campaigns in target of opportunity (ToO) mode (02-19 and 50-19) to observe two GRB radio afterglows (GRB 181201A and GRB 190114C) in single-dish mode with the new Sardinia Radio Telescope (SRT), characterised by a parabolic reflector with a diameter of 64 meters. These followup campaigns resulted in no detection of GRB afterglows during all the 10 observation epochs. This outcome suggested to analyse several detection methods for weak radio sources through single-dish imaging, in terms of data sensitivity and robustness (Chapter 6). These methods are included in a specific Python code for the analysis, that allows to measure the flux density and the uncertainty of a point-like source in an image not particularly crowded. The new methodology for the SRT data analysis I have come up with exploits the capabilities of SRT by optimising the detection of faint sources (as is the case for GRB afterglows or GW radio counterparts), thus pushing down the sensitivity limits with respect to more traditional techniques.

Except for a couple of ambiguous cases, L-GRBs are found to be associated with type Ic broad-line (BL) supernovae (SNe; hereafter, Ic-BL SNe) observable when, for example, a dim or rapidly declining GRB afterglow does not overshadow the SN component. Since these SNe are detectable – with current facilities – at redshift  $z \lesssim 1$ , the direct evidence of GRB/SN connection is possible only for nearby GRBs. These sources result in final evolutionary scenario of massive stars, they do not show hydrogen and helium in the external layers, and the broad lines in the optical spectrum are the signature of a high expansion velocity of the ejecta ( $\sim 20000$  km/s). Ic-BL SNe are more energetic than ordinary Type Ic SNe, with explosion kinetic energies of about  $10^{51}$  erg. The nature of GRB/SN connection, together with their progenitor stars and the circumstellar medium are open issues.

In general, not all Ic-BL SNe are accompanied by a GRB. Among several interpretations, the simplest one is (i) the absence of GRB; alternatively, (ii) the GRB jet is misaligned with respect to the line of sight of the observer (who therefore cannot see it; this is the so-called off-axis scenario), or (iii) the ejecta fail to make it out to the photosphere (the choked jet scenario), possibly because launched by a weak short-lived central engine, resulting in the production of a relativistic SN rather than a GRB counterpart. The emission mechanism concerning the shock heating of both SNe and GRB afterglows differ mainly in the ejecta velocity (relativistic for GRB afterglows, mildly or sub-relativistic for SNe). This results in synchrotron radiation from SNe, observed at radio and in X-ray frequencies.

In this context I focused on the GRB/SN association adapting sAGa to the SN emission, to extract its physical properties through a broadband approach. My workbench is SN 2014ad (Chapter 5), a very nearby Ic-BL SN ( $\sim 26$  Mpc) detected only in optical band, with no observational evidence of a GRB counterpart. To analyse the possible GRB association I considered two scenarios, both characterised by synchrotron emission: uncollimated non-relativistic ejecta (typical of ordinary SNe), and an off-axis relativistic jet (as seen in GRBs). I deeply analysed available X-ray and radio observations, but the source was undetected at these frequencies. The upper limits, thanks to the proximity of the source, enable very deep constraints on both the progenitor mass-loss rate and the total energy of the ejected matter that are, still today, open issues in the GRB/SN connection.

This PhD Thesis is organised in 6 Chapters as described above. In particular, Chapters 1 and 2 contain a brief summary of both observational and theoretical properties of GRBs to guide the reader to the understanding of the following chapters, and all the results are summarised in the [Conclusions](#).

# Chapter 1

## Gamma-Ray Bursts: observed properties

This chapter presents an overview about observative properties of the *gamma-ray burst* (GRB) phenomenon, to introduce the subjects of this Thesis. After a brief historical overview (Sect. 1.1), I present a phenomenological description of GRBs (Sect. 1.2), including their multi-wavelength emission, classification (Sect. 1.3), correlations (Sect. 1.3.4), progenitors and circumburst environments (Sect. 1.3.3). I then move on to the polarisation of the GRB signal (Sect. 1.4) and the connection between GRBs and supernovae (Sect. 1.5).

## 1.1 GRB history

Despite an average detection rate of about one GRB per day – with a full sky coverage – first GRBs were observed only during the 1960s. Since the atmosphere of the Earth is opaque to high-energy radiation (X- and gamma-ray), this emission is detectable through detectors aboard either space satellites or balloons. The first gamma-ray detectors were conceived to monitor nuclear weapon activities. During the cold war several nuclear detonations were carried, resulting in the danger of radioactive fallout. This led to the Partial Test Ban Treaty in 1963, signed and ratified by most countries (especially by the United States and the USSR). To verify the observance of this treaty and to enforce surveillance of spatial nuclear detonations, from 1963 to 1970 United States sent in orbit the six Vela satellites, built to detect X-ray and gamma-ray emission by nuclear weapons tested in space<sup>1</sup>.

A bright flash of gamma-ray radiation was detected on July 2, 1967, by the Vela satellites unlike any known nuclear weapons signature: this was GRB 670702<sup>2</sup>, the first GRB ever to be observed (Klebesadel et al. 1973). Other similar events followed, whose localisation (successfully performed) based on the triangulation of arrival time at different detectors, allowing to rule out both a terrestrial and a solar origin, thus supporting the cosmic origin.

After this discovery, initially progress has been slow, especially as the intrinsic brevity of GRBs and the technical difficulties in determining an accurate position (and hence the GRB distance) of gamma-rays, resulting in no detection of counterparts at lower frequencies. This problem caused a heated debate between the cosmological and the Galactic origin of GRBs, resulting in several hundred theories. This scenario improved significantly thanks to the InterPlanetary Network (IPN, e.g. Cline & Desai 1976), a network of spacecraft able to provide localisation accuracy of hundreds of arcminutes down to a few arcminutes, but with a delay of days to months, too long to detect an afterglow. The cosmological origin was further supported by Hartmann & Epstein (1989), that highlighted the isotropic distribution of a sample of 88 IPN-localised GRBs<sup>3</sup>. Nevertheless, the galactic origin theory still had significant support: in addition to the existence of theoretical models based on neutron stars (NSs), an event detected on March 5, 1979 Evans et al. (1979) was localised near a supernova remnant (SNR) in the large Magellanic Cloud, which provided a connection between GRBs and NSs<sup>4</sup>. The high transverse velocities of NSs (Frail et al. 1994) suggested that NSs could populate the galactic halo; an isotropic distribution of GRBs could therefore support the galactic NS origin.

The launch of the NASA *Compton Gamma-Ray Observatory* (CGRO) in 1991 was a crucial event for the GRB science. Among the instruments on board there was the Burst And Transient Source Experiment (BATSE, Meegan et al. 1992), a sensitive gamma-ray detector working in the 0.02 – 2 MeV band, designed for GRBs. BATSE was able to promptly notify a rough localisation (2 to 3 degrees, up to 20 degrees for low-luminosity events) and, thanks to its all-sky coverage, detected about 2700 GRBs (~ 1 GRB per day) during its nine years of operations. The sky distribution of BATSE GRBs (Fig. 1.1) turned out isotropic, therefore calling for a cosmological origin. On the other hand, there were still no direct measurements of distance, and hence both Galactic halo and solar system models were not ruled out. Other important results regarded

<sup>1</sup>The last satellite to be decommissioned was in function until 1984.

<sup>2</sup>The GRB naming convention follows the format GRB YYMMDD. For multiple detection on a single day the format GRB YYMMDDX is adopted, where X is a letter (A for the first detection, B for the second one, and so on). Since 2010, all GRB names follow the YYMMDDX convention (including the final letter) even if only one GRB is detected on a given day.

<sup>3</sup>Galactic events would be expected to concentrate in the Galactic plane.

<sup>4</sup>This event turned out not to be an actual GRB. It had an unusual light-curve and spectrum, and 16 more bursts were observed from the same source. It was later classified as a soft gamma repeater (SGR), originating in a magnetar (Paczynski 1992; Grindlay 1994)





a steep temporal index identified in the afterglow light-curves of several GRBs, interpreted as evidence for a jet geometry of the fireball (Rhoads 1999; Sari et al. 1999; Zhang & Mészáros 2002; Bloom et al. 2003; Berger et al. 2003; Zhang et al. 2004).

GRB science entered its modern era thanks to two highly successful – and still active – satellites, Swift and Fermi. The **Neil Gehrels Swift observatory** (Gehrels et al. 2004) – built by an international collaboration (USA, UK, Italy) – was launched on November 20, 2004 with three instruments onboard: a wide-field Burst Alert Telescope (BAT; Barthelmy et al. 2005), a narrow-field X-Ray Telescope (XRT; Burrows et al. 2005a), and a UV-Optical Telescope (UVOT; Roming et al. 2005). The BAT (15 – 350 keV) is a coded aperture hard X-ray imager, with 1.4 sr field of view. The XRT has a field of view  $23''.6 \times 23''.6$ , large enough to search for an X-ray counterpart in the BAT error box (typically a few arcminutes wide), and a typical slew time of about one minute; these characteristics allow to quickly catch the X-ray afterglow of the majority of detected GRBs and provide an arcsecond position. The UVOT is characterised by a 30 cm aperture, a field of view  $17' \times 17'$ . The accurate positions provided by XRT are promptly distributed to the ground-based and other spaceborn follow-up telescopes through the Gamma-ray Coordinates Network (GCN<sup>5</sup>), to promptly plan specific campaigns to search for counterparts at lower frequencies. The prompt slewing capability allowed Swift to detect numerous GRB afterglows, enabling direct observations of the very early GRB afterglow phase. In particular, it detected the faint afterglow of short-duration GRBs, leading to the identification of the host galaxies of several short GRBs and their relative locations with respect to the host. These results very different from those of long GRBs suggest that the progenitors of short GRBs harbour a different population (Gehrels et al. 2005; Barthelmy et al. 2005), likely associated with compact stars such as the coalescence of two neutron stars (NS – NS) or one neutron star and one black hole (NS – BH). The abundance of early afterglow data, especially in the X-ray band (e.g. Nousek et al. 2006; Evans et al. 2009), allowed to better understand the physical processes that shape the early afterglow light-curves (Zhang et al. 2006). The ordinary X-ray afterglow light-curve is composed by five distinct temporal components (Zhang et al. 2006), with the possible presence of erratic X-ray flares connected with the prompt gamma-ray emission, suggesting that the GRB central engine lasts longer than previously believed. Further broadband observations revealed a more complex “chromatic” behaviour for at least some GRBs, suggesting more complicated afterglow physics. Moreover, Swift observations challenged the separation between the long and short populations. In particular, duration can be ambiguous in the GRB short/long classification (e.g. Gehrels et al. 2006; Della Valle et al. 2006; Greiner et al. 2009), calling for more sophisticated classification criteria (Zhang et al. 2009). In addition, Swift greatly broadened the measured redshift range, allowing to study the evolution of the universe. In the low-redshift regime, Swift discovered several low-luminosity GRBs associated with SNe (e.g. GRB 060218/SN 2006aj Campana et al. 2006; Pian et al. 2006), suggesting that they likely represent a distinct population from ordinary more luminous ones (Liang et al. 2007; Virgili et al. 2009; Bromberg et al. 2012). The furthest GRBs discovered by Swift so far are GRB 080913 at  $z = 6.7$  (Greiner et al. 2009) and GRB 090429B at  $z = 9.4$  (Cucchiara et al. 2011).

The **Fermi Gamma-Ray Space Telescope** was launched on 11 June 2008. It carries two main instruments: the Large Area Telescope (LAT, 0.02 – 300 GeV), which covers 20% of the sky at any time and scans the entire sky every three hours, and the Gamma-ray Burst Monitor (GBM, 0.008 – 40 MeV), which scans the whole sky for any events (Meegan et al. 2009; Zhang 2019). The broad energy coverage allows to study the broadband spectra of GRB prompt emission with unprecedented detail. According to the second Fermi/LAT GRB catalogue (Ajello et al. 2019), LAT detected 169 GRBs above 100 MeV out of 2357 GRBs detected by GBM, suggesting external shock origin of the GeV emission. Sometimes, GeV emission shows a

<sup>5</sup>[https://gcn.gsfc.nasa.gov/gcn3\\_archive.html](https://gcn.gsfc.nasa.gov/gcn3_archive.html)



delayed onset with respect to the MeV emission, not predicted from known models<sup>6</sup>. Detailed spectral analysis in a wide spectral window provided important information to understand the composition of GRB jets and the physical mechanisms of prompt emission, showing a multi-component scenario (Zhang 2011; Guiriec et al. 2015). Moreover, photons with  $> 100$  GeV rest-frame energy have been detected in several GRBs (e.g., GRB 080916C Abdo et al. 2009 and GRB 130427A Ackermann et al. 2013), constraining the bulk Lorentz factor and consequently particle acceleration mechanisms in relativistic shocks.

The detection of gravitational waves due to mergers between two black holes with the gravitational wave (GW) detector, Advanced LIGO (aLIGO<sup>7</sup>), heralded the beginning of GW astronomy (Abbott et al. 2016). On 17 August 2017, a NS-NS merger event, GW 170817, was detected by the aLIGO and Advanced Virgo<sup>8</sup> gravitational wave detectors. The event was associated with a low-luminosity short GRB 170817A (Abbott et al. 2017b) and a multi-wavelength counterpart detected in optical, radio, and X-ray bands (e.g. Pian et al. 2017; Nicholl et al. 2017) in the nearby galaxy NGC 4993 at  $\sim 40$  Mpc. This historical achievement brought the GRB field formally into the so-called “multi-messenger era” (Abbott et al. 2017b). Moreover, the recent detection at TeV energies of two bright GRB afterglows (190114C, MAGIC Collaboration et al. 2019a,b; 180720B, Ronchi et al. 2019) thanks to MAGIC (Major Atmospheric Gamma-ray Imaging Cherenkov Telescope) and HESS (High Energy Stereoscopic System) ground-based Cherenkov telescopes, further extended the range of covered frequencies where GRBs can be analysed, strongly suggesting the signature of inverse Compton in their afterglow emission.

## 1.2 GRB Phenomenology

The observed properties of prompt and of afterglow emissions are summarised in Sect. 1.2.1 and 1.2.2, respectively.

### 1.2.1 The burst itself: the prompt emission

Following Zhang (2019) one could define the prompt emission of a GRB as “*the temporal phase during which excessive sub-MeV emission is detected by the GRB triggering detectors above the instrumental background emission level*”. Most of the energy released during the prompt emission is of electromagnetic origin; the isotropic–equivalent luminosity during the prompt ranges between  $10^{47}$  and  $10^{54}$  erg/s, and the isotropic–equivalent energy  $E_{iso}$ <sup>9</sup> ranges between  $10^{49}$  and  $10^{55}$  erg.

Observations of the prompt emission in frequencies lower than gamma-rays are rare, made difficult by the combination of unpredictability and short duration of GRBs<sup>10</sup>. Early data can be obtained if a precursor emission alerts the community or in the case of an exceptionally long duration GRB. In the optical domain, two types of components are observable (both may be present in the same burst): a component for which the peak of the optical emission is offset with respect to the peak of the gamma-ray emission (which points to a different physical origin), and a component that tracks the gamma-ray light-curve.

<sup>6</sup>Such delays (or the lack of) for photons with the highest energies place important constraints on the Lorentz Invariance Violation (LIV, Abdo et al. 2009).

<sup>7</sup><http://www.ligo.caltech.edu>

<sup>8</sup><http://www.virgo-gw.eu>

<sup>9</sup>The isotropic–equivalent energy is defined as the energy emitted in the  $1 - 10^4$  keV range in the rest-frame of the source assuming the emission to be spherically symmetric. In the case of collimated emission with a jet half-opening angle  $\theta_j$ , the beaming-corrected energy is  $E_{iso}(1 - \cos \theta_j)$ .

<sup>10</sup>To date, there are only two examples of a GRB observed from the optical to the GeV range during the prompt emission (GRB 130427A, Fraija et al. 2016 and GRB 160625B, Troja et al. 2017).

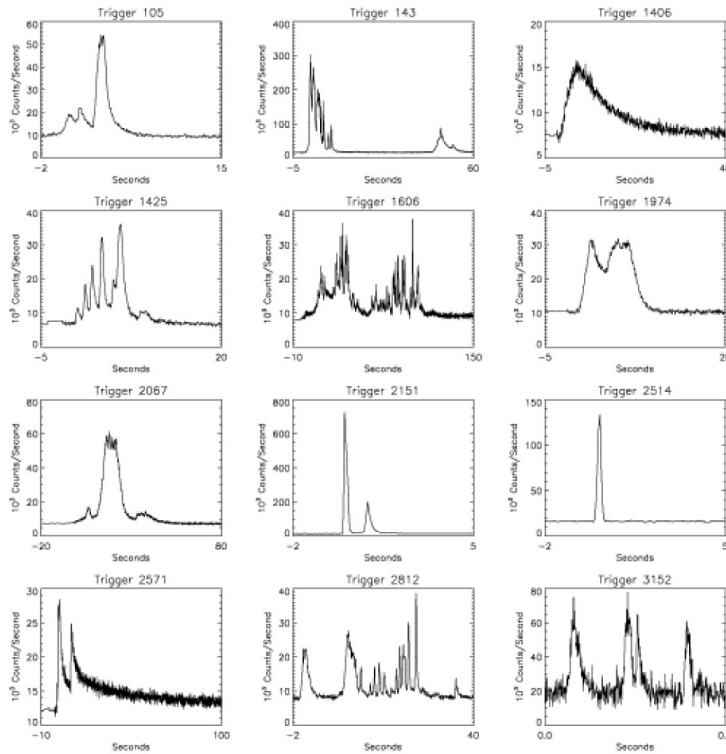


**Figure 1.2:** Diversity of GRB light-curves observed by BATSE. These light-curves show the variety in duration (milliseconds to tens of minutes), temporal structure, and pulse shape. Figure reproduced from [Fishman & Meegan \(1995\)](#).

### Temporal properties

The duration of a burst is generally characterised by  $T_{90}$ , defined as the time between which 5% and 95% of the total fluence<sup>11</sup> is collected by the detector.  $T_{90}$  is used to limit the uncertainty on the entire duration, as the start and the end of a GRB cannot be determined precisely due to background fluctuations; this value is detector-dependent, meaning that it is strongly dependent on the sensitivity of the instrument. Usually  $T_{90}$  ranges between a few tens of milliseconds and thousand seconds, with an average value of a few tens of seconds; the  $T_{90}$  distribution shows two log-normal components peaking at 0.2 – 0.3 s and 20 – 30 s, separated at  $\sim 2$  s (Fig. 1.7).

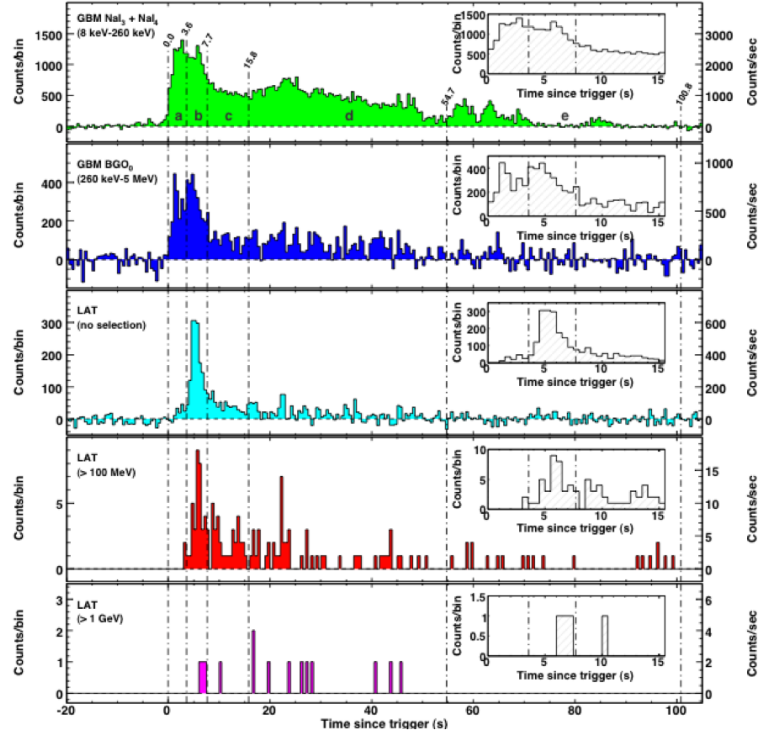
GRB light-curves can be (i) highly structured, with numerous and clearly distinct pulses, with an erratic behaviour, or (ii) simply composed by one or few single pulses (Fig. 1.2, [Fishman & Meegan 1995](#)). Each individual pulse – the duration of which is in timescales of seconds – typically shows a fast-rising and exponential-decay (FRED) shape.

Fig. 1.3 shows that the shape of a light-curve depends on the adopted energy band: in general, pulses are characterised by narrower profiles in harder bands.

GRB light-curves show no periodicity ([Beloborodov et al. 1998, 2000](#); [Guidorzi et al. 2012](#)). However, an interesting feature emerges when averaging the power density spectra (PDS) over many GRBs. For BATSE GRBs, the average PDS of some bright GRBs is a power-law with an index of  $\sim -5/3$  and a sharp break above  $\sim 1$  Hz ([Beloborodov et al. 2000](#)); for Swift GRBs, the PDS slope is steeper (from  $-1.7$  to  $-2$ ), without break at 1 Hz ([Guidorzi et al. 2012](#)). The  $-5/3$  index is the theoretical value of fully developed hydrodynamical turbulence ([Kolmogorov 1941](#)).

Some GRBs have a precursor – tens or hundreds of seconds before the GRB bulk – followed by a quiescent gap before the main burst comes out ([Zhang et al. 2016](#)); the emission properties of the precursor is similar to the main burst (e.g., [Lazzati 2005](#); [Burlon et al. 2008](#); [Hu et al. 2014](#)).

<sup>11</sup>The fluence is defined as the time-integrated flux of GRB radiation, and it is expressed in units of  $\text{erg cm}^{-2}$ .



**Figure 1.3:** The light-curve of GRB 080916C in different energy bands. Figure reproduced from [Abdo et al. \(2009\)](#).

Estimates of the fraction of GRBs with precursors range between 3% and  $\sim 20\%$  depending on the precise definition of a precursor event ([Burlon et al. 2009](#); [Lazzati 2005](#)).

### Spectral properties

GRB spectra usually reveal a highly non-thermal nature. However, unlike the seemingly chaotic temporal behaviour, they can be described by an empirical model that features two smoothly connected power-laws (Fig. 1.4). This model is known as the Band function ([Band et al. 1993](#)), with the photon number spectrum  $N(E)$  defined as:

$$N(E) = A \begin{cases} \left(\frac{E}{100}\right)^\alpha \exp\left[-\frac{E(2+\alpha)}{E_p}\right] & \text{if } E \leq \left(\frac{\alpha-\beta}{2+\alpha}\right)E_p \\ \left(\frac{E}{100}\right)^\beta \exp(\beta - \alpha) \left[\frac{(\alpha-\beta)E_p}{(2+\alpha)}\right]^{\alpha-\beta} & \text{if } E > \left(\frac{\alpha-\beta}{2+\alpha}\right)E_p \end{cases} \quad (1.1)$$

where  $A$  is the normalisation of the spectrum,  $\alpha$  and  $\beta$  are the photon spectra indices (both negatives),  $E_p$  is the peak energy in the  $E^2N(E)$  spectrum<sup>12</sup>,  $N(E)dE$  indicates the photon number in the energy bin  $dE$ . Typical values of broken power-law indices are  $-1.5 \leq \alpha \leq 0.5$  and  $-2.5 \leq \beta \leq -2$ ; typical peak energies  $E_p$  range between several keV and a few MeV. In a time-resolved analysis, these parameters evolve during the burst.

In the limit  $\beta \rightarrow \infty$ , Band function (Eq. 1.1) tends to a cut-off power-law function, often used to fit GRB spectra; this corresponds to the case of the limited detector bandpasses, resulting in no constraint of  $\beta$ . The limit  $\alpha \rightarrow \beta$  corresponds to a simple power-law.

Some GRB spectra call for additional components; for example, a power-law extending to high energies has been observed in e.g. GRB 090510 ([Ackermann et al. 2010](#)), and a subdominant quasi-thermal component has been seen in e.g. GRB 100724B ([Guiriec et al. 2011](#)). These

<sup>12</sup>This corresponds to  $\nu F_\nu$  spectrum. Moreover, the flux density spectrum  $F_E$  (or  $F_\nu$  in terms of frequency) corresponds to  $EN(E)$ ; this is also called spectral energy distribution (SED).

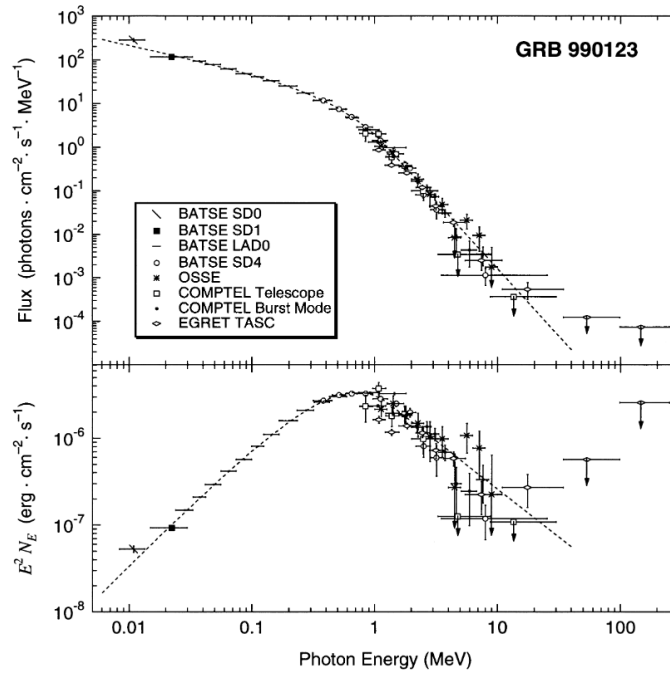


**Figure 1.4:** The time-averaged spectrum of GRB 990123 observed by CGRO. Top: flux spectrum in units of photon flux ( $N_E$ ) or brightness; this shows that most of the photons in a GRB are emitted at the low end of the energy range (into the hard X-ray bands). Bottom: the same spectrum ( $\nu F_\nu$ ) in units of energy flux shows that most of the energy of a burst is emitted in the gamma-ray range. Figure reproduced from Briggs et al. (1999).

properties suggest that the prompt emission spectrum may include three components (Zhang 2011): a Band component, a quasi-thermal component in a range of tens to hundreds keV, and a power-law extending to high energies.

Most GRBs are characterised by strong spectral evolution. This behaviour manifests itself in two different properties: (1) “spectral lags” observed in light-curves at different energy bands (Norris et al. 2000; Liang et al. 2006); (2) rapid temporal evolution of  $E_p$  observed in time-resolved spectra. There are two types of evolution patterns: hard-to-soft evolution – meaning that  $E_p$  decreases from the beginning of the pulse (Norris et al. 1986, 1996) – and intensity tracking from  $E_p$  (Golenetskii et al. 1983).

## 1.2.2 The afterglow emission

The prompt emission is followed by a long-lived, fading signal typically at lower frequencies, so-called “afterglow”. It is defined as the emission detected after the prompt sub-MeV emission phase, and both its spectrum and its light-curve are characterised by a multi-segment broken power-laws. GRB afterglows are usually observable on timescales of days, depending on the observational frequency (the lower the frequency, the longer the duration); in particular, a radio signal may be detected up to several months after the GRB.

The afterglow was theoretically predicted (Meszaros & Rees 1997) before its first discovery (Costa et al. 1997; van Paradijs et al. 1997; Frail et al. 1997); since then, the observations and interpretation of the GRB afterglows at several frequencies have made great strides. In a nutshell, ignoring the nature of the central engine, a GRB suddenly emits a huge amount of energy in a small volume, resulting in a fireball moving at relativistic speed (if baryon loading is not heavy). This relativistic ejecta loses speed and energy through the interaction with the circumburst medium (CBM); this deceleration creates a forward shock (FS), observable at

late-times (0.1 days/months with respect to the GRB trigger), propagating in the CBM as well as a reverse shock (RS), observable at early-times ( $\leq 0.1$  d), penetrating the ejecta and radiating at lower frequencies (radio/optical band). Electrons and protons are accelerated in the shocks, giving rise to bright broadband non-thermal emission through synchrotron radiation. As the fireball slows down, the strength of the shock reduces, resulting in a fading emission at low frequencies.

GRB afterglow flux density can usually be characterised – for each epoch and observing frequency – by:

$$F_\nu(t, \nu) \propto t^\alpha \nu^\beta \quad (1.2)$$

where  $\alpha$  and  $\beta$  indicate the temporal decay index and spectral index, respectively.

GRB afterglows are crucial to investigate many open issues in GRB science, in particular (i) relativistic shock microphysics, (ii) energetics, (iii) jet geometry, and (iv) the radiation mechanism(s) responsible for the prompt emission, in particular the possible presence of large-scale magnetic fields entrained in the ejecta. As predicted in the synchrotron external shock model (e.g., Meszaros & Rees 1997; Sari et al. 1998; Dermer et al. 2000; Sari & Esin 2001), the afterglow covers a very wide frequency range, from radio to the TeV range, and hence all these issues can be addressed effectively and uniquely through multi-frequency observations. Typically, observations start with the crude localisation given by the gamma-ray prompt emission (with an accuracy of 1 – 4 arcmin for Swift/BAT), and the slewing procedure for the detection by X-ray instruments with a refined position (down to a few arcseconds for Swift/XRT). The X-ray localisation allows narrow field telescopes to search for an optical counterpart. More than half of GRBs with a Swift X-ray afterglow are also detected in UV/IR frequencies. On the other hand, as we will see below, the detection rate of radio afterglows is low, because of the synchrotron self-absorption in the early radio afterglow and the insufficient sensitivity of current radio devices.

In the following we discuss the afterglow properties in several energy bands.

### X-ray afterglow

X-ray afterglows were discovered in 1997 by BeppoSAX (Costa et al. 1997). Prior to Swift, X-ray data were sparse, due to (i) the delay of several hours from the GRB detection needed to the NFI to start observing, and (ii) the rapidly fading of the emission. Swift dramatically improved this situation with minute-scale NFI observations due to which more than 95% of Swift GRBs have an X-ray afterglow and their light-curves are much more complete (starting seconds after the burst up to several days at least). These results yielded a canonical picture of the X-ray afterglow (Fig. 1.5, left).

The temporal evolution of X-ray afterglow light-curve is smooth, driven by an underlying continuum that may be composed of different segments and, sometimes, flaring activity. As we can see in Fig. 1.5 (left), usually the X-ray afterglow is characterised by five components:

1. *Steep decay phase.* The early X-ray afterglow is described by a steep decay phase, usually explained by the high-latitude “curvature effect”<sup>13</sup> (Kumar & Panaitescu 2000; Zhang et al. 2006); typical power-law indices are steeper than  $-3$ , sometimes even as steep as  $-10$ . This steep decay is smoothly connected to the tail of the prompt emission, when BAT and XRT data are both available (Barthelmy et al. 2005).
2. *Shallow decay phase.* After  $10^2 - 10^3$  s the steep decay may be followed by a plateau regime (with a slope  $\gtrsim -0.5$ ), occasionally even slightly rising in the beginning. These

<sup>13</sup>This effect describes the observed radiation from the relativistic GRB ejecta; it depends on the Doppler effect, and hence on the angle  $\theta$  between the emission direction and the observer.



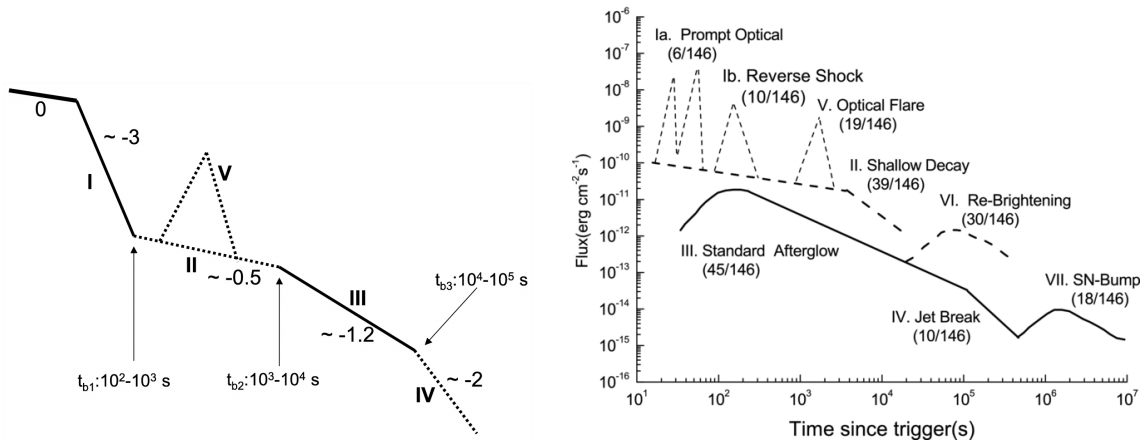


**Figure 1.5:** Synthetic cartoon of a light-curve of multiple emission components as observed by Swift/XRT (left) and by optical telescopes (right). For the X-ray case (left), the phase “0” denotes the prompt emission, segments I and III (solid lines) are most common, whereas the other three components (dashed lines) are less frequent. Figure reproduced from (left) Zhang et al. (2006) and (right) Li et al. (2012).

plateaus can be understood through the standard external shock model with continuous energy injection into the blastwave (e.g. Zhang et al. 2006; Nousek et al. 2006; Rees & Meszaros 1998; Zhang 2011).

3. *Normal decay phase.* This phase takes place at typical times  $10^3 - 10^4$  s, usually with index  $\sim -1$ , but sometimes with index  $\lesssim -3$ .
4. *Jet break phase.* A late time steep decay (index  $\lesssim -2$ ) can occasionally follow. This is compatible with the so-called jet break (Rhoads 1999; Sari et al. 1999 and Sect. 3.4).
5. *X-ray activity.* Nearly half of X-ray afterglows of Swift GRBs shows a flaring activity, consisting in one or more flares, suggesting a probable common origin with the prompt emission (Burrows et al. 2005b; Chincarini et al. 2010).

### Optical afterglow

In the pre-Swift era, GRB afterglows were observed in the optical bands several hours after the GRBs. The late-time optical light-curves usually exhibited a single power-law decay with a decay index  $\alpha \sim -1$ , and sometimes a two-segment broken power-law with a temporal break between  $\alpha_1 \sim -1$ , and  $\alpha_2 \sim -2$ , suggesting jetted emission (Sect. 2.3). These light-curves show seven different emission components (Fig. 1.5, right): (Ia) prompt optical flares, (Ib) early optical flares from RS, (II) early shallow decay segment, (III) the standard afterglow component (sometimes led by an afterglow onset hump due to deceleration), (IV) the post jet break phase, (V) optical flares, (VI) rebrightening humps, and (VII) late SN bumps (Zhang et al. 2016). The components II–V can find their X-ray counterparts (Melandri et al. 2008).

The peak time in these light-curves can be used to estimate the initial Lorentz factor  $\Gamma_0$  of the ejecta during the afterglow phase (e.g., Molinari et al. 2007; Melandri et al. 2010). Both  $L_p$  and the isotropic energy released by the onset bumps are correlated with  $E_{\gamma,iso}$  (Sect. 1.3.4).

In the standard external FS models (Sect. 2.1.3), optical and X-ray emission originate from the same synchrotron emission component, often characterised by achromatic hydrodynamic or geometrical temporal breaks<sup>14</sup> (e.g. the energy injection break and jet break) in the light-curves (Sect. 3.4 and 3.5). On the other hand, multi-frequency observations suggested that some GRBs

<sup>14</sup>An achromatic break should occur simultaneously in the optical and X-ray bands.

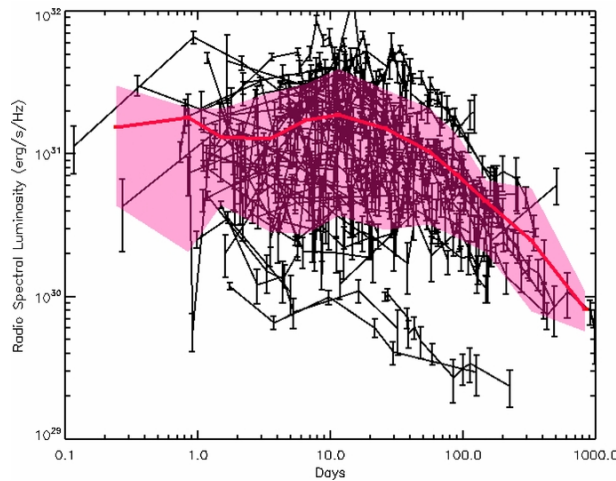


**Figure 1.6:** Radio light-curves at 8.5 GHz for the long GRBs in the observed time. The red solid line indicates the mean light-curve, and the pink shaded area represents the 75% confidence band. Figure reproduced from [Chandra & Frail \(2012\)](#).

showed chromatic behaviours in these two bands (e.g., [Panaitescu et al. 2006](#); [Liang et al. 2007](#)). A dedicated study showed that most of GRB afterglows are roughly achromatic, suggesting that the standard external shock models can be compatible with most of the afterglow observations ([Wang et al. 2015](#)).

### Radio afterglow

Radio observations of GRB afterglows are hampered by the faintness (mJy or sub-mJy) of the sources: to date the detection rate of radio afterglows is a mere  $\sim 30\%$ , to be compared with  $> 90\%$  in X-rays and  $> 70\%$  in the optical band ([Chandra & Frail 2012](#)), and this rate did not change before or after the launch of Swift. Some attempts have already been made, especially in interferometric mode (e.g., [Melandri et al. 2010](#); [Laskar et al. 2014, 2015, 2018a](#)) with the Karl Guthe Jansky Very Large Array (VLA), the Arcminute Microkelvin Imager (AMI) and the Giant Metrewave Radio Telescope (GMRT), but a conclusive picture of the radio GRB afterglow properties is still unavailable. Typically radio afterglow light-curves at 8.5 GHz show initial rising and a peak time around 3 – 6 weeks in the rest frame (Fig. 1.6, [Chandra & Frail 2012](#)), compatible with the standard external FS model where the peak corresponds to the crossing of the typical synchrotron frequency  $\nu_m$  or the self-absorption frequency  $\nu_{sa}$  in the radio band (Sect. 2.2). Moreover, radio afterglows are very important to constrain the presence of jets in GRBs (Sect. 2.3) and the synchrotron spectral slope (Sect. 2.2).

Predicting the radio flux is no easy task, as there is no obvious correlation between radio afterglows and other observables (such as the optical magnitude or the gamma-ray fluence) and modelling of the optical/X-ray emission and extrapolation to the radio band suffers from degeneracies in the model parameter space. Most radio afterglows have optical and X-ray counterparts ([Chandra & Frail 2012](#)). The most reasonable approach to maximise the chance to detect them is interpreting the optical and X-ray data through a simple synchrotron model. Some well-monitored bright GRBs show an early radio flare (e.g. GRB 990123, [Kulkarni et al. 1999](#); GRB 130427A, [Anderson et al. 2014](#)), which is usually attributed to the RS emission ([Sari & Piran 1999](#); [Kobayashi & Zhang 2003b](#)).

### High-energy afterglow

GRB afterglows at high-energies are important to understand the physics of GRB, such as the role of inverse Compton (Sect. 3.8). The first detection of high-energy afterglow – conventionally emission above 100 MeV – regarded the observation of GRB 940217 in GeV energies with CGRO (Hurley et al. 1994). Fermi/LAT detected a small fraction of GRBs in the GeV range (15 – 20 detection per year above 100 MeV, Ajello et al. 2019), because of the limited effective area; nevertheless, this rate exceeds expectations (10 – 12 GRBs per year above 100 MeV, Band et al. 2009) in large part due to the continuous improvements in event analysis and detection algorithms (Ajello et al. 2019). Usually these GRBs are characterised by high-energy emission with duration longer than the prompt emission itself, suggesting an afterglow origin (e.g., Abdo et al. 2009; Ackermann et al. 2010; Ghisellini et al. 2010). These light-curves typically show a power-law decay, with an early steep-to-shallow break transition (Zhang 2011; Ackermann et al. 2013; Ajello et al. 2019).

GeV/TeV afterglows can be observed by ground-based telescopes through the detection of the Cherenkov radiation, such as MAGIC, HESS, VERITAS (Very Energetic Radiation Imaging Telescope Array System), and in the coming future CTA (Cherenkov Telescope Array). After many unfruitful attempts, recently MAGIC telescopes revealed TeV radiation from a GRB for the first time, detecting intense, long-lasting emission between 0.2 and 1 TeV from GRB 190114C (MAGIC Collaboration et al. 2019a,b). Similarly, the High-Energy Stereoscopic System (hereafter, H.E.S.S.) imaging air Cherenkov telescope array collaboration reported the detection of GRB 180720B above 100 GeV (Ronchi et al. 2019 and references therein).

## 1.3 GRB classification: progenitors and correlations

GRBs are mainly classified in two categories based on their duration and hardness properties: short/hard (hereafter S-GRBs) and long/soft GRBs (hereafter L-GRBs), respectively, that has been attributed to two different progenitor types. Several correlations between temporal and spectral properties have been found; among them, one of the most important is the “Amati relation” (Amati et al. 2002; Amati 2006), relating the rest-frame peak energy of the  $\nu F_\nu$  spectrum,  $E_p$ , to the isotropic-equivalent released energy  $E_{\text{iso}}$  in the  $1 - 10^4$  keV rest-frame energy band,  $E_{\gamma,\text{iso}}$  (Sect. 1.3.4).

### 1.3.1 Short/hard vs. long/soft GRBs

The traditional phenomenological classification scheme (Kouveliotou et al. 1993) arises from the evidence of a bimodal distribution in the observer-frame<sup>15</sup>  $T_{90}$ /hardness ratio space (Fig. 1.7), where the spectral hardness is evaluated through the peak energy  $E_p$  in the  $E^2N(E)$  spectrum. As showed in Fig. 1.7, a rough separation between L-GRBs and S-GRBs is set at  $T_{90} = 2$  s, and L-GRBs tend to have a softer spectrum. S-GRBs and their afterglows are significantly fainter than L-GRBs and span a distribution of isotropic energies  $10^{49} - 10^{52}$  erg; moreover, the redshift of S-GRBs usually ranges between 0.1 and 3, with a median 0.5, much smaller than that of L-GRBs ( $z \sim 2$ ). Sometimes the same GRB – observed by two different instruments – could appear both short and long, as  $T_{90}$  depends on the energy band and the sensitivity of the detector (Sect. 1.2.1). In all observed samples, S-GRBs are less numerous than L-GRBs: for example, about 25% of BATSE GRBs and ( $\sim 10\%$  for Swift) are S-GRBs. This reflects both the fewer number of photons of S-GRBs and the inefficient effective area of instruments and a

<sup>15</sup>Since no GRB redshift is available at early-time (a few seconds), rest-frame duration is unknown; these works are therefore based on observer-frame duration.



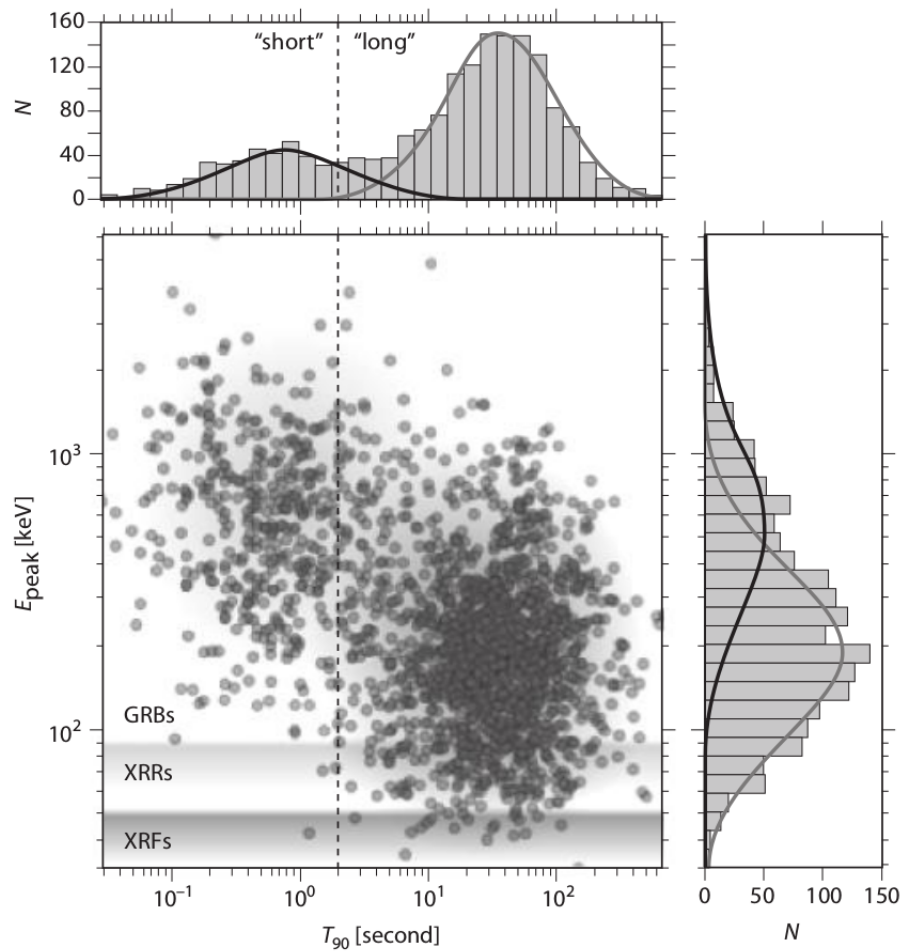


**Figure 1.7:** The spectral-duration distribution of GRBs, as seen by BATSE, shows the bimodal GRB distribution in terms of  $T_{90}$  (X-axis) and spectral hardness (Y-axis), evaluated through the peak energy  $E_p$ . Two regions can clearly be distinguished, even if there is a significant overlap between them. Outset histograms show the number of events in appropriate duration and energy bins. Figure reproduced from Bloom (2011).

poor coverage of detectors with observing energy above 100 keV: the same detector collects fewer photons for S-GRBs than L-GRBs, resulting in a worst statistics in the data analysis for S-GRBs. In this context, the High Energy (HE) unit onboard the Chinese “Hard X-ray Modulation Telescope” (HXMT) – launched in 2017 and designed for GRB observations – plays an important role because it is particularly suitable to detecting S-GRBs above a few hundreds of keV: in particular, its large effective area ( $\sim 5000 \text{ cm}^2$ ) and the broad energy range (0.2 – 3 MeV) allows to constrain – with unprecedented accuracy – the spectral shape of S-GRBs, in terms of the spectral peak energy  $E_p$  and the radiated energy (Wu et al. 2002, 2004; Li 2007).

Additional evidence for a distinct origin between long and short GRBs classes arises from the study of spectral lags, defined as a delay between the arrival time of high-energy photons with respect to lower energy ones. By definition, a positive spectral lag corresponds to the case where soft photons lag behind hard ones. In general, S-GRBs have negligible spectral lags, as opposed to L-GRBs which are characterised by positive lags (Norris et al. 2010).

### 1.3.2 Other GRB classifications

The simple and somewhat naive long/short GRB classification is complicated by other phenomenological aspects, in particular:

- among the class of L-GRBs, there is the sub-class based on their luminosities, with a separation line roughly at  $10^{48} - 10^{49} \text{ erg s}^{-1}$ . The so-called “low-luminosity GRBs” (ll-GRBs) are characterised by smoother light-curves and a local volumetric event rate density of  $\sim 100 \text{ Gpc}^{-3} \text{ yr}^{-1}$  (Guetta & Della Valle 2007; Liang et al. 2007), much larger than the traditional high-luminosity GRBs. However, the separation between ll-GRBs and HL-GRBs is still unclear.
- The existence as a separate class – to date under debate (Virgili et al. 2013; Zhang et al. 2014; Boer et al. 2015; Gao & Mészáros 2015) – of rare ultra-long GRBs, with durations  $T_{90} \gtrsim 1000 \text{ s}$ , discovered during the Swift era (Gendre et al. 2013; Levan et al. 2014).
- GRBs with both short and long GRB properties have been observed (e.g., GRB 060614 and GRB 060605 Della Valle et al. 2006; Fynbo et al. 2006; Gal-Yam et al. 2006). They seem to challenge the above dual classification scheme. Simulations suggest that the observer-frame duration does not increase substantially with increasing redshift because part of the signal falls below the background level (e.g., Lü et al. 2014).
- The existence – in addition to the long and short GRBs – of a third (and even of a fourth) class of intermediate duration GRBs (e.g., Ripa & Meszaros 2015), but the statistical support is limited and they do not seem to have any other distinctive property, that would help identify them as a physically separate class.
- There is a broadband afterglow-classification: GRBs can be classified as optically bright and optically dark GRBs (Jakobsson et al. 2004; Rol et al. 2005). The X-ray afterglow data suggests the classification between GRBs with X-ray flares and those without (Zhang et al. 2016), or those following a canonical multi-segment light-curve (Zhang et al. 2006; Nousek et al. 2006) and those following a single power-law decay (Evans et al. 2009; Liang et al. 2009).
- Some further prompt emission properties are useful for the duration classification scheme (Zhang et al. 2016). In particular, spectral lags are often used to discriminate between the two classes (e.g. Gehrels et al. 2006).

These properties help infer their physical origin and suggest possible more elaborate classification criteria/schemes. Based on observational properties and theoretical modelling of GRBs over the years, GRBs are physically classified into different categories:

- *Massive star (Type II) vs. Compact star (Type I) GRBs*: the former category – associated with deaths of massive stars – roughly correspond to the L-GRBs, and latter roughly correspond to the S-GRBs, even if there are ambiguous cases (e.g., [Gehrels et al. 2006](#); [Della Valle et al. 2006](#); [Levesque et al. 2010](#); [Antonelli et al. 2009](#)). This GRB classes are defined Type I and Type II GRBs, with a multiple observational criteria to identify the physical category of a certain GRB ([Zhang et al. 2006, 2007, 2009](#); [Kann et al. 2010, 2011](#)).
- *Successful vs. choked jets*: type II GRBs can be further classified into successful (associated with the traditional HL-GRBs) and choked (associated with some II-GRBs such as GRB 060218, e.g. [Nakar & Sari 2012](#); [Bromberg et al. 2012](#)) jets.
- *GRBs with different central engines*: For both long and short GRBs, two types of central engines models are described the literature: hyper-accreting BHs (e.g., [Narayan et al. 1992](#); [Woosley 1993](#); [Popham et al. 1999](#)) and rapidly rotating magnetars (e.g., [Usov 1992](#); [Metzger et al. 2011](#)). Signatures of magnetar spin-down have been detected in both long and short GRBs (e.g., [Lü & Zhang 2014](#)); in particular, a possible magnetar central engine for S-GRBs (e.g., [Dai et al. 2006](#); [Fan & Xu 2006](#); [Metzger et al. 2008](#)), if verified by future GW data, would have crucial implications in constraining poorly known NS equation of state (e.g., [Lasky et al. 2014](#); [Lü et al. 2015](#); [Gao et al. 2016](#)) and in searching for electromagnetic counterparts of GW events (e.g., [Gao et al. 2016](#); [Yu et al. 2013](#)).

### 1.3.3 GRB environments and progenitors

The GRB environment – both at a large scale and at a Galactic scale – suggests the nature of their progenitor systems. Usually, S-GRBs originate from old stellar populations, while L-GRBs are good indicators of star formation and hence are related to young, massive stellar populations.

#### Short GRBs

S-GRBs, as opposed to L-GRBs, are characterised by the heterogeneity of their host galaxies (early-type, late-type, or unknown-type), suggesting that their progenitors span a broad range of ages ([Fong et al. 2013](#); [Berger 2014](#)). In particular, about half of Swift S-GRBs are associated with a host galaxy; the resulting sample is mainly composed by S-GRBs associated with late-type galaxies ( $\sim 50\%$ ), usually characterised by young stellar populations ([Berger 2014](#)). However, the presence of S-GRBs in late-type galaxies is not necessarily the signature of a young progenitor, as in the case of GRB 050709, where there is no association with a star-forming region ([Fox et al. 2005](#)). Generally, S-GRBs under-represent their host light, and they are often discovered away from the galactic centre, suggesting that S-GRBs occur on average five times farther from the centre than L-GRBs ([Fong et al. 2010](#)), compatible with compact object binaries that travelled for enough time before merging, due to large natal kicks following SN explosions ([Paczynski 1998](#)).

Moreover, the specific star-formation rate of S-GRB hosts is much lower than that of L-GRB hosts, at less than  $1 M_{\odot} \text{yr}^{-1} (L/L_{*})^{-1}$  compared to  $\sim 10 M_{\odot} \text{yr}^{-1} (L/L_{*})^{-1}$ , where  $L$  indicates the luminosity of the galaxy and  $L_{*}$  is the characteristic luminosity compatible with that of the Milky Way. These aspects results in a progenitor consistent with the merger of compact objects (NS-NS and NS-BH mergers). The gravitational wave (GW) observations already confirmed the

NS-NS merger progenitor (GW 170817/GRB 170817A, [Abbott et al. 2017b](#)) and will tell whether NS-BH mergers can also make S-GRBs. Some indirect features to the NS-NS merger progenitor is the extended emission (e.g. [Norris & Bonnell 2006](#)), internal plateaus (e.g. [Rowlinson et al. 2010](#)), and X-ray flares (e.g. [Barthelmy et al. 2005](#)) following S-GRBs; these features suggest that the central engine of S-GRBs may be a stable or supra-massive magnetar (e.g. [Metzger et al. 2008](#); [Gao et al. 2013b](#); [Metzger & Piro 2014](#)), compatible with the NS-NS merger progenitor (a NS-BH merger would not result in a magnetar). S-GRBs can have a non-merger origin; for example, the scenario invoking accretion-induced collapse (AIC) of a NS to a BH (e.g. [Qin et al. 1998](#); [MacFadyen et al. 2005](#); [Dermer & Atoyan 2006](#)) seems to satisfy most of the observational constraints.

### Long GRBs

Usually L-GRBs are discovered in dwarf, blue, irregular galaxies with a high star-formation rate; in rare cases, a few nearby events occurred in star-forming regions of spiral galaxies ([Fruchter et al. 2006](#)). Moreover, L-GRBs are detected preferentially in the brightest regions of their hosts, suggesting a high specific star-formation rate ([Graham & Fruchter 2013](#)). The main type of progenitor star is the Wolf-Rayet (WR), a rapidly rotating massive star with hydrogen and helium envelope lost before core collapse ([Woosley 1993](#); [MacFadyen & Woosley 1999](#)). The association L-GRBs/Ic-SNe (Sect. 1.5) is consistent with such a progenitor. On the other hand, the progenitor stars of ultra-long GRBs could be characterised by a larger size, e.g. blue supergiants ([Mészáros & Rees 2001](#); [Kashiyama et al. 2013](#); [Greiner et al. 2015](#)), but to date no smoking-gun signature has been identified. To date, the only case of ultra-long GRB whose associated SN could be studied is GRB 111209A: the high luminosity and the low metallicity of the associated SN 2011kl can be explained by a model with energy injection from a magnetar, which has also been proposed as the explanation for super-luminous SNe ([Greiner et al. 2015](#)).

The main differences between long and short GRB host galaxies, in the same redshift range  $z \lesssim 1.1$ , consist in ([Berger 2009](#)):

- L-GRB hosts are subluminal with respect to S-GRB hosts by an average value of  $M_B \sim 1.1$  mag.
- The star-formation rate of L-GRB and S-GRB hosts are  $0.2 - 50 M_\odot \text{ yr}^{-1}$  and  $0.2 - 6 M_\odot \text{ yr}^{-1}$  respectively, and the specific star-formation rate of L-GRB hosts is  $3 - 40 M_\odot \text{ yr}^{-1} L_*^{-1}$ , one order of magnitude higher than that of S-GRB hosts.
- The metallicity of L-GRB hosts is lower than that of S-GRB hosts, with mean values of  $12 + \log(O/H) \approx 8.3$  and  $12 + \log(O/H) \approx 8.8 \approx 1 Z_\odot$ , respectively.
- Generally the stellar mass of L-GRB hosts is lower than that of S-GRB hosts, with mean values of  $10^{9.2} M_\odot$  and  $10^{10} M_\odot$ , respectively ([Berger 2014](#)); single stellar population models infer the mean age of the stellar population (60 Myr for L-GRBs and 0.25 Gyr for S-GRBs, [Leibler & Berger 2010](#)).

These considerations suggest that the progenitor of L-GRBs is connected with the death – near their birth place – of massive and short-lived stars.

### 1.3.4 GRB empirical correlations

The beaming-corrected total burst energy clustered around  $10^{51}$  erg ([Frail et al. 2001](#)) suggests a stellar origin, but unfortunately does not allow to use cosmological GRBs as standard luminosity

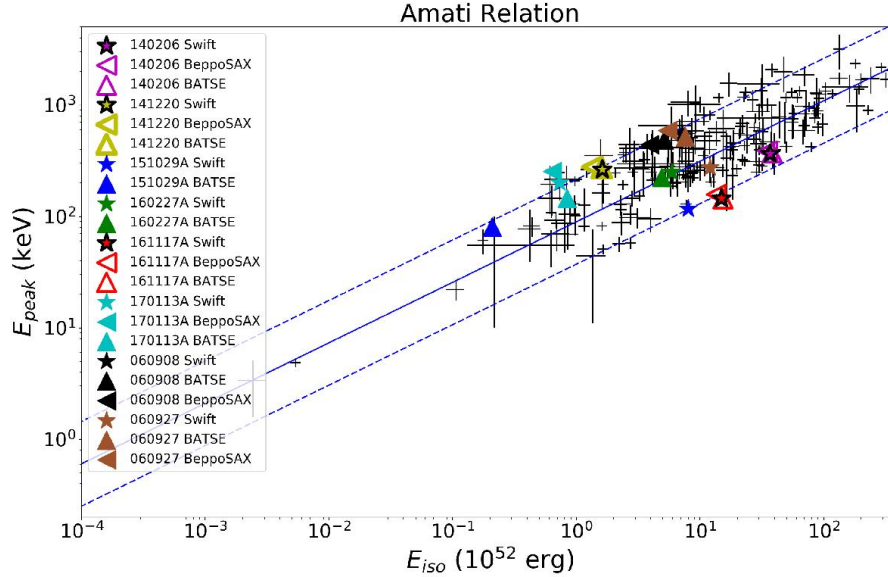


**Figure 1.8:** Amati correlation for cosmological GRBs. Figure reproduced from [Martone et al. \(2017\)](#).

candles, whose apparent brightness would provide a distance determination ([Mészáros 2006](#)). The search for empirical correlations between burst observable parameters is crucial to measure the distance of cosmological GRBs only with gamma-ray data; moreover, the search for these correlations help gain insight into the mechanism of the prompt gamma-ray emission and the activity from GRB central engine (e.g. [Kocevski 2012](#)). The exact origin of the correlations is still under debate: some groups suggest that they arise as a by-product of detector selection effects (e.g. [Nakar & Piran 2005](#)), but this interpretation is refuted by the existence of a given correlation in the time-resolved data (e.g. [Ghirlanda et al. 2010](#)).

As previously anticipated above, one of the most used and studied correlations is the Amati correlation, valid only for L-GRBs (Fig. 1.8). This correlation is characterised by a rather broad scatter and some outliers (such as the case of GRB 980425); S-GRBs follow a similar but different correlation ([Zhang et al. 2012](#); [Calderone et al. 2015](#)). The  $E_p - E_{\gamma,iso}$  correlation with 41 GRBs is defined as [Amati \(2006\)](#):

$$\frac{E_p}{1 \text{ keV}} = (81 \pm 2) \left( \frac{E_{\gamma,iso}}{10^{52} \text{ erg}} \right)^{0.57 \pm 0.02} \quad (1.3)$$

A tighter GRB correlation – so-called Ghirlanda relation ([Ghirlanda et al. 2004](#)) – between  $E_p$  and the beaming-corrected energy  $E_\gamma$  was calculated, assuming that the temporal breaks found in the pre-Swift afterglows are jet breaks, as:

$$\frac{E_p}{100 \text{ keV}} \simeq 4.8 \left( \frac{E_\gamma}{10^{51} \text{ erg}} \right)^{0.7} \quad (1.4)$$

Subsequent analysis suggested that the Ghirlanda relation becomes less tight, especially when the early-time jet breaks are included in the analysis ([Wang et al. 2018](#)).

Other correlations have been claimed; among these, there are the spectral lag  $\tau_{lag}$  – isotropic peak luminosity  $L_{iso}$  ([Norris et al. 2000](#)), the variability  $V - L_{iso}$  ([Reichart et al. 2001](#)), and the  $E_p - L_{iso}$  ([Yonetoku et al. 2004](#)).

## 1.4 Polarisation in the GRB emission

The main component of the GRB emission is the synchrotron (non-thermal) radiation (Sect. 2.2).



Synchrotron emission can be strongly polarised in an ordered magnetic field + non-spherical geometry, whereas the overall observed polarisation can be negligible in the case of random magnetic fields. The polarisation light-curves may provide useful constraints on the jet structure and the average magnetic configuration in the emitting region, but it is rather difficult to constrain each of these two ingredients separately (Granot 2007).

### 1.4.1 Afterglow emission

Linear polarisation of a few percent has been detected in the late-time optical/NIR afterglow of several GRBs (e.g., Covino et al. 2004), confirming that synchrotron radiation dominates the afterglow emission mechanism. This detection is compatible with the expectation of the external forward shock model (Sect. 2.1.3), in which the magnetic fields seem to be generated by plasma instabilities (e.g. Medvedev & Loeb 1999; Nishikawa et al. 2009) or macroscopic turbulence (e.g., Sironi & Goodman 2007). On the other hand, X-ray emission components (directly powered by the central engine) may be linearly polarised, with a moderately high polarisation degree (e.g., Fan et al. 2005), but – to date – there is no X-ray polarimeter with rapid slewing capability to observe the X-ray polarisation of GRBs (Zhang 2019).

Since the afterglow image is almost always never resolved, the only possible measurement is the average polarisation over the whole image. For this reason, a shock-produced magnetic field (symmetric about the shock normal) results in no net polarisation for a spherical flow; the production of net polarisation takes place from the break of the spherical symmetry of the flow, and hence considering a jetted outflow (e.g., Sari et al. 1999; Ghisellini & Lazzati 1999). In this scenario, the combination between a jet geometry and a line of sight slightly off-axis with respect the jet symmetry axis is crucial to break the symmetry of the afterglow image around the line of sight (e.g., Granot & Ramirez-Ruiz 2010).

The different predictions for the afterglow polarisation light-curves for different jet structures imply that afterglow polarisation observations could constrain the jet structure (e.g., Ghisellini & Lazzati 1999; Rossi et al. 2004). However, the situation is much more complicated, mainly since the observed polarisation depends not only on the jet geometry, but also on the magnetic field configuration within the emitting region; to date, several models have been proposed (e.g., Loeb & Perna 1998; Gruzinov 1999; Medvedev & Loeb 1999; Granot & Königl 2003), but the exact configuration is not well known.

Early-time optical afterglow observations revealed interesting polarisation signatures, using a ring imaging polarimeter on the robotic Liverpool Telescope (e.g. Steele et al. 2006, 2017). These observations showed signatures of reverse-shock emission in the light-curves, lending support to the presence of large-scale magnetic fields in mildly magnetised GRB ejecta (Steele et al. 2017). GRB 060418 is characterised by a smooth hump in its light-curve, suggesting a forward-shock-dominated light-curve, and it shows a derived upper limit on the polarisation of  $< 8\%$  (Mundell et al. 2007b); this is consistent with the late-time forward-shock synchrotron origin of the afterglow, in which no significant ordered B field is expected. On the other hand, GRB 090102 had a reverse-shock-dominated light-curve with a polarisation of  $10 \pm 2\%$  (Steele et al. 2009), suggesting that the emission region carries a significantly ordered magnetic field; this is compatible with the magnetised central engine scenario, where a bright reverse shock emission in a moderately magnetised ejecta takes place after a magnetic dissipation in the prompt emission phase (e.g., Fan et al. 2002; Zhang et al. 2003; Kumar & Panaitescu 2003). GRB 120308A, another GRB with a reverse-shock-dominated light-curve, was found to have a variable polarisation degree (Mundell et al. 2013); this is consistent with the transition from the reverse-shock-dominated phase to the forward-shock-dominated phase (Zhang et al. 2015b; Lan et al. 2016), again consistent with an (almost) ordered magnetic field in the ejecta. The

generation of ordered magnetic fields in the forward shock is still unclear, although a proposal was put forward (e.g., Uehara et al. 2012). Alternatively, a long-lasting reverse shock can also originate the desired afterglow decay index (Uhm et al. 2012). The high polarisation degree may then be expected, if emission from a long-lasting reverse-shock outshines the forward-shock component (Zhang 2019).

### 1.4.2 Prompt emission

Compared to the optical, NIR, or radio bands, at high-energy frequencies (hard X-rays/soft gamma-rays) the nature of the dominant emission mechanism remains uncertain, and it is very difficult to measure the linear polarisation.

An ordered magnetic field within the outflow (e.g., Granot & Königl 2003; Lyutikov et al. 2003), a shock-generated magnetic field (e.g., Granot 2003; Waxman 2003; Nakar et al. 2003) or bulk inverse-Compton scattering of an external photon field (Shaviv & Dar 1995; Lazzati et al. 2004) can produce a high net polarisation, of tens of percent, slightly smaller than the maximal polarisation of the local synchrotron emission. This requirement may be compatible with brightest GRBs, for which the prompt polarisation can be measured, as such bright events usually correspond to very narrow jets. Nevertheless, statistical studies over a sample of GRBs, or time resolved polarimetry of different emission episodes for a single very bright GRB, may allow (i) a better comprehension of the dominant emission mechanism, the jet structure, or the magnetic field configuration within the GRB outflow, and (ii) a better distinction between the different possible causes for polarisation.

The first claims of detection of a high degree of linear polarisation in the prompt emission of some GRBs have been rather controversial (e.g., Coburn & Boggs 2003; Rutledge & Fox 2004; Wigger et al. 2004; Willis et al. 2005; McGlynn et al. 2007; Götz et al. 2009), but the subsequent claimed detection are characterised by a better significance (Yonetoku et al. 2011, 2012). To date, despite the promising recent measurement with both the Chinese POLAR experiment aboard the China’s spacelab Tiangong-2 (Zhang et al. 2019) and the CZT Imager (CZTI) aboard AstroSat (Chattopadhyay et al. 2019), all GRBs with gamma polarimetry measurements are still characterised by a limited statistical significance ( $< 3 - 4\sigma$ , McConnell 2017)<sup>16</sup>. These observations show no clear picture of the polarisation properties of GRBs. On the other hand, data suggest that, at least for some bright GRBs, the prompt gamma-ray emission likely has a relatively large level of linear polarisation (typically,  $> 50\%$ ), suggesting a synchrotron emission associated with an ordered magnetic field structure within the GRB jet (McConnell 2017).

## 1.5 The GRB-SN connection

Prior to GRB discoveries, it had already been suggested that SN shock breakouts may generate an observable signature in gamma-rays (Colgate 1968, 1974). Later, Paczynski (1986) noted that if GRBs were to have cosmological origin, the energy released in gamma-rays would be compatible with that released by a typical SN. Theoretically the collapsar model (Woosley 1993) connected GRBs to SNe. Observationally, after about thirty years of unfruitful attempts caused by the inaccurate GRB localisation, *BeppoSAX* enabled the first direct evidence for a GRB-SN connection (SN 1998bw/GRB 980425; Galama et al. 1998). Successively, the rapid and accurate localisation of GRB afterglows on a routine basis allowed to pinpoint star-forming regions as GRB birthplaces (Bloom et al. 2002).

<sup>16</sup>Although the diminished systematic errors, the statistical significance is still at about  $3\sigma$  level, also due to the low polarisation found.

SNe are believed to originate in two types of explosions (e.i. [Maoz et al. 2014](#); [Woosley & Heger 2015](#)): (1) thermonuclear explosion of either an accreting white dwarf or, more likely, two merging white dwarfs; (2) explosive phenomena originating from the terminal gravitational collapses of the core of massive stars (core-collapse SNe). SNe are usually classified according to their spectral properties ([Filippenko 1997](#)). Among SN population, Type I SNe, characterised by the absence of hydrogen spectral lines, are subdivided in type Ia (presence of helium and silicon lines), type Ib (presence of helium lines, absence of silicon lines), and type Ic (absence of helium lines). White dwarf-related SNe are Ia SNe, whereas all other types originate from core-collapse events.

Usually GRB-SN connections are compatible with type Ib/c (e.g., [Liang et al. 2007](#); [Cano et al. 2017](#)), even though type II SNe have been occasionally suggested ([Garnavich et al. 2003](#); [Gorosabel et al. 2005](#)). GRB-SNe fall on the luminous end tail of the distribution of type Ib/c SNe and they are characterised by broad spectral lines<sup>17</sup>, implying a high ejecta velocity ( $\gtrsim 2 \times 10^4$  km s<sup>-1</sup>, e.g. [Mazzali et al. 2002](#); [Cano et al. 2017](#)),  $\sim 10^4$  km s<sup>-1</sup> faster than in “ordinary” Ic SNe ([Modjaz et al. 2016](#)), suggesting energetic explosions. Within type Ic SNe, a small fraction are broad-line (BL-Ic SNe) and, out of those, only a small fraction is observed with L-GRB counterparts. However, other features of this SN population do not seem to follow common behaviours: thus the distributions of peak brightness, rise times, or broadness of the spectral lines for instance are affected by a large dispersion.

Since SNe are detectable – through current facilities – at redshift  $z \lesssim 1$ , the direct evidence of GRB/SN connection is possible only for nearby GRBs.

### 1.5.1 Observational evidence

The first well-studied example of GRB-SN occurred for GRB 980425/SN 1998bw (e.g., [Kulkarni et al. 1998](#); [Li & Chevalier 1999](#); [Pian et al. 2000](#)) where the optical GRB afterglow, instead of fading, was getting brighter, suggesting that this signal was the rising emission from the bright and peculiar SN 1998bw ([Galama et al. 1998](#)). This SN was classified as BL-Ic SN, indicating that the optical spectral lines are broadened because the photosphere was expanding at high velocity ( $> 0.1c$ ). However, the proximity of GRB 980425 ( $z = 0.0085$ ), an unusual event with an extremely low energy output ([Kaneko et al. 2007](#)), did cast doubts on the possibility of extending the GRB-SN association to cosmological GRBs.

Supporting evidence for the GRB-SNe association was supplied by the observation of a SN-like bump in the optical afterglow ([Reichart 1997](#); [Bloom et al. 1999](#)), and the confirmation came through the spectroscopic identification of SN 2003dh following GRB 030329, exploded at  $z = 0.1685$  (e.g., [Hjorth et al. 2003](#); [Vanderspek et al. 2004](#); [Lipkin et al. 2004](#)). To the time of writing (end of 2019), a total of  $\sim 50$  GRB-SN associations have been identified (e.g. [Klose et al. 2019](#)).

### 1.5.2 Detectability of GRB-SN

The association of L-GRBs with star-forming environments (Sect. 1.3.3) and the first observations of GRB-SNe suggested that all L-GRBs could be connected to SNe; this scenario was corroborated by the collapsar model (Sect. 2.5.1), and it was believed that the absence of a SN counterpart was a characteristic of S-GRBs. However, subsequent observations showed that not all the BL-Ic SNe are connected with a GRB counterpart. In particular, in the local universe

<sup>17</sup>Doppler broadening of the spectral lines occurs when the SN ejecta moves in different directions, resulting in dispersion of the radial velocity; the higher the ejecta velocity, the larger the radial velocity dispersion, resulting in broader lines.



( $z \leq 0.1$ ) some BL-Ic SNe have also been found in association with mildly relativistic outflows in II-GRBs, which are too weak to be detected at larger distances, [Liang et al. 2007](#); as opposed to L-GRBs, II-GRBs show no evidence for jetted ejecta ([Kulkarni et al. 1998](#); [Soderberg et al. 2006a](#); [Bromberg et al. 2011](#)).

A possible interpretation of this observational lack of evidence for L-GRB counterparts in the majority of BL-Ic SNe could be the off-axis jet scenario ([Rhoads 1999](#); [Eichler & Levinson 1999](#); [Yamazaki et al. 2003](#); [Piran 2004](#); [Soderberg et al. 2006b](#); [Bietenholz 2014](#); [Corsi et al. 2016](#)), where the SN explosion powers a GRB-like jet that is misaligned with respect to the observer line of sight; as the jet velocity gradually decreases, resulting in a broader relativistic beaming, the emission becomes observable from increasingly larger viewing angles. Deep radio and X-ray observations extending to hundreds of days post explosion offer the opportunity to reveal the emission from off-axis jets as well as to recover weak GRBs that would not trigger current gamma-ray observing facilities.



# Chapter 2

## Theoretical framework of GRB emission

In this chapter I focus on the theoretical understanding of GRBs through the description of the standard framework – called fireball model – usually adopted by the community to describe GRBs and infer their physical nature. This model is very generic, and does not depend on the actual acceleration mechanism of the jet. Once a relativistic jet is launched from the progenitor, the model can give estimates on the consequent synchrotron radiation due to the internal and external dissipation processes. After the theoretical aspects of this model (Sect. 2.1), I present the physics of the GRB emission, based mainly on synchrotron radiation (Sect. 2.2). I then describe the jetted radiation of GRB ejecta (Sect. 2.3), and its transition to Newtonian regime (Sect. 2.4). Finally, I briefly review the central engines that have been proposed as GRB progenitor candidates (Sect. 2.5).

## 2.1 The fireball model

This model, first proposed by [Cavallo & Rees \(1978\)](#), is considered the standard framework to explain GRB observations. A fireball occurs when a compact source releases a large amount of energy ( $\sim 10^{53}$  erg), regardless of the central engine origin. The quasi-thermal equilibrium between radiation and matter generates an opaque radiation-electron-positron plasma accelerated to relativistic velocities (characterised by Lorentz factors of  $\gamma \sim 10^2 - 10^3$ ). The presence of baryons makes this plasma opaque to Thomson scattering, allowing the acceleration of the fireball until a considerable fraction of the initial energy has been converted into bulk kinetic energy ([Goodman 1986](#); [Paczynski 1986](#); [Shemi & Piran 1990](#)).

### 2.1.1 The compactness problem

The first theoretical clues to the ultra-relativistic nature of GRBs arose from the compactness problem, as first discussed by [Ruderman \(1975\)](#). This problem arises from the contradiction between the non-thermal spectrum observed for GRBs (Sect. 1.2.1) and the fact that the source appears to be optically thick (assuming non-relativistic expansion). The simplest way to see the compactness problem consists in the estimation of the average opacity of the high energy gamma-ray to pair production. First of all, the variability  $\delta t$  observed in the gamma-ray light-curves (up to tens of milliseconds) constrains the size  $R$  of the GRB emitting region. In this situation, the time taken by the photons to cross an object (the light crossing time) produces a natural timescale for  $\delta t$ ; a typical value  $\delta t \approx 10$  ms implies a compact source with size  $R \lesssim c\delta t \approx 3000$  km ([Piran 2004](#)).

A compact source implies a very large optical depth  $\tau_{\gamma\gamma} \sim \sigma_T R n_{ph}$ , where  $\sigma_T$  is the Thomson cross-section (for photon-photon interaction producing  $e^+/e^-$  pairs, Eq. 2.8), and  $n_{ph}$  is the target photon number density;  $n_{ph}$  could be approximated through the rate between the typical burst isotropic energy  $E = 4\pi S d_l^2 (1+z)^{-1}$  (where  $d_l$  is the luminosity distance,  $S_\gamma$  is the fluence of the burst, and  $z$  is the redshift of the source<sup>1</sup>) and the typical photon energy  $E_\gamma \approx m_e c^2$ , over the source volume  $4\pi R^3/3$ . This results in:

$$\tau_{\gamma\gamma} \approx \frac{3\sigma_T S_\gamma d_l^2}{(1+z)m_e c^2 R^2} \quad (2.1)$$

Typical values of  $\tau_{\gamma\gamma}$  for GRBs ( $\sim 10^{15}$ ) correspond to an optically thick source, incompatible with the observed non-thermal spectrum ([Piran 2004](#)). This conundrum is solved by admitting relativistic motion of the source towards the observer with Lorentz factor  $\gamma \gg 1$ , resulting in a lower value of  $\tau_{\gamma\gamma}$ , and hence in a source optically thin ([Ruderman 1975](#)). Two effects appear in this case:

1. a relativistically expanding source can appear much smaller than that resulting from  $\delta t$ , resulting in the squeezing of the successive photons for the observer. Therefore,  $\delta t$  corresponds to  $\delta t_0/(2\gamma^2)$ , where  $\delta t_0$  is the variability in the source rest-frame.
2. the observed photons are Doppler blueshifted, and hence their energy emitted in the source rest-frame is lower by  $\gamma$ ; this reduces  $\tau_{\gamma\gamma}$  by a factor  $\sim \gamma^{-2\beta}$  ([Piran 1999](#)), where  $\beta$  is the high energy spectral index, because of the reduction in the number of photons responsible for pair production.

<sup>1</sup>For a typical GRB observed with a gamma-ray fluence  $S_\gamma \sim 10^{-6}$  erg cm<sup>-2</sup> and located at a luminosity distance  $d_l \sim 2 \times 10^{28}$  cm (corresponding to a redshift  $z \sim 1$ ), the typical burst energy is  $E \sim 2.5 \times 10^{51}$  erg.

Therefore, this ultra-relativistic motion modifies the Eq. (2.1) in:

$$\tau_{\gamma\gamma} \approx \frac{1}{2\gamma^{4-2\beta}} \frac{3\sigma_T S_\gamma d_l^2}{(1+z)m_e c^2 R^2} \quad (2.2)$$

and hence the source becomes optically thin for typical Lorentz factors  $\gamma \gtrsim 50$ . GRBs may reach values  $\gamma \gtrsim 1000$ , making these sources very unique.

The radio observation – using a Very Long Baseline Interferometry (VLBI) observational campaign – of the apparent size evolution of the afterglow region in GRB 030329 at  $z = 0.1685$  (Taylor et al. 2004) and GW 170817/GRB 170817A at  $z = 0.0099$  (Mooley et al. 2018; Ghirlanda et al. 2019), resulting in an apparent ultra-relativistic expansion speed, is crucial to directly confirm the relativistic (superluminal) motion of GRB ejecta. The scintillation in radio observations (Sect. 3.7) – knowing the distribution of galactic electrons – allows to infer the source size, in particular through the analysis of the suppression of scintillation when the angular size of the source becomes larger than the electron fluctuation scale in the interstellar medium (ISM, Frail et al. 1997).

However, before the high-energy photons can escape, the ejected matter must reach relativistic velocities; the fireball explains this emission mechanism.

### 2.1.2 The dynamical fireball evolution

The dynamical evolution of the fireball (quantified by Goodman 1986; Meszaros & Rees 1993; Kobayashi et al. 1999) consists in three phases: acceleration, coasting, and deceleration.

Let us consider a spherical outflow of radius  $r_0$ , volume  $V$  and temperature  $T$ , with total energy  $E_0$  and mass  $M_0 \ll E_0/c^2$ , adiabatically expanding (due to the high optical depth). In the comoving frame,  $TV^{1-\gamma_a}$  is constant, where  $\gamma_a$  is the adiabatic index (in this case equal to  $4/3$  since the pressure is radiation-dominated). Since  $V \propto r^3$ , the temperature evolves as  $T \propto r^{-1}$ . Conservation of energy suggests that the decreasing internal energy per particle is balanced by an increase in the bulk kinetic energy per particle (or bulk Lorentz factor  $\gamma$ ), resulting in  $\gamma \propto r$ : this describes the acceleration phase, also called radiation-dominated regime, where the most of the energy is carried by photons.

This expansion takes place at the expense of the comoving frame internal energy. Since the bulk Lorentz factor per particle cannot increase beyond the initial value of random internal energy per particle,  $\eta = E_0/M_0c^2$ ,  $\gamma$  increases as long as it reaches a maximum Lorentz factor  $\gamma_{\max} \sim \eta$  (Mészáros 2006). This describes the evolution in the coasting phase, also called matter-dominated regime, where the matter ploughing in the fireball has most of its energy in the kinetic form; in this phase the matter essentially is characterised by a constant radial velocity, with  $\gamma = \text{const}$  (Paczynski 1986; Goodman 1986; Shemi & Piran 1990; Paczynski 1991).

Finally, the fireball is decelerated by the interaction with the circumburst medium (CBM); in this phase, called afterglow,  $\gamma \propto r^{-3/2}$ . The deceleration becomes important at the deceleration radius  $r_{\text{dec}}$ , where the initial bulk Lorentz factor  $\gamma_0^2$  has decreased to approximately half its original value.

### 2.1.3 Internal and external shocks

Once the fireball reaches relativistic velocities, an efficient conversion from kinetic bulk energy of the baryons to radiation is needed. The released energy must correspond to a perturbation of the trajectory of the particles, thanks to the presence of the shock, defined as sharp discontinuities

<sup>2</sup>This value corresponds to  $\gamma_{\max}$  during the coasting phase.

in the properties of a region (such as density, temperature, pressure) compared to those of a neighbouring one. There are two categories of shocks in the fireball model: internal shocks and external shocks.

### Internal shocks

Assuming that the relativistic particles ejected from the central engine are packaged in several shells emitted with slightly different Lorentz factors, an internal shock occurs when a fast-moving shell catches up with another slower one (Rees & Meszaros 1994). This interaction – since the density of matter is not high enough to allow a significant number of direct collisions – is mediated by long-range forces (probably of magnetic nature), enabling energy and momentum transfer. Internal shocks generally occur at radial distances  $\sim 10^{14} - 10^{15}$  cm from the emitting region, and explain the strong variability of the gamma-ray light-curves resulting from the emission of shells, characterised by different energies and Lorentz factors.

On the other hand, the conversion efficiency from kinetic to radiation energy is rather low. This is due to the fact that the relative velocity between the shells is limited: at most half of the shell energy may be extracted (Kobayashi et al. 1997). Despite this efficiency issue, the expected properties of internal shocks are the most accredited scenario for the prompt emission in the fireball model.

### External shocks

The fast-moving shell due to its interaction with the CBM (earlier emitted by the GRB progenitor) creates an external shock, resulting in the GRB afterglow emission. This shock becomes efficient only when the swept mass is large enough to significantly reduce the kinetic energy of the shell. External shock results in a forward shock (FS) propagating in the CBM as well as a reverse shock (RS) propagating back into the ejecta at lower frequencies (Meszaros & Rees 1993)<sup>3</sup>. The short-lived radiation from RS is initially in the optical band, with the characteristic production of optical flashes observed in several GRB afterglows (Sari & Piran 1999; Kobayashi 2000); as the reverse-shocked outflow adiabatically expands, the typical frequency goes down, and it is expected to come to the radio band days after the burst (Sari & Piran 1999; Kobayashi & Zhang 2003a; Kopač et al. 2015). Since the late-time optical and X-ray afterglow emission originates from the blast wave (i.e. forward-shocked ambient medium), the emission is rather insensitive to the properties of the original outflow. These two shocks create four regions: (1) the unshocked CBM, (2) the shocked CBM, (3) the shocked shell material, and (4) the unshocked shell material (e.g., Kobayashi 2000).

The CBM density profile is crucial to understand the evolution of external shocks. ISM-like CBM is characterised by a constant profile with a density of particles  $n \propto r^0$ , whereas stellar wind-like CBM is characterised by a profile  $n \propto r^{-2}$ , where  $r$  is the radial distance to the explosion centre.

The width of the ejected shell influences the dynamics of emission. There are two kinds of shell: thin and thick shells. When a shell is ejected from a source, is characterised by a high density; as the shell expands, its density decreases and hence the shock becomes relativistic – in the unshocked ejecta frame – while it is crossing the shell. In particular, in the thin shell scenario, usually RS is Newtonian and is too weak to decelerate the shell; on the other hand, in the thick

<sup>3</sup>Although RS emission is short-lived and at lower frequencies, RS and FS region contain about the same amount of energy at the onset of the afterglow. In the case of RS region, the same amount of energy is distributed among a larger number of electrons in the shocked ejecta (it is heavier than shocked ISM at the shock crossing time), resulting in a lower emission frequency.

shell scenario, RS becomes relativistic and is able to decelerate the shell (e.g., [Kobayashi et al. 1999](#); [van Eerten 2015](#)).

## 2.2 GRB synchrotron emission

In the internal/external shock model, the GRB spectrum originates from synchrotron emission of relativistic electrons gyrating in local magnetic fields ([Piran 1999](#)). The electrons are accelerated to relativistic speed by the 1st-order Fermi acceleration mechanism, which implies a power-law distribution in terms of energy, given by:

$$N(\gamma_e)d\gamma_e \propto \gamma_e^{-p}d\gamma_e \quad (2.3)$$

where  $\gamma_e$  is the electron Lorentz factor, and  $p$  is the electron energy distribution power-law index, usually constrained to  $1.5 \lesssim p \lesssim 3.5$  ([Granot & Sari 2002](#), hereafter GS02).

The minimum injected electron Lorentz factor  $\gamma_m$  ( $< \gamma_e$ ) in this distribution is defined as:

$$\gamma_m = \Gamma \epsilon_e \left( \frac{p-2}{p-1} \right) \frac{m_p}{m_e} \quad (2.4)$$

where  $\Gamma$  is the Lorentz factor of the shocked fluid (also known as blastwave Lorentz factor),  $\epsilon_e$  is the fraction of the shock energy distributed to electrons,  $m_e$  is the electron mass, and  $m_p$  is the proton mass. The efficiency of the shock in accelerating particles ( $\epsilon_e$ ) and in generating and amplifying turbulent magnetic fields ( $\epsilon_B$ ) is an important and yet unclear issue, and is currently believed to be of the order of a few percent to tens of percent by energy ([Sironi et al. 2013](#)). In the presence of the self-generated magnetic fields, these relativistic particles lose their energy emitting synchrotron radiation. The typical synchrotron frequency of a relativistic electron depends on its Lorentz factor and – in the observer frame – is given by:

$$\nu(\gamma_e) \simeq \Gamma \gamma_e^2 \frac{q_e B}{2\pi m_e c} \quad (2.5)$$

where  $q_e$  is the electron charge;  $B$  is the comoving magnetic field strength, defined as:

$$B = (8\pi e \epsilon_B)^{1/2} \quad (2.6)$$

where  $e$  is the energy density in the shocked region (assumed constant), and  $\epsilon_B$  indicates the fraction of the post-shock energy fraction in the magnetic field. The spectral power of a relativistic electron  $P_\nu$  with initial energy  $\gamma_e m_e c^2$  varies approximately as  $\nu^{1/3}$  when  $\nu < \nu(\gamma_e)$  and cuts off exponentially when  $\nu > \nu(\gamma_e)$ . The total emitted power can be expressed – in the observer frame – as:

$$P(\gamma_e) \simeq \frac{4}{3} \sigma_T c \Gamma^2 \gamma_e^2 \frac{B^2}{8\pi} \quad (2.7)$$

where  $\sigma_T$  is the electron Thomson cross-section, defined as:

$$\sigma_T = \frac{8\pi}{3} \left( \frac{q_e^2}{m_e c^2} \right) \simeq 6.65 \times 10^{-25} \text{ cm}^2 \quad (2.8)$$

The total peak spectral power occurs at  $\nu(\gamma_e)$ , where – in the observer frame – it has the approximate value:

$$P_{\nu, \max} \approx \frac{P(\gamma_e)}{\nu(\gamma_e)} \approx \frac{8\pi q_e^3 \Gamma B}{9m_e c^2} . \quad (2.9)$$

$P_{\nu, \max}$  does not depend on  $\gamma_e$ .

This picture is valid only in adiabatic condition, where the electron loses a negligible fraction of its energy to radiation. This regime is valid until  $\gamma_e$  is less than a critical Lorentz factor  $\gamma_c$ , defined as:

$$\gamma_c = \frac{6\pi m_e c}{\Gamma \sigma_T B^2 t}, \quad (2.10)$$

where  $t$  is the timescale (in observer-frame) within which an electron with an initial Lorentz factor  $\gamma_e > \gamma_c$  cools down to  $\gamma_c$ . Above  $\gamma_c$ , cooling by synchrotron radiation becomes significant, so that the electron distribution shape is modified in the  $\gamma_e > \gamma_c$  regime (Sari et al. 1998; Gao et al. 2013b).

The electron Lorentz factors  $\gamma_m$  and  $\gamma_c$  – evolving in time – define two characteristic emission frequencies  $\nu_m$  and  $\nu_c$  in the synchrotron spectrum. Depending on the order of  $\gamma_m$  and  $\gamma_c$ , the synchrotron spectrum falls into two broad categories: fast-cooling ( $\nu_m > \nu_c$ , or  $\gamma_m > \gamma_c$ ) and slow-cooling ( $\nu_m < \nu_c$ , or  $\gamma_m < \gamma_c$ ) regimes. In the first case, all electrons with Lorentz factors above  $\gamma_c$  cool rapidly; in the second case, only the highest energy electrons cool rapidly (e.g., GS02, Sari et al. 1998; Gao et al. 2013b). The prompt phase of GRBs is expected to be in the fast-cooling regime due to high shock/internal energy density and consequently high magnetic energy density; this allows highly variable gamma-ray emission as well as a high efficiency in the internal shocks (Piran 1999). Transition to the slow-cooling regime is expected to take place during the early stages of the afterglow (Meszaros & Rees 1997; Waxman 1997, GS02).

Another characteristic frequency is the synchrotron self-absorption  $\nu_{sa}$ , below which the synchrotron photons are self-absorbed, calculated through two methods: (i) the condition that the photon optical depth for self-absorption is unity (Rybicki & Lightman 1979), and (ii) equating the synchrotron flux and the flux of a blackbody (Sari & Piran 1999; Kobayashi & Zhang 2003a). During the afterglow phase,  $\nu_{sa}$  is usually the smallest among the three frequencies. In particular, only in fast-cooling regime the self-absorption frequency splits in  $\nu_{ac}$  and  $\nu_{sa}$ , where an optical depth of unity is produced by noncooled electrons and all electrons, respectively (Granot et al. 2000, GS02). When  $\nu_{sa} > \nu_c$ , the electron energy distribution may be significantly modified, resulting in inaccurate analytical models (Gao et al. 2013b).

## 2.2.1 Evolution of GRB synchrotron spectra and light-curves

The synchrotron spectrum (both FS and RS) evolves in time as the blastwave expands, with spectral transitions occurring when two or more break frequencies cross each other.

For the case of FS emission, different possible orderings of break frequencies result in five spectral regimes (GS02), displayed in Fig. 2.1. Regimes 1 – 2 and 4 – 5 correspond to slow cooling ( $\nu_m < \nu_c$ ) and fast cooling ( $\nu_m > \nu_c$ ), respectively, with different orderings of  $\nu_{sa}$ ; regime 3 describes an intermediate case, where the relative ordering of  $\nu_c$  and  $\nu_m$  is unimportant. The spectral indices are reported in Fig. 2.1; moreover, the “spherical model” columns in Table 2.1 report the evolution of spectral break frequencies and peak flux densities.

Like in the case of FS, a RS ploughing into GRB ejecta is expected to produce synchrotron radiation with its own characteristic frequencies ( $\nu_{sa,rs}$ ,  $\nu_{m,rs}$ , and  $\nu_{c,rs}$ ), and peak flux  $F_{\nu_{m,rs}}$ . These quantities are related to those of the FS when the RS just crosses the ejecta at the time  $t_X$ : for thin shells  $t_X = t_{dec}$ <sup>4</sup>, while for thick shells  $t_X = T_{90}$  (Kobayashi et al. 1999). The ratio between these two sets of break frequencies and fluxes help constrain the ejecta (Lorentz factor and magnetisation). As opposed to the case of a relativistic RS (thick shell regime, Sect. 2.1.3), the

<sup>4</sup>The deceleration time  $t_{dec}$  of the ejecta for an impulsive injection of a fireball with energy  $E$  and initial Lorentz factor  $\Gamma_0$  corresponds to the time at which the swept-up mass from the CBM is about  $1/\Gamma$  times that of the ejecta (Gao et al. 2013b).



evolution of the characteristic frequencies and fluxes for a Newtonian RS (thin shell regime, Sect. 2.1.3) also depends on index  $g$ , that describes the profile of the shocked ejecta  $\gamma \propto r^{-g}$ ; it ranges between  $3/2$  and  $7/2$  in ISM-like CBM, and between  $1/2$  and  $3/2$  in wind-like CBM, from theoretical arguments (Mészáros & Rees 1999; Kobayashi & Sari 2000; Gao et al. 2013b; Gao & Mészáros 2015). Further information about the RS synchrotron spectra is available in the reviews of Gao et al. (2013b) and Gao & Mészáros (2015).

The synchrotron light-curve at a given  $\nu_{obs}$  evolves with time, undergoing temporal transitions (or power-law breaks) whenever a characteristic frequency crosses  $\nu_{obs}$ . This translates in smoothly connected power-law segments: for example,  $t_m$  and  $t_c$  are the times at which  $\nu_m$  and  $\nu_c$  cross  $\nu_{obs}$ , respectively, that is  $\nu_m(t_m) = \nu_c(t_c) = \nu_{obs}$ . As described in Sari et al. (1998), the possible orderings of break times depend on the comparison between  $\nu_{obs}$  and  $\nu_0$ , defined as  $\nu_0 = \nu_c(t_0) = \nu_m(t_0)$ , where  $t_0$  is the transition time between fast and slow cooling regimes. The regime  $\nu_{obs} > \nu_0$  defines the high-frequency light-curve, where  $t_0 > t_m > t_c$ ; on the other hand, the regime  $\nu_{obs} < \nu_0$  defines the low-frequency light-curve, where  $t_0 < t_m < t_c$  (Fig. 2.2). The FS temporal indices are reported in Fig. 2.2. The case of the RS light-curves is well described in the reviews of Gao et al. (2013b) and Gao & Mészáros (2015).

## 2.3 Jetted emission

The GRB outflow usually shows evidence for the presence of a jet in the form of an achromatic break in the temporal power-law decay of the afterglow light-curves. This is usually interpreted as the edge of the jet becoming visible to the observer. Light-curves of GRB afterglows show that typical isotropic-equivalent luminosity at the peak time ( $L_{\gamma,iso} \sim 10^{52}$  erg s $^{-1}$ ) is much larger than the Eddington luminosity of a BH with mass of  $\sim 10 M_{\odot}$  ( $L_{Edd} \sim 10^{39}$  erg s $^{-1}$ ); collimation is therefore needed to continuously power the engine with gravitational energy (e.g., Zhang 2019). Estimating the jet opening angle is therefore required to measure the true (collimation-corrected) energetics.

In the literature there are two broad families of jets: uniform and structured. The first assumes an uniform distribution of energy and Lorentz factor within a jet cone with a sharp edge, the second assumes an angular distribution in energy and Lorentz factor (e.g. Granot 2007; Zhang 2019). In this Thesis I focus on the uniform jet regime, because is simpler than structured jet model, based on special relativistic hydrodynamics (e.g. De Colle et al. 2012; Granot et al. 2018), although in the latest years growing evidence has been found that favours the structured jet, as in the case of the S-GRB 170817A associated to GW 170817 (Alexander et al. 2018).

The uniform jet scenario assumes a simplified conical jet blastwave, with a half opening angle  $\theta_j$  and blastwave Lorentz factor  $\Gamma$ , where only the emission inside the  $1/\Gamma$  cone is detectable due to relativistic beaming. During the deceleration phase, caused by the interaction between the outflow and the CBM,  $\Gamma$  decreases gradually until  $1/\Gamma > \theta_j$  – for an observer in the line-of-sight of the jet – in the form of a break in the light-curve. An off-axis observer could not observe the GRB, and hence an orphan afterglow (i.e. an afterglow without the gamma-ray emission) could in principle be observed. The light-curve steepening can arise from two effects: the edge effect and the sideways expansion effect. The pure edge effect (e.g. Panaitescu et al. 1998) arises when an observer feels the deficit of flux outside the  $\theta_j$  cone, when  $1/\Gamma > \theta_j$  is satisfied. In this regime, the blastwave dynamics does not change during the jet break transition. The degree of steepening at the jet break time  $t_j$  for the flux densities is defined as  $\Delta\alpha = \alpha_{post,jet} - \alpha_{pre,jet} = (3 - k)/(4 - k)$ , where  $k$  describes the kind of CBM ( $k = 0$  for ISM-like,  $k = 2$  for wind-like, Granot 2007). The sideways expansion effect of a conical jet (Rhoads 1999; Sari et al. 1999) arises when  $\Gamma \sim \theta^{-1}$ , and the jet decelerates exponentially; this feature translates in the change of the evolution of both the spectral break frequencies and flux densities at  $t_j$ , as described in several papers (e.g.

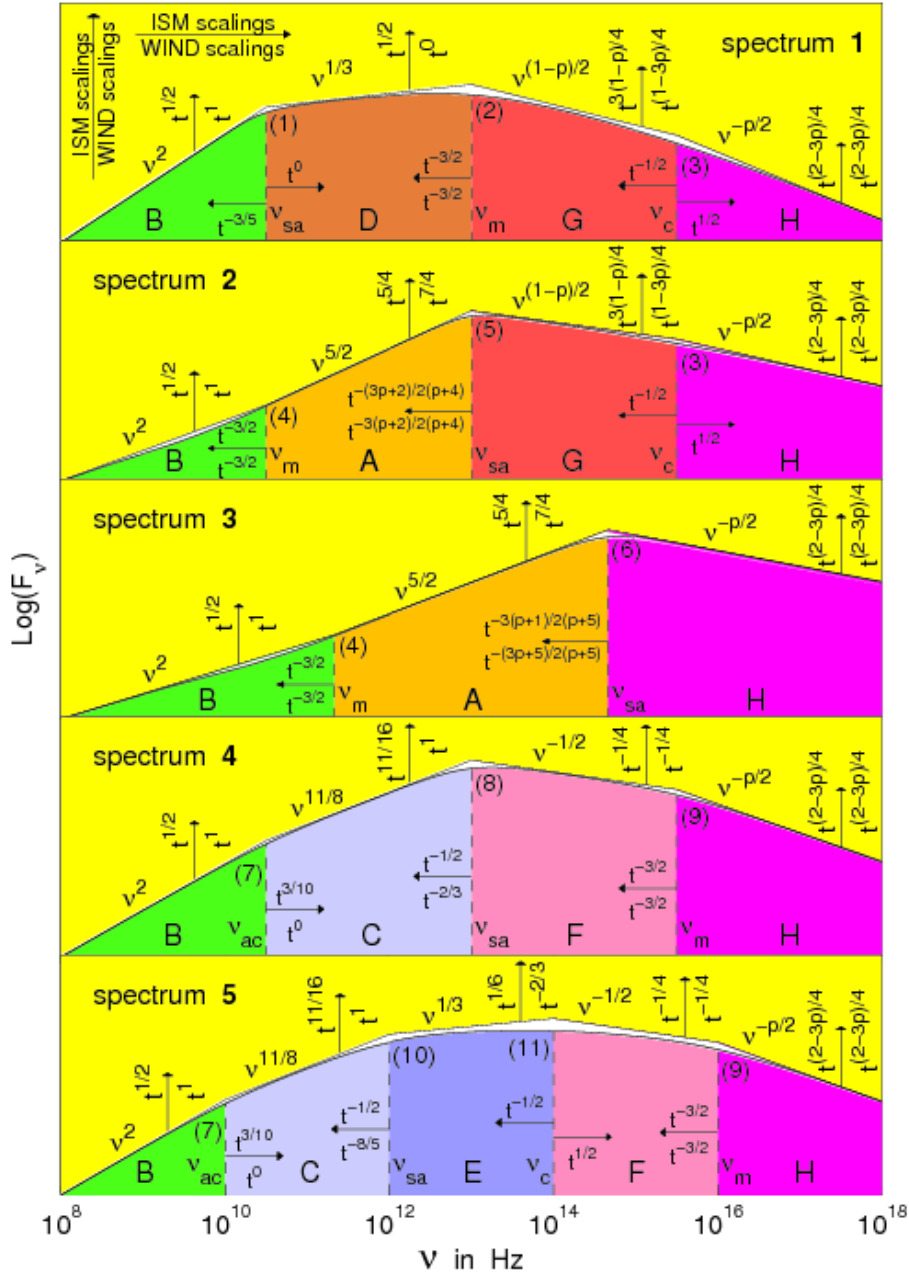


**Figure 2.1:** The five possible SEDs, calculated for the *Blandford & McKee (1976)* spherical self-similar solution, under standard assumptions, using the accurate form of the synchrotron spectral emissivity and integration over the emission from the whole volume of shocked material behind the FS (GS02). The different panels show the possible broadband spectra of the afterglow synchrotron emission, each corresponding to a different ordering of the spectral break frequencies, and time series. Figure reproduced from *Granot (2008)*.

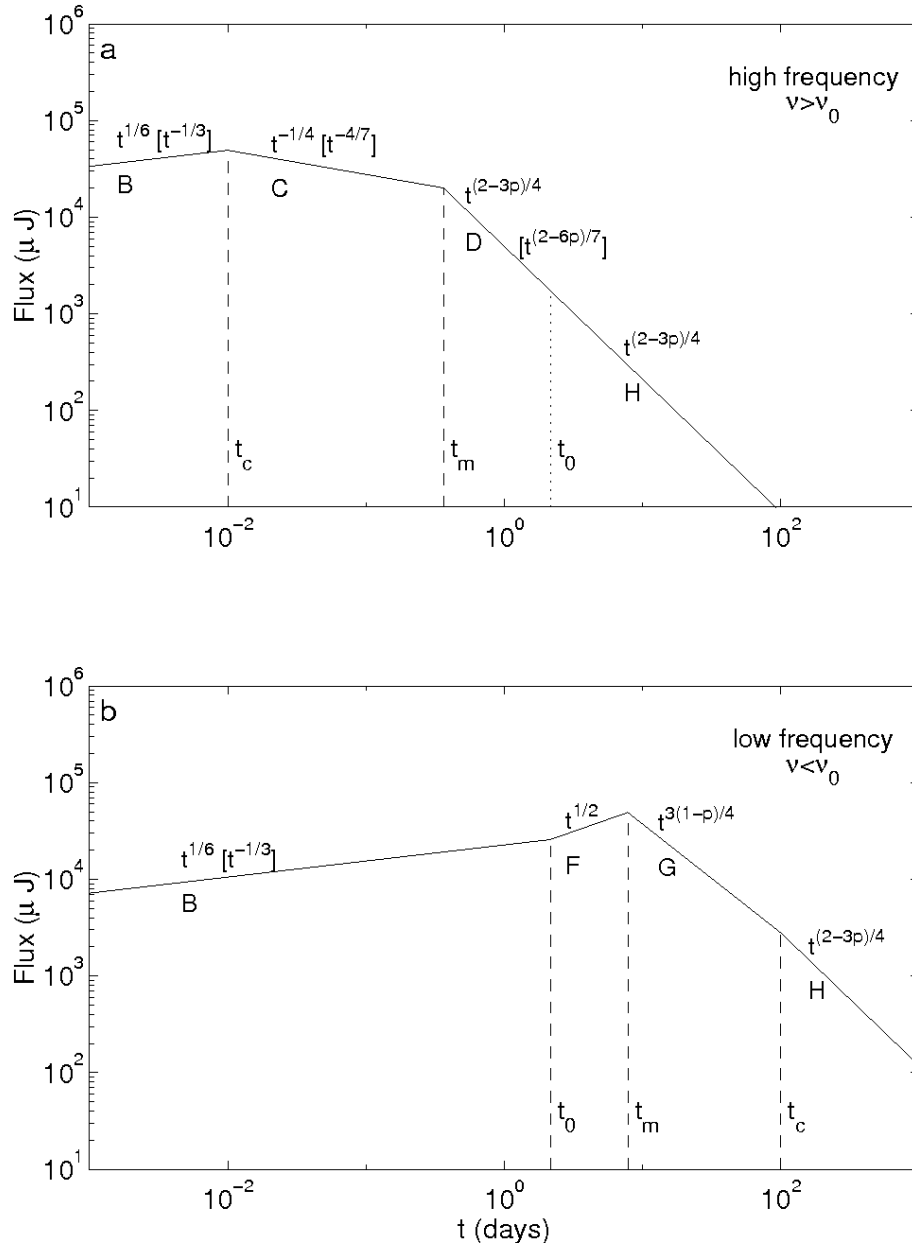


**Figure 2.2:** FS synchrotron light-curve from a spherical relativistic shock, ignoring the effect of self-absorption. (a) The high frequency case ( $v_{obs} > v_0$ ); (b) The low frequency case ( $v_{obs} < v_0$ ). The scalings within square brackets are for radiative evolution (restricted to  $t < t_0$ ) and the other scalings are for adiabatic evolution. Figure reproduced from [Sari et al. \(1998\)](#).

Sari et al. 1999; Sari 2006; Panaitescu & Kumar 2002) and summarised in Table 2.1. Several numerical simulations and sophisticated analytical treatments suggest that the contribution of sideways expansion is not important until  $\Gamma \gtrsim 2$  (Granot et al. 2001; Kumar & Granot 2003; Cannizzo et al. 2004; Zhang & MacFadyen 2009; Granot & Piran 2012; De Colle et al. 2012; van Eerten & MacFadyen 2012); nevertheless, this numerical simulations are compatible with this simple analytical model for post-jet-break light-curves (Zhang & MacFadyen 2009; Kumar & Zhang 2015; Zhang 2019)<sup>5</sup>.

These are purely geometrical or dynamical effects, suggesting the same behaviour in the light-curves at every wavelength. This means that the expected break in the light-curve of the afterglow caused by collimated emission – the so-called jet break – is achromatic<sup>6</sup>.  $\theta_j$  may be computed, both for ISM-like and wind-like CBM, from  $t_j$  (Waxman 1997; Rhoads 1999; Sari et al. 1999; Chevalier & Li 2000; Wang et al. 2018):

$$\theta_{j,\text{ISM}} = 9.25 \left( \frac{n_0}{E_{52,k,\text{iso}}} \right)^{1/8} \left( \frac{t_j}{1+z} \right)^{3/8} \text{ deg} \quad (2.11)$$

$$\theta_{j,\text{wind}} = 11.55 \left[ \frac{t_j A_*}{(1+z) E_{52,k,\text{iso}}} \right]^{1/4} \text{ deg} , \quad (2.12)$$

where  $n_0$  is the ISM-like CBM density in  $\text{cm}^{-3}$ ,  $t_j$  is expressed in days,  $z$  is the redshift of the source,  $E_{52,k,\text{iso}}$  is the kinetic energy of the blastwave (expressed in units of  $10^{52}$  erg), and  $A_*$  is a parameter (expressed in units of  $5 \times 10^{11} \text{ g cm}^{-1}$ ) connected with the wind-like density CBM<sup>7</sup>.

For L-GRBs, the typical half-opening angle  $\theta_j$  ranges between  $3^\circ$  and  $10^\circ$  (e.g., Berger 2014); this results in a beaming correction factor  $f_b = 1 - \cos \theta_j$  between  $\sim 10^{-3}$  and  $\sim 10^{-2}$ , suggesting that the true released energy is two or three orders of magnitude lower than the measured  $E_{\text{iso}}$  (with a typical value of a few  $10^{51}$  erg). On the other hand, measurements of  $\theta_j$  for S-GRBs are less frequent, mainly because of the faintness of their afterglows; the average  $\theta_j$  of S-GRBs seems to be larger than that of L-GRBs (Berger 2014), with beaming-corrected energies usually lower than  $10^{50}$  erg.

This picture is valid for an on-axis observer, but the light-curve behaviour also depends on the direction of the observer. Fitting X-ray data at late-time with numerical jet models suggests that the line of sight for most GRBs is misaligned from the jet axis (Ryan et al. 2015; Zhang et al. 2015a). For an off-axis observer, an orphan afterglow (an afterglow without the high-energy component) could in principle be observed at late-times. Several authors discussed the possibility of detecting orphan afterglows (e.g., Nakar et al. 2002; Totani & Panaitescu 2002). Recently Marcote et al. (2019) discovered a good candidate for an orphan afterglow of a L-GRB in the radio transient source FIRST J1419+3940, characterised by decreasing brightness over the last few decades.

Finally, besides these two forms of jets, more complicated structured jets have been discussed in the literature; several authors have discussed the two-component jet model. According to this

<sup>5</sup>As reported by Zhang (2019), it seems that the  $\alpha = -p$  post-jet-break decay could be a reasonable rough approximation.

<sup>6</sup>However, afterglow observations in the Swift era have shown a lack of achromatic breaks compared to the pre-Swift era (de Pasquale et al. 2009). Missing breaks are attributed to far off-axis observations (van Eerten & MacFadyen 2011), to bad quality of data (Curran et al. 2008), or to the break time falling beyond the end of *Swift*/XRT follow-up. Another possible interpretation is that the X-ray afterglow of many GRBs does not originate from external shocks but from a long-lasting central engine (Metzger et al. 2011), suggesting that only the optical light-curve may be suitable to identify jet breaks.

<sup>7</sup>In the density profile  $\rho(r) = Ar^{-2}$ ,  $r$  is the radius,  $A = \dot{M}_w 4\pi V_w \equiv 5 \times 10^{11} A_* \text{ g cm}^{-1}$  is a constant proportional to the progenitor mass-loss rate  $\dot{M}_w$  (assumed constant), for a given wind velocity  $V_w = 10^3 \text{ km s}^{-1}$  and  $\dot{M}_w = 10^{-5} M_\odot \text{ yr}^{-1}$  (Chevalier & Li 2000).

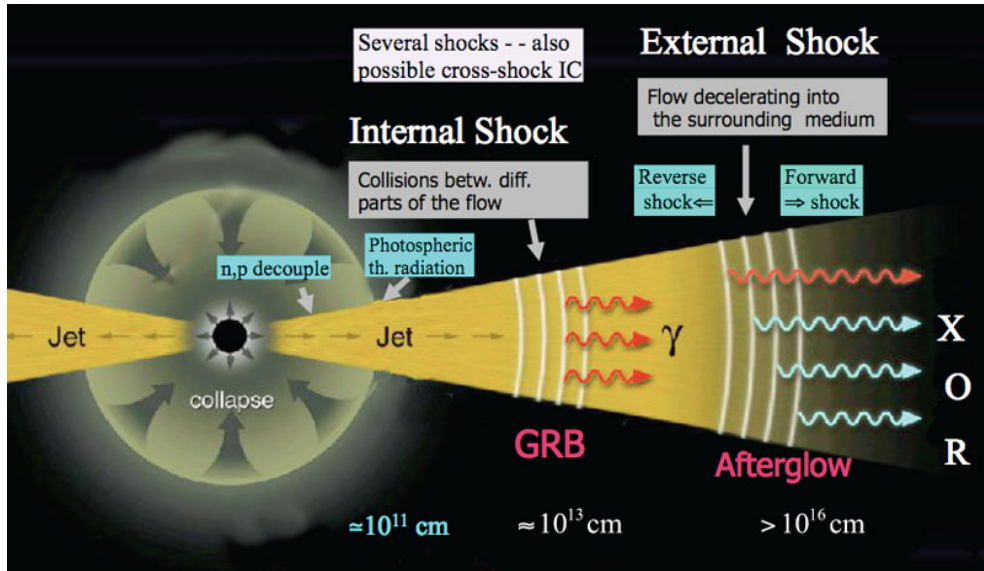


**Figure 2.3:** Cartoon for the GRB fireball model. (1) The source of energy is a collapsing massive star (or merger of NS-NS or NS-BH, not shown here). (2) Part of this energy generates a relativistic jet, mediated by hot photons (“fireball”), or by magnetic field. (3) The thermal photons decouple at the photosphere. (4) Part of the jet kinetic energy is dissipated (by internal collisions, in this picture) to produce the observed prompt emission in gamma-rays. (5) The remaining kinetic energy is deposited into the CBM, heating it and producing the observed afterglow at lower frequencies. Figure reproduced from [Meszaros & Rees \(2014\)](#).

model, the GRB outflow consists in a narrow jet component (usually characterised by a higher  $L_{\gamma,\text{iso}}$  and a larger  $\Gamma$ ), surrounded by a wider jet component (with a lower  $L_{\gamma,\text{iso}}$  and a smaller  $\Gamma$ ). Depending on the viewing angle, the two-component jet predicts some light-curve features, such as an early jet break and late-time re-brightening ([Huang et al. 2004](#); [Peng et al. 2005](#); [Wu et al. 2005](#)). This model was used to interpret the afterglow data for several GRBs, such as GRB 030329 ([Berger et al. 2003](#)) and GRB 080319B ([Racusin et al. 2008](#)). Moreover, this can be accommodated with the collapsar model (Sect. 2.5.1), where a narrow and highly relativistic jet emerging from a star is surrounded by a wider, less relativistic cocoon ([Ramirez-Ruiz & Lloyd-Ronning 2002](#); [Zhang et al. 2004](#)).

## 2.4 Non-relativistic transition

The relativistic blastwave, due to the interaction with the CBM, gradually decelerates, reaching the non-relativistic/Newtonian (NR) phase, when  $\gamma < \sqrt{2}$  and the electrons should be in the slow cooling scenario ( $v_m < v_c$ ), at the transition time

$$t_{\text{NR,ISM}} = 84(1+z) \left( \frac{E_{52,k,\text{iso}}}{n_0} \right)^{1/3} \text{ days} \quad (2.13)$$

for ISM-like CBM ([Waxman 1997](#)), and

$$t_{\text{NR,wind}} = 694(1+z) \left( \frac{E_{52,k,\text{iso}}}{A_*} \right) \text{ days} \quad (2.14)$$

for wind-like CBM ([Chevalier & Li 2000](#)).

In the deep Newtonian phase, the blastwave dynamics can be derived from simple scaling relations (e.g. [Wijers et al. 1997](#)). The light-curves in the Newtonian phase are steeper than those

in the relativistic phase, but are shallower than the post-jet-break phase in the relativistic regime (Zhang 2019). This feature suggests that the transition from relativistic to NR phase occurs after the jet break, probably in timescales of years (e.g. Livio & Waxman 2000; Zhang & MacFadyen 2009).

This holds for ISM-like environment at the late stage of the blastwave evolution, since a stellar wind ends at a termination shock beyond which the medium is already of ISM type (Gao et al. 2013b; Zhang 2019).

Observationally, in the optical band it is very difficult to observe the NR phase in the light-curves, since the afterglow emission is strongly contaminated by the host galaxy light before reaching the NR phase. On the other hand, this transition may be more easily observed in the radio band at late-time (timescales of years), especially in the case of nearby sources (e.g. GRB 030329, van der Horst et al. 2008).

The evolution of spectral break frequencies and peak flux densities in NR phase are reported in Table 2.1, according to calculations reported in several works (Frail et al. 2000; van Eerten et al. 2010; Leventis et al. 2012).

## 2.5 Central engines

The fireball model assumes a large quantity of released energy in a small volume regardless of its origin from the GRB progenitor. The characteristics of GRB emission, such as the energy budget and the spatial compactness, suggest a rapid accretion onto a BH; the observations are compatible with S-GRBs originating from binary NS mergers (Sect. 1.3.3), and L-GRBs from collapsars. Another progenitor candidate for the central engine is the magnetar, a highly magnetised NS.

### 2.5.1 Collapsars

The collapsar model (Woosley 1993; Popham et al. 1999) assumes a massive star origin for L-GRBs. Sometimes the gravitational pressure may directly lead to a catastrophic collapse to a BH, where the surrounding stellar matter falls towards the BH through the formation of an accretion disc. A pair of relativistic jets – removing angular momentum along the rotational axis – originates according three possible mechanisms: (i) neutrino/anti-neutrino annihilation along the rotational axis; (ii) the Blandford-Znajek mechanism<sup>8</sup> (Blandford & Znajek 1977); (iii) the highly magnetised accretion disc causes an eruption of magnetic blobs due to the differential rotation, resulting in the jets emission piercing through the stellar envelope<sup>9</sup>.

The main candidates to form collapsar events are the Wolf-Rayet (WR) stars, massive stars that lost most of their hydrogen envelopes. These stars are characterised by very high surface temperatures (in excess of  $\sim 3 \times 10^4$  K), strong stellar winds, and a large surface metallicity. WR progenitors are good candidates for the association between GRBs and type Ib/c broad-line supernovae (BL-SNe, Sect. 1.5). The localisation of L-GRBs in star-forming regions is a further signature of this connection. On the other hand, WR stars typically have a high metal abundance which results in angular momentum loss, but L-GRB progenitors must have low metallicity levels to stifle enough angular momentum to form the accretion disc.

<sup>8</sup>This mechanism consists in the extraction of energy from a rotating BH, where an accretion disc is equipped with a strong poloidal magnetic field that extracts the rotational energy.

<sup>9</sup>In case of thin enough envelope, these jets can leak from it with Lorentz factors  $\gamma \gtrsim 100$ .



### 2.5.2 Magnetars

Other candidates for the central engine are the rapidly spinning magnetars, characterised by period  $P \sim 1$  ms and surface magnetic field  $B_s \sim 10^{15}$  G; they seem to be able to power a GRB through spin-down (Usov 1992; Wheeler et al. 2000), and their total rotational energy  $E_{rot}$  can be written as:

$$E_{rot} \sim \frac{1}{2} I \Omega^2 \sim 1.5 \times 10^{52} \frac{M}{M_{\odot}} \left( \frac{R}{10^6 \text{ cm}} \right)^2 \left( \frac{P_0}{10^{-3} \text{ ms}} \right)^{-2} \text{ erg} \quad (2.15)$$

where  $M$  and  $R$  indicate the mass and the radius of the magnetar, respectively, and  $P_0$  is the initial period; for a typical magnetar with  $M \sim 1.4 M_{\odot}$ ,  $R \sim 10$  km, and  $P \sim 1$  ms, Equation (2.15) shows  $E_{rot, \text{typical}} \sim 2 \times 10^{52}$  erg. Only GRBs with energy below  $E_{rot, \text{typical}}$  may be powered by magnetars; this energy is compatible with the beaming-corrected value for most GRBs. Typical luminosity and duration can be reproduced.

The emission mechanism shows that the magnetar is initially very hot, and hence the neutrinos drive a significant wind, characterised by too many baryons to reach relativistic regime; despite this, after  $\sim 10$  s, the cooling down of the NS results in the weakening of this baryonic wind, producing a short-duration jet ( $\sim 30$  s) until the sudden drop of the neutrino emission. Energy injection in the form of Poynting flux could result from continuous spin-down. For further details, see e.g. Bucciantini et al. (2008) and Metzger et al. (2011).

### 2.5.3 Compact object mergers

The progenitors of S-GRBs, because of their short duration, can be discovered in systems with a dynamical timescale of the order of milliseconds, like the merging of compact binaries (double NS or NS-BH systems, Eichler et al. 1989; Narayan et al. 1992). The recent discovery of the binary NS-NS merger in the GW observation made by LIGO and Virgo (GW 170817, e.g. Abbott et al. 2017a) and the detection of associated electromagnetic counterparts, have given direct evidence of the NS-NS merger being a progenitor of a S-GRB. Specifically, the GRB jet emanating from GW 170817 was observed off-axis (e.g., Alexander et al. 2017a, 2018; Kathirgamaraju et al. 2018), with a successive faint afterglow emission at early-times (Hallinan et al. 2017).

The GW emission arises from the loss of energy and angular momentum in binary orbits of NS-NS merger, resulting in a faster decay and finally in a hyperaccreting compact object (e.g. BH); a similar scenario takes place for BH-NS mergers if the tidal disruption of the NS occurs outside the event horizon of the BH. Energy is released in a similar way as in the collapsar model, where a fast rotation and a high accretion rate could power neutrino-anti-neutrino annihilation or magneto-hydrodynamic processes, resulting in jetted ejecta.

## 2.6 Open issues on GRB science

Despite many facilities operating at several frequencies – from radio to gamma-rays – have improved the GRB science, several open issues remain. The broadband observations, and in particular the increase of radio campaigns, are crucial to better understand the physics of both GRBs and their progenitors.

One of the most critical issues in GRB physics is the composition of the relativistic ejecta. Baryonic-dominated ejecta are characterised by the presence of strong RS, and the ratio  $\sigma$  between the magnetic energy density and the bulk kinetic energy is  $\lesssim 1$ ; on the other hand, magnetic field-dominated ejecta are believed to produce faint RS emission (Mészáros & Rees 1999; Sari & Piran 1999; Zhang & Kobayashi 2005; Lyutikov & Camilo Jaramillo 2017).



Measuring a RS helps constrain the ejecta thickness, the bulk Lorentz factor  $\gamma$ , and the fireball magnetisation, through the analysis of its temporal and spectral evolution. Since the RS has the same origin of the FS in the afterglow emission, the observations of both shocks are crucial to understand the composition of the ejecta, and the yet unknown mechanism of energy extraction from the central engine. The expected observational signature of the RS is early-time flares in the optical and radio bands (e.g. [Sari & Piran 1999](#); [Kobayashi & Zhang 2003a](#)), and hence multi-wavelength observations are crucial to have a complete picture of the ejecta properties. To date only a small fraction ( $\sim 5\%$ ) of early-time optical light-curves show clear evidence of RS emission, probably because the typical synchrotron frequency of the RS already lies at radio frequencies ([Mundell et al. 2007a](#); [Melandri et al. 2010](#)). [Kopač et al. \(2015\)](#) suggest that the brightest and clearest RS radio signatures are detectable at early-times (0.1 – 1 d after the burst), emphasising the need for rapid response radio follow-up campaigns. Moreover, detecting a RS is easier mainly for bursts in ISM-like CBM with lower densities ( $n \leq 0.1 \text{ cm}^{-3}$ ), high isotropic energies, and at observing frequencies unaffected by synchrotron self-absorption suppression (typically above a few GHz).

These kinds of analysis are hampered by the limited sensitivity of radio telescopes, resulting in relatively few observations. In latest years, and especially after the NS-NS merger event connected with the detection of GW 170817/GRB 170817A ([Abbott et al. 2017b](#); [Pian et al. 2017](#); [Nicholl et al. 2017](#)) and the resulting birth of the multi-messenger era, several dedicated radio followup campaigns aimed to provide a good temporal and spectral RS and FS coverage (e.g. [Laskar et al. 2013, 2016, 2018a, 2019](#)), but a complete and systematic picture of GRB ejecta remains an open issue.

The high-accuracy prompt localisation provided by Swift allowed to carry out rapid multi-frequency follow-up observations of GRB afterglows. These resulting campaigns revealed new details in X-ray and optical light-curves, such as rapid and short flares ( $\Delta T/T \ll 1$ ), plateaus, and multi-frequency re-brightening episodes (e.g. [Liang et al. 2007](#); [Li et al. 2012](#); [Margutti et al. 2011a,b, 2013](#); [Zaninoni et al. 2013](#); [Laskar et al. 2015](#)). Broadband light-curves show unknown properties: for example, X-ray flares suggest late-time activity of the central engine (e.g. [Giannios 2006](#); [Falcone et al. 2007](#); [Chincarini et al. 2007, 2010](#)); plateaus have been explained invoking different interpretations: energy injection (e.g. powered by a spinning-down magnetar), or temporal evolution of the shock microphysical parameters (e.g. [Granot & Kumar 2006](#); [Zhang et al. 2006](#); [Nousek et al. 2006](#); [Panaitescu et al. 2006](#); [Jin et al. 2007](#); [Uhm & Zhang 2014](#); [Stratta et al. 2018b](#)).

High-redshift GRBs trace star formation throughout the Universe (potentially Population III stars). To date, these stars are entirely hypothetical and, despite intense searches, no Population III star has yet been observed. Thanks to their bright afterglows (even for  $z \gtrsim 9$ ) and their association with the core-collapse of massive stars, L-GRBs have been proposed as promising tracers of star formation (e.g. [Lamb & Reichart 2000](#); [Porciani & Madau 2001](#); [Tanvir et al. 2009](#); [Salvaterra et al. 2009, 2013](#)). UV emission from stars of population III can be utilised to probe the first epoch of star formation (e.g. [Bromm & Larson 2004](#)). Different studies based on the host galaxies of L-GRBs at high redshift have tried to obtain information on the relation between L-GRBs and Population III (e.g. [Kistler et al. 2008](#); [Robertson & Ellis 2012](#)), but these studies were characterised by biased and incomplete L-GRB samples and their host galaxies. In this context, several projects to create complete samples have been designed to address this issue ([Hjorth et al. 2012](#); [Salvaterra et al. 2012](#); [Perley et al. 2016](#)). It is believed that Population III explosions are characterised by large released energies and CBM with low densities, reflecting the predicted high masses and weak winds of these low-metallicity stars (e.g. [Heger et al. 2003](#); [Palmerio et al. 2019](#)). The analysis of the redshift evolution of these properties of the GRB progenitor population can be crucial to search for Population III signatures (e.g.

[Laskar et al. 2014](#)). This study requires broadband observations of high- $z$  candidate events, and multi-frequency modelling to determine the physical parameters of the explosion. In the context of the newborn multi-messenger and time-domain astrophysics, the Transient High Energy Sky and Early Universe Surveyor (THESEUS) proposed mission (accepted by ESA for phase A study) will boost the discovery and study of high-redshift GRBs (up to  $z \sim 10$ ), thus paving the way to study, on a systematic and unbiased way, key aspects of the early Universe, such as metallicity evolution, star formation at the reionisation epoch, identification of population III stars ([Amati et al. 2018](#); [Stratta et al. 2018a](#)).

Break frequency	Spectrum	Evolution of break frequency, $\nu \propto t^\alpha$				Evolution of flux density, $F_{\nu,b,ext} \propto t^\beta$			
		Spherical model		Spherical model		Spherical model		Spherical model	
		ISM	Wind	ISM	Wind	ISM	Wind	ISM	Wind
1 - $\nu_{sa}$	1	0	-3/5	-1/5	2/15	1/2	-1/5	-2/5	2/5
2 - $\nu_m$	1	-3/2	-3/2	-2	-7/3	0	-1/2	-1	3/5
3 - $\nu_c$	1,2	-1/2	1/2	0	-	$\frac{1-p}{2}$	$\frac{1}{2} - p$	-p	$-\frac{10-7p}{5}$
4 - $\nu_m$	2,3	-3/2	-3/2	-2	-7/3	-5/2	-2	-4	-32/5
5 - $\nu_{sa}$	2	$-\frac{3p+2}{2(p+4)}$	$\frac{3(p+2)}{3(p+4)}$	$-\frac{2(p+1)}{2(p+4)}$	$-\frac{7p+6}{3(p+4)}$	$-\frac{5p-5}{2(p+4)}$	$\frac{4p+1}{2(p+4)}$	$-\frac{4p+1}{4p}$	$\frac{7-12p}{3(p+4)}$
6 - $\nu_{sa}$	3	$-\frac{2(p+4)}{3(p+1)}$	$\frac{3p+5}{3(p+1)}$	$-\frac{p+4}{2(p+1)}$	$-\frac{p+4}{2(p+1)}$	$\frac{5(p-1)}{5(p-1)}$	$\frac{4p-5}{4p-5}$	$-\frac{p+4}{4p}$	$\frac{47-32p}{5(p+4)}$
7 - $\nu_{ac}$	4,5	$-\frac{2(p+5)}{2(p+5)}$	$-\frac{2(p+5)}{2(p+5)}$	$-\frac{p+5}{p+5}$	-	$-\frac{2(p+5)}{2(p+5)}$	$-\frac{2(p+5)}{2(p+5)}$	$-\frac{p+5}{p+5}$	-
8 - $\nu_{sa}$	4	3/10	0	2/5	-	11/10	1	4/5	-
9 - $\nu_m$	4,5	-1/2	-2/3	-2/3	-	6/5	1/12	-2/3	-
10 - $\nu_{sa}$	5	-3/2	-3/2	-2	-	-3	1/2	0	-
11 - $\nu_c$	5	-1/2	-8/5	-6/5	-	6/5	-8/5	-7/5	-
		-1/2	1/2	0	-	-1/5	-1/2	-1	-

**Table 2.1:** Evolution of spectral break frequencies and peak flux densities – connected with the spectra showed in Fig. 2.1 – before (GS02) and after (Sari et al. 1999; Sari 2006; Panaitescu & Kumar 2002) the jet break and the transition to non-relativistic expansion (Frail et al. 2000; van Eerten et al. 2010; Leventis et al. 2012).

# Chapter 3

## An analytical approach for broadband modelling of GRB afterglows

In this Chapter I focus on the analysis of GRB afterglows based on an analytical approach. The emission of GRB afterglows mainly consists in synchrotron radiation, but there are other radiation processes and additional aspects that are likely to contribute, such as the jetted emission and non-relativistic regime (Sect. 3.4), energy injection phenomenon (Sect. 3.5), absorption effects (Sect. 3.6), scintillation in radio frequencies (Sect. 3.7), and inverse Compton at high energies (Sect. 3.8).

This complex landscape is properly considered in a dedicated Python code, called `sAGA` (Software for AfterGlow Analysis), described in this Chapter. `sAGA` aims to model GRB afterglow data within a self-consistent physically grounded picture. Built adopting a Bayesian approach, all the data, from radio to gamma-rays, are modelled. By-products are plots of spectra and light-curves, and computation of the break frequencies and normalisations as a function of the shock microphysical parameters: the kinetic energy of the explosion ( $E_{K,iso}$ ), the CBM density ( $n_0$  for ISM-like CBM; the normalised mass-loss rate  $A_*$  for wind-like CBM), the power-law index of the electron energy distribution ( $p$ ), the fractions of the blastwave energy delivered to relativistic electrons ( $\epsilon_e$ ) and magnetic fields ( $\epsilon_B$ ). Dust extinction of optical along the sightline is also accounted for.

The capabilities of `sAGA` are successfully tested on three GRB afterglows: GRB 120521C, GRB 090423 and GRB 050904 (Sect. 3.9).

### 3.1 Broadband modelling of GRBs

All the previous open issues call for more observations (especially at lower frequencies), paralleled by adequate broadband modelling. The analysis of GRB afterglow spectra and light-curves is made possible using data from radio to X-ray frequencies. The significant improvements in sensitivity for broadband facilities, especially at radio frequencies (such as the Karl G. Jansky Very Large Array, VLA), give the opportunity to gain insight into the microphysical parameters with unprecedented accuracy.

The interpretation and analysis is performed by a sophisticated modelling code – fully self-consistent – developed in Python, called *sAGA* (Software for AfterGlow Analysis). This application receives in input two text-based files: the “observation data file” (mainly epoch of observation, flux density and its uncertainty, observing frequency) and the GRB “parameter file” (such as position and the redshift). *sAGA* performs a broadband data analysis through a new approach that consists in the manipulation of all the data at both each observing epoch and observing frequency in a single process; the analysis considers different radiation processes and other aspects, briefly described in following subsections, that the user can select at the beginning of the analysis. In output *sAGA* provides several plots of light-curves and spectra of the GRB afterglow (both for each epoch/observing frequency and global) and a text-based file reporting best-fit values associated with selected radiation processes and other aspects. The complete list of the available parameters for *sAGA* is reported in Table 3.1.

Hereafter, *sAGA* assumes  $\Lambda$ CDM cosmological parameters of  $\Omega_m = 0.31$ ,  $\Omega_\Lambda = 0.69$ , and  $H_0 = 68 \text{ km s}^{-1} \text{ Mpc}^{-1}$  (Planck Collaboration et al. 2016).

### 3.2 Markov Chain Monte Carlo

The best-fit solution is calculated through the maximisation of a likelihood function, using a Gaussian error model. The likelihood function for a data set composed of both detection and non-detection is given by (e.g., Laskar et al. 2014, hereafter L14):

$$\prod p(e_i)^{\delta_i} F(e_i)^{1-\delta_i} \quad (3.1)$$

where  $e_i$  are the residuals (the difference between the measurement or  $3\sigma$  upper limit and the predicted flux from the model),  $\delta_i$  is the detection parameter (equal to 0 for an upper limit and 1 for a detection),  $p(e_i)$  is the probability density function of the residuals, and  $F(e_i)$  is the cumulative distribution function of the residuals. For a Gaussian error model,

$$p(e_i) = \frac{1}{\sqrt{2\pi}\sigma_i} e^{-e_i^2/2\sigma_i^2} \quad (3.2)$$

and

$$F(e_i) = \frac{1}{2} \left[ 1 + \text{erf} \left( \frac{e_i}{\sqrt{2}\sigma_i} \right) \right] \quad (3.3)$$

where  $\sigma_i$  are the measurement uncertainties, and  $\text{erf}(x)$  is the error function<sup>1</sup>.

In *sAGA* the best-fit parameters are calculated through the maximisation of the likelihood function, using the sequential least squares programming tools available in the Python SciPy package<sup>2</sup> (Jones et al. 2001–). The large number of radiation processes – and other additional

<sup>1</sup>Eq. (3.1) is somehow questionable, as it overestimates the probability that the model lies above a given upper limit. This can be understood with a simple example: it assigns a probability of 16 % if the model is  $1\sigma$  above a  $3\sigma$  upper limit. So, the deviation should count as  $4\sigma$  not just  $1\sigma$ .

<sup>2</sup><http://www.scipy.org/>

**Table 3.1:** Free parameter space available for sAGA analysis.

Parameter	Unit	Description	Section
$p$	-	Power-law index of the electron energy distribution	Sect. 2.2
$\epsilon_e$	-	Fraction of the blastwave energy delivered to relativistic electrons	Sect. 2.2
$\epsilon_B$	-	Fraction of the blastwave energy delivered to magnetic fields	Sect. 2.2
$E_{K,iso}$	$10^{52}$ erg	Kinetic energy of the explosion (in units of $10^{52}$ erg)	Sect. 2.1.2, 2.1.3, 2.3
$n_0$	$\text{cm}^{-3}$	Density for ISM-like CBM	Sect. 2.1.3
$A_*$	$5 \times 10^{11}$ g $\text{cm}^{-1}$	Parameter connected with the wind-like density CBM	Sect. 2.3
$A_V$	mag	Extinction in the host galaxy	Sect. 3.6
$t_j$	d	Jet break time	Sect. 2.3
$t_{ei,1}$	d	Beginning time of the first injection	Sect. 3.5
$t_{ei,2}$	d	Beginning time of the second injection	Sect. 3.5
$m$	-	Injection index	Sect. 3.5
$m_2$	-	Injection index (in case of two bumps during the energy injection regime)	Sect. 3.5

aspects – involved in our broadband model inevitably introduces many free parameters (Table 3.1): in this high dimensional problem the algorithm would be stuck in local minima. This can be overcome through a Markov Chain Monte Carlo (MCMC) analysis using the Python-based code EMCEE<sup>3</sup> (Foreman-Mackey et al. 2013): this Bayesian approach leads to estimate uncertainties and correlations between the model parameters. EMCEE is particularly useful in high-dimensional problems – like the present one – where traditional MCMC methods spend large amounts of time exploring regions of parameter space with low likelihood values. Moreover, this tool is able to uncover degeneracies in the model parameters, especially in some of not well-constrained properties of the synchrotron spectrum (e.g.  $\nu_{sa}$ ) with the aid of corner plots (Foreman-Mackey 2016), an illustrative representation of different projections of samples in high dimensional spaces to reveal covariances.

In my analysis, I need to constrain these parameters through the definition of prior distributions that encode preliminary information. In the current version of sAGA I consider (i) uniform priors for the parameters that describe the exponential terms on the flux densities ( $A_v$ ) and the power-law indices ( $p$  and the injection index  $m$ ; Table 3.1 and Sect. 3.5), and (ii) Jeffreys priors (Jeffreys 1946), for the parameters that span different orders of magnitudes ( $E_{K,iso}$ ,  $n_0$ ,  $A_*$ ,  $\epsilon_e$ ,  $\epsilon_B$  and  $t_j$ ; Table 3.1).  $\epsilon_e$  and  $\epsilon_B$  are generally not expected to be larger than their equipartition values of 1/3 (e.g. L14), and hence I truncate the priors for these parameters at an upper bound of 1/3.

In the MCMC analysis, I begin to run the ensemble sampler until the convergence of the average likelihood across the chains and discard the initial (unstable) period as “burn-in”: I fixed 500 Markov chains for this phase. I then set up between  $10^3$  and  $10^4$  Markov chains, depending on the complexity of the problem. I plot the marginalised posterior density for all parameters and check for convergence by verifying the stability (over the length of the chain following burn-in) of the distributions. As reported by L14, the distributions frequently exhibit long tails, and hence I refer to quantiles (instead of mean or mode) to compute summary statistics and quote 68% credible regions around the median.

### 3.3 Synchrotron spectra and light-curves in sAGA

GRB afterglow radiation is thought to be the result of the relativistic ejecta being slowed down by the surrounding CBM (Meszaros & Rees 1997) and begins when a significant fraction of the energy of the ejecta is transferred to the shocked external medium. At the early-stage of the GRB afterglow (about the first few hours), the radiation process depends on the hydrodynamics of the shock (radiative phase), where  $\epsilon_e \sim 1$ ; later, the radiation process becomes less efficient as

<sup>3</sup><https://emcee.readthedocs.io/en/stable/>

long as it does not influence the hydrodynamics (adiabatic phase), where  $\epsilon_e \ll 1$  (Piran 2004). The hydrodynamics of the adiabatic phase, and the resulting synchrotron emission (described in Sect. 2.2), is based on the theory of relativistic blastwaves (Blandford & McKee 1976) consisting in a self-similar spherical solution for an adiabatic ultra relativistic blastwave in the limit  $\Gamma \gg 1$ .

In this context I modelled the synchrotron broadband spectrum with smoothly connected power-law segments, following the prescriptions described in GS02. Such a model includes synchrotron cooling and self-absorption for both ISM and wind-like environments, resulting in five different spectral regimes at any given time with 11 definitions of the break frequencies – corresponding to different orderings of the synchrotron frequencies – with the time-independent microphysical parameters  $E_{K,iso}$ ,  $p$ ,  $n_0$  (or  $A_*$ ),  $\epsilon_e$  and  $\epsilon_B$  as free parameters<sup>4</sup> (Table 2.1). The spectrum evolves from fast ( $v_c < v_m$ ) to slow cooling ( $v_c > v_m$ ), transitioning through the various spectral regimes (Fig. 2.1).

In sAGA light-curves are calculated through a specific time-dependent weighting scheme described in L14: the transition times between different spectral regimes are calculated through geometric average, since sometimes there are different equations for the same transition time (GS02).

### 3.4 Jet breaks and non-relativistic transition

The hydrodynamics presented in GS02 assume isotropic expansion but, as I described in Sect. 2.3, GRB outflows mostly occur through jets. I therefore consider the uniform jet regime, accounting for both the pure edge effect and sideways expansion (Sect. 2.3). In the pure edge effect the blastwave dynamics does not change during the jet break transition, and hence I modify only the evolution of the break flux densities after the break time  $t_j$  using the prescription  $\Delta\alpha = \alpha_{post,jet} - \alpha_{pre,jet} = (3 - k)/(4 - k)$ , where  $k = 0$  is for ISM-like CBM and  $k = 2$  is for wind-like CBM (Granot 2007). The sideways expansion effect, even though it becomes significant when  $\Gamma \lesssim 2$  (e.g. Granot et al. 2001; Kumar & Granot 2003; Zhang & MacFadyen 2009; De Colle et al. 2012; van Eerten & MacFadyen 2012), is a good approximation for post-jet-break light-curves (e.g. Zhang & MacFadyen 2009; Kumar & Zhang 2015). The relativistic blastwave, due to the interaction with the CBM, decelerates until it reaches the non-relativistic phase (Sect. 2.4) at the transition time  $t_{NR}$  (Eqs. 2.13 and 2.14).

sAGA is configured so that, at the beginning of the analysis, the user can select the desired effect; this choice modifies the evolution of the spectral break frequencies and flux densities at break epochs  $t_j$  (free parameter) and  $t_{NR}$ , smoothing  $t_j$  over the transition with a fixed smoothing parameter<sup>5</sup>. For completeness, I reported the post-break (sideways expansion) and Newtonian evolution of the spectral break frequencies in Table 2.1, following several papers (Sari et al. 1999; Frail et al. 2000; Panaitescu & Kumar 2002; Sari 2006; van Eerten et al. 2010; Leventis et al. 2012, GS02).

### 3.5 Energy injection

As the shock propagates into the surrounding medium, the blastwave decelerates: this is observed through the decay evolution in the observed light-curves of GRB afterglows. Sometimes, these observed light-curves are characterised by plateaus, probably due to the re-brightening of the GRB afterglow (e.g. Nousek et al. 2006; Liang et al. 2007; Margutti et al. 2010; Hascoët et al. 2012). This effect consists in the energy injection into the blastwave shock due to possible

<sup>4</sup>If the redshift  $z$  is unknown, it can also set as a free parameter

<sup>5</sup>I set  $s = 5$  for these breaks (e.g. Granot et al. 2001).



alternative mechanisms: long-lasting central engine activity, deceleration of a Poynting flux dominated outflow, or the presence of substantial ejecta mass (and hence kinetic energy) at low Lorentz factors (e.g. [Dai & Lu 1998](#); [Rees & Meszaros 1998](#); [Sari & Mészáros 2000](#); [Zhang & Mészáros 2002](#); [Zhang et al. 2006](#); [Granot & Kumar 2006](#); [Uhm et al. 2012](#)).

Some models invoke a long-lasting central engine such as a spinning-down millisecond magnetar ([Dai & Lu 1998](#); [Zhang & Mészáros 2001](#)) where the blastwave is fed by a long-lasting Poynting-flux-dominated wind. This flux is defined by a power-law decay with time:

$$L(t) = L_0 \left( \frac{t}{t_0} \right)^{-q} \quad (3.4)$$

where  $t$  is the central engine time (the same as the observer time of GRB afterglow),  $L_0$  is the luminosity at the reference time  $t_0$ , and  $q \geq 0^6$ . This corresponds to the temporal evolution of the blastwave energy  $E \propto t^{1-q} = t^m$ , where  $m = 1 - q$  is the “injection index”. These models predict plateaus in X-ray light-curves but do not generally lead to a re-brightening. The energy injection becomes significant when  $E_{inj} > E_{imp}$ , where  $E_{imp}$  is the impulsively injected energy during the prompt emission phase ([Zhang & Mészáros 2001](#)).

There is an alternative type of energy injection, occurring when the central engine injects a stratified ejecta with a continuous distribution of bulk Lorentz factor  $\gamma$ , defined as the ejecta mass above a certain Lorentz factor ([Rees & Meszaros 1998](#); [Sari & Mészáros 2000](#); [Uhm et al. 2012](#)):

$$M(> \gamma) = \gamma^{-s} . \quad (3.5)$$

The ejecta is moving between a maximum  $\gamma_{max}$  – corresponding to the Lorentz factor of the blastwave at the onset of energy injection  $t_{0,ei}$ ,  $\Gamma(t_{0,ei})$  – and a minimum Lorentz factor  $\gamma_{min}$ . In this model there is a difference between the blastwave (powered by an initial shell of fast-moving ejecta) and the leading edge of the remaining ejecta (travelling at  $\gamma_{max}$ ). As the blastwave decelerates, energy injection takes place when  $\Gamma(t_{0,ei}) \approx \gamma_{max}$  and hence the slower ejecta shells begin depositing energy into the blastwave. This regime lasts until the lowest energy ejecta located at  $\gamma_{min}$  have transferred their energy to the blastwave. Later, the afterglow proceeds like a standard regime, but powered by a blastwave with increased energy and Lorentz factor  $\gamma_{min}$  (determined from modelling the subsequent afterglow evolution).

These two energy injection mechanisms can be considered equivalent connecting the two injection parameters  $s$  and  $q$  as follows:

$$s = \frac{10 - 3k - 7q + 2kq}{2 + q - k} \quad (3.6)$$

$$q = \frac{10 - 2s - 3k + ks}{7 + s - 2k} \quad (3.7)$$

where  $k$  is the exponent of the density profile  $n = A r^{-k}$  ( $k = 0$  for ISM-like CBM, and  $k = 2$  for wind-like CBM). From Eqs 3.6 and 3.7 I obtain

$$\begin{aligned} s &= \frac{10 - 7q}{2 + q} \\ q &= \frac{10 - 2s}{7 + s} \end{aligned} \quad (3.8)$$

<sup>6</sup>The same approach sometimes is based on  $L(t) = L_0(t/t_0)^q$  and  $q \leq 0$  (e.g. [Misra et al. 2007](#); [Marshall et al. 2011](#); [van Eerten 2014](#); [Laskar et al. 2015](#)).

for the ISM-like CBM, and

$$s = \frac{4 - 3q}{q} \quad (3.9)$$

$$q = \frac{4}{3 + s}$$

for the wind-like CBM (Zhang et al. 2006). In particular, from Eq. (3.7) I obtain

$$m = \frac{(3 - k)(s - 1)}{7 + s - 2k}, \quad (3.10)$$

where  $m$  ranges between 0 and 3 for ISM-like CBM (between 0 and 1 for wind-like CBM). Moreover,  $s$  is bounded 1 and  $\infty$  for both ISM-like CBM and wind-like CBM. In the absence of energy injection, the standard hydrodynamic evolution requires that  $m = 0$ ,  $s = 1$  or  $q = 1$  in the above expressions (e.g. Gao et al. 2013b).

sAGA accounts for energy injection – ranging between  $t_{ei,i}$  and  $t_{ei,f}$  (in units of days) – selecting the number of “bumps” of injected energy from the central engine (1 or 2)<sup>7</sup>. In particular, I change the kinetic energy in the standard afterglow regime (e.g. GS02) according the following broken power-law function (Laskar et al. 2015):

$$E_{52,k,iso}(t) = \begin{cases} E_{52,k,iso,f} & t \geq t_{ei,f} \\ E_{52,k,iso,f} \left(\frac{t}{t_{ei,f}}\right)^m & t_{ei,i} \leq t \leq t_{ei,f} \\ E_{52,k,iso,i} \equiv E_{52,k,iso,f} \left(\frac{t_{ei,i}}{t_{ei,f}}\right)^m & t \leq t_{ei,i} \end{cases} \quad (3.11)$$

for one bump of energy injection, where  $E_{52,k,iso,i}$  and  $E_{52,k,iso,f}$  are the initial and final energy of the blastwave (in units of  $10^{52}$  erg), respectively, and

$$E_{52,k,iso}(t) = \begin{cases} E_{52,k,iso,f} & t > t_{ei,f} \\ E_{52,k,iso,f} \left(\frac{t}{t_{ei,f}}\right)^{m_1} & t_{ei,i_2} < t < t_{ei,f} \\ E_{52,k,iso,f} \left(\frac{t_{ei,i_2}}{t_{ei,f}}\right)^{m_1} \left(\frac{t}{t_{ei,i_2}}\right)^{m_2} & t_{ei,i_1} < t < t_{ei,i_2} \\ E_{52,k,iso,f} \left(\frac{t_{ei,i_2}}{t_{ei,f}}\right)^{m_1} \left(\frac{t_{ei,i_1}}{t_{ei,i_2}}\right)^{m_2} & t < t_{ei,i_1} \end{cases} \quad (3.12)$$

for two consecutive bumps of energy injection, where  $m_1$  and  $m_2$  are the injection indices referred to the first and second bump, respectively, and  $t_{ei,i_1}$  is the beginning time of the first injection, lasting up to  $t_{ei,i_2}$ .

Through these broken power-law functions for  $E_{52,k,iso}$  (Eqs. 3.11 and 3.12), I assume the temporal evolution ( $t$  in units of days) of  $\Gamma$  from the standard afterglow regime (GS02, Laskar et al. 2015):

$$\Gamma(t) = 3.65 \left(\frac{E_{52,k,iso}(t)}{n_0}\right)^{1/8} \left(\frac{t}{z+1}\right)^{-3/8} \quad (3.13)$$

for ISM-like CBM and

$$\Gamma(t) = 3.72 \left(\frac{E_{52,k,iso}(t)}{A_*}\right)^{1/4} \left(\frac{t}{z+1}\right)^{-1/4} \quad (3.14)$$

for wind-like CBM.

If the energy injection switch is enabled, sAGA works in iterative mode: the first step consists in the MCMC analysis (Sect. 3.2) of the simple FS (eventually with absorption and/or jet approach) for the data after  $t_{ei,f}$  (fixed by the observer and obtained by independent modelling of broadband light-curves) to determine the microphysical parameters of the GRB afterglow ( $E_{52,k,iso,f}$  included). Successively, these values are assumed as starting point for the analysis of the data at  $t < t_{ei,f}$  to obtain the free parameters  $t_{ei,i}$  and  $m$  ( $q$ ) in the energy injection regime.

<sup>7</sup>This number will be implemented for higher values.

## 3.6 Extinction and absorption processes

sAG<sub>A</sub> accounts for possible dust extinction in optical and photoelectric absorption caused in X-rays.

The typical size of dust grains in ISM is comparable to the frequency of blue light. This results in a strong absorption and scattering by the dust grains of the blue light coming from distant objects, making (for an observer on Earth) these objects dimmer (extinction) and redder (reddening) than they really are. GRB afterglows are subject to optical extinction, which is caused by the contribution of (1) the Galactic dust along the line of sight (Galactic) and (2) the dust within the host galaxy (intrinsic). A detailed knowledge of the latter is crucial for (1) determining the intrinsic luminosity of GRB afterglows from X-ray to near-IR frequencies; (2) constraining the nature of the GRB progenitors and their environments; and (3) probing the ISM of high-redshift galaxies and the cosmic star formation history (Li 2007). Nevertheless, dust extinction in GRB host galaxies is still poorly known; to date there are different extinction curves that can be assumed to properly model optical afterglow SEDs (e.g. Kann et al. 2006; Li et al. 2008; Stratta et al. 2011; Zonca et al. 2016).

I adopt the extinction curves as parametrised by Pei (1992), modelled using Milky Way (MW), or the dust models for Small and Large Magellan Clouds (SMC and LMC, respectively), in order to determine the extinction  $A_V$ , measured in the V band. The extinction correction is not applied to the data, but only to the model during fitting and plotting phase.

UV frequencies often are affected by the absorption by neutral hydrogen, from  $z \gtrsim 1$ . sAG<sub>A</sub> accounts for this effect through a sight-line-averaged model for the optical depth of the intergalactic medium (IGM) as described by Madau (1995), to compute the IGM transmission as a function of wavelength at the redshift of the GRB; this model considers the Ly $\alpha$  absorption by neutral hydrogen along the line of sight and photoelectric absorption by intervening systems. This effect is contained in `ETAU_MADAU` library of `SYNPHOT` Python package (STScI development Team 2018).

Moreover, X-ray frequencies are usually affected by the interstellar photoelectric absorption. Where the X-ray data are subject to photoelectric absorption, sAG<sub>A</sub> accounts for this effect through the related hydrogen-equivalent column density  $N_H$  (in units of  $10^{22} \text{ cm}^{-2}$ ), obtained by a polynomial fit of the effective absorption cross-section per hydrogen atom as a function of energy in the 0.03–10 keV range assuming a given abundance pattern (Morrison & McCammon 1983).

## 3.7 Radio interstellar scintillation

Inhomogeneities in the electron density distribution in the Milky Way along the GRB line of sight scatter the flux at low frequencies ( $\lesssim 10$  GHz), causing variations in measured flux density of the source. This effect, called interstellar scintillation (ISS), is significant when the source size subtended at the scattering screen is comparable to the size of the inhomogeneities and becomes negligible as the blastwave expands (Rickett 1990; Goodman 1997; Walker 1998; Goodman & Narayan 2006; Granot & van der Horst 2014). GRBs display often a similar behaviour in their radio light-curves (e.i. Goodman 1997; Frail et al. 1997, 2000); these variations occur between observations on timescales ranging between hours and days.

In the standard (and easy) picture, ISS is assumed to occur at a single “thin screen” at some intermediate distance  $d_{scr}$ , typically  $\sim 1$  kpc for high Galactic latitudes. The spectrum of the electron density inhomogeneities in the ISM is described by the Kolmogorov spectrum

(Armstrong et al. 1995; Cordes & Lazio 2002)

$$P(\mathbf{q}) = C_N^2 q^{-11/3}, \quad (3.15)$$

where  $\mathbf{q}$  is the wave-vector and  $C_N^2$  is a normalisation constant depending on the position of the inhomogeneity in the Galaxy. The scattering measure  $SM$  is defined as the integral of  $C_N^2$  from the observer to  $d_{scr}$ ,

$$SM = \int_0^{d_{scr}} C_N^2(x) dx. \quad (3.16)$$

$SM$  is measured in units of  $\text{kpc m}^{-20/3}$ . In the ISS effect on observations of an extra-Galactic source, the Fresnel scale  $r_F$  plays a crucial role. It is defined as the transverse separation over which the phase delay is 1 rad, and is related to  $d_{scr}$  and the observing frequency  $\nu_{obs}$  through the relation (Rickett 1990):

$$r_F = 1.2 \times 10^{11} \sqrt{\frac{d_{scr, \text{kpc}}}{\nu_{\text{obs, GHz}}}} \text{ cm} \quad (3.17)$$

The strength of the scattering is quantified by a dimensionless parameter, defined as (Walker 2001)

$$\xi = 7.9 \times 10^3 SM^{0.6} d_{scr}^{0.5} \nu_{\text{GHz}}^{-1.7}. \quad (3.18)$$

There are in general two types of ISS: weak and strong scattering. In weak scattering ( $\xi \ll 1$ ) there are only small phase changes over  $r_F$  due to fluctuations in the density of free electrons in the medium (usually in the Galactic ISM) between us and the source. The strong scattering regime ( $\xi \gg 1$ ) occurs when the wavefront is highly distorted on scales smaller than  $r_F$ , resulting in much larger flux modulations than weak scattering (Granot & van der Horst 2014). Strong scattering can be divided up into: (i) refractive scintillation, caused by focusing and defocusing of the wave front by large-scale inhomogeneities, which is a broadband process; and (ii) diffractive scintillation, caused by interference between rays diffracted by small-scale irregularities in the interstellar medium, which is modulating the flux over a narrow frequency band (Granot & van der Horst 2014).

ISS depends strongly on frequency: at high radio frequencies only modest flux variations are expected, while at low frequencies strong ISS effects are important. The transition frequency  $\nu_{trans}$  between strong and weak ISS is defined as the frequency at which  $\xi = 1$  (Goodman 1997):

$$\nu_{trans} = 10.4 SM_{-3.5}^{6/17} d_{scr}^{5/17} \text{ GHz} \quad (3.19)$$

where  $SM_{-3.5} = (SM/10^{-3.5} \text{ m}^{-20/3} \text{ kpc})$ . In the strong ISS regime, diffractive scintillation can produce large flux variations on timescales of minutes to hours but is only coherent across a bandwidth  $\Delta\nu = (\nu/\nu_{trans})^{3.4}$  (Goodman 1997; Walker 1998). Refractive scintillation is broadband and varies more slowly, on timescales of hours to days.

In all regimes,  $\xi$  decreases with time at all frequencies as the size of the emitting region expands, with diffractive ISS quenching before refractive ISS. The source expansion also increases the typical timescale of the variations for both diffractive and refractive ISS (Resmi 2017). In this complex situation, the contribution of ISS for each regime is defined by the modulation index  $m_{scint}$ , defined as the rms fractional flux density variation. Accurate prescription about the behaviour of  $m_{scint}$  is described in Walker (1998) and Granot & van der Horst (2014): this prescription is strictly correct only in the asymptotic regimes ( $\xi \ll 1$  for weak ISS and  $\xi \gg 1$  for strong ISS), and allows to analyse ISS only in weak/ strong refractive or weak/strong diffractive scenario. Another approach for the analysis of ISS is based on a dedicated fitting function that including both diffractive and refractive contributions (Goodman & Narayan 2006).

sAGA accounts for this process following a dedicated fitting function that includes both diffractive and refractive contributions to compute  $m_{scint}$  (Goodman & Narayan 2006). The values of  $\nu_{trans}$  and SM are estimated through the NE2001<sup>8</sup> model for the Galactic electron distribution (Cordes & Lazio 2002). The expected ISS contribution in the model-predicted flux density  $F_{model}$  is defined as:

$$\Delta F_{scint} = m_{scint} F_{model} . \quad (3.20)$$

To take into account the ISS effect in the analysis, I sum  $\Delta F_{scint}$  to the uncertainty of flux densities before to perform the MCMC optimisation (Sect. 3.2); usually this action influences the quality of the radio data, especially in the C-band (4–8 GHz; e.g. Misra et al. 2019), but it is extremely useful to reduce the ISS effect in the fit process. Moreover, I use Eq. (3.20) to highlight the ISS area in the spectra and light-curves produced by sAGA at the end of the analysis.

### 3.8 Inverse-Compton regime

At high frequencies, synchrotron photons produced in the GRB blastwave can emit inverse-Compton (IC) radiation, occurring when  $\epsilon_B \ll \epsilon_e$  (Blandford & McKee 1976; Rybicki & Lightman 1979; Panaitescu et al. 1998; Panaitescu & Kumar 2000; Sari & Esin 2001). The energies involved are very large, and hence the ejecta is in a regime in which the IC cross-section decreases rapidly; as a result, a photon undergoes only a single scattering.

The contribute of IC emission – in terms of flux density – typically is negligible compared to synchrotron radiation, but the IC mechanism can influence the cooling for the shock-accelerated electrons and hence dominate the total cooling rate (e.g. Sari & Esin 2001; Zhang et al. 2007). The effects of IC depend on the Compton  $y$ -parameter  $y^9$ , defined as

$$y = \frac{-1 + \sqrt{1 + 4\eta\epsilon_e/\epsilon_B}}{2} \quad (3.21)$$

where  $\eta$  is the fraction of energy that has been radiated away due both to synchrotron and IC radiation. At early-time, during the fast cooling stage of the GRB afterglow, where most of the electron energy is lost,  $\eta = 1$  and IC emission dominates over synchrotron; on the other hand, during the slow cooling stage at late-time,  $\eta$  decreases ( $\eta = (\nu_c/\nu_m)^{-(p-2)/2}$ ) and hence the synchrotron component begins to dominate over IC scattering component (Sari & Esin 2001). Moreover, if  $y < 1$ , the IC regime can be neglected; otherwise a high-energy component (of the order of 10 MeV) appears in the spectrum and the cooling timescale is shortened by a factor  $y$  (Sari & Esin 2001; Piran 2004). As in the case of synchrotron emission, since temporal evolution of the GRB afterglow emission depends on the CBM, IC radiation is different in the case of the ISM-like and wind-like CBM.

Recently, for the first time TeV emission has been recorded from a couple of bright GRB afterglows: 190114C (MAGIC Collaboration et al. 2019b) and 180720B (Abdalla et al. 2019). The SEDs showed a double-peaked shape, with the TeV emission best explained in terms of inverse Compton up-scattering of synchrotron photons by high-energy electrons.

sAGA accounts for IC cooling by computing the Compton  $y$ -parameter from the FS parameters<sup>10</sup>, and hence scaling the spectral break frequencies and flux densities of the synchrotron spectrum by the appropriate powers of  $1 + y$  (Sari & Esin 2001, L14, GS02).

<sup>8</sup><http://www.astro.cornell.edu/~cordes/NE2001/>

<sup>9</sup>Note that this equation does not take the Klein–Nishina correction into account (Nakar et al. 2009; Wang et al. 2010; Gao et al. 2013a; Laskar et al. 2018a). This frequency-dependent correction is expected to be important only at very high frequencies,  $\nu \gtrsim 10^{18}$  Hz at  $t \gtrsim 1$  d (e.g. Zhang et al. 2007). I therefore do not consider this effect further in my PhD Thesis.

<sup>10</sup>At the time of writing, this implementation is still work in progress.



### 3.9 Test cases for sAGA

sAGA was been tested on broadband data of GRB afterglows. Hereafter, I briefly compare the sAGA results with what is reported the literature for some well studied GRBs.

#### 3.9.1 GRB 120521C

GRB 120521C was discovered with the *Swift*/BAT (Barthelmy et al. 2005) on 2012 May 21 at 23:22:07 UT (Baumgartner et al. 2012). This burst is characterised by a duration  $T_{90} = (26.7 \pm 0.4)$  s (Markwardt et al. 2012) and a high redshift ( $z \approx 6$ , L14). The afterglow of GRB 120521C was observed with several facilities from radio to X-rays (VLA, optical/NIR telescopes, *Swift*/XRT) between  $\sim 10^{-3}$  d to  $\sim 200$  d after the GRB trigger time, and it is described in terms of FS emission with jet break and optical extinction.

As reported by L14, data prior to 0.25 d are ignored because the X-ray light-curve displays a steep decline before  $\sim 0.01$  d, possibly connected to the high-latitude component of the prompt emission (e.g. Kumar & Panaitescu 2000), followed by a plateau phase extending up to  $\sim 0.25$  d, usually attributed to the energy injection (e.g. Nousek et al. 2006; Zhang et al. 2006). The broadband analysis of the GRB 120521C data after 0.25 d with sAGA is compared with the results by L14: in both treatments, an ISM model provides a good fit to the broadband data. My best-fit model is shown in Fig. 3.1 and the corresponding physical parameters are listed in Table 3.2.

Several parameters are consistent with those reported by L14 within  $\sim 1\sigma$  ( $\epsilon_e$ ,  $\epsilon_B$ ,  $E_{52}$ ,  $A_v$ ,  $t_j$  and  $\theta_j$ ), and  $\sim 2\sigma$  ( $p$ ). Moreover, using the functional dependence of the micro-physical parameters ( $\epsilon_e$ ,  $\epsilon_B$ ,  $n_0$ , and  $E_{52}$ ) on the measured break frequencies ( $\nu_{sa}$ ,  $\nu_m$ , and  $\nu_c$ ), my micro-physical parameters are inside the constraints derived by L14:  $2.8 \times 10^{-4} \lesssim n_0/\text{cm}^{-3} = 6.8 \times 10^{-2} \lesssim 27$ ,  $2.9 \lesssim E_{52} = 26 \lesssim 29$ ,  $3.5 \times 10^{-4} \lesssim \epsilon_B = 2.4 \times 10^{-3} \lesssim 1/3$ ,  $3.4 \times 10^{-2} \lesssim \epsilon_e = 5.4 \times 10^{-2} \lesssim 1/3$ . The self-absorption frequency obtained with sAGA lies below the VLA frequencies, and is therefore not fully constrained; this conclusion is compatible with L14, who also constrained this frequency between  $1.75 \times 10^8$  Hz and  $2.7 \times 10^9$  Hz, with my value lying in between ( $4.5 \times 10^8$  Hz).

Finally, I show that the two values of  $p$  (Table 3.2) are also compatible with the one inferred from the optical/X-ray SEDs alone<sup>11</sup>. In this approach, an empirical power-law fit of the optical/X-ray SED at  $\sim 0.3$  d after the explosion yields  $\beta = -0.58_{-0.06}^{+0.08}$ . At this time the afterglow spectrum is in slow cooling regime ( $\nu_m < \nu_c$ ), resulting in  $\beta = (1 - p)/2$ , and hence  $p = 1 - 2\beta = 2.16_{-0.16}^{+0.12}$ , compatible with both analyses.

#### 3.9.2 GRB 090423

GRB 090423 was discovered with the *Swift*/BAT (Barthelmy et al. 2005) on 2009 April 23 at 7:55:19 UT (Krimm et al. 2009). This burst is characterised by a duration  $T_{90} = 10.3 \pm 1.1$  s (Palmer et al. 2009) and a high redshift ( $z = 8.26$ , Salvaterra et al. 2009; Tanvir et al. 2009). The afterglow of GRB 090423 was observed with several facilities from radio to high-energies (VLA, CARMA, optical/NIR telescopes, *Swift*/XRT) between  $\sim 10^{-2}$  d to  $\sim 280$  d after the GRB triggering, and it is described in terms of forward shock, jet break, and optical extinction.

The millimeter data are ignored because they are probably affected by RS radiation (L14). sAGA results are found to agree with those of L14, obtaining a very good fit with an ISM model. I followed the same approach as those authors and fixed the power-law index of the electron energy distribution ( $p = 2.56$ , based on their best-fit value); my result obtained is in good

<sup>11</sup>For further details about this kind of approach see Sect. 4.3.1.

**Table 3.2:** Summary statistics from MCMC analysis obtained through the analysis of L14 (first column) and sAGA (second column) with broadband data (from radio to X-ray frequencies) of GRB 120521C for a model based on a jetted (sideways-regime) FS emission with optical absorption, in ISM-like CBM. sAGA makes use of the  $\chi^2$  test to quantify the goodness of fit. Since L14 do not report any statistic that quantifies the goodness of the fit, for comparison I report for L14 the  $\chi_r^2$  obtained by fixing the parameter set found by those authors. All the uncertainties are reported at 68% ( $1\sigma$ ).

Parameter	Unit	L14	sAGA
$p$	-	$2.17^{+0.09}_{-0.07}$	$2.34 \pm 0.07$
$\epsilon_e$	-	$(4.5^{+6.7}_{-2.4}) \times 10^{-2}$	$(5.4^{+1.7}_{-1.3}) \times 10^{-2}$
$\epsilon_B$	-	$(7.0^{+0.2}_{-6.0}) \times 10^{-3}$	$(2.4^{+1.3}_{-1.1}) \times 10^{-3}$
$n_0$	$\text{cm}^{-3}$	$(2.0^{+1.0}_{-0.7}) \times 10^{-3}$	$(6.8^{+4.4}_{-2.8}) \times 10^{-2}$
$E_{52}$	$10^{52}$ erg	$(2.2^{+3.7}_{-1.4}) \times 10^1$	$(2.6^{+4.8}_{-5.9}) \times 10^1$
$A_v$	mag	$< 0.05$	$(3.1^{+2.1}_{-2.0}) \times 10^{-2}$
$t_j$	d	$6.8^{+3.8}_{-2.4}$	$3.2^{+2.3}_{-1.3}$
$\theta_j$	deg	$3.0^{+2.3}_{-1.1}$	$3.2^{+0.8}_{-0.6}$
$\nu_m^a$	Hz	$5.5 \times 10^{11}$	$7.6 \times 10^{11}$
$\nu_c^a$	Hz	$1.2 \times 10^{16}$	$7.4 \times 10^{16}$
$\nu_{sa}^a$	Hz	$\lesssim 5.0 \times 10^9$	$4.5 \times 10^8$
$\nu_{ac}^a$	Hz	-	$1.8 \times 10^{10}$
$\chi_r^2$	-	1.4	1.1

<sup>a</sup> Measured at  $t_{obs} = 1$  d.

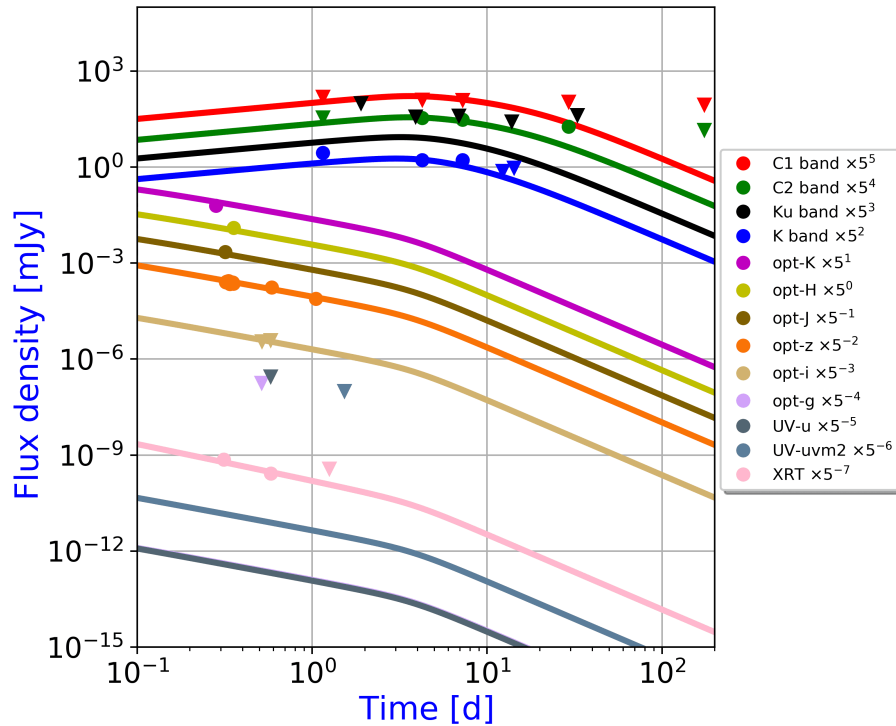


**Figure 3.1:** Broadband modelling of GRB 120521C for a FS model with an ISM-like CBM (GS02). Filled circles indicate detections, and inverted triangles indicate  $3\sigma$  upper limits. The physical parameters of the burst derived from the best-fit solution are listed in Table 3.2.



**Table 3.3:** Summary statistics from the modelling obtained through the analysis of L14 (first column), C10 (second column), and sAGA (third and fourth columns) with broadband data (from radio to X-ray frequencies) of GRB 090423 for a model based on a jetted (sideways-regime) FS emission with optical absorption, in ISM-like CBM. The uncertainties are reported at 68% ( $1\sigma$ ).

Parameter	Unit	L14	sAGA	sAGA
$p$	-	2.56 (fixed)	2.56 (fixed)	$2.31^{+0.17}_{-0.09}$
$\epsilon_e$	-	$(2.7^{+2.0}_{-0.7}) \times 10^{-2}$	$(5.1^{+1.0}_{-0.8}) \times 10^{-2}$	$(3.0^{+1.0}_{-0.4}) \times 10^{-2}$
$\epsilon_B$	-	$(4.8^{+9.5}_{-3.9}) \times 10^{-2}$	$(6.7^{+5.9}_{-3.1}) \times 10^{-3}$	$(2.2^{+0.8}_{-1.7}) \times 10^{-1}$
$n_0$	$\text{cm}^{-3}$	$(2.5^{+0.6}_{-0.3}) \times 10^{-5}$	$(0.6^{+0.8}_{-0.4}) \times 10^{-5}$	$(4.4^{+6.4}_{-3.1}) \times 10^{-5}$
$E_{52}$	$10^{52}$ erg	$(3.4^{+1.1}_{-1.4}) \times 10^2$	$(1.8 \pm 0.4) \times 10^2$	$(1.3^{+2.1}_{-0.6}) \times 10^2$
$A_v$	mag	$0.15 \pm 0.02$	$0.11 \pm 0.02$	$(8.8^{+2.7}_{-1.9}) \times 10^{-2}$
$t_j$	d	$14.6^{+2.7}_{-2.3}$	$13.5 \pm 2.7$	$7.6^{+5.5}_{-1.5}$
$\theta_j$	deg	$1.5^{+0.7}_{-0.3}$	$2.2 \pm 0.3$	$1.3 \pm 0.5$
$\nu_m^a$	Hz	$7.7 \times 10^{12}$	$8.1 \times 10^{12}$	$3.9 \times 10^{12}$
$\nu_c^a$	Hz	$4.5 \times 10^{17}$	$4.9 \times 10^{17}$	$1.3 \times 10^{16}$
$\nu_{sa}^a$	Hz	$\lesssim 8.0 \times 10^9$	$3.0 \times 10^7$	$1.8 \times 10^8$
$\nu_{ac}^a$	Hz	-	$1.0 \times 10^9$	$2.3 \times 10^9$
$\chi_r^2$	-	1.2	0.9	1.3

<sup>a</sup> Measured at  $t_{obs} = 1$  d.

accordance. My best-fit model in ISM-like CBM is shown in Fig. 3.2 and the corresponding physical parameters are listed in Table 3.3 (third column). Both solutions are consistent with each other within  $\sim 1\sigma$ . Moreover, thanks to sAGA I estimated that the non-relativistic regime occurs at  $t_{NR} = (5.1^{+1.7}_{-1.3}) \times 10^4$  d since the GRB. Finally, the self-absorption frequency  $\nu_{sa}$  obtained with sAGA is not fully constrained because it lies below the VLA frequencies, compatibly with L14, who also constrained this frequency between  $6.8 \times 10^6$  Hz and  $3.1 \times 10^8$  Hz, with my value being  $3 \times 10^7$  Hz.

The fixed parameter  $p = 2.56$  is also compatible with what inferred from optical/X-ray SEDs alone. In this approach, the empirical power-law fit of the optical/X-ray SEDs at 0.07 d and 0.7 d implies  $\beta = -0.7 \pm 0.2$ . Since the synchrotron spectrum is in slow cooling regime ( $\nu_m < \nu_c$ ) at these epochs,  $\beta = (1 - p)/2$  (Fig. 2.1), and hence  $p = 1 - 2\beta = 2.4 \pm 0.4$ . Therefore, I analysed the broadband data from GRB 090423 with  $p$  as a free parameter, obtaining the results reported in Table 3.3 (fourth column). Fig. 3.3 shows my best-fit model in ISM-like CBM. Both solutions are consistent with each other within  $\sim 1\sigma$ . The non-relativistic regime sets in at  $t_{NR} = (1.1 \pm 0.3) \times 10^5$  d after the GRB. Finally, the different value of  $t_j$  (and  $\theta_j$ ) obtained through this approach is part of a debate about the presence of jetted emission for this GRB: for example, a previous analysis of GRB 090423 claimed no jet break up to  $\sim 45$  d (Chandra et al. 2010).

### 3.9.3 GRB 050904

This GRB was discovered with *Swift*/BAT on 2005 September 4 at 1:51:44 UT (Cummings et al. 2005) and it is characterised by a high redshift ( $z = 6.29$ , Tagliaferri et al. 2005; Haislip et al. 2006; Kawai et al. 2006). Broadband data (at radio, optical and X-ray frequencies) are taken from the papers of Gou et al. 2007 (hereafter G07) and L14, which describe the GRB afterglow emission in terms of forward shock, jet break, and optical extinction. I compare my results with G07 and L14; as in previous studies of this burst (Frail et al. 2006, G07 and L14), I find that an ISM model works better than a wind one. My best-fit model is shown in Fig. 3.4 and the

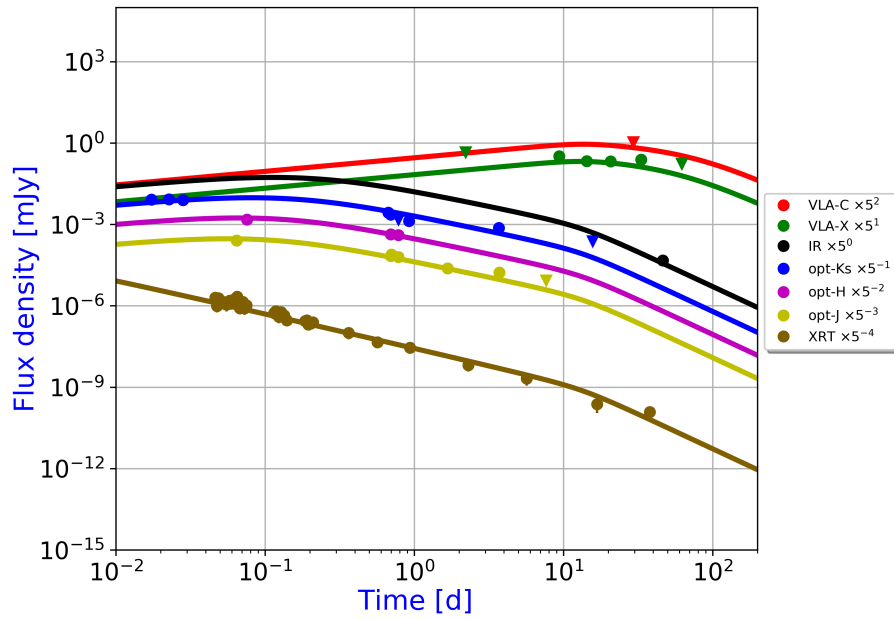


**Figure 3.2:** Broadband modelling of GRB 090423 for a FS model with an ISM-like CBM (GS02), with  $p = 2.56$ . Filled circles indicate detections, and inverted triangles indicate  $3\sigma$  upper limits. The physical parameters of the burst derived from the best-fit solution are listed in Table 3.3 (third column).

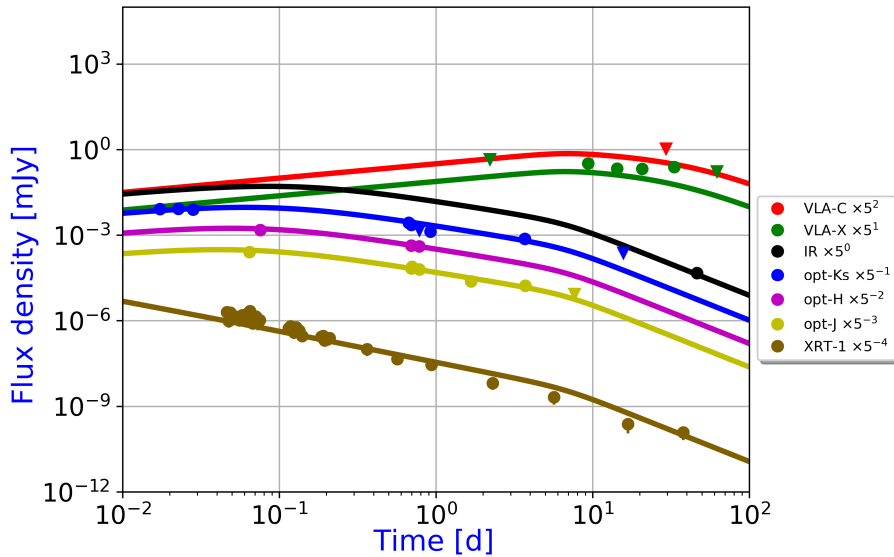


**Figure 3.3:** Broadband modelling of GRB 090423 for a FS model with an ISM-like CBM (GS02), with  $p$  as free parameter. Filled circles indicate detections, and inverted triangles indicate  $3\sigma$  upper limits. The physical parameters of the burst derived from the best-fit solution are listed in Table 3.3 (fourth column).

**Table 3.4:** Summary statistics from the modelling obtained through the analysis of G07 (first column), L14 (second column), and sAGA (third column) with broadband data (from radio to X-ray frequencies) of GRB 050904 for a model based on a jetted (sideways-regime) FS emission with optical absorption, in ISM-like CBM. All the uncertainties are reported at 68% ( $1\sigma$ ).

Parameter	Unit	G07	L14	sAGA
$p$	-	$2.15 \pm 0.04$	$2.07 \pm 0.02$	$2.29 \pm 0.03$
$\epsilon_e$	-	$(3.1^{+2.5}_{-1.8}) \times 10^{-2}$	$(1.2^{+1.5}_{-0.5}) \times 10^{-2}$	$(2.5^{+0.6}_{-0.5}) \times 10^{-2}$
$\epsilon_B$	-	$(2.0^{+1.9}_{-1.5}) \times 10^{-1}$	$(1.3^{+2.2}_{-1.1}) \times 10^{-2}$	$(1.3^{+0.5}_{-0.2}) \times 10^{-3}$
$n_0$	$\text{cm}^{-3}$	$84.4^{+188.6}_{-58.4}$	$(6.3 \pm 0.1) \times 10^2$	$(9.5^{+7.5}_{-3.8}) \times 10^2$
$E_{52}$	$10^{52} \text{ erg}$	$(2.2^{+3.1}_{-0.9}) \times 10^1$	$(1.7^{+1.2}_{-1.0}) \times 10^2$	$(3.5^{+1.1}_{-0.9}) \times 10^1$
$A_v$	mag	$3.4^{+4.6}_{-1.6} \times 10^{-2}$	$< 0.05$	$(7.5^{+37.6}_{-5.7}) \times 10^{-4}$
$t_j$	d	$3.2 \pm 0.2$	$1.5^{+0.2}_{-0.1}$	$3.6^{+0.7}_{-0.4}$
$\theta_j$	deg	$7.3^{+3.0}_{-0.5}$	$6.2^{+3.3}_{-1.4}$	$8.2^{+1.1}_{-0.9}$
$\nu_m^a$	Hz	-	-	$3.7 \times 10^{12}$
$\nu_c^a$	Hz	-	-	$3.5 \times 10^{14}$
$\nu_{sa}^a$	Hz	-	-	$7.8 \times 10^{10}$
$\nu_{ac}^a$	Hz	-	-	$3.4 \times 10^{11}$
$\chi_r^2$	-	$1.4^b(1.02)^c$	1.4	0.73

<sup>a</sup> Measured at  $t_{obs} = 0.1$  d.

<sup>b</sup> Value reported in Gou et al. (2007).

<sup>c</sup> This value is obtained with sAGA fixing the parameters to those of G07.

corresponding physical parameters are listed in Table 3.4 (third column).

Almost all the parameters obtained with sAGA are consistent with those in the literature within  $\sim 1\sigma$  ( $\epsilon_e$ ,  $A_v$ , and  $\theta_j$ ) and  $\sim 2\sigma$  ( $\epsilon_B$ ,  $E_{52}$ ); moreover, I estimated that the non-relativistic regime occurs at  $t_{NR} = (4.3^{+1.1}_{-0.9}) \times 10^2$  d after the GRB. The jet break time of  $t_j = 3.6$  d inferred by my analysis is later than different values reported in the literature ( $t_j = 2.6 \pm 1$  d, Tagliaferri et al. 2005;  $t_j = 2.63 \pm 0.37$  d, Kann et al. 2007; Table 3.4), but it is consistent with them within  $\sim 2\sigma$ .

Finally, my derived value of the  $p$  is compatible with the value obtained by G07 within  $\sim 2\sigma$ , and apparently incompatible with the value obtained by L14. This value, as reported by G07, is explainable through the achromatic break interpretation of GRB afterglow light-curves, where the post-jet-break decay index is predicted to be  $\alpha = -p$  (Sect. 2.3); as reported by Tagliaferri et al. (2005), in the jetted scenario the multiple NIR light-curves of the afterglow after  $t_j$  are described by a decay with power-law index  $\alpha = p = 2.4 \pm 0.4$ , consistent with the values of  $p$  reported in Table 3.4.

### 3.9.4 Overview of my test results

sAGA has been successfully tested on the broadband data of the afterglows of GRB 120521C, GRB 090423, and GRB 050904. My results are consistent with those reported in the literature (especially L14, who make use of a similar approach for the characterisation of the GRB afterglow) within  $\lesssim 2\sigma$ . Moreover, the values of  $p$  obtained from my modelling are compatible with the inferences based on the lines of reasoning based on the observation of the optical/X-ray SEDs.

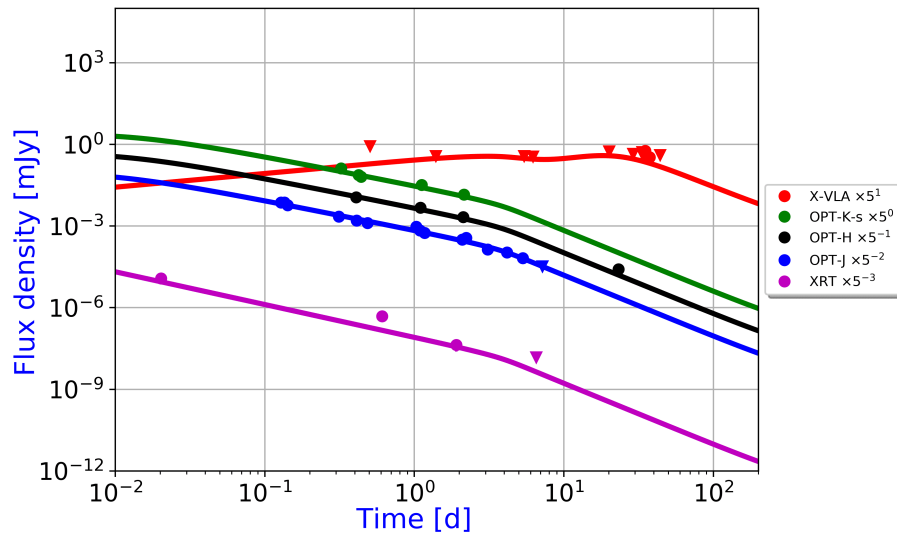


**Figure 3.4:** Broadband modelling of GRB 050904 for a FS model with an ISM-like CBM (GS02). Filled circles indicate detections, and inverted triangles indicate  $3\sigma$  upper limits. The physical parameters of the burst derived from the best-fit solution are listed in Table 3.4.



## Chapter 4

# Broadband modelling of the afterglow of GRB 160131A

The standard model of the GRB afterglow and the capabilities of sAG<sub>A</sub> (Chapter 3) are tested in the case of GRB 160131A, a long GRB observed through deep followup campaigns from radio all the way up X-rays. Multi-frequency light-curves show the signature of energy injection, and jetted emission. The rich radio data set acquired with VLA for this source is remarkably challenging: the radio light-curves are affected by several peaks, maybe suggestive of either interstellar scintillation (ISS) effects or multi-component structure. Here I present preliminary results, which will be the subject of a dedicated paper.

## 4.1 Introduction

GRB 160131A is a very long-GRB ( $T_{90} = 328$  s)<sup>1</sup>, with an estimated isotropic-equivalent  $E_{\gamma, \text{iso}} = 8.3 \times 10^{53}$  erg in the 0.02 – 15 MeV range (Tsvetkova et al. 2016) at a redshift  $z = 0.972$  (Malesani et al. 2016; de Ugarte Postigo et al. 2016). Prompt gamma-ray polarimetric measurements in the 100 – 300 keV band showed that GRB 160131A is possibly highly polarised ( $94 \pm 33$  %, although the confidence level is  $< 3\sigma$ , Chattopadhyay et al. 2019). This suggests that the GRB is due to synchrotron emission within a time-dependent, ordered magnetic field (Nakar et al. 2003; Granot & Königl 2003; Waxman 2003), with an initial bulk Lorentz factor of  $\Gamma_0 = 460 \pm 50$  and jet opening angle of  $\theta_j = 3_{-1.8}^{+3}$  ° (Chattopadhyay et al. 2019).

Optical analysis of a sample of 119 GRB afterglow light-curves (Mazaeva et al. 2018) shows that GRB 160131A is characterised by deviations (inhomogeneities) from broken power-law, called wiggles<sup>2</sup>, of the early GRB afterglow at early-time ( $\lesssim 0.5$  d since GRB trigger). Optical and X-ray light-curves are characterised by a plateau between  $\sim 0.1$  d and  $\sim 0.8$  d (Fig. 4.3), suggestive of energy injection as a possible explanation (Sect. 4.5.1). Moreover, they show a steep decay following the plateau ( $\sim 0.8$  d) that calls for a jet break; an independent analysis suggests a jet-break at  $1.2 \pm 0.3$  d (Mazaeva et al. 2018).

Radio light-curves and SEDs are crucial to constrain (1) the synchrotron characteristic frequencies (Sect. 4.3.1 and 4.3.4), and (2) the jetted emission (Sect. 4.3.3). On the other hand, radio data from 0.6 to 37 GHz are a conundrum for this source because SEDs and light-curves (Sect. 4.3.2) are affected by several peaks, possibly due to either interstellar scintillation (ISS) effects in the ISM of the Milky Way or multi-component structure. Moreover, there is no signature of energy injection in the form of a plateau in radio data because of the absence of data prior to 0.8 d.

Here I present multi-frequency observations of GRB 160131A spanning from  $\sim 430$  s to  $\sim 163$  d since the burst at 26 frequencies from  $6 \times 10^8$  to  $7 \times 10^{17}$  Hz. I start loosely constraining the nature of the circumburst environment and the behaviour of the characteristic frequencies of the synchrotron emission, using optical and X-rays. I then test the compatibility of the radio data set with the information inferred from the preliminary analysis of optical and X-ray data within the context of the broadband afterglow model. Finally, I fit the entire multiwavelength data set simultaneously to come up with an exhaustive and self-consistent description of the microphysics, geometry, and dynamics of the afterglow.

## 4.2 Broadband followup campaigns

GRB 160131A was discovered with the *Swift*/BAT on January 16 at 08:20:31 UT, 2016 (Page & Barthelmy 2016) at  $\alpha = 5^{\text{h}}12^{\text{m}}44^{\text{s}}$ ,  $\delta = -7^{\circ}04'02''$  with an uncertainty of 3 arcmin (radius, 90% containment, including systematic uncertainty).

### 4.2.1 X-ray followup

*Swift*/XRT observed the region of GRB 160131A in photon counting mode from 69.7 s to 9.25 d after the BAT trigger (Page & Barthelmy 2016). XRT found a bright, uncatalogued X-ray source located at  $\alpha = 5^{\text{h}}12^{\text{m}}40.32^{\text{s}}$ ,  $\delta = -7^{\circ}02'59.4''$  (J2000), with an uncertainty of 1.4 arcsec (radius, 90% containment)<sup>3</sup>. The specific *Swift* online repository pipeline<sup>4</sup> shows that the spectrum of

<sup>1</sup><https://swift.gsfc.nasa.gov/results/batgrbcats/GRB160131A/web/GRB160131A.html>

<sup>2</sup>A wiggle consists in wave-like variations with transition from positive to negative (and vice versa) residuals.

<sup>3</sup>[https://www.swift.ac.uk/xrt\\_positions/00672236/](https://www.swift.ac.uk/xrt_positions/00672236/)

<sup>4</sup>[https://www.swift.ac.uk/xrt\\_spectra/00672236/](https://www.swift.ac.uk/xrt_spectra/00672236/)



GRB 160131A is well fitted by a highly absorbed power law with photon index  $\Gamma_X = 1.98 \pm 0.06$  and intrinsic hydrogen column  $N_{H,int} = (4.0^{+0.9}_{-0.8}) \times 10^{21} \text{ cm}^{-2}$ , which is significantly in excess of the Galactic column  $N_{H,Gal} = 1.15 \times 10^{21} \text{ cm}^{-2}$  in the direction of GRB 160131A. From this repository I use  $\Gamma_X$  and the unabsorbed counts-to-flux conversion rate ( $4.81 \times 10^{-11} \text{ erg cm}^{-2} \text{ ct}^{-1}$ ) to convert the 0.3 – 10 keV count rate light-curve to flux density at 2.75 keV for subsequent analysis.

## 4.2.2 Optical followup

The UltraViolet and Optical Telescope (UVOT; [Roming et al. 2005](#)) onboard *Swift* observed the region of GRB 160131A from 78 s to  $\sim 6$  d after the BAT trigger. UVOT found a source located at  $\alpha = 5^{\text{h}}12^{\text{m}}40.34^{\text{s}}$ ,  $\delta = -7^{\circ}02'59.1''$ , with an uncertainty of 0.61 arcsec (radius, 90% containment). This position is 7.5 arcsec from the center of the XRT error circle. I analyse the UV band data using HEASOFT (v. 6.22)<sup>5</sup>, the dedicated software package for optical/X-ray astronomical spectral, timing, and imaging data analysis.

In visible band, GRB 160131A was observed for the first time with the 2-m Faulkes Telescope North (FTN), which is operated by Las Cumbres Observatory Global Network (LCOGT; [Brown et al. 2013](#)), on January 31 at 09:37 UT ( $\sim 77$  minutes after the GRB trigger) with Y and Z filters, detecting the afterglow ([Page & Barthelmy 2016](#)) at the position  $\alpha = 5^{\text{h}}12^{\text{m}}41.5^{\text{s}}$ ,  $\delta = -7^{\circ}03'09.81''$  ([Guidorzi et al. 2016](#)). Observations in visible frequencies continued until  $\sim 7$  d after the GRB trigger ([Mazaeva et al. 2016](#)). Bias and flat-field corrections were applied using the specific LCOGT pipeline ([Brown et al. 2013](#)).

I also collected all optical photometry for this event published in GCN circulars (Sect. 1.1)<sup>6</sup>. In my analysis all magnitudes are already corrected for Galactic extinction along the line of sight<sup>7</sup>.

## 4.2.3 Radio followup with VLA

VLA followup observations were carried out from February 1, 2016 to May 27, 2016, i.e. from  $\sim 1$  to  $\sim 117$  d post explosion (Sect. 4.2.2) under Proposal VLA/15A-235 (PI: Berger). Data were taken in five spectral windows at C-band (with baseband central frequency of 6 GHz), X-band (10 GHz), Ku-band (15 GHz), K-band (22.25 GHz), and Ka-band (33.25 GHz), with a nominal bandwidth of  $\sim 0.4$  GHz. 3C48 and J0522+0113 were used as flux/bandpass and phase/amplitude calibrators, respectively. To eventually observe multi-component behaviour in radio data, we split each radio band in eight parts, from 4.6 to 37.4 GHz, resulting in  $\sim 300$  VLA flux densities. The Common Astronomy Software Application (CASA, v. 5.1.1-4, [McMullin et al. 2007](#))<sup>8</sup> was used to calibrate, flag and image the data. Images were formed from the visibility data using the CLEAN algorithm ([Högbom 1974](#)). The image size was set to  $(240 \times 240)$  pixels, the pixel size was determined as 1/5 of the nominal beam width and the images were cleaned using natural weighting. The upper limits on the flux densities were calculated at a  $3\sigma$  confidence level.

<sup>5</sup><https://heasarc.gsfc.nasa.gov/lheasoft/download.html>

<sup>6</sup>[https://gcn.gsfc.nasa.gov/gcn/gcn3\\_archive.html](https://gcn.gsfc.nasa.gov/gcn/gcn3_archive.html)

<sup>7</sup>I assumed these extinctions ([Schlafly & Finkbeiner 2011](#)):  $A_{\lambda} = 0.471$  mag for U-band,  $A_{\lambda} = 0.394$  mag for B-band,  $A_{\lambda} = 0.298$  mag for V-band,  $A_{\lambda} = 0.359$  mag for g-band,  $A_{\lambda} = 0.248$  mag for r-band,  $A_{\lambda} = 0.184$  mag for i-band,  $A_{\lambda} = 0.137$  mag for z-band.

<sup>8</sup><https://casa.nrao.edu/>

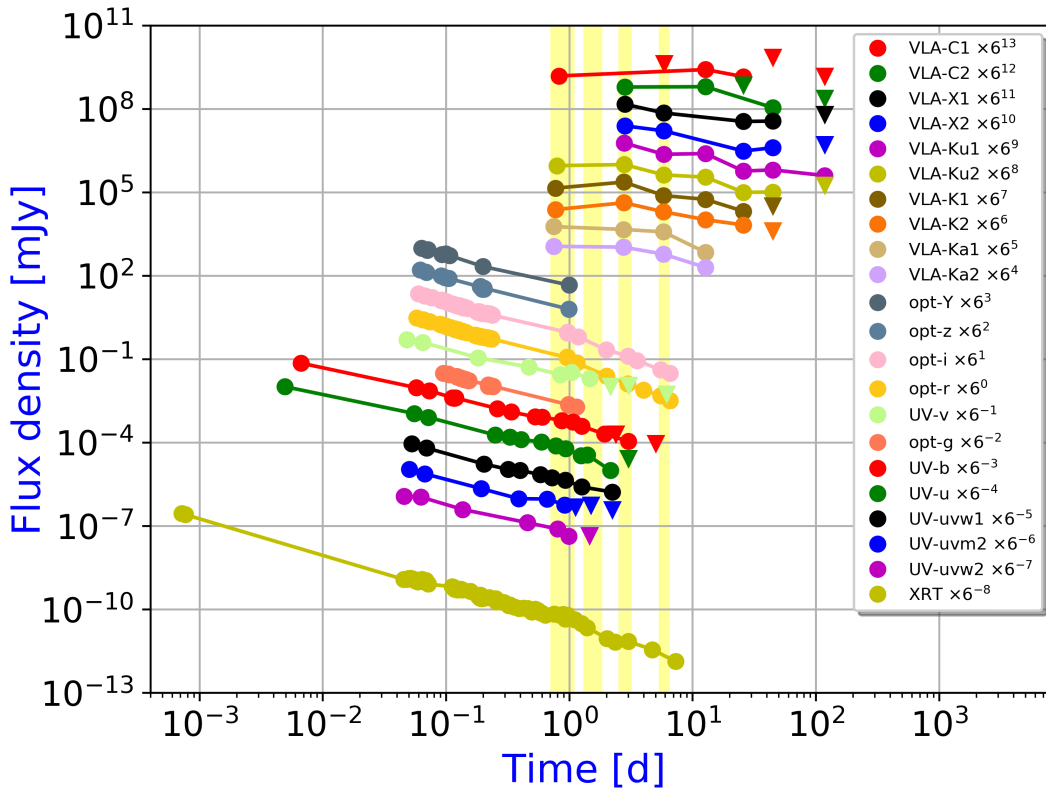


**Figure 4.1:** GRB 160131A light-curves from radio to X-rays. Yellow shaded areas show the time intervals (centred to 0.8 d, 1.7 d, 2.7 d, and 5.8 d) where SEDs have been empirically analysed. Filled circles indicate detections, and inverted triangles indicate  $3\sigma$  upper limits.

### 4.3 Characterisation of the afterglow

First of all, I analyse the broadband observations in the context of synchrotron emission arising from relativistic shocks (Sect. 2.2), following the standard afterglow model of GS02.

I analysed the spectral evolution for the time-intervals displayed in Fig. 4.1, looking for a connection between radio on one side and optical and X-rays on the other side. To this aim, I linearly interpolated data (Fig. 4.2, red points) at four epochs (0.8 d, 1.7 d, 2.7 d, and 5.8 d); the high-energy side of the SEDs (Fig. 4.2) is well fitted by a power law with a mean value of  $\beta = -1.09 \pm 0.06$  (obtained neglecting the data in the range  $10^{15} - 10^{16}$  Hz, heavily affected by dust extinction), corresponding to a photon index  $\Gamma = 1 - \beta = 2.09 \pm 0.06$ , compatible with  $\Gamma_X$  obtained from XRT data (Sect. 4.2.1). This constrains the behaviour of the break frequencies (especially  $\nu_c$  and  $\nu_m$ ), as well as the possible jet break, the time evolution of the blastwave, and the kind of environment (ISM vs. wind).

#### 4.3.1 Synchrotron ( $\nu_m$ ), cooling ( $\nu_c$ ) frequencies and circumburst density profile

The optical and X-ray fluxes decay with temporal index  $\alpha \sim -1.25$  up to  $\sim 0.1$  d, followed by a plateau in the temporal range  $\sim 0.1 - 0.8$  d ( $\alpha \sim -0.7$ ), suggesting energy injection (Fig. 4.3). After the plateau the flux decay steepens to  $\alpha \sim -1.8$  and can be interpreted in terms of a jet break.

According to the standard afterglow model, the spectral index inferred from multi-epoch SEDs from optical to X-rays ( $\beta = -1.09$ ) suggests that  $\nu_m$  and  $\nu_c$  must lie in the same spectral

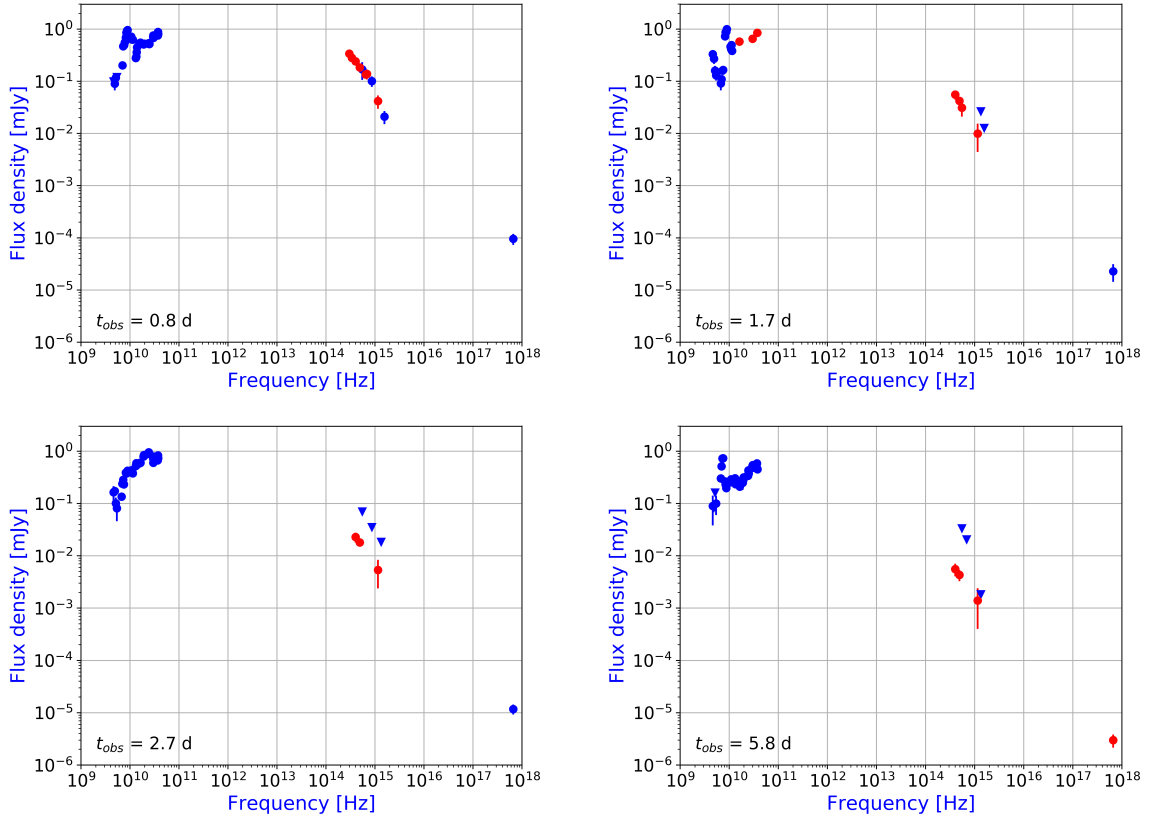


**Figure 4.2:** Broadband SEDs of GRB 160131A at 0.8 d (top left), 1.7 d (top right), 2.7 d (bottom left), and 5.8 d (bottom right). Blue (red) points are measured (linearly interpolated) data. These SEDs display radio peaks (at 0.8 d, 1.7 d, and 5.8 d) and optical absorption (especially at 0.8 d). Filled circles indicate detections, and inverted triangles indicate  $3\sigma$  upper limits.

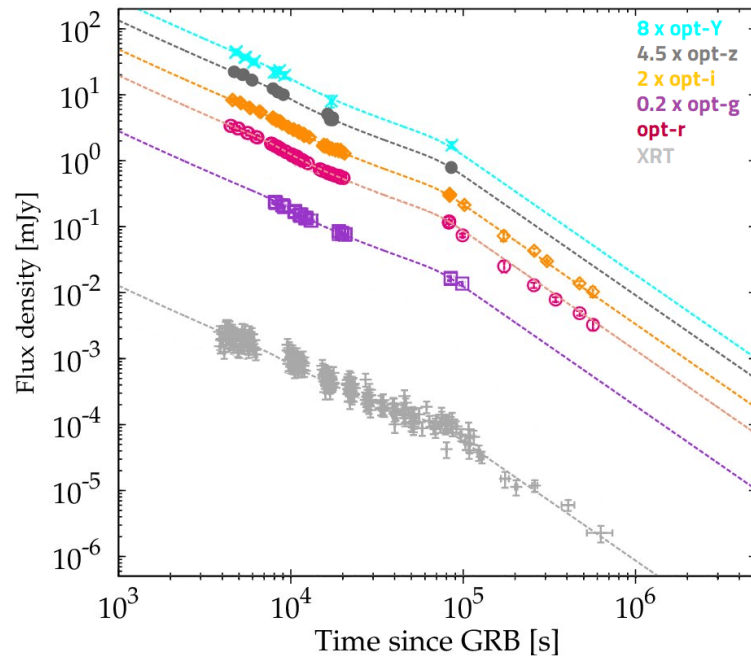


**Figure 4.3:** Light-curves for GRB 160131A of visible and X-ray data modelled with double broken power-law (Eq. 4.3).

regime either below or above the optical/X-ray frequencies  $\nu_{opt,X}$  at the first epoch of observations (0.005 d). In particular, with the help of Fig. 2.1:

**Fast cooling regime.**  $\nu_{opt,X} < \nu_c < \nu_m$  is incompatible with this regime because the optical/X-ray spectra are expected to show only positive values of  $\beta$  ( $1/3 \lesssim \beta \lesssim 2$  for any possible spectrum, Fig. 2.1). Moreover,  $\nu_c < \nu_{opt,X} < \nu_m$  is incompatible with this regime because the optical/X-ray spectra are expected to show  $\beta \sim -0.5$  (Fig. 2.1) instead the observed  $\beta = -1.09$ . Finally,  $\nu_c < \nu_m < \nu_{opt,X}$  case is compatible with fast cooling regime, because, following the indices  $\alpha$  and  $\beta$  calculated for different spectral regimes in GS02, it requires an electron energy index  $p = -2\beta \sim 2.18$  and a decay rate  $\alpha = (2 - 3p)/4 \sim -1.14$  (regardless of the CBM), compatible with  $\alpha \sim -1.25$  of multi-frequency light-curves from optical to X-ray band; this suggests that  $\nu_m$  is just below optical frequencies at 0.005 d.

**Slow cooling regime.**  $\nu_{opt,X} < \nu_m < \nu_c$  is incompatible with this regime because the optical/X-ray spectra are expected to show only positive values of  $\beta$  ( $1/3 \lesssim \beta \lesssim 2$  for any possible spectrum, Fig. 2.1). Moreover,  $\nu_m < \nu_{opt,X} < \nu_c$  is incompatible with this regime, because it requires  $p = 1 - 2\beta \sim 3.18$  and  $\alpha \sim -1.64$  for an ISM-like CBM ( $\alpha \sim -2.14$  for a wind-like CBM), too steep for real light-curves (GS02). Finally,  $\nu_m < \nu_c < \nu_{opt,X}$  case is compatible with slow cooling regime, because it requires  $p = -2\beta \sim 2.18$  and  $\alpha = (2 - 3p)/4 \sim -1.14$  (the same regime of fast cooling case), suggesting that  $\nu_m$  is well below optical frequencies at 0.005 d.

This picture constrains  $\nu_m$  and  $\nu_c$  below  $\nu_{opt} = 3 \times 10^{14}$  Hz at 0.005 d. Moreover, the absence of any break in these light-curves until  $\sim 0.1$  d (after which energy injection and jet break occur) suggests a decreasing behaviour of  $\nu_c$ , thus favouring an ISM-like CBM over wind-like CBM in the standard afterglow model (GS02, Sect. 2.2, and Fig. 2.1).

Knowing an upper limit and the temporal scaling for  $\nu_m$  ( $t^{-3/2}$ , from theory), I constrain  $\nu_m$  as follows: the passage of  $\nu_m$  in Ku-band is expected at  $t_{obs} < 2.1$  d, in K-band at  $t_{obs} < 2.8$  d, in Ka-band at  $t_{obs} < 3.6$  d, in X-band at  $t_{obs} < 4.7$  d, and in C-band at  $t_{obs} < 6.7$  d. The same line of reasoning can be applied to  $\nu_c$ : using  $\nu_c \propto t^{-1/2}$  (for ISM-like CBM, GS02),  $\nu_c$  is expected to cross the radio bands at late-time (Ku-band at  $t_{obs} > 4 \times 10^5$  d), and hence virtually unobservable.

Summing up, (1) the CBM is preferably described by ISM, (2) the transition between fast and slow cooling regime is not constrained by optical/X-ray observations, (3)  $p \sim 2.18$ , and (4) both  $\nu_m$  and  $\nu_c$  lie below  $\nu_{opt} = 3 \times 10^{14}$  Hz already at  $t_{obs} = 0.005$  d. Nevertheless, a more precise identification of the break frequencies requires a self-consistent broadband modelling as in Section 4.5.

### 4.3.2 Radio data analysis

To corroborate the analysis at optical/X-ray frequencies, I analyse both the radio SED at each epoch from 0.8 d to 117 d and the light-curves at each VLA frequency from 4.6 GHz to 37.4 GHz.

This analysis was initially done by fitting data adopting empirical functions for both SEDs and light-curves. I assumed three kind of empirical functions:

- Single power-law:

$$F_x = F_0 \left( \frac{x}{x_0} \right)^\gamma \quad (4.1)$$

where  $F_0$  is the flux density at the reference parameter  $x$ , corresponding to the frequency  $\nu_0$  (I fixed  $\nu_0 = 1$  GHz) for SEDs and the epoch  $t_0$  (I fixed  $t_0 = 1$  d) for the light-curves, and  $\gamma$  is the slope index, corresponding to the spectral index  $\beta$  for SEDs and the decay index  $\alpha$  for the light-curves.

- Broken power-law:

$$F_x = F_b \left[ \frac{1}{2} \left( \frac{x}{x_b} \right)^{-s\gamma_1} + \frac{1}{2} \left( \frac{x}{x_b} \right)^{-s\gamma_2} \right]^{-1/s} \quad (4.2)$$

where  $F_b$  is the flux density at the reference break parameter  $x_b$ , corresponding to the break frequency  $\nu_b$  for SEDs and the break time  $t_b$  for the light-curves,  $s$  is the sharpness factor (I fixed  $s = 5$ ),  $\gamma_1$  and  $\gamma_2$  are the slope indices before and after  $x_b$ , corresponding to the spectral index  $\beta$  for SEDs and the decay index  $\alpha$  for the light-curves.

- Double broken power-law:

$$F_x = F_{b,1} \left[ \frac{1}{2} \left( \frac{x}{x_{b,1}} \right)^{-s\gamma_1} + \frac{1}{2} \left( \frac{x}{x_{b,1}} \right)^{-s\gamma_2} \right]^{-s^{-1}} \times \left[ 1 + \left( \frac{x}{x_{b,2}} \right)^{-w(\gamma_2 - \gamma_3)} \right]^{-w^{-1}} \quad (4.3)$$

where  $F_{b,1} = F(x_{b,1})$ ,  $s$  and  $w$  are the sharpness factors (I fixed  $s = w = 5$ );  $\gamma_1$ ,  $\gamma_2$  and  $\gamma_3$  are the slope indices among the break parameters  $x_{b,1}$  and  $x_{b,2}$ , corresponding to the spectral index  $\beta$  for SEDs and the decay index  $\alpha$  for the light-curves.

### Radio SEDs

One of the most impressive features in radio SEDs is the presence of spectral bumps or peaks at several epochs (Fig. 4.4, red circles). The large uncertainties on flux densities both in C-band and at late-time (from 25 to 117 d) do not allow to analyse the late-time SEDs and low frequency ( $\nu_{obs} \lesssim 8$  GHz) light-curves. The simplest interpretation one would come up with is the presence of RS at radio frequencies in addition to a FS. Since the RS emission is expected to peak at lower frequencies than the FS and the RS spectrum is expected to cut off steeply above the RS cooling frequency (Kobayashi & Sari 2000), the peak at low frequency could be more naturally compatible with RS emission. I will touch on this aspect in Section 4.5. I preliminarily analysed radio SEDs ignoring the peaks with single power-law or broken power-law, to compare the resulting spectral indices with those expected from the synchrotron emission of GRB afterglows (GS02, Table 2.1 and Fig. 2.1).

- **0.8 d radio SED.** This SED shows a peak at  $\sim 9$  GHz (Fig. 4.4, top left). Neglecting this peak, this SED is described by a broken power-law (Eq. 4.2; Table 4.1). The constraints on  $\nu_m$  described in Sect. 4.3.1 suggest that for this epoch  $\nu_m \lesssim 150$  GHz; the values of  $\beta$  suggest that  $\nu_{sa}$  crossed the radio band in slow cooling regime (scenario 1,  $\nu_{sa} < \nu_m < \nu_c$ , GS02). Unfortunately, the presence of the extra-component peaking at  $\sim 9$  GHz prevents me from better constraining  $\nu_{sa}$ .
- **2.7 d radio SED.** This SED is characterised by a peak at  $\sim 25$  GHz (Fig. 4.4, top right). I fitted this SED with a broken power-law (Eq. 4.2; Fig. 4.4, middle right; Table 4.1). The constraints described in Sect. 4.3.1 suggest that for this epoch  $\nu_m \lesssim 22$  GHz. This SED seems to be compatible with slow cooling regime (scenario 1,  $\nu_{sa} < \nu_m < \nu_c$ , GS02):  $\beta_2$  is steeper than  $1/3$  for this regime, suggesting probably the proximity of  $\nu_b \sim \nu_m$  with  $\nu_{sa}$ .
- **12.7 d radio SED.** This SED shows two peaks at  $\sim 6$  and  $\sim 9$  GHz, and after 10 GHz the flux density decreases over the frequency, suggesting the passage of a synchrotron break frequency between 6 and 13 GHz. Ignoring these peaks (Fig. 4.4, middle right) the SED can be described with a broken power-law (Eq. 4.2; Table 4.1). Since at this

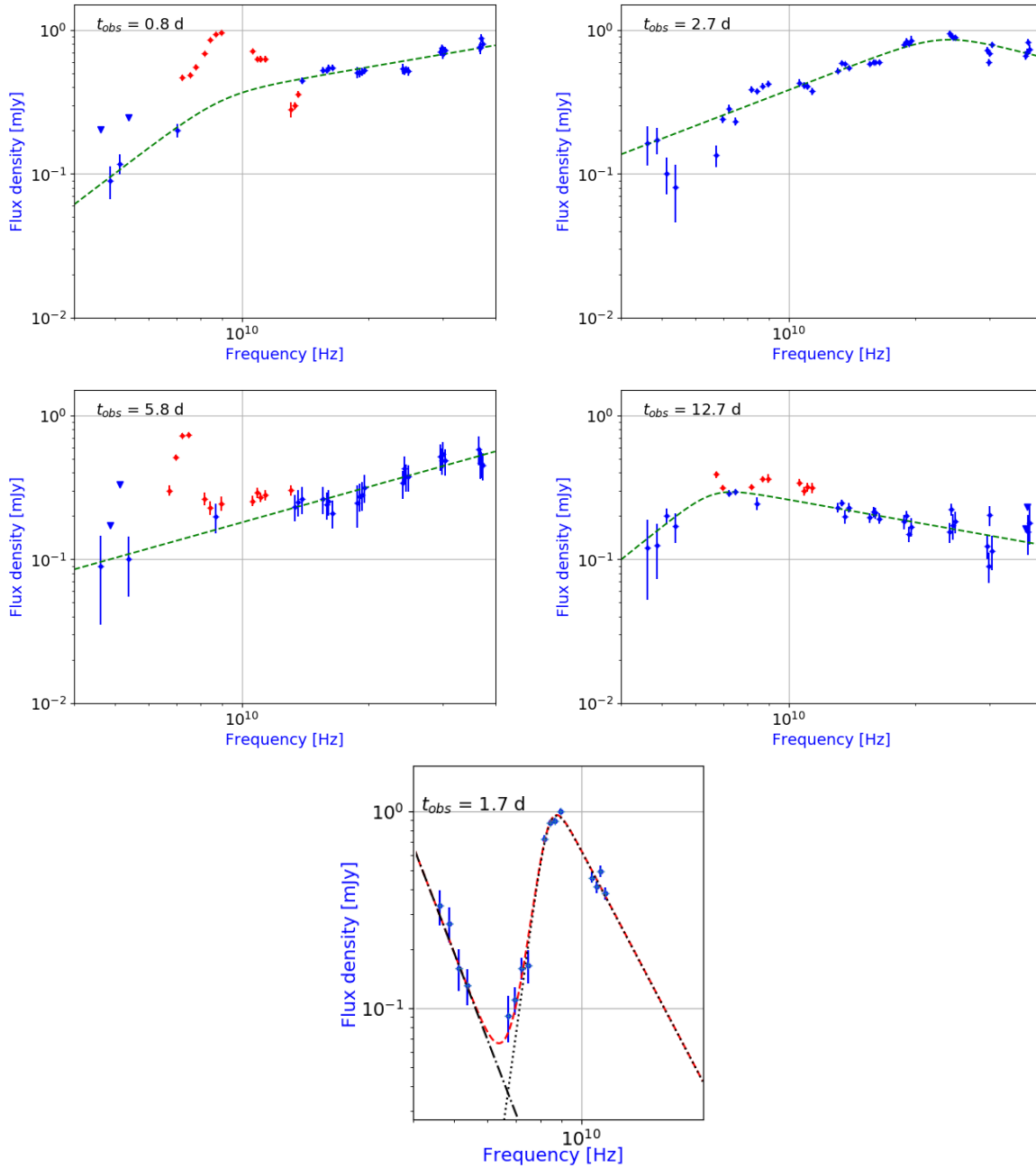


**Figure 4.4:** Radio SEDs of GRB 160131A from 0.8 to 12.7 d. Top left: data together with a broken power-law (Eq. 4.2) at 0.8 d; red points identify the bump and were ignored by the fit. Top right: radio SED at 2.8 d fitted with a broken power-law. Middle left: data together with an empirical single power-law (Eq. 4.1) at 5.8 d; red points identify the bump  $\sim 8$  GHz and were ignored by the fit. Middle right: radio SED at 12.7 d fitted with a broken power-law. Green dashed lines show the resulting modelling. Bottom: radio data at 1.7 d together with a sum (red dashed line) between a single power-law (dotted line) and a broken power-law (dashdot line); these points were ignored in SAGA analysis. Filled circles indicate detections, and inverted triangles indicate  $3\sigma$  upper limits; moreover



**Table 4.1:** Parameters for empirical fits to radio SEDs of GRB 160131A from 0.8 to 12.7 days after the GRB trigger. “pl” indicates a single power-law model (Eq. 4.1) and “bpl” indicates a broken power-law model (Eq. 4.2).  $\nu_b$  indicates the break frequency corresponding to the flux density  $F_b$ ,  $\beta_{1,bpl}$  and  $\beta_{2,bpl}$  indicate the spectral indices for broken power-law, and  $\beta_{pl}$  indicates the spectral index for a single power-law.  $\chi_r^2$  indicates the reduced chi-squared of the best-fit model.

Parameter	0.8 d	1.7 d	2.8 d	5.8 d	12.7 d
Model	bpl	pl + bpl	bpl	pl	bpl
$\nu_b^a$	$8.96 \pm 0.04$	$8.4 \pm 0.4$	$23.1 \pm 0.2$	-	$6.40 \pm 0.03$
$F_b^b$	$0.32 \pm 0.02$	$0.9 \pm 0.2$	$0.85 \pm 0.10$	-	$0.28 \pm 0.01$
$\beta_{pl}$	-	$-5.6 \pm 0.5$	-	$0.82 \pm 0.07$	-
$\beta_{1,bpl}$	$2.2 \pm 0.4$	$15.6 \pm 1.8$	$1.12 \pm 0.03$	-	$2.35 \pm 0.82$
$\beta_{2,bpl}$	$0.50 \pm 0.05$	$-4.1 \pm 0.4$	$-0.75 \pm 0.11$	-	$-0.52 \pm 0.07$
$\chi_r^2$	1.04	0.97	1.13	1.02	1.07

<sup>a</sup> In units of GHz.

<sup>b</sup> In units of mJy.

epoch it is  $\nu_m \lesssim 2.3$  GHz (Sect. 4.3.1), this behaviour is compatible with slow cooling regime (scenario 2,  $\nu_m < \nu_{sa} < \nu_c$ , GS02), where  $\nu_{sa} = \nu_b$  ranges between  $\beta_1 = 2.5$  and  $\beta_2 = (1 - p)/2$  (suggesting  $p = 2.04 \pm 0.14$ ).

For completeness, I also describe the radio SEDs at 5.8 d (Fig. 4.4, middle left) and 1.7 d (Fig. 4.4, bottom), whose behaviour is not ascribable to simple forward shock emission.

- **5.8 d radio SED.** This SED shows a strong peak at  $\sim 7$  GHz, and a faint peak at  $\sim 10$  GHz (Fig. 4.4, middle left). Ignoring these peaks, the radio SED is described by a power-law (Eq. 4.1; Fig. 4.4, bottom left; Table 4.1). For this epoch  $\nu_m \lesssim 7.3$  GHz (Sect. 4.3.1), suggesting slow cooling regime; nevertheless, the value of  $\beta$  is incompatible with regimes described in the standard afterglow model (GS02). I discuss this behaviour in Sect. 4.5.
- **1.7 d radio SED.** I describe this SED (Fig. 4.4, bottom) by means of a combination of single and broken power-laws. The single power-law component at low-frequencies ( $\lesssim 5$  GHz) is characterised by a spectral index  $\beta = -5.6 \pm 0.5$ , whereas the peak is well constrained by a broken power-law, with parameters for empirical fit showed in Table 4.1. As opposed to the other SEDs, the absence of data at high frequencies in this SED does not enable to obtain further information about the afterglow. I describe in Sect. 4.5.4 the possible interpretation ascribable to RS emission for this radio SED.

Summing up, (1) the radio SEDs suggest that the slow cooling regime occurs at  $t \lesssim 0.8$  d, and (2) the 12.7 d radio SED shows that  $\nu_{sa} \sim 6.4$  GHz at this epoch. The 5.8 d and 1.7 d radio SEDs show behaviours incompatible with standard GRB afterglow model; I delve further into them in Sect. 4.5.

### Radio light-curves

I analysed the radio light-curves ignoring the data corresponding to the peaks described in the previous sections, in an attempt to explain the continuum in terms of FS, under the assumptions that the peaks are additional components.



- **Light-curves in the range 4 – 8 GHz.** These light-curves are characterised by high variability, probably caused by strong ISS (Sect. 3.7), and consequently the rise and decline rates are not well constrained.
- **Light-curves in the range 8 – 14 GHz.** These light-curves exhibit decreasing power-law, with a temporal index  $\alpha$  that decreases from  $\sim -0.6$  to  $\sim -0.8$ . In particular, the light-curve at 8.93 GHz can be fit with a simple power-law (Eq. 4.1) with  $\alpha = -0.61 \pm 0.02$  (Fig. 4.5, top left). The same analysis for the light-curve at 11.4 GHz results in  $\alpha = -0.69 \pm 0.05$  (Fig. 4.5, top right). In agreement with what inferred from the high-energy data analysis (Sect. 4.3.1), this regime suggests that  $\nu_c$  crosses these frequencies at  $t \gtrsim 45$  d and the passage of  $\nu_m$  occurs at  $t \lesssim 3$  d (Sect. 2.2.1, Fig. 2.2, Sari et al. 1998).
- **Light-curves in the range 14 – 24.6 GHz.** The identification of  $\nu_b \sim 23$  GHz with  $\nu_m$  observed in the SED at  $t_{obs} = 2.8$  d (Fig. 4.4 and Table 4.1) indicates that the light-curve at  $\nu_{obs} \sim \nu_b$  would peak at  $t_{obs}$ . This behaviour was observed in the light-curve at 24.6 GHz (Fig. 4.5, middle left); broken power-law (Eq. 4.2) shows a peak at  $3.0 \pm 0.5$  d (with flux density  $0.87 \pm 0.05$  mJy) with temporal indices  $\alpha_1 = 0.48 \pm 0.05$  and  $\alpha_2 = -1.16 \pm 0.30$  (compatible with  $\alpha_2 = -1.25$  of optical/X-ray light-curves), perfectly compatible with the passage of  $\nu_m$  in the light-curves of standard afterglow model (Sect. 2.2.1, Fig. 2.2, Sari et al. 1998). The light-curves in the range 14 – 24.6 GHz are already characterised by a bump at the same epoch (2.5 – 3.5 d), but the sparseness of the radio data around this epoch results in a strong degeneracy about the exact position of this peak (e.g., Fig. 4.5, middle left). The decreasing temporal indices evolve from  $\sim -0.8$  at 14 GHz to  $\sim -1.2$  at 24 GHz, suggesting that  $\nu_c$  crosses these observing frequencies above  $\sim 120$  d, and the passage of  $\nu_m$  at these observing frequencies is very close to 3 d (Sect. 2.2.1, Fig. 2.2, Sari et al. 1998).
- **Light-curves above 24.6 GHz.** These light-curves show a steep decay of the flux densities at  $t_b$  ranging between  $\sim 3$  and  $\sim 5$  d, compatible with jet break; in this regime,  $-0.07 \lesssim \alpha_1 \lesssim 0.1$  and  $-2 \lesssim \alpha_2 \lesssim -1.6$ . For example, the light-curve at 30.4 GHz (Fig. 4.5, bottom left) shows a broken power-law (Eq. 4.2) with a peak at  $4.5 \pm 0.2$  d (and flux density  $0.71 \pm 0.12$  mJy) between  $\alpha_1 = 0.07 \pm 0.05$  and  $\alpha_2 = -1.95 \pm 0.35$ ; another light-curve at 37.1 GHz (Fig. 4.5, bottom) shows a broken power-law (Eq. 4.2) with a peak at  $4.25 \pm 0.2$  d (and flux density  $0.7 \pm 0.1$  mJy) between  $\alpha_1 = -0.05 \pm 0.02$  and  $\alpha_2 = -1.6 \pm 0.4$ .

Summing up, these radio light-curves suggest that (1)  $\nu_c$  and  $\nu_m$  cross the radio band at  $t \gtrsim 120$  d  $t \sim 3$  d, respectively, and (2) a steep decay of the flux densities, compatible with jet break, occurs at  $t_b$  ranging between  $\sim 3$  and  $\sim 5$  d.

### 4.3.3 Jet break

In the standard afterglow model, a jet break arises at the time  $t_j$  when the bulk Lorentz factor  $\Gamma$  decreases below the inverse opening angle of the jet  $\theta_j^{-1}$  and its edges become visible by an observer (Section 2.3).

Once  $\nu_m$  has crossed the observing frequency, the flux density decays steeply following a jet break. In this regime, the steepening in the radio light-curves is expected to follow that of the steepening in the X-ray and optical light-curves, depending on the time it takes for  $\nu_m$  to pass through the radio frequencies (Laskar et al. 2015). This behaviour is compatible with the passage of  $\nu_m$  at  $\sim 23$  GHz in the SED at 2.8 d (Sect. 4.3.2); the radio light-curves above this frequency, and after  $\sim 3 - 5$  d, decline increasingly steeply ( $\alpha \sim -1.8$ , compatible with

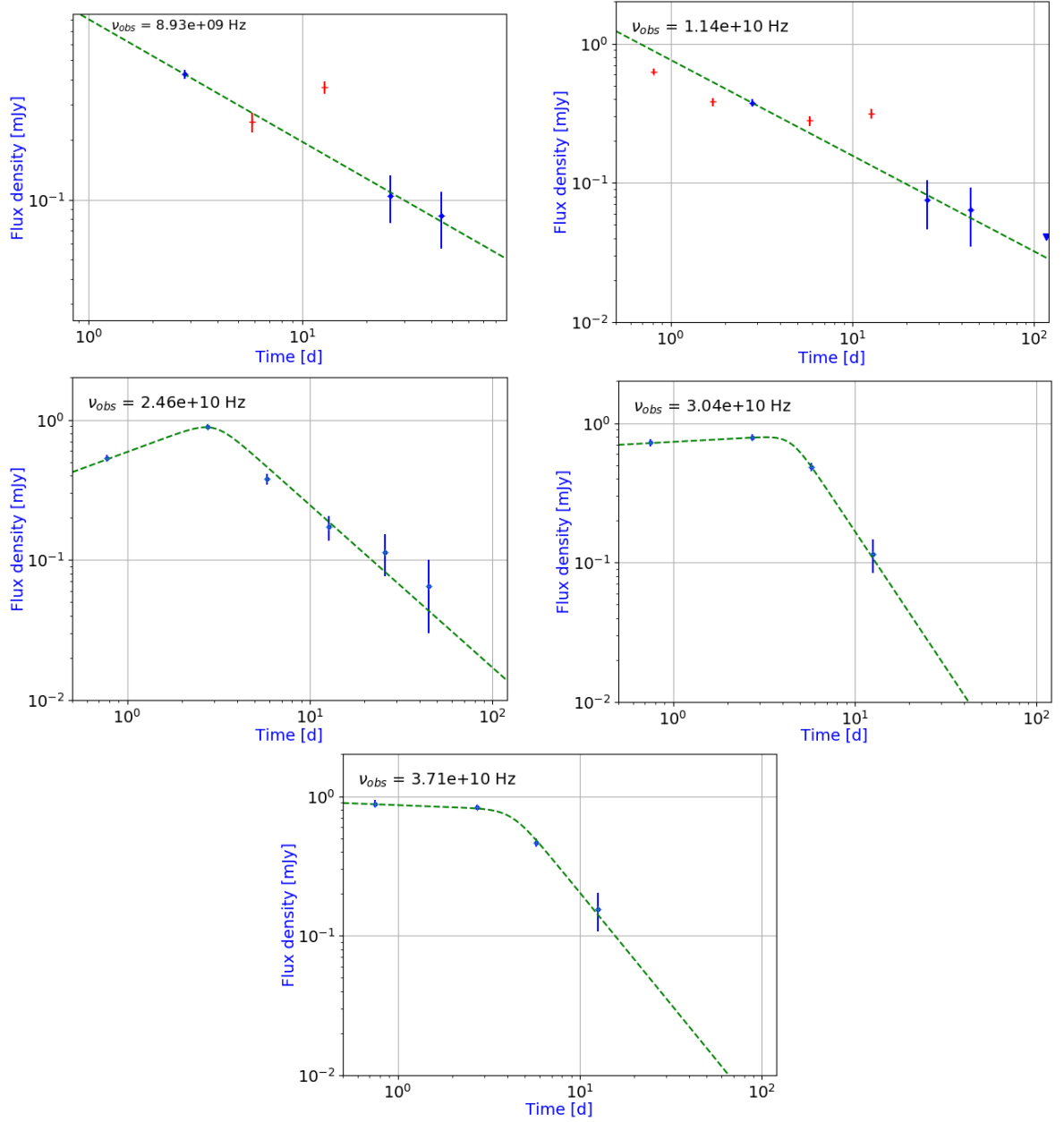


**Figure 4.5:** Radio light-curves of GRB 160131A in the range 9 – 37 GHz. 8.93 GHz (top left) and 11.4 GHz (top right) fitted with single power-law (Eq. 4.1); the other light-curves (24.6 GHz, middle left; 30.4 GHz, middle right; 37.1 GHz, bottom) are fitted with broken power-law (Eq. 4.2). Blue filled circles indicate detections, and inverted triangles indicate  $3\sigma$  upper limits; red circles indicate the ignored points corresponding to the peaks observed in radio SEDs (Fig. 4.4), and green lines show the resulting model.

optical/X-ray light-curves), resulting in an achromatic break for the jetted emission (Sects. 4.3.2 and 2.3). At  $t = t_j \sim 1$  d, as inferred from optical/X-ray light-curves,  $\nu_m$  lies close to  $\sim 10^{11}$  GHz, that is well below optical and X-rays: this is consistent with the steep decline observed around the same epoch in these bands.

In conclusion, an achromatic break in the X-ray and optical light-curves occurs at  $t_j \sim 1$  d; the addition of radio light-curves with achromatic break signatures suggests  $\nu_m \sim 23$  GHz at  $\sim 3$  d after the GRB explosion.

### 4.3.4 Self-absorption frequency ( $\nu_{sa}$ )

Typically, at  $\nu < 10$  GHz information on  $\nu_{sa}$  can be inferred. In this analysis, radio SEDs between 5 to 10 GHz (in the temporal range 0.8–12.7 d) suggest that  $\nu_{sa} \sim 7$  GHz until  $\sim 13$  d, when  $\nu_{sa}$  begins to decrease with time. This behaviour (Sect. 4.3.2) favours ISM over wind. Nevertheless, the uncertainties on flux density in the SEDs at  $\nu < 5$  GHz inevitably affects the determination of  $\nu_{sa}$ .

## 4.4 Broadband modelling

Once I estimated the main spectral features (breaking frequencies and jet break time) of the GRB afterglow, I model it using the smoothly connected power-law synchrotron spectra for the FS in ISM as described by GS02. Synchrotron radiation from relativistic shocks expanding adiabatically results in spectra where the peaks move to lower frequencies and fade with time (Sari et al. 1998). I compute the break frequencies and normalisations using the micro-physics parameters: the electron energy distribution index ( $p$ ), the kinetic energy of the explosion ( $E_{k,iso}$ ), the CBM density ( $n_0$ ), the fractions of the dissipated energy that go to relativistic electrons ( $\epsilon_e$ ) and magnetic fields ( $\epsilon_B$ ). I also use the optical extinction in the host galaxy ( $A_V$ ) and the UV absorption by neutral hydrogen (Sect. 3.6), the IC regime by computing the Compton  $y$ -parameter from the FS parameters (Sect. 3.8), the energy injection (with  $q$  and  $m$  parameters, Sect. 3.5), the jet break  $t_j$  in uniform jet regime (Sect. 2.3), the effect of non-relativistic ejecta ( $t_{NR}$ , Eq. 2.13), and the ISS effect (Sect. 3.7).

sAGA (Chapter 3) is built upon the formalism described above. As described in Sect. 3.2, I adopted uniform and Jeffreys priors for the parameters, adopting the following intervals:  $1.5 \leq p \leq 3.5$  (GS02),  $10^{-3} \leq n_0 \leq 10^2$ ,  $10^{-2} \leq E_{k,iso,52} \leq 10^3$ ,  $0 \leq A_V \leq 10$ , and  $0 \leq m \leq 3$ ; moreover, I set up  $10^{-4} \leq \epsilon_e \leq 1/3$  and  $10^{-4} \leq \epsilon_B \leq 1/3$  (Santana et al. 2014), with the upper limits (1/3) set by the equipartition of the post-shock energy density of the emitting material between relativistic electrons and magnetic fields. I adopted as starting points:  $p = 2.2$ ,  $\epsilon_B = 0.01$ ,  $n_0 = 1 \text{ cm}^{-3}$ ,  $E_{k,iso,52} = 50$ ,  $A_V = 0.1$ ,  $t_j = 1$  d, and  $m = 0.2$ . Moreover, according to a method to constrain  $\epsilon_e$  through the identification of the radio peaks (observed in the radio light-curves) connected with the passage of  $\nu_m$  (Beniamini & van der Horst 2017), I used the peak (with a flux density  $F \sim 0.9$  mJy) observed in the 24.6 GHz light-curve at  $t_{obs} \sim 3$  d (Sect. 4.3.2) to estimate  $\epsilon_e \sim 0.1$  as a starting point.

### 4.4.1 Preliminary results for GRB 160131A

The radio peaks and bumps described above are responsible for the failure of sAGA to model self-consistently the entire multi-frequency data set. The complexity of the problem imposes an iterative analysis (visible, optical, optical/X-ray, optical/X-ray/radio) in order to explore the physical characteristics of the afterglow of GRB 160131A. I considered in this analysis a jetted

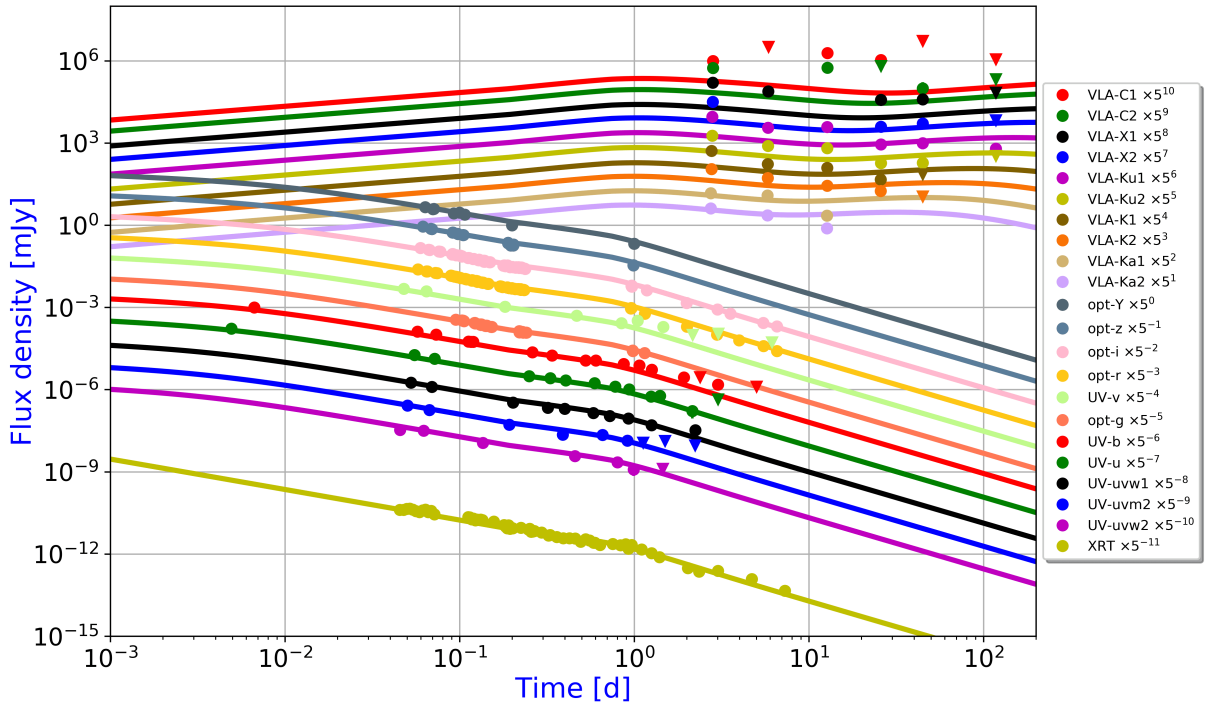


**Figure 4.6:** Broadband modelling (from optical to X-ray frequencies) of GRB 160131A for a FS model with a ISM-like CBM (GS02); I considered in this analysis a jetted emission with optical absorption and energy injection. Filled circles indicate detections, and triangles indicate upper limits. For completeness I include the radio data, although they were not modelled.

(edge-regime) FS emission with optical absorption and energy injection, in ISM-like CBM. The modelling ignored the data at  $t < 4 \times 10^{-3}$  d, when the prompt emission was not over yet.

### From optical to X-ray frequencies

Preliminary results of the iterative process of modelling from  $3 \times 10^{14}$  to  $6.6 \times 10^{17}$  Hz are reported in Table 4.2 (in the first three columns) and the broadband light-curve (for optical/X-ray bands) is displayed in Fig. 4.6.

Preliminary results (Table 4.2) show that  $p$  changes as long as additional data taken at different frequencies are included. Moreover, the spectrum is in fast cooling until  $\sim 0.05$  d and the non-relativistic regime occurs at  $\sim 200$  d; the Compton  $y$ -parameter is 0.02, indicating that cooling due to IC scattering (Sect. 3.8) is negligible.

As can be seen from Fig. 4.7, sAGA also estimates the behaviour of the synchrotron break frequency over time. With reference to the lines of reasoning argued in Sect. 4.3.1 ( $\beta = -1.09$  inferred from optical/X-ray SEDs suggests that  $\nu_m$  and  $\nu_c$  must lie in the same spectral regime below the optical/X-ray frequencies  $\nu_{opt,X}$  at the first epoch of observations  $t = 0.005$  d), the temporal evolution of  $\nu_c$  and  $\nu_m$  are in accordance with sAGA results. On the other hand, with reference to what was argued in Sect. 4.3.4 (radio SEDs suggest that  $\nu_{sa} \sim 7$  GHz until  $\sim 13$  d), the temporal evolution of  $\nu_{sa}$  showed in Fig. 4.7 is incompatible with sAGA results ( $\nu_{sa} \sim 80$  GHz at  $t \sim 13$  d), caused by the lack of radio data in this analysis.

Fig. 4.6 shows also the radio data (not include in this analysis), that do not match the high-energy sample. I show and discuss these challenging data in the next section.

**Table 4.2:** Summary statistics from MCMC preliminary analysis obtained with sAGa applied to the radio and X-ray data of GRB 160131A for a model based on a jetted (edge-regime) FS emission with optical absorption and energy injection, in ISM-like CBM.  $t_{trans,51}$  and  $t_{trans,12}$  indicate the transition time between FS spectral regimes (5  $\rightarrow$  1 and 1  $\rightarrow$  2, respectively) as described in GS02;  $\chi_r^2$  indicates the reduced chi-squared of the best-fit model.

Parameter	Visible	Optical	Optical/X-ray	Radio/optical/X-ray
$p$	$2.27 \pm 0.08$	$2.26^{+0.07}_{-0.06}$	$2.08^{+0.04}_{-0.03}$	$2.011^{+0.003}_{-0.002}$
$\epsilon_e$	$(6.5^{+1.9}_{-1.7}) \times 10^{-3}$	$(1.1^{+0.5}_{-0.3}) \times 10^{-2}$	$(2.3^{+1.8}_{-1.1}) \times 10^{-2}$	$(2.8^{+0.4}_{-0.6}) \times 10^{-1}$
$\epsilon_B$	$(1.0^{+1.2}_{-1.0}) \times 10^{-1}$	$(9.9^{+12.8}_{-7.7}) \times 10^{-2}$	$(1.9^{+1.0}_{-1.4}) \times 10^{-1}$	$(1.3^{+0.3}_{-0.7}) \times 10^{-3}$
$n_0^a$	$5.0^{+25.3}_{-4.2}$	$(1.3^{+3.7}_{-1.1}) \times 10$	$(4.1^{+4.1}_{-3.2}) \times 10$	$(1.2^{+0.3}_{-0.2}) \times 10$
$E_{52}^b$	$(8.6^{+3.1}_{-2.6}) \times 10$	$(4.1^{+1.9}_{-1.3}) \times 10$	$(4.0^{+3.2}_{-1.8}) \times 10$	$(1.1 \pm 0.2) \times 10$
$A_v^c$	$(6.1^{+7.4}_{-4.0}) \times 10^{-2}$	$(4.1^{+3.4}_{-2.3}) \times 10^{-2}$	$(7.1^{+5.0}_{-3.8}) \times 10^{-2}$	$1.2^{+0.5}_{-0.2} \times 10^{-2}$
$t_j^d$	$0.94^{+0.24}_{-0.11}$	$0.93^{+0.19}_{-0.10}$	$0.88^{+0.16}_{-0.06}$	$1.15^{+0.16}_{-0.13}$
$\theta_j^e$	$5.0^{+1.2}_{-1.1}$	$6.1 \pm 1.2$	$6.7^{+1.3}_{-1.2}$	$7.7^{+0.7}_{-0.5}$
$t_{b,0}^d$	$(1.98^{+0.02}_{-0.04}) \times 10^{-1}$	$(1.98^{+0.01}_{-0.03}) \times 10^{-1}$	$0.17 \pm 0.02$	$0.18^{+0.01}_{-0.03}$
$m$	$0.30 \pm 0.01$	$0.27 \pm 0.01$	$0.27 \pm 0.02$	$(1.05^{+0.09}_{-0.04}) \times 10^{-2}$
$\nu_m^f$	$3.3 \times 10^{11}$	$4.5 \times 10^{11}$	$5.1 \times 10^{11}$	$5.7 \times 10^{10}$
$\nu_c^f$	$4.0 \times 10^{12}$	$2.3 \times 10^{12}$	$1.3 \times 10^{11}$	$3.6 \times 10^{15}$
$\nu_{sa}^f$	$3.4 \times 10^{11}$	$4.2 \times 10^{11}$	$4.1 \times 10^{11}$	$6.3 \times 10^{10}$
$\nu_{ac}^f$	$2.3 \times 10^{12}$	$1.5 \times 10^{12}$	$2.4 \times 10^{12}$	$5.0 \times 10^{12}$
$t_{trans,51}^d$	$1.5 \times 10^{-2}$	$4.8 \times 10^{-2}$	0.3	$3.6 \times 10^{-6}$
$t_{trans,12}^d$	0.6	0.98	0.4	0.5
$\chi_r^2$	1.3	1.15	0.8	2.0

<sup>a</sup> In units of  $\text{cm}^{-3}$ .

<sup>b</sup> In units of  $10^{52}$  erg.

<sup>c</sup> In units of mag.

<sup>d</sup> In units of days.

<sup>e</sup> In units of deg.

<sup>f</sup> In units of Hz at  $t_{obs} = 1$  d.

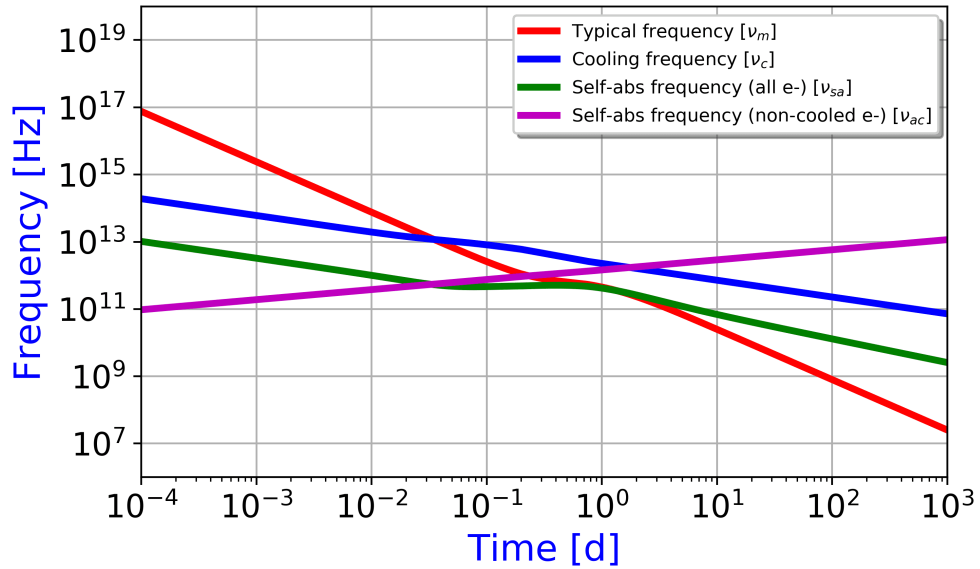


**Figure 4.7:** Temporal evolution of the synchrotron break frequencies for afterglow emission of GRB 160131A, based on analysis of optical data (Table 4.2, second column). I considered in this analysis a jetted (edge-regime) FS emission with optical absorption and energy injection, in ISM-like CBM. As seen in Sect. 2.2, the self-absorption frequency produced by noncooled electrons  $\nu_{ac}$  makes sense only in fast-cooling regime ( $\lesssim 0.05$  d).

### From radio to X-ray frequencies

I move on and include the radio data set from 1.28 to 92.5 GHz, yet ignoring the data points affected by the bumps. I also considered the ISS effect (Fig. 4.8), typical of radio frequencies, by summing in quadrature the real flux density uncertainty with the ISS component, following the procedure described in Sect. 3.7.

To verify the stability and robustness of the best-fit solution, I repeated the analysis assuming three different starting values for  $p$  (2.1, 2.4, 2.9), obtaining  $p \sim 2$  (i.e., lower than that estimated from the high-energy approach).

Unsurprisingly, the best-fit model has a very high  $\chi_r^2$  ( $\sim 2$ ). This is indicative of the problems faced by the standard GRB afterglow model as long as a rich data set at low frequencies is available (Fig. 4.9). Preliminary results (Table 4.2) show that the jet break time of 1.15 d translates into a jet opening angle  $\theta_j \sim 8$  degrees, the spectrum is in fast cooling until  $\sim 4 \times 10^{-6}$  d, and the non-relativistic regime occurs at  $\sim 200$  d. Moreover, Fig. 4.9 shows that the model works well at X-ray and radio (except for  $\nu < 8$  GHz), partially well at UV frequencies, and poorly in the visible band. This behaviour suggests other radiation mechanisms responsible for the afterglow emission for this GRB; I will focus on this aspect in Sect. 4.5. As in the case of the analysis of optical/X-ray data (Sect. 4.4.1), the Compton  $y$ -parameter is 0.02, indicating that cooling due to IC scattering (Sect. 3.8) is negligible. As can be seen from Fig. 4.10, the temporal evolution of the cooling frequency  $\nu_c$  suggests that it lies above the X-rays (as opposed to  $\nu_{sa}$  and  $\nu_m$ ), in contrast to the behaviour expected from considerations based on the optical/X-ray spectra (Sects. 4.3.1 and 4.3.4).

## 4.5 Discussion

The addition of radio data set in the afterglow modelling considerably complicates the broadband analysis, challenging the standard GRB afterglow model.

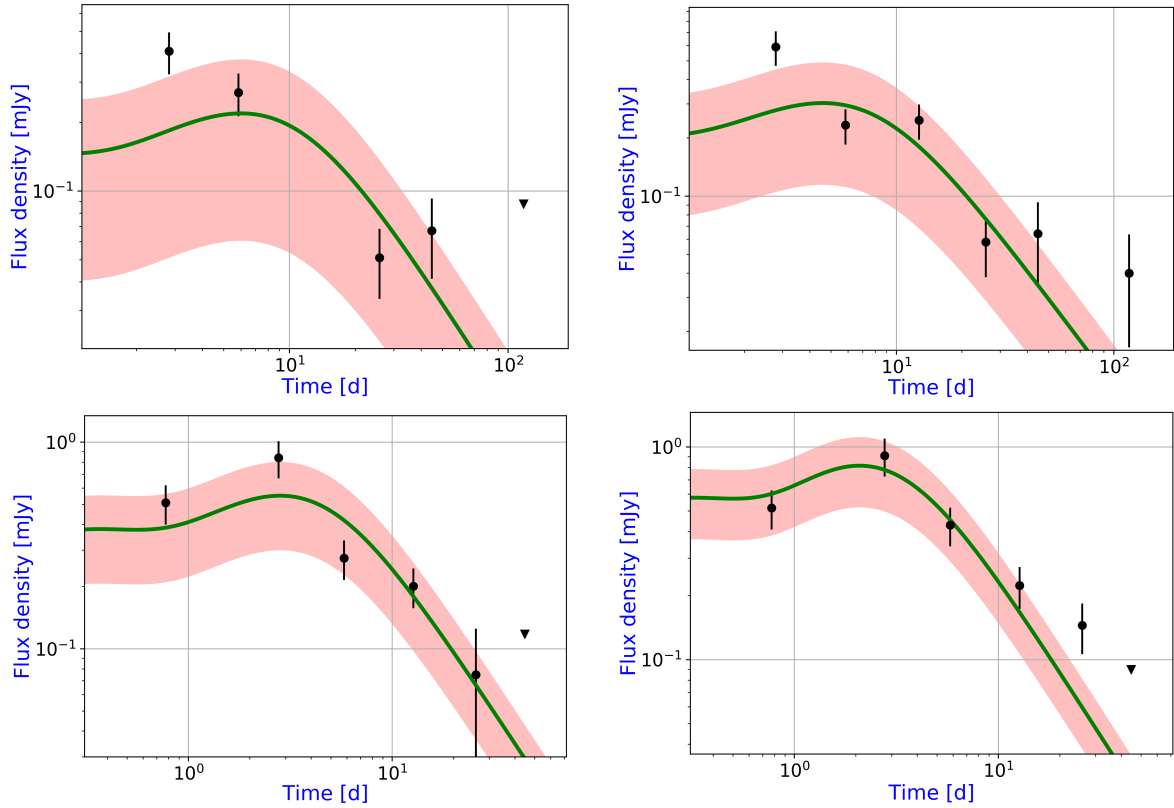


**Figure 4.8:** Radio light-curves of GRB 160131A at 11.4 GHz (top left), 13 GHz (top right), 18.8 GHz (bottom left), and 24.6 GHz (bottom right), obtained through a broadband modelling (from radio to X-ray frequencies) for a FS model with a ISM-like CBM (GS02); I considered in this analysis a jetted (edge-regime) emission with ISS effect, optical absorption and energy injection. Filled circles indicate detections, and inverted triangles indicate  $3\sigma$  upper limits; the red shaded regions represent the expected variability due to ISS effect, obtained through the prescription described in Sect. 3.7.



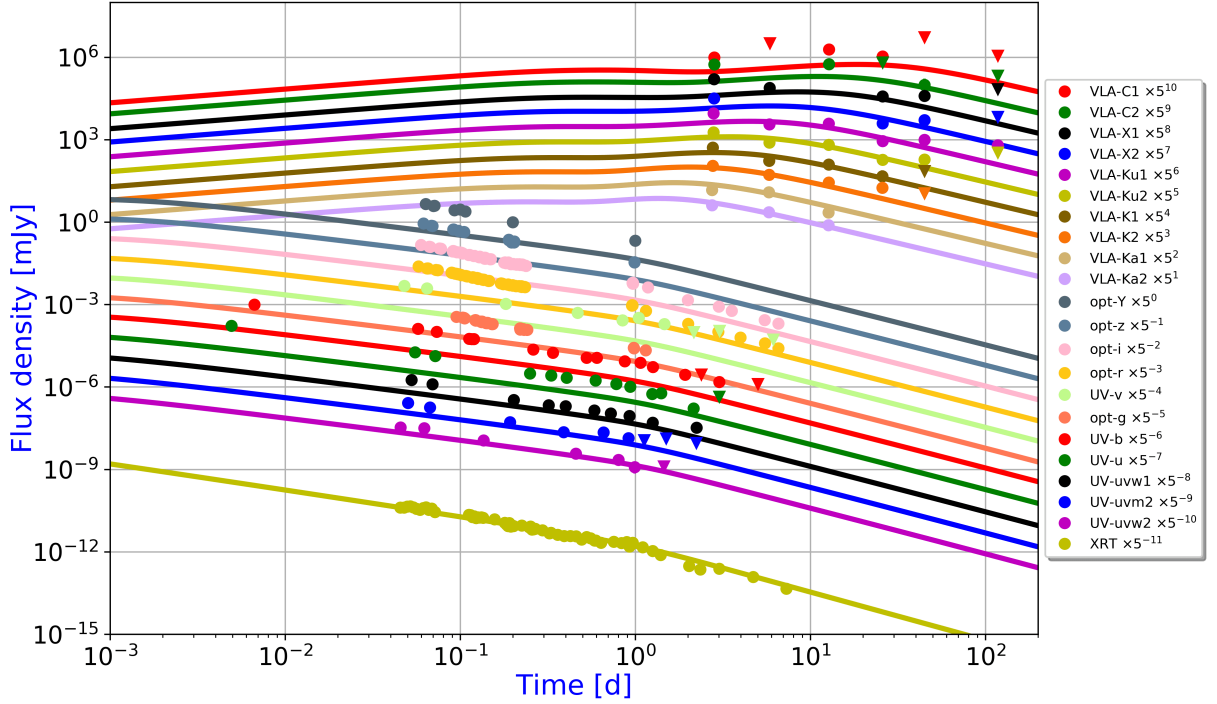


**Figure 4.9:** Broadband modelling of GRB 160131A (from radio to X-ray frequencies) for a FS model with an ISM-like CBM (GS02); I considered in this analysis a jetted (edge-regime) emission with optical absorption and energy injection. Filled circles indicate detections, and triangles indicate upper limits. For completeness I include the radio data, not included in this modelling.

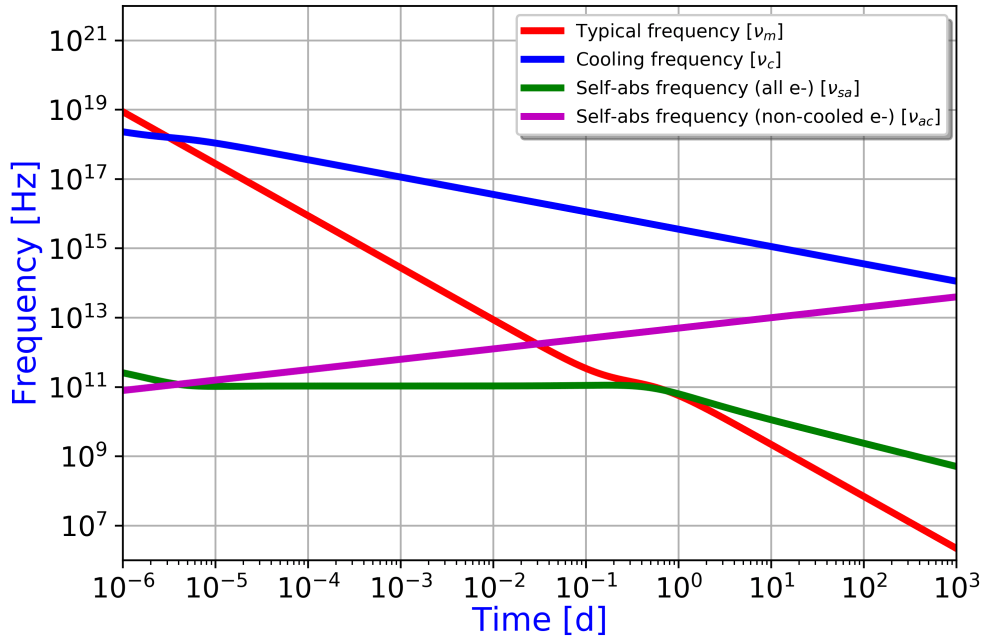


**Figure 4.10:** Temporal evolution of the synchrotron break frequencies for afterglow emission of GRB 160131A, based on analysis of broadband data (from radio to X-ray frequencies; Table 4.2, third column). I considered in this analysis a jetted (edge-regime) FS emission with optical absorption and energy injection, in ISM-like CBM. As seen in Sect. 2.2, the self-absorption frequency produced by noncooled electrons  $\nu_{ac}$  makes sense only in fast-cooling regime ( $\lesssim 4 \times 10^{-6}$  d).

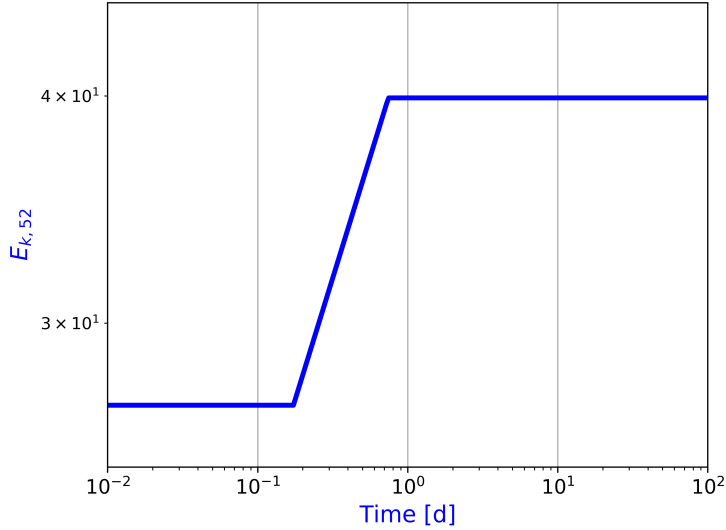


**Figure 4.11:** Isotropic equivalent kinetic energy  $E_{k,52}$  (in units of  $10^{52}$  erg) as a function of time, as determined from fitting the optical/X-ray data set (Tab 4.2).

I point out three problematic features in radio frequencies:

- SEDs up to  $\sim 25$  d share the same rather constant peak at  $\sim 8$  GHz, whose width  $\Delta\nu/\nu$  evolves from  $\sim 0.5$  at 1.7 d to  $\sim 0.1$  at  $\sim 25$  d, with a temporary disappearance at  $\sim 2.7$  d (Fig. 4.4). For example, in the radio SED of GRB 181201A (the first case of a SED instantaneously and clearly decomposed into RS and FS components), the peak at lower frequency bands (probably ascribed to RS emission) is much broader, having  $\Delta\nu/\nu \sim 3$  (Laskar et al. 2019);
- the SED at 5.8 d evolves with  $\beta \sim 0.8$  (Table 4.1 and Fig. 4.4), a value which is incompatible with slow cooling regimes (Sect. 4.3.1; Section 2.2.1 and Fig. 2.1).
- flux densities at low frequencies ( $\lesssim 7$  GHz) seem to be constant over time.

### 4.5.1 Energy injection

A flattening in the optical/X-rays light-curves of GRB 160131A naturally calls for energy injection (Sect. 3.5). The inferred value  $p \sim 2.2$  (Sect. 4.3) suggests  $\nu_c < \nu_X$ , where the flux density is  $F_{\nu > \nu_c} \propto E_{K,iso}^{(2+p)/4} t^{(2-3p)/4}$  (GS02); in this regime I obtain  $F_{\nu > \nu_c} \propto E_{K,iso}^{1.1} t^{-1.3}$ . The temporal evolution of the injected energy is parameterised as  $E \propto t^m$ , and hence  $F_{\nu > \nu_c} \propto t^{1.1m-1.3}$ . Fitting the X-ray light-curve with a simple power law from  $\sim 0.2$  d to  $\sim 0.8$  d, roughly corresponding to the flattening, I obtain  $\alpha_{X,ei} = -1.0 \pm 0.1$ , implying  $m = 0.27 \pm 0.10$ , or, equivalently,  $q = 1 - m = 0.73 \pm 0.10$ . As seen in Sect. 3.5, the case  $q \geq 0$  turns into light-curves characterised by a plateau (and not generally by a re-brightening) and could be explained in terms of energy injection from the spindown of a newborn magnetar. My preliminary results based on optical/X-ray data analysis (Sect. 4.4.1 and Table 4.2, third column) show that the isotropic equivalent kinetic energy  $E_{k,iso}$  increases from  $\sim 2.5 \times 10^{53}$  erg to  $\sim 4 \times 10^{53}$  erg because of the energy injection from the central engine (Fig. 4.11). This conclusion is compatible with my preliminary optical/X-ray results, that show  $m = 0.27 \pm 0.02$ .

### 4.5.2 Multi-component SEDs in radio frequencies

In addition to the continuum associated with FS emission, radio SEDs and light-curves (Sect. 4.3.2) suggest other three distinct emission components: A, B, and C. Component A is responsible for the low-frequency peak in the spectrum at 0.8, 1.7, 5.8, 12.7 and 25.8 d (Fig. 4.4); component B shows up in the radio SEDs at 1.7 and 2.8 d; component C appears at four epochs (0.8, 5.8, 12.7, and 25.8 d) and is characterised by a faint peak around 10 GHz.

These components do not fit in the FS model discussed in Sect. 4.4. A possible explanation for the radio excess at early times is RS emission. There are many examples in the literature (e.g., [Gomboc et al. 2008](#); [Alexander et al. 2017b](#); [Laskar et al. 2018a](#)). For example, [Laskar et al. \(2018b\)](#) suggest that an early-time radio peak is consistent with emission from a refreshed RS produced by the violent collision of two shells with different Lorentz factors emitted at different times. A recent work ([Laskar et al. 2019](#)) showed for the first time that within a SED it is possible to disentangle the contributions of RS and of FS in the radio band. Nevertheless, in the case of GRB 160131A these peaks do not evolve as expected from the RS prescriptions, calling for something else that comes into play. In the hindsight, these features could have possibly been observed in more sparse radio data sets from past GRBs as well, and erroneously interpreted as RS evidence.

An alternative explanation to RS could be the diffractive ISS (Sect. 3.7, Fig. 4.8) or other extreme scattering effects, as seen in other GRBs (i.e. GRB 160625B, [Alexander et al. 2017b](#)). Future broadband GRB observations with denser time sampling will enable a more detailed characterisation of such variability and help resolve the contribution of ISS from intrinsic variations to the source.

Another possible explanation could be the two-component jet, one in which the optical and X-ray emission arise from a narrower, faster jet than that producing the radio observations (e.i. [Peng et al. 2005](#); [Racusin et al. 2008](#); [Holland et al. 2012](#)).

Finally, another explanation for the radio spectral bumps could be the presence of a population of thermal electrons, not accelerated by the FS passage into a relativistic power-law distribution, characterised by a Maxwellian distribution at lower energies ([Eichler & Waxman 2005](#)). This spectral component would likely require a different electron distribution, where the typical Lorentz factor of the thermal electrons is much lower than the minimum Lorentz factor of the shock-accelerated electrons (“cold electron model”, [Ressler & Laskar 2017](#)).

### 4.5.3 Challenges for the standard afterglow model

Preliminary results suggest that radio data are incompatible with the optical and X-ray data – especially at early-time and at lower frequencies – according to the behaviour predicted by the standard GRB afterglow model. This is not the first case: for example, recently [Kangas & Fruchter \(2019\)](#) reported the lack of visible jet breaks in the radio light-curves of a sample of 15 GRB afterglows, whereas X-rays seem to support it. However, I underline that they (1) considered only one regime (5-1-2) of afterglow emission in GS02, (2) assumed the sideways expansion for jetted emission (Sect. 2.3) in their analysis, and (3) ignored any observed rise period of the light-curve and any early features attributed to flares, plateau or RS in the literature. They interpret the long-lasting single power-law decline of the radio emission in terms of a two-component jet described above.

Last but not least, there is another assumption that might not necessarily hold true for GRB 160131A: constant micro-physical parameters. There has been found evidence that is unlikely to be the case for GRB 190114C ([Misra et al. 2019](#)).

### 4.5.4 Reverse shock

In Section 4.5.2 I discussed the multi-component structure observed in the radio SEDs between 0.8 and 117 d. I now consider whether each spectral peak from 0.8 to 25.8 d can in turn be ascribed to RS emission. When the outflow from the GRB central engine impacts on the ambient medium and produce a blast wave, a transient shock called RS is generated inside the flow itself (Sections 2.1.3 and 2.2.1). After the RS has crossed the ejecta (timescale of days), the flux above  $\nu_{c,rs}$  declines rapidly because no electron is newly accelerated within the ejecta (Laskar et al. 2018b); in this regime I assume  $\nu_{c,rs}$  to be located near each observed radio spectral peak, in order to compute a conservative lower limit to the optical light-curve.

The evolution of  $\nu_{c,rs}$  for a relativistic RS (thick shell regime, Sects. 2.1.3 and 2.2.1) scales as  $t^{-73/48}$  for ISM-like CBM, and  $t^{-15/8}$  for wind-like CBM (e.g., Gao et al. 2013b). On the other hand, for a Newtonian RS (thin shell regime, Sects. 2.1.3 and 2.2.1)  $\nu_{c,rs}$  scales as  $t^{-(15g+24)/(14g+7)}$  (Mészáros & Rees 1999; Kobayashi & Sari 2000; Gao et al. 2013b; Gao & Mészáros 2015), where  $g$  describes the Lorentz factor profile of the shocked ejecta  $\gamma \propto r^{-g}$  (Sect. 2.2.1); the different intervals assumed for  $g$  (based on the kind of CBM, Sect. 2.2.1) constrain the expected evolution of this characteristic frequency between  $\sim t^{-1.7}$  and  $\sim t^{-1.4}$  for ISM-like CBM (between  $\sim t^{-2.3}$  and  $\sim t^{-1.7}$  for wind-like CBM). Moreover, for relativistic RS the peak flux density evolves as  $F_{\nu,pk} \propto t^{-47/48}$  in ISM-like CBM ( $F_{\nu,pk} \propto t^{-9/8}$  in wind-like CBM), whereas for Newtonian RS this peak flux density evolves as  $F_{\nu,pk} \propto t^{-(11g+12)/(14g+17)}$ , ranging between  $\sim t^{-1.0}$  and  $\sim t^{-0.9}$  for ISM-like CBM (between  $\sim t^{-1.25}$  and  $\sim t^{-1.0}$  for wind-like CBM).

At radio frequencies, the first spectral peak takes place at  $F \approx 0.9$  Jy in X-band ( $\sim 9$  GHz) at 0.8 d (Fig. 4.4). Assuming  $\nu_{c,rs} \approx 9$  GHz and  $F_{\nu,pk} \approx 0.9$  Jy at this epoch, the Y-band ( $\sim 3 \times 10^{14}$  Hz) would be crossed by a relativistic RS (ISM) at  $t_{pk} \sim 8.5 \times 10^{-4}$  d with  $F_{\nu,pk} \sim 730$  Jy ( $t_{pk} \sim 3.1 \times 10^{-3}$  d and  $F_{\nu,pk} \sim 465$  Jy for wind). Unfortunately, there are no optical data at those epochs, and hence I scale  $F_{\nu,pk}$  at  $t_{pk}$  knowing that the observed Y-band light-curve evolves as  $\sim t^{-1.25}$  (Sect. 4.3.1), obtaining  $F_{\nu,pk} \sim 920$  Jy for ISM-like CBM ( $F_{\nu,pk} \sim 180$  Jy at  $\sim 3.1 \times 10^{-3}$  d for wind-like CBM); this behaviour is incompatible with the relativistic RS regime.

In Newtonian RS approach, for the same spectral peak I obtain the passage of  $\nu_{c,rs}$  in Y-band (1) in the range  $\approx (1.7 - 0.5) \times 10^{-3}$  d (corresponding to  $F_{\nu,pk} \sim 450 - 728$  Jy) for ISM-like CBM, and (2) in the range  $\approx (8.6 - 1.7) \times 10^{-3}$  d (corresponding to  $F_{\nu,pk} \sim 260 - 450$  Jy) for wind-like CBM. Also in this case, there are no optical data at those epochs to verify this assumption; the observed Y-band light-curve evolves as  $\sim -1.25$ , resulting in  $F_{\nu,pk} \sim 390 - 1930$  Jy for ISM-like CBM ( $F_{\nu,pk} \sim 50 - 390$  Jy for wind-like CBM); this behaviour seems to be compatible with the predicted Y-band light-curve.

The radio peak observed in the 1.7 d SED at the same frequency is incompatible with this peak, because I would observe this peak at  $\sim 3$  GHz in ISM-like CBM ( $\sim 2$  GHz in wind-like CBM).

Although the present analysis shows that the spectral peak at  $F \approx 0.9$  Jy in X-band ( $\sim 9$  GHz) at 0.8 d could be ascribable to Newtonian RS emission, I discussed in Sect. 4.5 that SEDs up to  $\sim 25$  d share the same rather constant peak at  $\sim 8$  GHz (Fig. 4.4), with  $\Delta\nu/\nu < 0.5$ , that is narrower than those observed in the radio SED of GRB 181201A ( $\Delta\nu/\nu \sim 3$ ), the first case of a SED instantaneously and clearly decomposed into RS and FS components (Laskar et al. 2019). This feature could suggest another origin for the peaks in radio SEDs, probably ascribed to ISS effect (Fig. 4.8 and Sect. 3.7).

### 4.5.5 Afterglow parameters obtained with sAGA

The analysis with sAGA of the afterglow of GRB 160131A, for which I considered a jetted (edge-regime) FS emission with optical absorption and energy injection (ISM environment), ended up with these preliminary time-independent constraints:  $p \sim 2.2$ ,  $\epsilon_e \sim 0.01$ ,  $\epsilon_B \sim 0.1$ ,  $n_0 \gtrsim 5 \text{ cm}^{-3}$ ,  $E_{K,iso} \gtrsim 10^{53} \text{ erg}$ ,  $A_v \sim 0.06$ ,  $t_j \sim 1 \text{ d}$ ; the spectrum is in fast cooling until  $\sim 0.1 \text{ d}$  and the non-relativistic regime sets in at  $\sim 200 \text{ d}$ .

In particular, the constrain on  $t_j$  leads to an estimate of the jet half opening angle of  $\theta_j \sim 7^\circ$ , corresponding to a beaming-corrected kinetic energy of  $E_K = E_{K,iso}(1 - \cos \theta_j) \gtrsim 7.5 \times 10^{50} \text{ erg}$ ; the lower limit on  $E_K$  and the value of  $\theta_j$  are consistent with the typical values of L-GRBs (Figs. 21 and 22 on Laskar et al. 2015). Moreover, the estimated lower limit on  $n_0$  and the strong observed correlation – highlighted in several analyses (e.g., GRB 160509A in Laskar et al. 2016, GRB 161219B in Laskar et al. 2018a, and GRB 181201A in Laskar et al. 2019) – between broadband detections of RS emission and CBM characterised by low densities (typically  $n_0 \lesssim 10^{-2} \text{ cm}^{-3}$  in ISM-like CBM, and  $A_* \lesssim 10^{-2}$  in wind-like CBM), suggest that the RS is unlikely to play a dominant role in radio data of GRB 160131A. This conclusion strengthens the ISS origin for the pronounced radio variability.

Finally, the energy injection parameter  $m \sim 0.3$  (and hence  $q = 1 - m \sim 0.7$ ) is compatible with what is expected ( $m \sim 0.27$ ) for an injection process that is powered by a spinning down magnetar. For example, a similar energy injection process was discussed for GRB 100418A, for which it was found  $m \sim 0.7$  (Marshall et al. 2011; Laskar et al. 2015).

## 4.6 Summary and conclusions

In this chapter I presented my preliminary results on the broadband modelling of the afterglow of GRB 160131A, whose observations span from  $\sim 430 \text{ s}$  to  $\sim 160 \text{ d}$  post explosion at 26 frequencies from  $6 \times 10^8 \text{ Hz}$  to  $7 \times 10^{17} \text{ Hz}$ . I interpreted this GRB afterglow using two independent approaches: (i) by means of general considerations based on the standard afterglow model, that built upon the results of an empirical modelling of the light-curves/spectra; (ii) through a self-consistent data modelling with sAGA.

- The optical/X-ray light-curves show a plateau in the temporal range  $\sim 0.1\text{--}0.8 \text{ d}$ , suggesting energy injection, followed by a steeper  $\alpha \sim -1.8$  that is interpreted as a jet break. The optical/X-ray observations support the following properties: (1) an ISM-like CBM, (2)  $p \sim 2.18$ , and (3) both  $\nu_m$  and  $\nu_c$  lie below  $\nu_{opt} = 3 \times 10^{14} \text{ Hz}$  already at  $t_{obs} = 0.005 \text{ d}$  for an ISM-like CBM. Radio data allow for a more precise identification of the break frequencies, jetted emission, and cooling regime. Specifically,  $\nu_m$  and  $\nu_c$  cross the radio band at  $t \sim 3 \text{ d}$  and  $t \gtrsim 120 \text{ d}$ , respectively, while  $\nu_{sa} \sim 6.4 \text{ GHz}$  at  $12.7 \text{ d}$ . The slow cooling regime sets in at  $t \sim 0.8 \text{ d}$  and the jet break occurs at  $t_b \sim 3\text{--}5 \text{ d}$ .
- In the broadband modelling with sAGA I considered a jetted (edge-regime) FS emission with optical absorption and energy injection, in ISM-like CBM. My preliminary results on the optical/X-ray data alone are in accord with the results obtained through the previous approach:  $p \sim 2.2$ ,  $\epsilon_e \sim 0.01$ ,  $\epsilon_B \sim 0.1$ ,  $n_0 \gtrsim 5 \text{ cm}^{-3}$ ,  $E_{K,iso} \gtrsim 10^{53} \text{ erg}$ ,  $A_v \sim 0.06$ ,  $t_j \sim 1 \text{ d}$  (and hence  $\theta_j \sim 7^\circ$ ). The spectrum is in fast cooling until  $\sim 0.1 \text{ d}$ , the non-relativistic regime sets in at  $\sim 200 \text{ d}$ , and  $m \sim 0.3$  inferred by modelling is compatible with theoretical assumptions ( $m \sim 0.27$ ), suggesting energy injection from a magnetar as a plausible interpretation. Moreover, the temporal evolution of  $\nu_c$  and  $\nu_m$  inferred by sAGA agree with what inferred in the other approach. Conversely, the temporal evolution of  $\nu_{sa}$  is

incompatible with sAG<sub>A</sub> results ( $\nu_{sa} \sim 80$  GHz at  $t \sim 13$  d), probably caused by the lack of radio data in this analysis.

The radio data – when it is as rich as in this case – show the presence of spectral bumps in several SEDs, incompatible with a simple standard GRB afterglow model and probably ascribable with ISS or other extreme scattering effects. This incompatibility is corroborated by the broadband modelling from radio to high energies, where the model works well at X-ray and radio (except for  $\nu < 8$  GHz), partially well at UV frequencies, and poorly in the visible band. This is not the first case: for example, recently [Kangas & Fruchter \(2019\)](#) show the lack of visible jet breaks in the radio light-curves of a sample of 15 GRB afterglows, even when one is seen in X-rays. In addition, in some cases, as for the afterglow of GRB 190114C, there is evidence for time varying shock micro-physics parameters ([Misra et al. 2019](#)).

Summing up, these results challenge the standard GRB afterglow model, and highlight the key role and as-yet poorly understood physics that manifests itself especially in the radio bands. Future broadband followup of GRB afterglows, particularly at radio frequencies with the latest and forthcoming generation facilities – especially in interferometric mode – such as the Very Large Baseline Array (VLBA<sup>9</sup>), LOw Frequency ARray (LOFAR, [van Haarlem et al. 2013](#)) or the next generation Square Kilometer Array (SKA, e.i. [Johnston et al. 2008](#)), are essential to reach an exhaustive comprehension of the GRB afterglow physics, particularly within the newborn era of so-called multi-messenger astronomy.

---

<sup>9</sup><https://science.nrao.edu/facilities/vlba>



# Chapter 5

## Constraints on the environment and energetics of BL-Ic SN2014ad from deep radio and X-ray observations

Except for a couple of ambiguous cases, L-GRBs are found to be associated with type BL-Ic supernovae, hydrogen-stripped core-collapse explosions of massive stars ( $M_{ZAMS} \gtrsim 8M_{\odot}$ ) that show no evidence for hydrogen and helium in their spectra. These SNe are characterised by high ejecta velocity ( $\gtrsim 10^4 \text{ km s}^{-1}$ ) and, at the time of writing, the exact nature of their progenitors is unclear, although the first precursor emission for a Ic-BL has recently been observed (Ho et al. 2019). In particular, the reason why a small fraction of BL-Ic SNe harbour relativistic jets is not known; a possible interpretation could be the off-axis jet scenario, where the SN explosion powers a GRB-like jet that is misaligned with respect to the observer. Since these SNe are detectable – with current facilities – at redshift  $z \lesssim 1$ , the direct evidence of GRB/SN connection is doable only for nearby GRBs. As stressed in this thesis (e.g., Chapters 4 and 6), broadband observations extended to lower frequencies – such as the radio band – are crucial to have a complete picture of the involved physics; in this regard, deep radio and X-ray observations are crucial to constrain the high-velocity ejecta and possibly reveal the emission from off-axis jets as well as to uncover weak GRBs undetected by current gamma-ray observing facilities.

In this context I present deep X-ray and radio observations of the BL-Ic SN 2014ad extending from 10 to 900 days post explosion. SN 2014ad – discovered only in optical band – was not detected at either frequency and has no evidence for a GRB association. The proximity of SN 2014ad ( $d \sim 26 \text{ Mpc}$ ) allows to deeply constrain the progenitor mass-loss rate  $\dot{M}$  and the total energy of the fast ejecta  $E$ . I interpret these deep radio and X-ray upper limits in the context of two synchrotron emission regimes, using a wind-like CSM (typical of SN environments): (i) mildly relativistic and isotropic ejecta, as seen usually in ordinary Ic SNe, and (ii) relativistic ejecta, as seen in GRB-like jet. My analysis shows that off-axis low-energy jets expanding in a low-density medium ( $\dot{M} \lesssim 10^{-6} M_{\odot} \text{ yr}^{-1}$ ) cannot be ruled out – as was thought so far (e.g. Smith 2014) – even for the most nearby BL-Ic SNe. Deep radio and X-ray followup programmes at early and at late times of a large sample of nearby BL-Ic SNe will clarify if these sources harbour a GRB counterpart.

This work was published as Marongiu et al. (2019) in The Astrophysical Journal in July 2019<sup>1</sup>. A copy of the full text (editorial version) of this paper is reported in Appendix A.

---

<sup>1</sup>DOI: <https://doi.org/10.3847/1538-4357/ab25ef>





# Chapter 6

## Optimised methods for the detection and analysis of weak radio sources with single-dish observations

Followup programmes of GRB afterglows at radio frequencies help decipher a wealth of information (as stressed in the analysis of radio VLA data described in Chapter 4), in particular: (1) constrain the self-absorption frequency of the underlying synchrotron radiation, (2) track the presence and evolution of RS in the ejecta – that can clarify the nature of GRB progenitors – and hence derive the ejecta magnetisation and initial Lorentz factor, (3) constrain the degree of ejecta collimation and hence the released energy corrected for relativistic beaming, (4) derive the size of the afterglow using scintillation methods, and (5) better understand the hydrodynamics of relativistic outflows. GRB radio afterglows are typically faint sources (mJy or sub-mJy) and hence the main issue for their detection is the instrumental sensitivity and the confusion limit; these aspects are usually more crucial for single-dish radiotelescopes (whose sensitivity can typically reach a few hundred  $\mu\text{Jy}$  integrating over many hours) rather than interferometric arrays as the VLA and VLBI (whose sensitivity can reach the same limit within a few minutes on source exposure). At this flux density level, observations with single-dish radiotelescopes require (1) an accurate knowledge of the background (both instrumental and astronomical), (2) good sky opacity conditions to ensure an accurate calibration, and (3) a reliable and well-defined source detection method. Recently, several specific radio followup campaigns improved the observational coverage of the lower part of the emission spectrum, but an exhaustive picture of GRB afterglows is still missing.

In this context, I present three detection methods for the analysis of weak sources in single-dish mode in terms of sensitivity and robustness: ‘quick-look’ (Method A, a smart but rough approach), ‘source extraction’ (Method B, typically adopted in X-ray/gamma-ray astronomy), and fit procedure with a 2-Dimensional Gaussian (Method C, a more sophisticated approach). I developed a specific Python code using GRB radio afterglows as suitable targets. I tested these methods through a specific followup programme with Sardinia Radio Telescope (SRT) at 6.9 GHz in the framework of the observing project 23-18 for the afterglow of GRB 181201A (PI: M. Marongiu) and the ToO request 02-19 for the afterglow of GRB 190114C (PI: M. Marongiu), resulting in no detection; as a further test, I applied these methods to the SRT data of the Galactic binary GRS 1915+105. This new methodology makes use of simulations, as a useful complement of actual radio observations, and optimises the detection of faint sources (as is the case for GRB afterglows or GW radio counterparts), pushing down the sensitivity limits of SRT – with respect to more traditional techniques – at  $\sim 1.8$  mJy for a typical observation of 6 hours.

This work was submitted to *Experimental Astronomy* and it is currently under peer review.

A copy of the full text of the submitted version is reported in Appendix [B](#).

# Conclusions

The transient sky astronomy has made great strides in recent years, thanks to the increasing state-of-the-art technology for the detection of new sources throughout the Universe. This enables to better understand the physics of these astrophysical objects and to address open issues of astrophysics and cosmology (such as the formation of compact binaries and the dark matter nature). The multi-messenger astronomy was officially born with the broadband observations – from radio to X-ray frequencies – of the low-luminosity and nearby short GRB 170817A, associated with the binary neutron star (BNS) merger event GW 170817 detected by LIGO/VIRGO facilities. The recent detection at TeV energies of two bright GRB afterglows (190114C and 180720B) thanks to MAGIC and H.E.S.S. Cherenkov telescopes, further extended the range of covered frequencies where GRB afterglows can be analysed, strongly suggesting the signature of inverse Compton in the afterglow emission. Relativistic explosions – characterised by Lorentz factors ranging between a few to a few hundreds – play a fundamental role because they are characteristic of astrophysical objects such as GW counterparts, gamma-ray bursts (GRBs) and supernovae (SNe).

This context is the background that gives birth to my PhD thesis, focused on the modelling of multi-frequency data sets of relativistic explosions, such as GRBs and SNe. Broadband analysis of GRB afterglows is key to understand the radiation mechanism(s) at work, the relativistic shock microphysics, the energetics and the jet geometry. Yet, an exhaustive picture of GRB afterglows is missing. The magnetisation of the ejecta, which is still of the main open issues in the GRB science, can be addressed effectively and uniquely through observations at lower frequencies, especially the radio band, studying the reverse shock observed in GRB radio afterglows. Unfortunately, these sources are very faint (mJy or sub-mJy events) and hence their observations are hampered by the limited sensitivity of radiotelescopes (both in interferometric and, especially, in single-dish mode). In the latest years, several dedicated radio followup programmes aimed to provide a good temporal and spectral reverse and forward shock coverage, but a complete picture of GRB ejecta remains an open issue.

I therefore developed a specific Python code called sAGa (Software for AfterGlow Analysis) that analyses the broadband emission of GRB afterglows based on an analytical approach. After successfully testing the capabilities of sAGa on various GRB afterglows (such as GRB 120521C, GRB 090423 and GRB 050904), I analysed long GRB 160131A, whose afterglow is a challenging workbench for sAGa and for the standard GRB afterglow model. Multi-frequency light-curves showed the signature of energy injection and jetted emission; moreover, radio light-curves are affected by several peaks, maybe suggestive of either strong interstellar scintillation (ISS) effects or multi-component structure. My preliminary results showed that joining a rich radio data set to the optical and X-ray ones, calls for new mechanisms in addition to what is predicted by the standard GRB afterglow model.

In the context of the radio detection of GRB afterglows, I supervised a dedicated followup programme in single-dish mode with Sardinia Radio Telescope (SRT), resulted in upper limits for GRB 181201A and GRB 190114C. I analysed a new detection method – especially suited for faint radio sources – considering a fitting procedure with a 2-Dimensional Gaussian; this

method is compared with two more traditional techniques in terms of sensitivity and robustness: the smart but rough ‘quick-look’ method and the ‘source extraction’, typical of high-energy astronomy. These methods are included in a specific tool for the analysis, that allows to measure the flux density and the uncertainty of a point-like source, such as the radio counterparts of GRBs or GWs. The most accurate and robust method is the fitting procedure with a 2-Dimensional Gaussian; this new methodology for the SRT data analysis pushes down the sensitivity limits of this radiotelescope – with respect to more traditional techniques – at  $\sim 1.8$  mJy, allowing to improve the upper limit estimation up to 40% of the initial value. This analysis suggests that the detection of faint sources requests a deep knowledge of the radio background to estimate an accurate flux density.

Long-GRBs are very characterised by their association with type Ic broad-lined supernovae (Ic-BL SNe), hydrogen-stripped core-collapse explosions of massive stars showing high ejecta velocity ( $\gtrsim 10^4$  km s $^{-1}$ ). I analysed the available X-ray and radio observations (resulting in upper limits) of the nearby Ic-BL SN 2014ad ( $\sim 26$  Mpc), characterised by no observational evidence of a GRB counterpart. These upper limits, thanks to the proximity of the source, enable very deep constraints on both the SN progenitor mass-loss rate ( $\dot{M}$ ) and the total energy of the ejecta ( $E$ ). For this analysis I adapted sAGa to the SN emission, to extract the physical properties through a broadband approach. In this analysis I considered two synchrotron radiation scenarios: uncollimated non-relativistic ejecta (typical of ordinary SNe), and off-axis relativistic jet (typical of GRBs). My study shows that these two emission regimes cannot be ruled out even in the most nearby BL-Ic SNe; deep radio and X-ray followup programmes of a large sample of nearby BL-Ic SNe will clarify if jetted emission (typical of GRBs) is a common feature in BL-Ic SNe. Moreover, I cannot reject the possibility of a radio synchrotron emission dominated by the cocoon created by an off-axis GRB jet, ploughing the stellar progenitor, as expected for relativistic SNe.

Future multi-messenger followup programmes will be fundamental to understand astrophysical sources involving relativistic explosions, such as GRB afterglows and Ic-BL SNe, with the radio band playing a unique role in this context. The next-generation facilities on the coming decade in radio (SKA), optical-NIR (E-ELT, JWST), X-rays (ATHENA) and TeV (CTA) bands, characterised by high sensitivity, will make it possible to solve a number of puzzles in the transient sky astrophysics.

# Acknowledgments

I'm writing these lines at the end of an extraordinary and constructive path that began in 2016 and ended with the PhD viva. Even if it was hard, my stubbornness and strong motivation have constantly pushed me to go on. That is why, first of all, I wish to thank my parents Giuseppe and AnnaMaria, who from Sardinia have greatly supported me during these years, and my sister Roberta, who often came to visit me both in Ferrara and in Bath. I owe special thanks to Veronica, my girlfriend, who understood my choice and supported, endured and encouraged me in these three years; we have always been close, supporting each other, even if far away.

I warmly thank my Supervisor, Dr. Cristiano Guidorzi, for introducing me to the wonderfully interesting world of gamma-ray bursts and, with great temperament, for making me grow up humanly and professionally during the PhD. I thank the external evaluators – Prof. Shiho Kobayashi (ARI/LJMU) and Dr. Giulia Stratta (INAF/OAS-BO) – that, thanks to their amount of very useful advice, helped me to improve remarkably the present thesis.

I cannot thank enough my PhD mates Renato, Pietro, and Giuseppe, who helped me survive in this adventure. I sincerely thank the family of the Cagliari Astronomical Observatory (INAF/OAC) and of the Sardinia Radio Telescope, chaired by Dr. Emilio Molinari, for the great availability they have shown me, in particular Alberto, Elise, Andrea M., Giuseppe, Raimondo, Andrea P., Noemi, Matteo B., Matteo M., Federica, Valentina, Paolo S., Sergio, Delphine, and Sara (now working at INAF/OACT). A special thanks to all the collaborators who have worked with me during these three years, in particular: Prof. Filippo Frontera from Ferrara University; Raffaella and Deanne from Northwestern University (USA); Marcello and Monica from INAF/IRA-BO; Dr. Lorenzo Amati, Luciano, Eliana and Andrea R. from INAF/OAS-BO; Giancarlo Ghirlanda from INAF/OA-Brera.

My sincere thanks to Prof. Carole Mundell, my supervisor during the experience at the University of Bath (UK), together with Nuria Jordana, Tanmoy Laskar, Hendrik Van Eerten and Patricia Shady for their warm hospitality. I thank all the PhD students and researchers of the University of Bath, where I spent three wonderful months: Thijs, Georgia, Eliot, Caroline, Abi, Anastasia, Lewis, Vaihi and Stijn. Thanks to my Bath roommates James and Sheila for their availability and hospitality.

Special thanks to all the researchers (Enrico, Massimo, Francesco, Roberto and Rupal), Prof. Piero Rosati, the PhD students (in particular Camilo, Tais, Silvia, Luca, Lisa, and all the PhD mates of XXXII Cycle), the technical and administrative staff of the University of Ferrara I interacted during these years with.

I also thank my girlfriend's family – Claudio, Marcella and Eleonora – who welcomed me into their family, showing me great respect and a lot of love. A sincerely thank Ingrid, who in Ferrara was like a second mother to me. I also thank all my Sardinian friends, who in these three years I have seen less because of the distance: Luca, Giuseppe, Mattia and Ilaria, Alessio and Silvia, Patrizia and Donato, Andrea and Mattia, Riccardo, Matteo and everyone else. I warmly thank Filippo, who with his family was the first one to welcome me in Ferrara for the PhD admission exam; I thank him for his availability, and for the days spent at the Mazza stadium to watch the Spal soccer matches! I lovely thank the guys of “Il Cenacolo” residence, with whom

## ACKNOWLEDGMENTS

---

I had a lot of fun, shared great time and felt at home: Beatrice, Francesco, Alt(h)ea, Mario, Lorenza, Simona, Riccardo and Lorenza, Ivano and Deborah, Alessandra and Andrea, Matteo and Alexis, Eleonora, Gianluca, Andrea B., Luca, Mathilde, Maria Vittoria and Valeria, Silvia, Francesco, Maria Rosaria and Bernardo, and all the others.

I warmly thank all those who did not believe in my potential, because it is also thanks to them that I achieved this important milestone.

I wish to address a final word of thanks, the deepest, to all my loved ones who support me from the Heaven, and they share with me this important milestone of my life.

GRAZIE A TUTTI



# Bibliography

- Abbott, B. P., Abbott, R., Abbott, T. D., et al. 2016, *Physical Review X*, 6, 041015
- Abbott, B. P., Abbott, R., Abbott, T. D., et al. 2017a, *ApJ*, 848, L13
- Abbott, B. P., Abbott, R., Abbott, T. D., et al. 2017b, *ApJ*, 848, L12
- Abdalla, H., Adam, R., Aharonian, F., et al. 2019, *Nature*, 575, 464
- Abdo, A. A., Ackermann, M., Arimoto, M., et al. 2009, *Science*, 323, 1688
- Ackermann, M., Ajello, M., Asano, K., et al. 2013, *ApJS*, 209, 11
- Ackermann, M., Asano, K., Atwood, W. B., et al. 2010, *ApJ*, 716, 1178
- Ajello, M., Arimoto, M., Axelsson, M., et al. 2019, *ApJ*, 878, 52
- Akerlof, C., Balsano, R., Barthelmy, S., et al. 1999, *Nature*, 398, 400
- Alexander, K. D., Berger, E., Fong, W., et al. 2017a, *ApJ*, 848, L21
- Alexander, K. D., Laskar, T., Berger, E., et al. 2017b, *ApJ*, 848, 69
- Alexander, K. D., Margutti, R., Blanchard, P. K., et al. 2018, *ApJ*, 863, L18
- Amati, L. 2006, *MNRAS*, 372, 233
- Amati, L., Frontera, F., Tavani, M., et al. 2002, *A&A*, 390, 81
- Amati, L., O'Brien, P., Götz, D., et al. 2018, *Advances in Space Research*, 62, 191
- Anderson, G. E., van der Horst, A. J., Staley, T. D., et al. 2014, *MNRAS*, 440, 2059
- Antonelli, L. A., D'Avanzo, P., Perna, R., et al. 2009, *A&A*, 507, L45
- Armstrong, J. W., Rickett, B. J., & Spangler, S. R. 1995, *ApJ*, 443, 209
- Band, D., Matteson, J., Ford, L., et al. 1993, *ApJ*, 413, 281
- Band, D. L., Axelsson, M., Baldini, L., et al. 2009, *ApJ*, 701, 1673
- Barthelmy, S. D., Barbier, L. M., Cummings, J. R., et al. 2005, *Space Sci. Rev.*, 120, 143
- Baumgartner, W. H., Barthelmy, S. D., Burrows, D. N., et al. 2012, *GRB Coordinates Network*, 13318, 1
- Beloborodov, A. M., Stern, B. E., & Svensson, R. 1998, *ApJ*, 508, L25
- Beloborodov, A. M., Stern, B. E., & Svensson, R. 2000, *ApJ*, 535, 158

- Beniamini, P. & van der Horst, A. J. 2017, MNRAS, 472, 3161
- Berger, E. 2009, ApJ, 690, 231
- Berger, E. 2014, ARA&A, 52, 43
- Berger, E., Kulkarni, S. R., Pooley, G., et al. 2003, Nature, 426, 154
- Bietenholz, M. F. 2014, PASA, 31, e002
- Blandford, R. D. & McKee, C. F. 1976, Physics of Fluids, 19, 1130
- Blandford, R. D. & Znajek, R. L. 1977, MNRAS, 179, 433
- Bloom, J. S. 2011, What are Gamma-Ray Bursts? (Princeton and Oxford: Princeton University Press)
- Bloom, J. S., Frail, D. A., & Kulkarni, S. R. 2003, ApJ, 594, 674
- Bloom, J. S., Kulkarni, S. R., Djorgovski, S. G., et al. 1999, Nature, 401, 453
- Bloom, J. S., Kulkarni, S. R., Price, P. A., et al. 2002, ApJ, 572, L45
- Boer, M., Gendre, B., & Stratta, G. 2015, ApJ, 800, 16
- Briggs, M. S., Band, D. L., Kippen, R. M., et al. 1999, ApJ, 524, 82
- Bromberg, O., Nakar, E., Piran, T., & Sari, R. 2011, ApJ, 740, 100
- Bromberg, O., Nakar, E., Piran, T., & Sari, R. 2012, ApJ, 749, 110
- Bromm, V. & Larson, R. B. 2004, ARA&A, 42, 79
- Brown, T. M., Baliber, N., Bianco, F. B., et al. 2013, PASP, 125, 1031
- Bucciantini, N., Quataert, E., Arons, J., Metzger, B. D., & Thompson, T. A. 2008, MNRAS, 383, L25
- Burlon, D., Ghirlanda, G., Ghisellini, G., Greiner, J., & Celotti, A. 2009, A&A, 505, 569
- Burlon, D., Ghirlanda, G., Ghisellini, G., et al. 2008, ApJ, 685, L19
- Burrows, D. N., Hill, J. E., Nousek, J. A., et al. 2005a, Space Sci. Rev., 120, 165
- Burrows, D. N., Romano, P., Falcone, A., et al. 2005b, Science, 309, 1833
- Calderone, G., Ghirlanda, G., Ghisellini, G., et al. 2015, MNRAS, 448, 403
- Campana, S., Mangano, V., Blustin, A. J., et al. 2006, Nature, 442, 1008
- Cannizzo, J. K., Gehrels, N., & Vishniac, E. T. 2004, ApJ, 601, 380
- Cano, Z., Wang, S.-Q., Dai, Z.-G., & Wu, X.-F. 2017, Advances in Astronomy, 2017, 8929054
- Cavallo, G. & Rees, M. J. 1978, MNRAS, 183, 359
- Chandra, P. & Frail, D. A. 2012, ApJ, 746, 156

- Chandra, P., Frail, D. A., Fox, D., et al. 2010, *ApJ*, 712, L31
- Chattopadhyay, T., Vadawale, S. V., Aarthy, E., et al. 2019, *ApJ*, 884, 123
- Chevalier, R. A. & Li, Z.-Y. 2000, *ApJ*, 536, 195
- Chincarini, G., Mao, J., Margutti, R., et al. 2010, *MNRAS*, 406, 2113
- Chincarini, G., Moretti, A., Romano, P., et al. 2007, *ApJ*, 671, 1903
- Cline, T. L. & Desai, U. D. 1976, *Astrophysics and Space Science*, 42, 17
- Coburn, W. & Boggs, S. E. 2003, *Nature*, 423, 415
- Colgate, S. A. 1968, *Canadian Journal of Physics Supplement*, 46, 476
- Colgate, S. A. 1974, *ApJ*, 187, 333
- Cordes, J. M. & Lazio, T. J. W. 2002, arXiv e-prints, arXiv:0207156
- Corsi, A., Gal-Yam, A., Kulkarni, S. R., et al. 2016, *ApJ*, 830, 42
- Costa, E., Frontera, F., Heise, J., et al. 1997, *Nature*, 387, 783
- Covino, S., Ghisellini, G., Lazzati, D., & Malesani, D. 2004, in *Astronomical Society of the Pacific Conference Series*, Vol. 312, *Gamma-Ray Bursts in the Afterglow Era*, ed. M. Feroci, F. Frontera, N. Masetti, & L. Piro, 169
- Cucchiara, A., Levan, A. J., Fox, D. B., et al. 2011, *ApJ*, 736, 7
- Cummings, J., Angelini, L., Barthelmy, S., et al. 2005, *GRB Coordinates Network*, 3910, 1
- Curran, P. A., Starling, R. L. C., O'Brien, P. T., et al. 2008, *A&A*, 487, 533
- Dai, Z. G. & Lu, T. 1998, *Phys. Rev. Lett.*, 81, 4301
- Dai, Z. G., Wang, X. Y., Wu, X. F., & Zhang, B. 2006, *Science*, 311, 1127
- De Colle, F., Granot, J., López-Cámara, D., & Ramirez-Ruiz, E. 2012, *ApJ*, 746, 122
- de Pasquale, M., Evans, P., Oates, S., et al. 2009, *MNRAS*, 392, 153
- de Ugarte Postigo, A., Thoene, C. C., & Sanchez-Ramirez, R. 2016, *GRB Coordinates Network*, 18966, 1
- Della Valle, M., Chincarini, G., Panagia, N., et al. 2006, *Nature*, 444, 1050
- Dermer, C. D. & Atoyan, A. 2006, *ApJ*, 643, L13
- Dermer, C. D., Böttcher, M., & Chiang, J. 2000, *ApJ*, 537, 255
- Eichler, D. & Levinson, A. 1999, *ApJ*, 521, L117
- Eichler, D., Livio, M., Piran, T., & Schramm, D. N. 1989, *Nature*, 340, 126
- Eichler, D. & Waxman, E. 2005, *ApJ*, 627, 861

- Evans, D., Kiebesadel, R., Baros, J., et al. 1979, *International Astronomical Union Circular*, 3356, 1
- Evans, P. A., Beardmore, A. P., Page, K. L., et al. 2009, *MNRAS*, 397, 1177
- Falcone, A. D., Morris, D., Racusin, J., et al. 2007, *ApJ*, 671, 1921
- Fan, Y.-Z., Dai, Z.-G., Huang, Y.-F., & Lu, T. 2002, *Chinese J. Astron. Astrophys.*, 2, 449
- Fan, Y.-Z. & Xu, D. 2006, *MNRAS*, 372, L19
- Fan, Y. Z., Zhang, B., & Proga, D. 2005, *ApJ*, 635, L129
- Filippenko, A. V. 1997, *ARA&A*, 35, 309
- Fishman, G. J. & Meegan, C. A. 1995, *ARA&A*, 33, 415
- Fong, W., Berger, E., Chornock, R., et al. 2013, *ApJ*, 769, 56
- Fong, W., Berger, E., & Fox, D. B. 2010, *ApJ*, 708, 9
- Foreman-Mackey, D. 2016, *The Journal of Open Source Software*, 24
- Foreman-Mackey, D., Hogg, D. W., Lang, D., & Goodman, J. 2013, *PASP*, 125, 306
- Fox, D. B., Frail, D. A., Price, P. A., et al. 2005, *Nature*, 437, 845
- Fraija, N., Lee, W., & Veres, P. 2016, *ApJ*, 818, 190
- Frail, D. A., Cameron, P. B., Kasliwal, M., et al. 2006, *ApJ*, 646, L99
- Frail, D. A., Goss, W. M., & Whiteoak, J. B. Z. 1994, *The Astrophysical Journal*, 437, 781
- Frail, D. A., Kulkarni, S. R., Nicastro, L., Feroci, M., & Taylor, G. B. 1997, *Nature*, 389, 261
- Frail, D. A., Kulkarni, S. R., Sari, R., et al. 2001, *ApJ*, 562, L55
- Frail, D. A., Waxman, E., & Kulkarni, S. R. 2000, *ApJ*, 537, 191
- Fruchter, A. S., Levan, A. J., Strolger, L., et al. 2006, *Nature*, 441, 463
- Fynbo, J. P. U., Watson, D., Thöne, C. C., et al. 2006, *Nature*, 444, 1047
- Gal-Yam, A., Ofek, E. O., Poznanski, D., et al. 2006, *ApJ*, 639, 331
- Galama, T., Groot, P. J., Vanparadijs, J., et al. 1997, *Nature*, 387, 479
- Galama, T. J., Vreeswijk, P. M., van Paradijs, J., et al. 1998, *Nature*, 395, 670
- Gao, H., Lei, W.-H., Wu, X.-F., & Zhang, B. 2013a, *MNRAS*, 435, 2520
- Gao, H., Lei, W.-H., Zou, Y.-C., Wu, X.-F., & Zhang, B. 2013b, *New Astronomy Reviews*, 57, 141
- Gao, H. & Mészáros, P. 2015, *ApJ*, 802, 90
- Gao, H., Zhang, B., & Lü, H.-J. 2016, *Phys. Rev. D*, 93, 044065

- Garnavich, P. M., Stanek, K. Z., Wyrzykowski, L., et al. 2003, *ApJ*, 582, 924
- Gehrels, N., Chincarini, G., Giommi, P., et al. 2004, *ApJ*, 611, 1005
- Gehrels, N., Norris, J. P., Barthelmy, S. D., et al. 2006, *Nature*, 444, 1044
- Gehrels, N., Sarazin, C. L., O'Brien, P. T., et al. 2005, *Nature*, 437, 851
- Gendre, B., Stratta, G., Atteia, J. L., et al. 2013, *ApJ*, 766, 30
- Ghirlanda, G., Ghisellini, G., & Lazzati, D. 2004, *ApJ*, 616, 331
- Ghirlanda, G., Nava, L., & Ghisellini, G. 2010, *A&A*, 511, A43
- Ghirlanda, G., Salafia, O. S., Paragi, Z., et al. 2019, *Science*, 363, 968
- Ghisellini, G., Ghirlanda, G., Nava, L., & Celotti, A. 2010, *MNRAS*, 403, 926
- Ghisellini, G. & Lazzati, D. 1999, *MNRAS*, 309, L7
- Giannios, D. 2006, *A&A*, 457, 763
- Golenetskii, S. V., Mazets, E. P., Aptekar, R. L., & Ilinskii, V. N. 1983, *Nature*, 306, 451
- Gomboc, A., Kobayashi, S., Guidorzi, C., et al. 2008, *ApJ*, 687, 443
- Goodman, J. 1986, *ApJ*, 308, L47
- Goodman, J. 1997, *New A*, 2, 449
- Goodman, J. & Narayan, R. 2006, *ApJ*, 636, 510
- Gorosabel, J., Fynbo, J. P. U., Fruchter, A., et al. 2005, *A&A*, 437, 411
- Götz, D., Laurent, P., Lebrun, F., Daigne, F., & Bošnjak, Ž. 2009, *ApJ*, 695, L208
- Gou, L. J., Fox, D. B., & Mészáros, P. 2007, *ApJ*, 668, 1083
- Graham, J. F. & Fruchter, A. S. 2013, *ApJ*, 774, 119
- Granot, J. 2003, *ApJ*, 596, L17
- Granot, J. 2007, in *Revista Mexicana de Astronomia y Astrofisica Conference Series*, Vol. 27, *Revista Mexicana de Astronomia y Astrofisica*, vol. 27, 140–165
- Granot, J. 2008, arXiv e-prints, arXiv:0811.1657
- Granot, J., De Colle, F., & Ramirez-Ruiz, E. 2018, *MNRAS*, 481, 2711
- Granot, J. & Königl, A. 2003, *ApJ*, 594, L83
- Granot, J. & Kumar, P. 2006, *MNRAS*, 366, L13
- Granot, J., Miller, M., Piran, T., Suen, W. M., & Hughes, P. A. 2001, in *Gamma-ray Bursts in the Afterglow Era*, ed. E. Costa, F. Frontera, & J. Hjorth, 312
- Granot, J. & Piran, T. 2012, *MNRAS*, 421, 570

- Granot, J., Piran, T., & Sari, R. 2000, in American Institute of Physics Conference Series, Vol. 526, Gamma-ray Bursts, 5th Huntsville Symposium, ed. R. M. Kippen, R. S. Mallozzi, & G. J. Fishman, 489–493
- Granot, J. & Ramirez-Ruiz, E. 2010, arXiv e-prints, arXiv:1012.5101
- Granot, J. & Sari, R. 2002, *ApJ*, 568, 820
- Granot, J. & van der Horst, A. J. 2014, *PASA*, 31, 8
- Greiner, J., Clemens, C., Krühler, T., et al. 2009, *A&A*, 498, 89
- Greiner, J., Mazzali, P. A., Kann, D. A., et al. 2015, *Nature*, 523, 189
- Grindlay, J. E. 1994, *The Astrophysical Journal Supplement Series*, 92, 465
- Gruzinov, A. 1999, *ApJ*, 525, L29
- Guetta, D. & Della Valle, M. 2007, *ApJ*, 657, L73
- Guidorzi, C., Dichiara, S., Kobayashi, S., et al. 2016, *GRB Coordinates Network*, 18953, 1
- Guidorzi, C., Margutti, R., Amati, L., et al. 2012, *MNRAS*, 422, 1785
- Guiriec, S., Connaughton, V., Briggs, M. S., et al. 2011, *ApJ*, 727, L33
- Guiriec, S., Kouveliotou, C., Daigne, F., et al. 2015, *ApJ*, 807, 148
- Haislip, J. B., Nysewander, M. C., Reichart, D. E., et al. 2006, *Nature*, 440, 181
- Hallinan, G., Corsi, A., Mooley, K. P., et al. 2017, *Science*, 358, 1579
- Hartmann, D. & Epstein, R. I. 1989, *ApJ*, 346, 960
- Hascoët, R., Daigne, F., Mochkovitch, R., & Vennin, V. 2012, *MNRAS*, 421, 525
- Heger, A., Fryer, C. L., Woosley, S. E., Langer, N., & Hartmann, D. H. 2003, *ApJ*, 591, 288
- Hjorth, J., Malesani, D., Jakobsson, P., et al. 2012, *ApJ*, 756, 187
- Hjorth, J., Sollerman, J., Møller, P., et al. 2003, *Nature*, 423, 847
- Ho, A. Y. Q., Goldstein, D. A., Schulze, S., et al. 2019, arXiv e-prints, arXiv:1904.11009
- Högbom, J. A. 1974, *A&AS*, 15, 417
- Holland, S. T., De Pasquale, M., Mao, J., et al. 2012, *ApJ*, 745, 41
- Hu, Y.-D., Liang, E.-W., Xi, S.-Q., et al. 2014, *ApJ*, 789, 145
- Huang, Y. F., Wu, X. F., Dai, Z. G., Ma, H. T., & Lu, T. 2004, *ApJ*, 605, 300
- Hurley, K., Dingus, B. L., Mukherjee, R., et al. 1994, *Nature*, 372, 652
- Jakobsson, P., Hjorth, J., Fynbo, J. P. U., et al. 2004, *ApJ*, 617, L21
- Jeffreys, H. 1946, *Proceedings of the Royal Society of London Series A*, 186, 453

- Jin, Z. P., Yan, T., Fan, Y. Z., & Wei, D. M. 2007, *ApJ*, 656, L57
- Johnston, S., Taylor, R., Bailes, M., et al. 2008, *Experimental Astronomy*, 22, 151
- Jones, E., Oliphant, T., Peterson, P., et al. 2001–, SciPy: Open source scientific tools for Python, [Online; accessed <today>]
- Kaneko, Y., Ramirez-Ruiz, E., Granot, J., et al. 2007, *ApJ*, 654, 385
- Kangas, T. & Fruchter, A. 2019, arXiv e-prints, arXiv:1911.01938
- Kann, D. A., Klose, S., & Zeh, A. 2006, *ApJ*, 641, 993
- Kann, D. A., Klose, S., Zhang, B., et al. 2011, *ApJ*, 734, 96
- Kann, D. A., Klose, S., Zhang, B., et al. 2010, *ApJ*, 720, 1513
- Kann, D. A., Masetti, N., & Klose, S. 2007, *AJ*, 133, 1187
- Kashiyama, K., Ioka, K., & Mészáros, P. 2013, *ApJ*, 776, L39
- Kathirgamaraju, A., Barniol Duran, R., & Giannios, D. 2018, *MNRAS*, 473, L121
- Kawai, N., Kosugi, G., Aoki, K., et al. 2006, *Nature*, 440, 184
- Kistler, M. D., Yüksel, H., Beacom, J. F., & Stanek, K. Z. 2008, *ApJ*, 673, L119
- Klebesadel, R. W., Strong, I. B., & Olson, R. A. 1973, *ApJ*, 182, L85
- Klose, S., Schmidl, S., Kann, D. A., et al. 2019, *A&A*, 622, A138
- Kobayashi, S. 2000, *ApJ*, 545, 807
- Kobayashi, S., Piran, T., & Sari, R. 1997, *ApJ*, 490, 92
- Kobayashi, S., Piran, T., & Sari, R. 1999, *ApJ*, 513, 669
- Kobayashi, S. & Sari, R. 2000, *ApJ*, 542, 819
- Kobayashi, S. & Zhang, B. 2003a, *ApJ*, 597, 455
- Kobayashi, S. & Zhang, B. 2003b, *ApJ*, 582, L75
- Kocevski, D. 2012, *ApJ*, 747, 146
- Kolmogorov, A. 1941, *Akademiia Nauk SSSR Doklady*, 30, 301
- Kopač, D., Mundell, C. G., Kobayashi, S., et al. 2015, *ApJ*, 806, 179
- Kouveliotou, C., Meegan, C. A., Fishman, G. J., et al. 1993, *ApJ*, 413, L101
- Krimm, H. A., Beardmore, A. P., Evans, P. A., et al. 2009, *GRB Coordinates Network*, 9198, 1
- Kulkarni, S. R., Djorgovski, S. G., Odewahn, S. C., et al. 1999, *Nature*, 398, 389
- Kulkarni, S. R., Frail, D. A., Wieringa, M. H., et al. 1998, *Nature*, 395, 663
- Kumar, P. & Granot, J. 2003, *ApJ*, 591, 1075



- Kumar, P. & Panaitescu, A. 2000, *ApJ*, 541, L51
- Kumar, P. & Panaitescu, A. 2003, *MNRAS*, 346, 905
- Kumar, P. & Zhang, B. 2015, *Phys. Rep.*, 561, 1
- Lamb, D. Q. & Reichart, D. E. 2000, *ApJ*, 536, 1
- Lan, M.-X., Wu, X.-F., & Dai, Z.-G. 2016, *ApJ*, 816, 73
- Laskar, T., Alexander, K. D., Berger, E., et al. 2016, *ApJ*, 833, 88
- Laskar, T., Alexander, K. D., Berger, E., et al. 2018a, *ApJ*, 862, 94
- Laskar, T., Berger, E., Margutti, R., et al. 2015, *ApJ*, 814, 1
- Laskar, T., Berger, E., Margutti, R., et al. 2018b, *ApJ*, 859, 134
- Laskar, T., Berger, E., Tanvir, N., et al. 2014, *ApJ*, 781, 1
- Laskar, T., Berger, E., Zauderer, B. A., et al. 2013, *ApJ*, 776, 119
- Laskar, T., van Eerten, H., Schady, P., et al. 2019, *ApJ*, 884, 121
- Lasky, P. D., Haskell, B., Ravi, V., Howell, E. J., & Coward, D. M. 2014, *Phys. Rev. D*, 89, 047302
- Lazzati, D. 2005, *MNRAS*, 357, 722
- Lazzati, D., Rossi, E., Ghisellini, G., & Rees, M. J. 2004, *MNRAS*, 347, L1
- Leibler, C. N. & Berger, E. 2010, *ApJ*, 725, 1202
- Levan, A. J., Tanvir, N. R., Starling, R. L. C., et al. 2014, *ApJ*, 781, 13
- Leventis, K., van Eerten, H. J., Meliani, Z., & Wijers, R. A. M. J. 2012, *MNRAS*, 427, 1329
- Levesque, E. M., Bloom, J. S., Butler, N. R., et al. 2010, *MNRAS*, 401, 963
- Li, A., Liang, S. L., Kann, D. A., et al. 2008, *ApJ*, 685, 1046
- Li, L., Liang, E.-W., Tang, Q.-W., et al. 2012, *ApJ*, 758, 27
- Li, T.-P. 2007, *Nuclear Physics B Proceedings Supplements*, 166, 131
- Li, Z.-Y. & Chevalier, R. A. 1999, *ApJ*, 526, 716
- Liang, E., Zhang, B., Virgili, F., & Dai, Z. G. 2007, *ApJ*, 662, 1111
- Liang, E.-W., Lü, H.-J., Hou, S.-J., Zhang, B.-B., & Zhang, B. 2009, *ApJ*, 707, 328
- Liang, E. W., Zhang, B., O'Brien, P. T., et al. 2006, *ApJ*, 646, 351
- Lipkin, Y. M., Ofek, E. O., Gal-Yam, A., et al. 2004, *ApJ*, 606, 381
- Livio, M. & Waxman, E. 2000, *ApJ*, 538, 187
- Loeb, A. & Perna, R. 1998, *ApJ*, 495, 597

- Lü, H.-J. & Zhang, B. 2014, *ApJ*, 785, 74
- Lü, H.-J., Zhang, B., Lei, W.-H., Li, Y., & Lasky, P. D. 2015, *ApJ*, 805, 89
- Lü, H.-J., Zhang, B., Liang, E.-W., Zhang, B.-B., & Sakamoto, T. 2014, *MNRAS*, 442, 1922
- Lyutikov, M. & Camilo Jaramillo, J. 2017, *ApJ*, 835, 206
- Lyutikov, M., Pariev, V. I., & Blandford, R. D. 2003, *ApJ*, 597, 998
- MacFadyen, A. I., Ramirez-Ruiz, E., & Zhang, W. 2005, arXiv e-prints, astro
- MacFadyen, A. I. & Woosley, S. E. 1999, *ApJ*, 524, 262
- Madau, P. 1995, *ApJ*, 441, 18
- MAGIC Collaboration, Acciari, V. A., Ansoldi, S., et al. 2019a, *Nature*, 575, 455
- MAGIC Collaboration, Acciari, V. A., Ansoldi, S., et al. 2019b, *Nature*, 575, 459
- Malesani, D., D’Elia, V., D’Avanzo, P., et al. 2016, *GRB Coordinates Network*, 18965, 1
- Maoz, D., Mannucci, F., & Nelemans, G. 2014, *ARA&A*, 52, 107
- Marcote, B., Nimmo, K., Salafia, O. S., et al. 2019, *ApJ*, 876, L14
- Margutti, R., Bernardini, G., Barniol Duran, R., et al. 2011a, *MNRAS*, 410, 1064
- Margutti, R., Chincarini, G., Granot, J., et al. 2011b, *MNRAS*, 417, 2144
- Margutti, R., Genet, F., Granot, J., et al. 2010, *MNRAS*, 402, 46
- Margutti, R., Zaninoni, E., Bernardini, M. G., et al. 2013, *MNRAS*, 428, 729
- Markwardt, C. B., Barthelmy, S. D., Baumgartner, W. H., et al. 2012, *GRB Coordinates Network*, 13333, 1
- Marongiu, M., Guidorzi, C., Margutti, R., et al. 2019, *ApJ*, 879, 9
- Marshall, F. E., Antonelli, L. A., Burrows, D. N., et al. 2011, *ApJ*, 727, 132
- Martone, R., Izzo, L., Della Valle, M., et al. 2017, *A&A*, 608, A52
- Mazaeva, E., Pozanenko, A., & Minaev, P. 2018, *International Journal of Modern Physics D*, 27, 1844012
- Mazaeva, E., Reva, I., Volnova, A., Kusakin, A., & Pozanenko, A. 2016, *GRB Coordinates Network*, 19004, 1
- Mazzali, P. A., Deng, J., Maeda, K., et al. 2002, *ApJ*, 572, L61
- McConnell, M. L. 2017, *New A Rev.*, 76, 1
- McGlynn, S., Clark, D. J., Dean, A. J., et al. 2007, *A&A*, 466, 895
- McMullin, J. P., Waters, B., Schiebel, D., Young, W., & Golap, K. 2007, in *Astronomical Society of the Pacific Conference Series*, Vol. 376, *Astronomical Data Analysis Software and Systems XVI*, ed. R. A. Shaw, F. Hill, & D. J. Bell, 127

- Medvedev, M. V. & Loeb, A. 1999, *ApJ*, 526, 697
- Meegan, C., Lichti, G., Bhat, P. N., et al. 2009, *ApJ*, 702, 791
- Meegan, C. A., Fishman, G. J., Wilson, R. B., et al. 1992, *Nature*, 355, 143
- Melandri, A., Kobayashi, S., Mundell, C. G., et al. 2010, *ApJ*, 723, 1331
- Melandri, A., Mundell, C. G., Kobayashi, S., et al. 2008, *ApJ*, 686, 1209
- Mészáros, P. 2006, *Reports on Progress in Physics*, 69, 2259
- Meszáros, P. & Rees, M. J. 1993, *ApJ*, 405, 278
- Meszáros, P. & Rees, M. J. 1997, *ApJ*, 476, 232
- Mészáros, P. & Rees, M. J. 1999, *MNRAS*, 306, L39
- Mészáros, P. & Rees, M. J. 2001, *ApJ*, 556, L37
- Meszáros, P. & Rees, M. J. 2014, arXiv e-prints, arXiv:1401.3012
- Metzger, B. D., Giannios, D., Thompson, T. A., Bucciantini, N., & Quataert, E. 2011, *MNRAS*, 413, 2031
- Metzger, B. D. & Piro, A. L. 2014, *MNRAS*, 439, 3916
- Metzger, B. D., Quataert, E., & Thompson, T. A. 2008, *MNRAS*, 385, 1455
- Metzger, M. R., Djorgovski, S. G., Kulkarni, S. R., et al. 1997, *Nature*, 387, 878
- Misra, K., Bhattacharya, D., Sahu, D. K., et al. 2007, *A&A*, 464, 903
- Misra, K., Resmi, L., Kann, D. A., et al. 2019, arXiv e-prints, arXiv:1911.09719
- Modjaz, M., Liu, Y. Q., Bianco, F. B., & Graur, O. 2016, *ApJ*, 832, 108
- Molinari, E., Vergani, S. D., Malesani, D., et al. 2007, *A&A*, 469, L13
- Mooley, K. P., Deller, A. T., Gottlieb, O., et al. 2018, *Nature*, 561, 355
- Morrison, R. & McCammon, D. 1983, *ApJ*, 270, 119
- Mundell, C. G., Kopac, D., Arnold, D. M., et al. 2013, *Nature*, 504, 119
- Mundell, C. G., Melandri, A., Guidorzi, C., et al. 2007a, *ApJ*, 660, 489
- Mundell, C. G., Steele, I. A., Smith, R. J., et al. 2007b, *Science*, 315, 1822
- Nakar, E., Ando, S., & Sari, R. 2009, *ApJ*, 703, 675
- Nakar, E. & Piran, T. 2005, *MNRAS*, 360, L73
- Nakar, E., Piran, T., & Granot, J. 2002, *ApJ*, 579, 699
- Nakar, E., Piran, T., & Waxman, E. 2003, *J. Cosmology Astropart. Phys.*, 2003, 005
- Nakar, E. & Sari, R. 2012, *ApJ*, 747, 88

- Narayan, R., Paczynski, B., & Piran, T. 1992, *ApJ*, 395, L83
- Nicholl, M., Williams, P. K. G., Berger, E., et al. 2017, *ApJ*, 843, 84
- Nishikawa, K. I., Niemić, J., Hardee, P. E., et al. 2009, *ApJ*, 698, L10
- Norris, J. P. & Bonnell, J. T. 2006, *ApJ*, 643, 266
- Norris, J. P., Gehrels, N., & Scargle, J. D. 2010, *ApJ*, 717, 411
- Norris, J. P., Marani, G. F., & Bonnell, J. T. 2000, *ApJ*, 534, 248
- Norris, J. P., Nemiroff, R. J., Bonnell, J. T., et al. 1996, *ApJ*, 459, 393
- Norris, J. P., Share, G. H., Messina, D. C., et al. 1986, *ApJ*, 301, 213
- Nousek, J. A., Kouveliotou, C., Grupe, D., et al. 2006, *ApJ*, 642, 389
- Paczynski, B. 1986, *ApJ*, 308, L43
- Paczynski, B. 1991, *Acta Astron.*, 41, 257
- Paczynski, B. 1992, *Acta Astronomica*, 42, 145
- Paczyński, B. 1998, *ApJ*, 494, L45
- Page, K. L. & Barthelmy, S. D. 2016, *GRB Coordinates Network*, 18951, 1
- Palmer, D. M., Barthelmy, S. D., Baumgartner, W. H., et al. 2009, *GRB Coordinates Network*, 9204, 1
- Palmerio, J. T., Vergani, S. D., Salvaterra, R., et al. 2019, *A&A*, 623, A26
- Panaitescu, A. & Kumar, P. 2000, *ApJ*, 543, 66
- Panaitescu, A. & Kumar, P. 2002, *ApJ*, 571, 779
- Panaitescu, A., Mészáros, P., Burrows, D., et al. 2006, *MNRAS*, 369, 2059
- Panaitescu, A., Meszaros, P., & Rees, M. J. 1998, *ApJ*, 503, 314
- Pei, Y. C. 1992, *ApJ*, 395, 130
- Peng, F., Königl, A., & Granot, J. 2005, *ApJ*, 626, 966
- Perley, D. A., Krühler, T., Schulze, S., et al. 2016, *ApJ*, 817, 7
- Pian, E., Amati, L., Antonelli, L. A., et al. 2000, *ApJ*, 536, 778
- Pian, E., Fruchter, A. S., Bergeron, L. E., et al. 1998, *The Astrophysical Journal*, 492, L103
- Pian, E., Mazzali, P. A., Masetti, N., et al. 2006, *Nature*, 442, 1011
- Pian, E., Tomasella, L., Cappellaro, E., et al. 2017, *MNRAS*, 466, 1848
- Piran, T. 1999, *Phys. Rep.*, 314, 575
- Piran, T. 2004, *Reviews of Modern Physics*, 76, 1143

- Planck Collaboration, Ade, P. A. R., Aghanim, N., et al. 2016, *A&A*, 594, A13
- Popham, R., Woosley, S. E., & Fryer, C. 1999, *ApJ*, 518, 356
- Porciani, C. & Madau, P. 2001, *ApJ*, 548, 522
- Qin, B., Wu, X.-P., Chu, M.-C., Fang, L.-Z., & Hu, J.-Y. 1998, *ApJ*, 494, L57
- Racusin, J. L., Karpov, S. V., Sokolowski, M., et al. 2008, *Nature*, 455, 183
- Ramirez-Ruiz, E. & Lloyd-Ronning, N. M. 2002, *New A*, 7, 197
- Rees, M. J. & Meszaros, P. 1992, *MNRAS*, 258, 41P
- Rees, M. J. & Meszaros, P. 1994, *ApJ*, 430, L93
- Rees, M. J. & Meszaros, P. 1998, *ApJ*, 496, L1
- Reichart, D. E. 1997, *ApJ*, 485, L57
- Reichart, D. E., Lamb, D. Q., Fenimore, E. E., et al. 2001, *ApJ*, 552, 57
- Resmi, L. 2017, *Journal of Astrophysics and Astronomy*, 38, 56
- Ressler, S. M. & Laskar, T. 2017, *ApJ*, 845, 150
- Rhoads, J. E. 1999, *ApJ*, 525, 737
- Rickett, B. J. 1990, *ARA&A*, 28, 561
- Ripa, J. & Meszaros, A. 2015, arXiv e-prints, arXiv:1507.05761
- Robertson, B. E. & Ellis, R. S. 2012, *ApJ*, 744, 95
- Rol, E., Wijers, R. A. M. J., Kouveliotou, C., Kaper, L., & Kaneko, Y. 2005, *ApJ*, 624, 868
- Roming, P. W. A., Kennedy, T. E., Mason, K. O., et al. 2005, *Space Sci. Rev.*, 120, 95
- Ronchi, M., Fumagalli, F., Ravasio, M. E., et al. 2019, arXiv e-prints, arXiv:1909.10531
- Rossi, E. M., Lazzati, D., Salmonson, J. D., & Ghisellini, G. 2004, *MNRAS*, 354, 86
- Rowlinson, A., O'Brien, P. T., Tanvir, N. R., et al. 2010, *MNRAS*, 409, 531
- Ruderman, M. 1975, in *Seventh Texas Symposium on Relativistic Astrophysics*, ed. P. G. Bergman, E. J. Fenyves, & L. Motz, Vol. 262, 164–180
- Rutledge, R. E. & Fox, D. B. 2004, *MNRAS*, 350, 1288
- Ryan, G., van Eerten, H., MacFadyen, A., & Zhang, B.-B. 2015, *ApJ*, 799, 3
- Rybicki, G. B. & Lightman, A. P. 1979, *Radiative processes in astrophysics*
- Salvaterra, R., Campana, S., Vergani, S. D., et al. 2012, *ApJ*, 749, 68
- Salvaterra, R., Della Valle, M., Campana, S., et al. 2009, *Nature*, 461, 1258
- Salvaterra, R., Maio, U., Ciardi, B., & Campisi, M. A. 2013, *MNRAS*, 429, 2718

- Santana, R., Barniol Duran, R., & Kumar, P. 2014, *ApJ*, 785, 29
- Sari, R. 2006, in *American Institute of Physics Conference Series*, Vol. 856, *Relativistic Jets: The Common Physics of AGN, Microquasars, and Gamma-Ray Bursts*, ed. P. A. Hughes & J. N. Bregman, 33–56
- Sari, R. & Esin, A. A. 2001, *ApJ*, 548, 787
- Sari, R. & Mészáros, P. 2000, *ApJ*, 535, L33
- Sari, R. & Piran, T. 1999, *ApJ*, 520, 641
- Sari, R., Piran, T., & Halpern, J. P. 1999, *ApJ*, 519, L17
- Sari, R., Piran, T., & Narayan, R. 1998, *ApJ*, 497, L17
- Schlafly, E. F. & Finkbeiner, D. P. 2011, *ApJ*, 737, 103
- Shaviv, N. J. & Dar, A. 1995, *ApJ*, 447, 863
- Shemi, A. & Piran, T. 1990, *ApJ*, 365, L55
- Sironi, L. & Goodman, J. 2007, *ApJ*, 671, 1858
- Sironi, L., Spitkovsky, A., & Arons, J. 2013, *ApJ*, 771, 54
- Smith, N. 2014, *ARA&A*, 52, 487
- Soderberg, A. M., Kulkarni, S. R., Nakar, E., et al. 2006a, *Nature*, 442, 1014
- Soderberg, A. M., Nakar, E., Berger, E., & Kulkarni, S. R. 2006b, *ApJ*, 638, 930
- Steele, I. A., Bates, S. D., Carter, D., et al. 2006, in *Proc. SPIE*, Vol. 6269, 62695M
- Steele, I. A., Kopač, D., Arnold, D. M., et al. 2017, *ApJ*, 843, 143
- Steele, I. A., Mundell, C. G., Smith, R. J., Kobayashi, S., & Guidorzi, C. 2009, *Nature*, 462, 767
- Stratta, G., Ciolfi, R., Amati, L., et al. 2018a, *Advances in Space Research*, 62, 662
- Stratta, G., Dainotti, M. G., Dall’Osso, S., Hernandez, X., & De Cesare, G. 2018b, *ApJ*, 869, 155
- Stratta, G., Gallerani, S., & Maiolino, R. 2011, *A&A*, 532, A45
- STScI development Team. 2018, *synphot: Synthetic photometry using Astropy*
- Tagliaferri, G., Antonelli, L. A., Chincarini, G., et al. 2005, *A&A*, 443, L1
- Tanvir, N. R., Fox, D. B., Levan, A. J., et al. 2009, *Nature*, 461, 1254
- Taylor, G. B., Frail, D. A., Berger, E., & Kulkarni, S. R. 2004, *ApJ*, 609, L1
- Totani, T. & Panaitescu, A. 2002, *ApJ*, 576, 120
- Troja, E., Lipunov, V. M., Mundell, C. G., et al. 2017, *Nature*, 547, 425
- Tsvetkova, A., Golenetskii, S., Aptekar, R., et al. 2016, *GRB Coordinates Network*, 18974, 1

- Uehara, T., Toma, K., Kawabata, K. S., et al. 2012, *ApJ*, 752, L6
- Uhm, Z. L. & Zhang, B. 2014, *ApJ*, 789, 39
- Uhm, Z. L., Zhang, B., Hascoët, R., et al. 2012, *ApJ*, 761, 147
- Usov, V. V. 1992, *Nature*, 357, 472
- van der Horst, A. J., Kamble, A., Resmi, L., et al. 2008, *A&A*, 480, 35
- van Eerten, H. 2014, *MNRAS*, 442, 3495
- van Eerten, H. J. 2015, *Journal of High Energy Astrophysics*, 7, 23
- van Eerten, H. J., Leventis, K., Meliani, Z., Wijers, R. A. M. J., & Keppens, R. 2010, *MNRAS*, 403, 300
- van Eerten, H. J. & MacFadyen, A. I. 2011, *ApJ*, 733, L37
- van Eerten, H. J. & MacFadyen, A. I. 2012, *ApJL*, 747, L30
- van Haarlem, M. P., Wise, M. W., Gunst, A. W., et al. 2013, *A&A*, 556, A2
- van Paradijs, J., Groot, P. J., Galama, T., et al. 1997, *Nature*, 386, 686
- Vanderspek, R., Sakamoto, T., Barraud, C., et al. 2004, *ApJ*, 617, 1251
- Virgili, F. J., Liang, E.-W., & Zhang, B. 2009, *MNRAS*, 392, 91
- Virgili, F. J., Mundell, C. G., Pal'shin, V., et al. 2013, *ApJ*, 778, 54
- Walker, M. A. 1998, *MNRAS*, 294, 307
- Walker, M. A. 2001, *MNRAS*, 321, 176
- Wang, F. Y., Dai, Z. G., Yi, S. X., & Xi, S. Q. 2015, *ApJS*, 216, 8
- Wang, X.-G., Zhang, B., Liang, E.-W., et al. 2018, *ApJ*, 859, 160
- Wang, X.-Y., He, H.-N., Li, Z., Wu, X.-F., & Dai, Z.-G. 2010, *ApJ*, 712, 1232
- Waxman, E. 1997, *ApJ*, 491, L19
- Waxman, E. 2003, *Nature*, 423, 388
- Wheeler, J. C., Yi, I., Höflich, P., & Wang, L. 2000, *ApJ*, 537, 810
- Wigger, C., Hajdas, W., Arzner, K., Güdel, M., & Zehnder, A. 2004, *ApJ*, 613, 1088
- Wijers, R. A. M. J., Rees, M. J., & Meszaros, P. 1997, *Monthly Notices of the Royal Astronomical Society*, 288, L51
- Willis, D. R., Barlow, E. J., Bird, A. J., et al. 2005, *A&A*, 439, 245
- Wosley, S. E. 1993, *ApJ*, 405, 273
- Wosley, S. E. & Heger, A. 2015, in *Astrophysics and Space Science Library*, Vol. 412, *Very Massive Stars in the Local Universe*, ed. J. S. Vink, 199



- Wu, X. F., Dai, Z. G., Huang, Y. F., & Lu, T. 2005, *MNRAS*, 357, 1197
- Wu, Y., Ren, D., & You, Z. 2002, in 34th COSPAR Scientific Assembly, Vol. 34, 16
- Wu, Y. P., Ren, D. H., & You, Z. 2004, *Advances in Space Research*, 34, 2667
- Yamazaki, R., Yonetoku, D., & Nakamura, T. 2003, *ApJ*, 594, L79
- Yonetoku, D., Murakami, T., Gunji, S., et al. 2012, *ApJ*, 758, L1
- Yonetoku, D., Murakami, T., Gunji, S., et al. 2011, *ApJ*, 743, L30
- Yonetoku, D., Murakami, T., Nakamura, T., et al. 2004, *ApJ*, 609, 935
- Yu, Y.-W., Zhang, B., & Gao, H. 2013, *ApJ*, 776, L40
- Zaninoni, E., Bernardini, M. G., Margutti, R., Oates, S., & Chincarini, G. 2013, *A&A*, 557, A12
- Zhang, B. 2011, *Comptes Rendus Physique*, 12, 206
- Zhang, B. 2019, *The Physics of Gamma-Ray Bursts* (Cambridge University Press)
- Zhang, B., Dai, X., Lloyd-Ronning, N. M., & Mészáros, P. 2004, *ApJ*, 601, L119
- Zhang, B., Fan, Y. Z., Dyks, J., et al. 2006, *ApJ*, 642, 354
- Zhang, B. & Kobayashi, S. 2005, *ApJ*, 628, 315
- Zhang, B., Kobayashi, S., & Mészáros, P. 2003, *ApJ*, 595, 950
- Zhang, B., Liang, E., Page, K. L., et al. 2007, *ApJ*, 655, 989
- Zhang, B. & Mészáros, P. 2001, *ApJ*, 552, L35
- Zhang, B. & Mészáros, P. 2002, *ApJ*, 571, 876
- Zhang, B., Zhang, B.-B., Virgili, F. J., et al. 2009, *ApJ*, 703, 1696
- Zhang, B.-B., van Eerten, H., Burrows, D. N., et al. 2015a, *ApJ*, 806, 15
- Zhang, B.-B., Zhang, B., & Castro-Tirado, A. J. 2016, *ApJ*, 820, L32
- Zhang, B.-B., Zhang, B., Murase, K., Connaughton, V., & Briggs, M. S. 2014, *ApJ*, 787, 66
- Zhang, F.-W., Shao, L., Yan, J.-Z., & Wei, D.-M. 2012, *ApJ*, 750, 88
- Zhang, S., Jin, Z.-P., & Wei, D.-M. 2015b, *ApJ*, 798, 3
- Zhang, S.-N., Kole, M., Bao, T.-W., et al. 2019, *Nature Astronomy*, 3, 258
- Zhang, W. & MacFadyen, A. 2009, *ApJ*, 698, 1261
- Zonca, A., Cecchi-Pestellini, C., Mulas, G., Casu, S., & Aresu, G. 2016, *ApJ*, 829, 22



## **Appendix A**

# **Constraints on the Environment and Energetics of the Broad-line Ic SN 2014ad from Deep Radio and X-Ray Observations**



## Constraints on the Environment and Energetics of the Broad-line Ic SN2014ad from Deep Radio and X-Ray Observations

M. Marongiu<sup>1,2</sup>, C. Guidorzi<sup>1</sup>, R. Margutti<sup>3</sup>, D. L. Coppejans<sup>3</sup>, R. Martone<sup>1,2</sup>, and A. Kamble<sup>4</sup>

<sup>1</sup>Department of Physics and Earth Science, University of Ferrara, via Saragat 1, I-44122, Ferrara, Italy

<sup>2</sup>ICRANet, Piazzale della Repubblica 10, I-65122, Pescara, Italy

<sup>3</sup>Center for Interdisciplinary Exploration and Research in Astrophysics (CIERA) and Department of Physics and Astronomy, Northwestern University, Evanston, IL 60208, USA

<sup>4</sup>Formerly at Harvard-Smithsonian Center for Astrophysics, 60 Garden St., Cambridge, MA 02138, USA

Received 2019 April 16; revised 2019 May 27; accepted 2019 May 29; published 2019 July 10

### Abstract

Broad-line type Ic Supernovae (BL-Ic SNe) are characterized by high ejecta velocity ( $\gtrsim 10^4$  km s<sup>-1</sup>) and are sometimes associated with the relativistic jets typical of long duration ( $\gtrsim 2$  s) Gamma-Ray Bursts. The reason why a small fraction of BL-Ic SNe harbor relativistic jets is not known. Here we present deep X-ray and radio observations of the BL-Ic SN 2014ad extending from 13 to 930 days post explosion. SN 2014ad was not detected at either frequency and has no observational evidence of a GRB counterpart. The proximity of SN 2014ad ( $d \sim 26$  Mpc) enables very deep constraints on the progenitor mass-loss rate  $\dot{M}$  and on the total energy of the fast ejecta  $E$ . We consider two synchrotron emission scenarios for a wind-like circumstellar medium (CSM): (i) uncollimated nonrelativistic ejecta, and (ii) off-axis relativistic jet. Within the first scenario our observations are consistent with GRB-less BL-Ic SNe characterized by a modest energy budget of their fast ejecta ( $E \lesssim 10^{45}$  erg), like SNe 2002ap and 2010ay. For jetted explosions, we cannot rule out a GRB with  $E \lesssim 10^{51}$  erg (beam-corrected) with a narrow opening angle ( $\theta_j \sim 5^\circ$ ) observed moderately off-axis ( $\theta_{\text{obs}} \gtrsim 30^\circ$ ) and expanding in a very low CSM density ( $\dot{M} \lesssim 10^{-6} M_\odot \text{yr}^{-1}$ ). Our study shows that off-axis low-energy jets expanding in a low-density medium cannot be ruled out even in the most nearby BL-Ic SNe with extensive deep observations, and might be a common feature of BL-Ic SNe.

*Key words:* gamma-ray burst: general – supernovae: general – supernovae: individual (2014ad) – techniques: interferometric

### 1. Introduction

Ic SNe are hydrogen-stripped core-collapse explosions (CCSNe) of massive stars with  $M_{\text{ZAMS}} \gtrsim 8 M_\odot$  that show no evidence for hydrogen and helium in their spectra (Filippenko 1997). Potential candidates for Ic SN progenitors are massive Wolf–Rayet (WR) stars and stars in close binary systems (Ensmann & Woosley 1988; Gal-Yam 2017). At the time of writing the exact nature of their progenitors is unclear (Podsiadlowski et al. 1992; Smartt 2009, 2015; Yoon 2010; Eldridge et al. 2013; Dessart 2015; Dessart et al. 2015, 2017). Notable in this respect is the recent detection of the progenitor system of the Ic SN 2017ein (Kilpatrick et al. 2018; Van Dyk et al. 2018), which pointed to a massive stellar progenitor with  $M \sim 60 M_\odot$  in a binary system.

Ic SNe typically show a bell-shaped radio spectrum powered by synchrotron emission and extending all the way to the X-ray band. The spectral peak frequency describes the transition between the optically thick part of the spectrum—below which synchrotron self-absorption (SSA) takes place—and the optically thin portion of the spectrum (Rybicki & Lightman 1979; Chevalier 1998; Chevalier & Fransson 2006). The synchrotron emission is produced by electrons that are accelerated at the shock front between the SN ejecta and the circumstellar medium (CSM). As the shock wave expands, the optical depth to SSA decreases and hence the spectral peak frequency cascades down to lower frequencies with time. In an SN explosion, the X-ray and radio emission resulting from the SN shock propagation in the medium track the fastest material ejected by the explosion, while the optical emission is of thermal origin and originates from the inner ejecta layers.

A small fraction ( $\sim 4\%$ ; Shivvers et al. 2017) of Ic SNe, called broad-line Ic SNe (BL-Ic SNe), are characterized by broad lines in the optical spectrum implying large expansion velocities of the ejecta ( $\gtrsim 2 \times 10^4$  km s<sup>-1</sup>, e.g., Mazzali et al. 2002; Cano et al. 2017),  $\sim 10^4$  km s<sup>-1</sup> faster than in “ordinary” Ic SNe (Modjaz et al. 2016). Some BL-Ic SNe are associated with ultra-relativistic jets that generate long duration ( $\gtrsim 2$  s) Gamma-Ray Bursts (L-GRBs, e.g., Cano et al. 2017), which are observable at cosmological distances up to  $z \sim 10$  (e.g., Cucchiara et al. 2011). In the local universe ( $z \leq 0.1$ ) some BL-Ic SNe have also been found in association with mildly relativistic outflows in low-luminosity GRBs (II-GRBs, which are too weak to be detected at larger distances, Liang et al. 2007). As opposed to L-GRBs, II-GRBs show no evidence for collimation of their fastest ejecta, i.e., no jet (Kulkarni et al. 1998; Soderberg et al. 2006b; Bromberg et al. 2011).

A possible interpretation of the observational lack of evidence for L-GRB counterparts in the majority of BL-Ic SNe is the off-axis jet scenario (Eichler & Levinson 1999; Rhoads 1999; Yamazaki et al. 2003; Piran 2004; Soderberg et al. 2006a; Bietenholz 2014; Corsi et al. 2016), where the explosion powers a GRB-like jet that is misaligned with respect to the observer line of sight. In this scenario, as the jet velocity gradually decreases and relativistic beaming becomes less severe, the emission becomes observable from increasingly larger viewing angles. Deep radio and X-ray observations extending to hundreds of days post explosion offer the opportunity to reveal the emission from off-axis jets as well as to recover weak GRBs that would not trigger current  $\gamma$ -ray observing facilities.

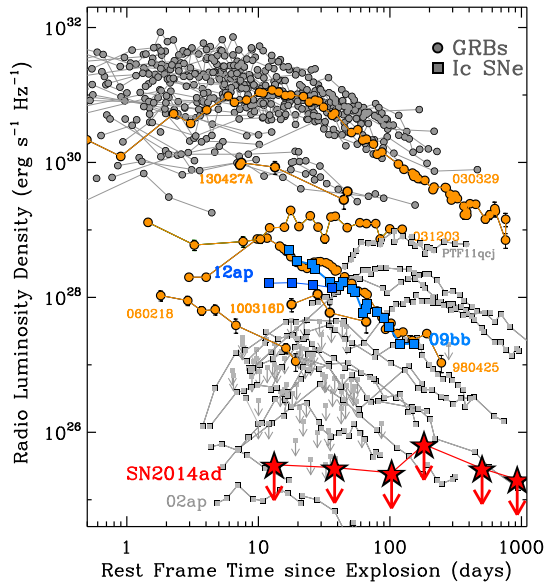


**Figure 1.** Deep radio limits on the emission from SN 2014ad (red stars) in the context of L-GRBs (circles; gray is for cosmological GRBs, while orange is for GRBs at  $z \leq 0.3$ ) and H-stripped CCSNe (squares; gray is for normal SNe, blue is for SNe with relativistic ejecta). Our deep radio limits on the emission from the BL-Ic SN 2014ad are consistent with a luminosity comparable to that of SN 2002ap. The detected radio emission from SN 2002ap points to a nonrelativistic (shock velocity  $\sim 0.3c$ ) uncollimated explosion with a small energy budget of the fast ejecta ( $E \sim 1.5 \times 10^{51}$  erg; Berger et al. 2002).

Here we present extensive ( $\delta t \sim 10$ –1000 days) broadband (radio to X-ray) observations of SN 2014ad, a BL-Ic SN that exploded in the galaxy PGC 37625 (Mrk 1309) at  $d = 26.44$  Mpc (Sahu et al. 2018). SN 2014ad is among the closest BL-Ic SNe discovered to date, which enables very deep limits on its radio and X-ray emission (Figure 1 and Table 1). We present constraints on the progenitor mass-loss rate  $\dot{M}$  and the total energy of the fast ejecta  $E$  in two scenarios: (i) mildly relativistic, nearly isotropic, synchrotron self-absorbed radio emission due to the SN ejecta plowing through a wind-like CSM; (ii) synchrotron emission from a relativistic off-axis GRB-like jet.

The analysis of the optical emission from SN 2014ad by Sahu et al. (2018) and Stevance et al. (2017) revealed that the bulk of its ejecta velocity is  $\sim 3 \times 10^4$  km s $^{-1}$  at early times, with kinetic energy  $E_k \sim (1.0 \pm 0.3) \times 10^{52}$  erg, larger than in SNe-Ic, and similar to BL-Ic SNe and GRB-SNe. The metallicity of the host galaxy of SN 2014ad is  $\sim 0.5 Z_{\odot}$ . The total explosion ejecta mass inferred by Sahu et al. (2018) and Stevance et al. (2017) is  $M_{\text{ej}} \sim (3.3 \pm 0.8) M_{\odot}$  suggesting a massive progenitor star with  $M_{\text{ZAMS}} \gtrsim 20 M_{\odot}$ . Spectropolarimetry by Stevance et al. (2017) also suggests a mild deviation from a spherical geometry of the ejecta.

This paper is organized as follows. In Section 2 we describe our radio and X-ray observations; in Section 3 we present the constraints on the environment derived from our X-ray limits, whereas in Section 4 we present environment constraints derived from the radio and X-ray broadband modeling in two different scenarios (i.e., an “ordinary” isotropic SN outflow,

and a beamed relativistic jet). Our results and analysis are discussed in Section 5 and conclusions are drawn in Section 6.

## 2. Observations

SN 2014ad was discovered by Howerton et al. (2014) on 2014 March 12.4 (MJD 56,728.4) in public images from the Catalina Real-Time Transient Survey (Djorgovski et al. 2011) at  $\alpha = 11^{\text{h}}57^{\text{m}}44^{\text{s}}.44$ ,  $\delta = -10^{\circ}10'15''.7$ . Throughout this paper we assume an SN explosion date  $t_0 = 56725 \pm 3$  MJD (Sahu et al. 2018); times given are in reference to this explosion date unless otherwise noted.

### 2.1. Radio Observations with the Karl G. Jansky Very Large Array

Very Large Array (VLA) follow-up observations were carried out between 2014 March 22 (MJD 56,738) and 2016 September 23 (MJD 57,654), from  $\sim 13$  to  $\sim 930$  days post explosion, under Proposal VLA/14A-531 (PI: Kamble). Data were taken in eight spectral windows at L-band (with baseband central frequencies of 1.3 and 1.7 GHz, respectively), C-band (5 and 7 GHz), X-band (8.5 and 11 GHz), Ku-band (13.5 and 16 GHz), with a nominal bandwidth of  $\sim 1$  GHz ( $\sim 0.4$  GHz for L-band). 3C286 and J1330-1449 were used as flux/bandpass and phase/amplitude calibrators, respectively. The Common Astronomy Software Application (CASA, v. 4.7.2, McMullin et al. 2007)<sup>5</sup> was used to calibrate, flag, and image the data. Images were formed from the visibility data using the CLEAN algorithm (Högbom 1974). The image size was set to  $(1024 \times 1024)$  pixels, the pixel size was determined as one-fifth of the nominal beam width and the images were cleaned using natural weighting. The upper limits on the flux densities were calculated at a  $3\sigma$  confidence level (Table 1).

### 2.2. X-Ray Observations with Swift-XRT

The X-Ray Telescope (XRT; Burrows et al. 2005) on board the *Swift* spacecraft (Gehrels et al. 2004) observed the region of SN 2014ad in Photon Counting (PC) mode several times from 2014 March 19 to 2017 March 11. We find no evidence for statistically significant X-ray emission at the location of SN 2014ad. We extracted the 0.3–10 keV light curve, consisting of  $3\sigma$  upper limits, using the web interface provided by Leicester University,<sup>6</sup> which used HEASOFT (v. 6.22). We performed flux calibration by assuming an absorbed simple power-law spectral model (WABS\*POWERLAW within XSPEC) with column density frozen to the Galactic value along the SN line of sight,  $N_{\text{H,Gal}} = 3.1 \times 10^{20}$  cm $^{-2}$  (Kalberla et al. 2005). We assumed a conservative value for the photon index,  $\Gamma = 2$ , and derived the upper limit to the flux density at 1 keV. Finally, we calculated three light curves with different integration times:  $10^5$ ,  $2 \times 10^5$ , and  $5 \times 10^5$  s, respectively. Table 2 reports the values for the longest timescale having the deepest limits. We also calculated the corresponding  $3\sigma$  upper limits on the 0.3–10 keV luminosity.

## 3. Constraints on the Environment Density from Inverse Compton Emission

Inverse Compton (IC) emission from the upscattering of optical photospheric photons into the X-ray band by relativistic

<sup>5</sup> <https://casa.nrao.edu/>

<sup>6</sup> [http://www.swift.ac.uk/user\\_objects/](http://www.swift.ac.uk/user_objects/)

**Table 1**  
Log of VLA Observations of SN 2014ad

$t_{\text{mid}}$ (MJD)	$t_e$ (days)	VLA Configuration	$\theta_{\text{FWHM}}$ (arcsec)	$\nu_c$ (GHz)	$\Delta\nu$ (GHz)	$\sigma_S$ ( $\mu\text{Jy}$ )	$S(3\sigma)$ ( $\mu\text{Jy}$ )	$L_{25}$ ( $\text{erg s}^{-1} \text{Hz}^{-1}$ )
56738.19	13.19	A	1.42	1.26	0.384	28.8	86.4	12.1
		A	0.93	1.80	0.384	30.8	92.4	12.9
		A	0.34	5.0	0.896	9.0	27.0	3.8
		A	0.24	7.1	0.896	8.1	24.3	3.4
		A	0.19	8.6	0.896	7.9	20.7	3.3
		A	0.15	11.0	0.896	7.8	23.4	3.3
		A	0.13	13.5	0.896	7.7	23.1	3.2
		A	0.11	16.0	0.896	9.1	27.3	3.8
56763.21	38.21	A	1.42	1.26	0.384	31.6	94.8	13.2
		A	0.93	1.80	0.384	31.4	94.2	13.1
		A	0.34	5.0	0.896	10.5	31.5	4.4
		A	0.24	7.1	0.896	7.2	21.6	3.0
		A	0.19	8.6	0.896	8.0	24.0	3.4
		A	0.15	11.0	0.896	10.3	30.9	4.3
		A	0.13	13.5	0.896	7.3	21.9	3.1
		A	0.11	16.0	0.896	7.6	22.8	3.2
56828.96	103.96	AnD	12.02	5.0	0.896	6.9	20.7	2.9
		AnD	7.93	7.1	0.896	5.2	15.6	2.2
		AnD	0.20	8.6	0.896	6.0	18.0	2.5
		AnD	0.15	11.0	0.896	6.3	18.9	2.6
56906.76	181.76	D	12.02	5.0	0.896	13.9	41.7	5.8
		D	7.93	7.1	0.896	10.8	32.4	4.5
		D	6.98	8.6	0.896	15.7	47.1	6.6
		D	5.46	11.0	0.896	16.8	50.4	7.0
57227.81	502.81	A	0.34	5.0	0.896	9.9	26.7	4.1
		A	0.24	7.1	0.896	9.4	27.7	3.9
		A	0.19	8.6	0.896	6.9	20.7	2.9
		A	0.15	11.0	0.896	10.1	30.3	4.2
57654.66	929.66	B	1.15	5.0	0.896	6.6	19.8	2.8
		B	0.79	7.1	0.896	6.3	18.9	2.6
		B	0.65	8.6	0.896	7.0	21.0	2.9
		B	0.51	11.0	0.896	6.8	20.4	2.8

**Note.** Observation central time  $t_{\text{mid}}$ , epoch  $t_e = t_{\text{mid}} - t_0$  since the estimated explosion date  $t_0$ , VLA array configuration, beam size  $\theta_{\text{FWHM}}$ , central frequency  $\nu_c$  and its bandwidth  $\Delta\nu$ , the uncertainty  $\sigma_S$ , the upper limit on the flux density  $S$  (at  $3\sigma$ ), and the relative luminosity  $L_{25}$  (in units of  $10^{25} \text{ erg s}^{-1} \text{ Hz}^{-1}$ ) of the source. In no case was the source detected with  $\geq 3\sigma$  confidence.

**Table 2**  
*Swift*-XRT  $3\sigma$  Upper Limits on the Flux Density at 1 keV ( $F_{\nu}$ , 1 keV) and 0.3–10 keV Luminosity ( $L_{0.3-10}$ )

$t_{\text{mid}}$ (MJD)	$t_e$ (days)	$\Delta t$ (days)	$F_{\nu}$ , 1 keV ( $\mu\text{Jy}$ )	$L_{0.3-10}$ ( $\text{erg s}^{-1}$ )
56738.1	13.1	5.8	$<1.3 \times 10^{-2}$	$<1.0 \times 10^{42}$
56743.9	18.9	5.8	$<1.2 \times 10^{-2}$	$<9.0 \times 10^{41}$
56749.6	24.6	5.8	$<1.7 \times 10^{-2}$	$<1.3 \times 10^{42}$
56755.4	30.4	5.8	$<4.1 \times 10^{-2}$	$<3.2 \times 10^{42}$
57774.0	1049.0	5.8	$<0.11$	$<8.5 \times 10^{42}$
57808.7	1083.7	5.8	$<1.1$	$<8.5 \times 10^{43}$
57820.2	1095.2	5.8	$<6.7 \times 10^{-2}$	$<5.2 \times 10^{42}$

**Note.**  $t_e = t_{\text{mid}} - t_0$  is the epoch since the estimated SN explosion date  $t_0$ ,  $\Delta t$  is the bin time.

electrons at the shock front has been demonstrated to dominate the X-ray emission from H-stripped CCSNe that explode in low-density environments ( $\dot{M} \lesssim 10^{-5} M_{\odot} \text{ yr}^{-1}$ ) at  $\delta t \lesssim 30$  days (e.g., Björnsson & Fransson 2004; Chevalier & Fransson 2006). We adopt the IC formalism by Margutti et al. (2012) modified to account for the outer density structure of progenitors of BL-Ic SNe (which are likely to be compact) as in Margutti et al. (2014). The IC emission depends on (i) the

density structure of the SN ejecta and of the CSM, (ii) the electron distribution responsible for the upscattering, (iii) explosion parameters (ejecta mass  $M_{\text{ej}}$  and kinetic energy  $E_k$ ), and (iv) the bolometric luminosity of the SN:  $L_{\text{IC}} \propto L_{\text{bol}}$ .

For compact progenitors that are relevant here, the density scales as  $\rho_{\text{SN}} \propto r^{-n}$  with  $n \sim 10$  (see, e.g., Matzner & McKee 1999; Chevalier & Fransson 2006). We further assume a power-law electron distribution  $n_e(\gamma) \propto \gamma^{-p}$  with  $p \sim 3$  as found in radio observations of type H-stripped CCSNe (Chevalier & Fransson 2006) and a fraction of energy into relativistic electrons  $\epsilon_e = 0.1$ . We use the explosion parameters  $E_k = (1 \pm 0.3) \times 10^{52} \text{ erg}$  and  $M_{\text{ej}} = (3.3 \pm 0.8) M_{\odot}$ . For a wind-like CSM structure  $\rho_{\text{CSM}} \propto r^{-2}$  with a typical wind velocity  $v_w = 1000 \text{ km s}^{-1}$  as appropriate for massive stars (and hence BL-Ic SN progenitors, e.g., Smith 2014), the *Swift*-XRT nondetections at  $\delta t < 30$  days yield  $\dot{M} < 5 \times 10^{-5} M_{\odot} \text{ yr}^{-1}$ .

#### 4. Broadband Modeling

We interpret our deep radio and X-ray limits in the context of synchrotron self-absorbed (SSA) emission from either

<sup>7</sup> This is the kinetic energy carried by the slowly moving material powering the optical emission.

(i) uncollimated (i.e., spherical) nonrelativistic ejecta (Section 4.1), or (ii) relativistic GRB-like jet (Section 4.2).

#### 4.1. SSA Emission from Nonrelativistic Uncollimated Ejecta

We follow Soderberg et al. (2005) and adopt their formalism in the context of the radio emission from nonrelativistic SN ejecta interacting with a wind-like CSM. The brightness temperature of a source is:

$$T_B = \frac{c^2}{2\pi k} \frac{f_\nu d^2}{(v_{\text{ph}} t)^2 \nu^2}, \quad (1)$$

where  $c$  is the speed of light,  $k$  is the Boltzmann constant,  $f_\nu$  is the flux density at observed frequency  $\nu$ ,  $d$  is the source distance,  $v_{\text{ph}}$  is the photospheric velocity and  $t$  is the observational epoch. For SN 2014ad we find  $T_B \lesssim 2.8 \times 10^{11}$  K at  $t \sim 13.2$  d, where  $v_{\text{ph}} \sim 3.2 \times 10^4$  km s $^{-1}$  and  $f_\nu < 86.4$   $\mu$ Jy at  $\nu = 1.26$  GHz (Table 1). Our inferred  $T_B$  does not violate the  $10^{12}$  K limit of the inverse Compton catastrophe (ICC; Kellermann & Pauliny-Toth 1981), consistent with the expectations from a nonrelativistic spherical SSA source.

In the SSA model radiation originates from an expanding spherical shell of shock-accelerated electrons with radius  $r$  and thickness  $r/\eta$  (here we assume the standard scenario of a thin shell with  $\eta = 10$ ; e.g., Li & Chevalier 1999; Soderberg et al. 2005). As the shock wave propagates through the CSM, it accelerates relativistic electrons into a power-law distribution  $N(\gamma) \propto \gamma^{-p}$  for  $\gamma \geq \gamma_m$ , where  $\gamma_m$  is the minimum Lorentz factor of the electrons (Chevalier 1982, 1998). In this analysis we assume  $p \sim 3$  as typically found in H-stripped core-collapse SNe (e.g., Chevalier & Fransson 2006). The post-shock energy fraction in the electrons and magnetic field is given by  $\epsilon_e$  and  $\epsilon_B$ , respectively; we further adopt equipartition of the post-shock energy density of the radio-emitting material between relativistic electrons and magnetic fields ( $\epsilon_e = \epsilon_B = 1/3$ ).

The synchrotron emission from SNe typically peaks at radio frequencies on timescales of a few days to weeks after the SN explosion (e.g., Corsi et al. 2014); this emission is suppressed at low frequencies by absorption processes. Chevalier (1998) showed that the dominant absorption process is internal SSA for H-stripped SNe, and external free-free absorption (FFA) in H-rich SNe, as H-rich SNe tend to explode in higher density media.

Following Soderberg et al. (2005), the temporal evolution of the magnetic field  $B(t)$ , minimum Lorentz factor  $\gamma_m(t)$ , shock radius  $r(t)$ , and the ratio  $\mathcal{J} = \epsilon_e/\epsilon_B$  can be parameterized as:

$$B = B_0 \left( \frac{t - t_e}{t_0 - t_e} \right)^{\alpha_B} \quad \gamma_m = \gamma_{m,0} \left( \frac{t - t_e}{t_0 - t_e} \right)^{\alpha_\gamma} \quad (2)$$

$$r = r_0 \left( \frac{t - t_e}{t_0 - t_e} \right)^{\alpha_r} \quad \mathcal{J} = \mathcal{J}_0 \left( \frac{t - t_e}{t_0 - t_e} \right)^{\alpha_{\mathcal{J}}}, \quad (3)$$

where  $r_0$ ,  $B_0$ ,  $\mathcal{J}_0$ , and  $\gamma_{m,0}$  are measured at an arbitrary reference epoch  $t_0$ , and  $t_e$  is the explosion time. In this paper we adopt  $t_0 = 13.2$  days (for which  $r_0 \sim v_{\text{ph}} \times t_0 = 4 \times 10^{15}$  cm) and  $t_e = 0$  days. The temporal indices  $\alpha_r$ ,  $\alpha_B$ ,  $\alpha_{\mathcal{J}}$ , and  $\alpha_\gamma$  are determined by the hydrodynamic evolution of the ejecta, as described in Soderberg et al. (2005). In particular,  $\alpha_r$  and  $\alpha_{\mathcal{J}}$

can be expressed as:

$$\alpha_r = \frac{n-3}{n-s}, \quad (4)$$

$$\alpha_{\mathcal{J}} = -s\alpha_r + \alpha_\gamma - 2\alpha_B, \quad (5)$$

where  $n$  and  $s$  describe the density profile of the outer SN ejecta ( $\rho_{\text{ej}} \propto r^{-n}$ ), and of the CSM ( $\rho_{\text{CSM}} \propto r^{-s}$ ),<sup>8</sup> respectively. The self-similar conditions  $s < 3$  and  $n > 5$  result in  $\sim 0.5 < \alpha_r < 1$  (Chevalier 1982). In this work we consider a wind-like CSM case (i.e.,  $s = 2$ ), and  $n = 10$  as appropriate for massive compact stars that are thought to be progenitors of H-stripped CCSNe. In the standard scenario (Chevalier 1996),  $\epsilon_e$  and  $\epsilon_B$  do not vary with time, from which we derive through Equation (3) that  $\alpha_{\mathcal{J}} = 0$ , implying that:

$$\alpha_B = \left( \frac{2-s}{2} \right) \alpha_r - 1, \quad (6)$$

$$\alpha_\gamma = 2(\alpha_r - 1). \quad (7)$$

Since  $\alpha_{\mathcal{J}} = 0$  and under the equipartition hypothesis ( $\mathcal{J} = 1$ ; Equation (3)), it follows that  $\alpha_r = 0.875$  (Equation (4)),  $\alpha_B = -1$  (Equation (6)) and  $\alpha_\gamma = -0.25$  (Equation (7)).

Under these assumptions and through Equation (2), the characteristic synchrotron frequency is:

$$\begin{aligned} \nu_m(t) &= \gamma_m^2 \frac{qB}{2\pi m_e c} = \gamma_{m,0}^2 \frac{qB_0}{2\pi m_e c} \left( \frac{t}{t_0} \right)^{2\alpha_\gamma + \alpha_B} \\ &= \nu_{m,0} \left( \frac{t}{t_0} \right)^{2\alpha_\gamma + \alpha_B}, \end{aligned} \quad (8)$$

where  $q$  is the electron charge and  $m_e$  is the electron mass. The frequency  $\nu_{m,0} \equiv \nu_m(t_0)$  depends on  $\gamma_{m,0}$  and  $B_0$  as follows:

$$\nu_{m,0} = \gamma_{m,0}^2 \frac{qB_0}{2\pi m_e c}. \quad (9)$$

The radio flux density at a given observing frequency  $\nu$  and epoch  $t$  is thus given by:

$$\begin{aligned} F(t, \nu) &= 10^{26} C_f \left( \frac{t}{t_0} \right)^{(4\alpha_r - \alpha_B)/2} (1 - e^{-\tau_\nu^\xi})^{1/\xi} \\ &\quad \times \nu^{5/2} F_3(x) F_2^{-1}(x) \text{ mJy} \end{aligned} \quad (10)$$

with the optical depth  $\tau_\nu$ :

$$\tau_\nu(t) = C_\tau \left( \frac{t}{t_0} \right)^{\alpha_r + (3+p/2)\alpha_B + (p-2)\alpha_\gamma + \alpha_{\mathcal{J}}} \nu^{-(p+4)/2} F_2(x). \quad (11)$$

$C_f$  and  $C_\tau$  are normalization constants (see Appendix A2 of Soderberg et al. 2005),  $F_2(x)$  and  $F_3(x)$  are Bessel functions with  $x = 2/3(\nu/\nu_m)$ ,  $\xi = [0, 1]$  describes the sharpness of the spectral break between optically thin and thick regimes. We adopt  $\xi = 1$ .

As we can see from Equations (10), (11), (4), and (8),  $F(t, \nu)$  depends on  $C_f$ ,  $C_\tau$ ,  $p$ ,  $n$ ,  $s$ ,  $\nu_{m,0}$ , and  $\xi$ . From Equations (6)–(8) of Soderberg et al. (2005)  $C_f$  and  $C_\tau$  can be expressed in terms of  $r_0$ ,  $B_0$ , and  $\eta$ ; thus, also using (9),  $F(t, \nu)$  can be expressed as a function of  $r_0$ ,  $B_0$ ,  $p$ ,  $n$ ,  $s$ ,  $\gamma_{m,0}$ ,  $\eta$ , and  $\xi$ , which are all fixed apart from  $B_0$  and  $\gamma_{m,0}$ . These two free parameters can be further

<sup>8</sup>  $s = 0$  corresponds to the case of ISM-like CSM and  $s = 2$  correspond to the case of wind-like CSM.



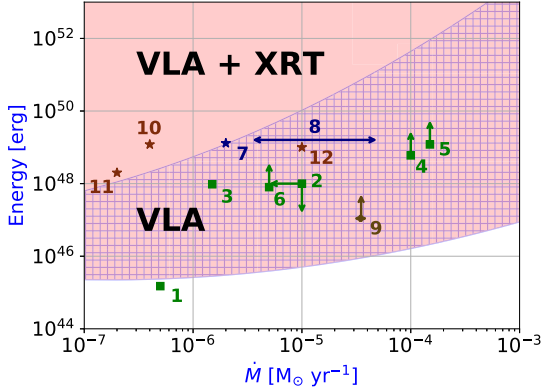


**Figure 2.** Regions of the total kinetic energy of the fast ejecta–mass-loss rate space excluded by VLA (hatched area) and VLA + XRT (red area) upper limits (see Table 1), as derived assuming the SSA model for a mildly relativistic, nearly isotropic explosion (Section 4.1). In addition, we show some peculiar BL-Ic SNe (in green) (1) SN 2002ap (Berger et al. 2002), (2) SN 2010ay (Sanders et al. 2012), (3) SN 2007bg (Salas et al. 2013), (4–6) PTF 11cmh–PTF 11qej–PTF 14dby (Corsi et al. 2016); the relativistic SNe (in blue) (7) SN 2009bb (Soderberg et al. 2010) and (8) SN 2012ap (Chakraborti et al. 2015); (9) SN 2016coi (brown; Terreran et al. 2019); the II-GRBs (in red) (10) SN 1998bw/GRB 980425 (Li & Chevalier 1999), (11) SN 2006aj/GRB 060218 (Soderberg et al. 2006b), and (12) SN 2010bh/GRB 100316D (Margutti et al. 2013).

expressed as a function of physically more useful quantities,<sup>9</sup> the SN progenitor mass-loss rate ( $\dot{M}$ ) and the total kinetic energy of the radio-bright (fast) ejecta ( $E$ ):

$$B_0 = \left( \frac{2\eta\epsilon_e}{3\gamma_0^3} \right)^{1/2} E^{1/2} \quad (12)$$

$$\gamma_{m,0} = \left( \frac{p-2}{p-1} \right) \frac{2m_p\epsilon_e v_w}{m_e c^2 r_0} \left( \frac{E}{\dot{M}} \right), \quad (13)$$

where  $m_p$  is the proton mass and  $v_w$  is the wind velocity. Consequently, we express  $\nu_{m,0}$  as a function of  $\dot{M}$  and  $E$  from (9):

$$\nu_{m,0} = \left( \frac{p-2}{p-1} \right)^2 \frac{2q}{\pi m_e c} \left( \frac{m_p v_w}{m_e c^2} \right)^2 \left( \frac{2\eta\epsilon_e^5}{r_0^3 \gamma_0} \right)^{1/2} \left( \frac{E^{5/2}}{\dot{M}^2} \right). \quad (14)$$

As a result,  $F(t, \nu)$  just depends on  $\dot{M}$  and  $E$ .

We use a grid of  $\dot{M}$  and  $E$  values to compare our VLA upper limits (Table 1) with the flux densities derived from (10). In Figure 2 we explore the kinetic energy versus mass-loss rate parameter space considering the (i) radio upper limits (hatched) and (ii) the radio limits plus the X-ray limits (red), which results in more stringent constraints:  $E \lesssim 10^{45}$  erg for  $\dot{M} \lesssim 10^{-6} M_\odot \text{ yr}^{-1}$  and  $E \lesssim 10^{46}$  erg for  $\dot{M} \lesssim 10^{-4} M_\odot \text{ yr}^{-1}$ . We end by noting that at these low mass-loss rates the effects of FFA are negligible (e.g., Weiler et al. 1986; Fransson & Björnsson 1998).

#### 4.2. SSA Emission from a Relativistic GRB-like Jet

We generated a grid of radio light curves powered by synchrotron emission from off-axis relativistic jets using the

<sup>9</sup> These parameters are shown in Equations (13) and (14) of Soderberg et al. (2005), respectively.

BOXFIT code (v2; van Eerten et al. 2012), which is based on high-resolution, two-dimensional relativistic hydrodynamical simulations of relativistic jets. All the synthetic light curves were compared to our VLA upper limits (Table 1) to determine the allowed region in the parameter space, using the same procedure as in Coppejans et al. (2018).

The radio emission from an off-axis jet depends on the following physical parameters: (1) isotropic-equivalent total kinetic energy  $E_{k,\text{iso}}$ ; (2) CSM density, either for an ISM-like ( $n$  constant) or a wind-like CSM ( $\rho_{\text{CSM}} = \dot{M}/(4\pi R^2 v_w)$ ) produced by a constant  $\dot{M}$ ; (3) microphysical shock parameters  $\epsilon_e$  and  $\epsilon_B$ ; (4) jet opening angle  $\theta_j$ ; and (5) observer angle with respect to the jet axis  $\theta_{\text{obs}}$ . We fix the power-law index of the shocked electron energy distribution for a typical value in the range  $p = 2-3$ , as derived from GRB afterglow modeling (e.g., Curran et al. 2010; Wang et al. 2015) and we generate a model for a range of  $\dot{M}$  for an assumed wind velocity of  $v_w = 1000 \text{ km s}^{-1}$ .

We explored a grid of parameters, specifically  $10^{-3} \text{ cm}^{-3} \leq n \leq 10^2 \text{ cm}^{-3}$ ;  $10^{-8} M_\odot \text{ yr}^{-1} \leq \dot{M} \leq 10^{-3} M_\odot \text{ yr}^{-1}$ . Two different jet opening angles were used, which encompass representative measured values for other GRBs:  $\theta_j = 5^\circ$  and  $30^\circ$ . We considered three observer angles ( $\theta_{\text{obs}} = 30^\circ, 60^\circ$ , and  $90^\circ$ ) and isotropic-equivalent kinetic energies in the range  $10^{50} \text{ erg} \leq E_{k,\text{iso}} \leq 10^{55} \text{ erg}$ . These ranges describe the typical parameters derived from accurate broadband modeling of GRB afterglows (e.g., Schulze et al. 2011; Laskar et al. 2013, 2016; Perley et al. 2014). Moreover, in this analysis we discuss the results for  $\epsilon_e = 0.1$  and  $\epsilon_B = 0.01$ , but for completeness we show the results for other typical values in Figures 3 and 4. We find that our radio limits are consistent with the expected emission from off-axis ( $\theta_{\text{obs}} \geq 60^\circ$ ) narrow ( $\theta_j = 5^\circ$ ) jets expanding in a low-density CSM environment with  $\dot{M} \lesssim 10^{-5} M_\odot \text{ yr}^{-1}$  that are typical of BL-Ic SNe and GRBs. The allowed beaming-corrected kinetic energy values are  $E_k \leq 4 \times 10^{49}$  erg.

## 5. Discussion

Here we put our results on the environment and on the energetics of SN 2014ad into the broader context of nearby ( $z \lesssim 0.2$ ) BL-Ic SNe with or without an associated GRB.

### 5.1. Constraints on Uncollimated Outflows in SN 2014ad

In the case of subrelativistic and nearly isotropic ejecta (Section 4.1) expanding in a wind-like CSM, assuming equipartition ( $\epsilon_e = \epsilon_B = 1/3$ ), Figure 2 shows that the combination of VLA + XRT data constrains the fast ejecta kinetic energy to  $E \lesssim 10^{45}$  erg for  $\dot{M} \lesssim 10^{-6} M_\odot \text{ yr}^{-1}$  and to  $E \lesssim 10^{46}$  erg for  $\dot{M} \lesssim 10^{-4} M_\odot \text{ yr}^{-1}$ . These very deep constraints rule out outflows with properties similar to (i) relativistic SNe, such as SN 2009bb (Soderberg et al. 2010) and SN 2012ap (Chakraborti et al. 2015), for which no GRB counterpart was detected, and (ii) SN 1998bw, a prototypical GRB-SN associated with a low-luminosity GRB, propagating into a similar environment (Figure 2). Our limits also point to very low-density environments, consistent with previous findings that BL-Ic SNe favor low-density media (e.g., see Figure 5 from Margutti et al. 2018), as was also the case for SN 2002ap (Berger et al. 2002) and SN 2010ay (Sanders et al. 2012).

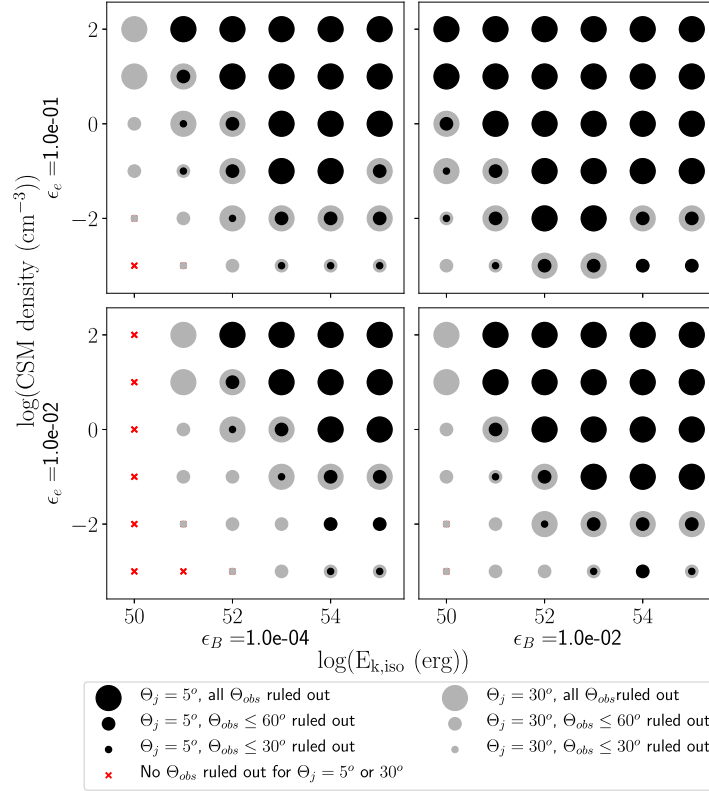


**Figure 3.** Constraints on jetted outflows in an ISM-like density profile in the CSM, based on the VLA upper limits of SN 2014ad and hydrodynamic simulations with the BOXFIT(v2) code (Section 4.2). Black circles represent jet opening angles of  $\theta_j = 5^\circ$ , whereas gray circles represent jet opening angles of  $\theta_j = 30^\circ$ . The symbol size indicates the observer angle ( $\theta_{\text{obs}}$ ) out to which we can rule out the corresponding jet, with larger symbols corresponding to larger  $\theta_{\text{obs}}$ . Red crosses indicate that we cannot rule out an off-axis relativistic jet with the given parameters in SN 2014ad. The top (bottom) panels are  $\epsilon_e = 0.1$  ( $\epsilon_e = 0.01$ ), and the left (right) panels are  $\epsilon_B = 0.0001$  ( $\epsilon_B = 0.01$ ).

### 5.2. Is SN 2014ad Associated with an Off-axis GRB-like Jet?

Our VLA radio observations place stringent constraints on off-axis relativistic jets expanding into an ISM-like (Figure 3) and a wind-like CSM (Figure 4), respectively (Section 4.2). First, we consider the case of a wind-like CSM and a highly collimated jet with  $\theta_j = 5^\circ$  (as is typical for cosmological GRBs) viewed off-axis, for  $\epsilon_e = 0.1$  and  $\epsilon_B = 0.01$  (top right panel, Figure 4). These off-axis narrow jets are ruled out regardless of the observer angle for  $\dot{M} \gtrsim 10^{-5} M_\odot \text{yr}^{-1}$  and  $E_{k,\text{iso}} \gtrsim 10^{52}$  erg (typical value for a GRB). Hence, GRB-like jets expanding either in a low-density CSM typical of BL-Ic SNe ( $\dot{M} \lesssim 10^{-5} - 10^{-6} M_\odot \text{yr}^{-1}$  in Table 1 of Smith 2014; see also Li & Chevalier 1999 and Soderberg et al. 2006b) or in typical GRB environments ( $10^{-7} \lesssim \dot{M} \lesssim 10^{-5} M_\odot \text{yr}^{-1}$ ; Laskar et al. 2014, 2015) cannot be ruled out.

In the case of off-axis jets with larger opening angles  $\theta_j = 30^\circ$ , for  $\epsilon_e = 0.1$  and  $\epsilon_B = 0.01$  (top right panel, Figure 4), we obtain stronger constraints, due to their larger jet energy. Specifically, regardless of the observer angle, we can rule out scenarios where  $\dot{M} \gtrsim 10^{-6} M_\odot \text{yr}^{-1}$  and  $E_{k,\text{iso}} \gtrsim 10^{52}$  erg. Mass-loss rates typically found in the winds of WR stars ( $\dot{M} \lesssim 10^{-5} - 10^{-6} M_\odot \text{yr}^{-1}$ ; Smith 2014) are mostly ruled out. In the case of wide ( $\theta_j = 30^\circ$ ), slightly off-

axis ( $\theta_{\text{obs}} \leq 30^\circ$ ) jets, for  $\epsilon_e = 0.1$  and  $\epsilon_B = 0.01$  (top right panel, Figure 4), we can rule out the combination of  $\dot{M} \gtrsim 10^{-8} M_\odot \text{yr}^{-1}$  and  $E_{k,\text{iso}} \gtrsim 10^{51}$  erg. Assuming a progenitor wind velocity of  $1000 \text{ km s}^{-1}$ , all the CSM profiles of all the detected SNe Ibc and most of the GRBs detected to date are rejected (see Figure 5 in Coppejans et al. 2018). We also report the results for a jet propagating into an ISM-like CSM, as the modeling of GRB afterglows often indicates an ISM environment as opposed to a wind-like density profile (e.g., Laskar et al. 2014, 2018). For  $\epsilon_e = 0.1$  and  $\epsilon_B = 0.01$  (top right panel, Figure 3), highly collimated jets with  $\theta_j = 5^\circ$  are ruled out regardless of the observer angle for  $n \gtrsim 10 \text{ cm}^{-3}$  and  $E_{k,\text{iso}} \gtrsim 10^{50}$  erg, or for  $n \gtrsim 10^{-1} \text{ cm}^{-3}$  and  $E_{k,\text{iso}} \gtrsim 10^{52}$  erg. A jet with  $\theta_j = 30^\circ$  is ruled out for  $n \gtrsim 10^{-1} \text{ cm}^{-3}$  and  $E_{k,\text{iso}} \gtrsim 10^{50}$  erg. We obtain deeper constraints for jets with  $\theta_{\text{obs}} < 60^\circ$ : for  $\theta_j = 5^\circ$  and  $\theta_{\text{obs}} = 60^\circ$  a jet is ruled out for  $n \gtrsim 10^{-3} \text{ cm}^{-3}$  and  $E_{k,\text{iso}} \gtrsim 10^{52}$  erg. Hence, GRB-like jets expanding in an ISM-like medium with  $n \lesssim 10^{-2} \text{ cm}^{-3}$  and  $E_{k,\text{iso}} \lesssim 10^{50}$  erg cannot be ruled out: these densities are compatible with those of some GRBs ( $10^{-5} \lesssim n \lesssim 10^3 \text{ cm}^{-3}$ ; e.g., Laskar et al. 2014, 2015).

We conclude that we cannot rule out the case of an off-axis ( $\theta_{\text{obs}} \gtrsim 30^\circ$ ), narrow ( $\theta_j = 5^\circ$ ) GRB-like jet plowing through

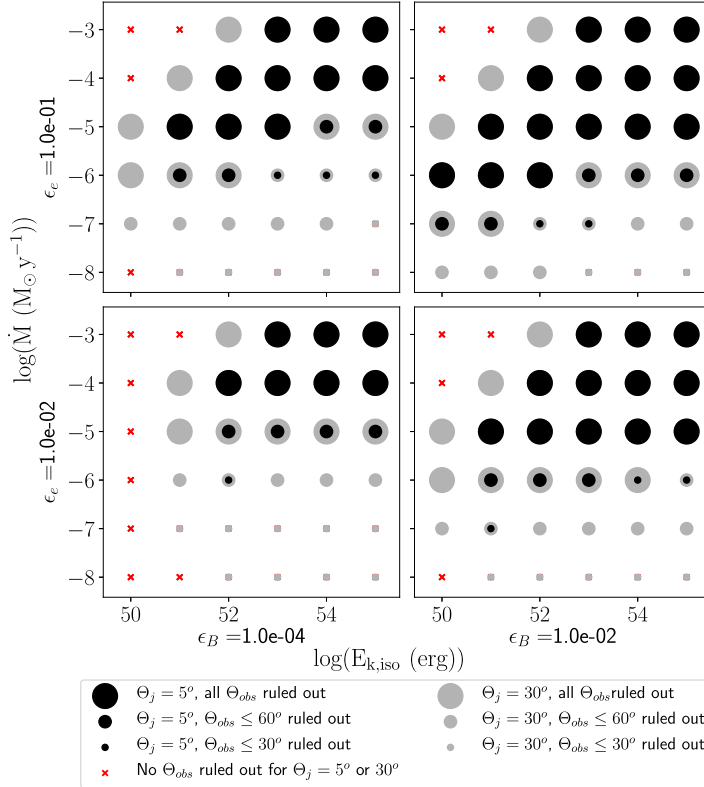


**Figure 4.** Constraints on jetted outflows in a wind-like density profile in the CSM ( $\rho \propto r^{-2}$ ), based on the VLA upper limits of SN 2014ad and hydrodynamic simulations with BOXFIT(v2) code (Section 4.2). See the caption of Figure 3 for a full description of the symbols.

low-density CSM typical of BL-Ic SNe and GRBs; this scenario allows for beaming-corrected kinetic energies  $E_{k,\text{iso}} \lesssim 10^{52}$  erg in environments sculpted by  $\dot{M} \lesssim 10^{-6} M_{\odot} \text{yr}^{-1}$ .

### 5.3. Constraining the $E_k(\Gamma\beta)$ Distribution of the Ejecta of SN 2014ad

Compared with BL-Ic GRB-less SNe, GRB-SNe seemed to show (i) high mass of  $^{56}\text{Ni}$  synthesized in the SN explosion, (ii) higher degree of asphericity in the SN explosion, and (iii) low metallicity of the SN environment (e.g., Cano 2013). However, Taddia et al. (2019) recently showed that the distributions of these observables for the two classes of BL-Ic SNe are still compatible within uncertainties. Another way to investigate the differences between the two classes is offered by the slope  $x$  of the kinetic energy profile ( $E_k$ ) as a function of the ejecta four-velocity ( $\Gamma\beta$ ), parameterized as  $E_k \propto (\Gamma\beta)^x$ . What is more, this may help to reveal the nature of the explosion (see Figure 2, Margutti et al. 2014). Steep profiles ( $x \lesssim -2.4$ ) indicate a short-lived central engine, and hence an ordinary Ibc SN (Lazzati et al. 2012); flat profiles ( $x \gtrsim -2.4$ ) indicate the presence of a mildly short-lived central engine, and hence a possible GRB-SN (Margutti et al. 2013); very flat profiles ( $x = -0.4$ ) are typical of ordinary GRBs in the decelerating Blandford–McKee phase (Blandford & McKee 1976), whereas

very steep profiles ( $x = -5.2$ ) are characteristic of a pure hydrodynamical spherical explosion (Tan et al. 2001).

For SN 2014ad we explored a grid of parameters in the  $E_k\text{--}\Gamma\beta$  space.  $\Gamma$  is calculated at  $t = 1$  day applying the standard formulation of the fireball dynamics with expansion in a wind-like CSM (e.g., Chevalier & Li 2000)

$$\Gamma_{(t=1 \text{ day})} \sim 18.7 \left( \frac{E_{k,\text{iso}}}{10^{54} \text{ erg}} \right)^{1/4} \left( \frac{A_*}{0.1} \right)^{-1/4}, \quad (15)$$

where  $A_*$  is the circumstellar density, defined with respect to progenitor mass-loss rate  $\dot{M}$  and wind velocity  $v_w$  as:

$$A_* = \left( \frac{\dot{M}}{10^{-5} M_{\odot} \text{yr}^{-1}} \right) \left( \frac{v_w}{1000 \text{ km s}^{-1}} \right). \quad (16)$$

The allowed regions are derived through the conditions described in Section 5.2 for the case of a highly collimated jet with  $\theta_j = 5^\circ$  (as typical for cosmological GRBs) viewed off-axis in a wind-like CSM (Figure 4; top right panel). Figure 5 shows the allowed region of the beaming-corrected energy  $E_k$ —ejecta velocity  $\Gamma\beta$  space (in the relativistic regime). Relativistic jets for SN 2014ad are possible for progenitors with very low densities ( $\dot{M} \lesssim 10^{-7} M_{\odot} \text{yr}^{-1}$ ); for example, a faster-moving ejecta (with a beaming-corrected energy  $E_k \sim 10^{51}$  erg) plowing through a wind-like CSM with a very

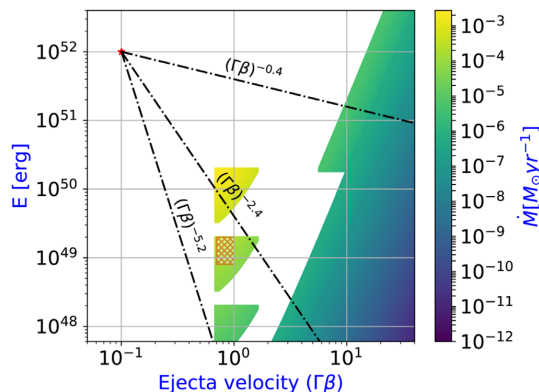


**Figure 5.** Region of the beaming-corrected energy  $E_k$ —ejecta velocity  $\Gamma\beta$  (with  $\Gamma$  estimated at  $t = 1$  day) space allowed by our upper limits of SN 2014ad (in wind-like CSM for relativistic regime). The color scale shows the allowed progenitor mass-loss rate  $\dot{M}$ . The dashed-dotted lines indicate the slope  $x$  of the kinetic energy profile. The orange hatched area indicates the region of relativistic SNe, where the cocoon emission might be observable (De Colle et al. 2018a, 2018b).

low density  $\dot{M} \sim 10^{-7} M_{\odot} \text{yr}^{-1}$  has  $\Gamma\beta \sim 24$  (at  $t = 1$  day), compatible with the flat profile ( $x = -0.4$ ) of ordinary GRBs. The lack of any associated GRB suggests a possible off-axis GRB propagating in a wind-like CSM with a very low density ( $\dot{M} \lesssim 10^{-7} M_{\odot} \text{yr}^{-1}$ ).

#### 5.4. Constraints on Cocoon Emission in SN 2014ad

The interaction between the jet emission and the outer layers of the progenitor star causes the swelling of the outer envelope of the jet, called the cocoon. The recent broadband spectroscopic analysis of Izzo et al. (2019) of a BL-Ic GRB-SN (SN 2017iuk/GRB 171205A) shows the first direct evidence for the cocoon emission. This cocoon is characterized by a very high expansion velocity ( $\sim 0.3c$ ) and probably originates from the energy injection of a mildly relativistic GRB jet. This discovery could explain the lack of GRBs observed in association with some BL-Ic SNe: the jet, because it transfers a significant part of its total energy to the cocoon, produces the typical GRB emission only if it manages to completely pierce the star photosphere. This conclusion is in agreement with the analysis of De Colle et al. (2018a, 2018b): they show that the radio emission observed in relativistic SNe can be explained as synchrotron emission from the cocoon created by an off-axis GRB jet (either failed or successful), that propagates through the progenitor star. Figure 5 shows the allowed region (red hatched area) for relativistic SNe, where the cocoon emission in principle might be observable: even if the radio emission from SN 2014ad is much fainter than SN 2009bb and SN 2012ap (Figure 1), this region is compatible with  $E_k$  of the fast ejecta for an SN 2014ad progenitor with mildly low densities ( $\dot{M} \sim 10^{-5} M_{\odot} \text{yr}^{-1}$ ). De Colle et al. (2018a) suggest that, in the off-axis GRB scenario, the cocoon synchrotron emission at radio frequencies dominates (i) always for failed GRB/cocoon or weak GRB observed off-axis, or (ii) only at early times for energetic off-axis jets with late-time peaks (timescale of years).

A more quantitative discussion of the cocoon emission for SN 2014ad is beyond the scope of the present investigation.

## 6. Conclusions

We present deep X-ray and radio limits of the BL-Ic SN 2014ad. Radio and X-ray observations are crucial for probing the fastest moving ejecta in the explosion, as the optical emission is produced by the slow-moving ejecta. Previous studies of this source showed that it has a number of properties that, taken together, suggest a possible GRB counterpart. These include a large bulk energy  $E_k$  of the slow ejecta, the asphericity in the explosion and ejecta velocity, the large inferred nickel mass, and the low progenitor mass-loss rate  $\dot{M}$ . Consequently, we investigated two different physical scenarios for SN 2014ad: (i) a subrelativistic, nearly isotropic explosion of an ordinary BL-Ic SN in a wind-like CSM (Section 4.1); (ii) an off-axis relativistic jet (Section 4.2). These models place strong constraints on the total energy of the fast ejecta ( $E$ ), the progenitor mass-loss rate ( $\dot{M}$ ), the jet opening angle ( $\theta_j$ ), and the observer angle ( $\theta_{\text{obs}}$ ). We obtained the following results:

1. Assuming that the dominant source of X-ray emission at early times is IC emission from the upscattering of optical photospheric photons into the X-ray band by relativistic electrons at the shock front (Section 3), we infer  $\dot{M} < 5 \times 10^{-5} M_{\odot} \text{yr}^{-1}$ , for a wind velocity  $v_w = 1000 \text{ km s}^{-1}$  for a spherical outflow.
2. If SN 2014ad launched a subrelativistic and isotropic outflow (Section 4.1), assuming equipartition ( $\epsilon_e = \epsilon_B = 0.33$ ) we derive limits of  $E \lesssim 10^{45} \text{ erg}$  for  $\dot{M} \lesssim 10^{-6} M_{\odot} \text{yr}^{-1}$  and  $E \lesssim 10^{46} \text{ erg}$  for  $\dot{M} \lesssim 10^{-4} M_{\odot} \text{yr}^{-1}$ . These deep constraints rule out outflows with properties similar to (i) relativistic SN 2009bb and SN 2012ap, for which no associated GRB was reported, and (ii) SN 1998bw, a prototypical GRB-SN, propagating into a similar environment.  $E$  and  $\dot{M}$  of the kind seen in the GRB-less SN 2002ap and SN 2010ay, which are characterized by a modest energy budget in the fast ejecta, are not ruled out.
3. If SN 2014ad launched a relativistic jet, we (i) rule out collimated on-axis jets of the kind detected in GRBs and (ii) put strong constraints on the energies and CSM densities for an off-axis jet (Figures 3 and 4). We cannot rule out an off-axis GRB in very low-density CSM environments (e.g.,  $\theta_{\text{obs}} \gtrsim 30^\circ$ ,  $\theta_j = 5^\circ$ , in a CSM sculpted by  $\dot{M} \lesssim 10^{-6} M_{\odot} \text{yr}^{-1}$ , typical of BL-Ic SNe and GRBs). Moreover, we cannot reject the possibility of a radio synchrotron emission dominated by the cocoon created by a GRB jet viewed off-axis that propagates through the stellar progenitor, as expected for relativistic SNe.

With our analysis of the off-axis jet scenario we have demonstrated that it is not possible to rule out off-axis jets expanding into low-density environments (as previously found by Bietenholz 2014 for other SNe). For SN 2014ad we find  $\dot{M} \lesssim 10^{-6} M_{\odot} \text{yr}^{-1}$  (Figure 5). If SN 2014ad was indeed powered by an off-axis relativistic jet, our X-ray and radio observations imply extremely low environment densities and energies coupled to jet (unless the jet was far off-axis).

Deep radio and X-ray observations at early and late times of a large sample of nearby BL-Ic SNe will clarify whether or not relativistic jets are ubiquitous in BL-Ic SNe.

We thank D. K. Sahu for kindly sharing bolometric light curves. M.M. thanks M. Orienti and E. Eggen for their precious suggestions about VLA data reduction and Bath University for the hospitality during the final stages of this work. We acknowledge University of Ferrara for use of the local HPC facility cofunded by the “Large-Scale Facilities 2010” project (grant 7746/2011). We thank University of Ferrara and INFN–Ferrara for the access to the COKA GPU cluster. This research was supported in part through the computational resources and staff contributions provided for the Quest high performance computing facility at Northwestern University, which is jointly supported by the Office of the Provost, the Office for Research, and Northwestern University Information Technology. We gratefully acknowledge Piero Rosati for granting us usage of proprietary HPC facility. Development of the BOXFIT code was supported in part by NASA through grant NNX10AF62G issued through the Astrophysics Theory Program and by the NSF through grant AST-1009863. Simulations for BOXFITv2 have been carried out in part on the computing facilities of the Computational Center for Particle and Astrophysics of the research cooperation “Excellence Cluster Universe” in Garching, Germany. Support for this work was provided by Università di Ferrara through grant FIR 2018 “A Broad-band study of Cosmic Gamma-Ray Burst Prompt and Afterglow Emission” (PI Guidorzi). The National Radio Astronomy Observatory is a facility of the National Science Foundation operated under cooperative agreement by Associated Universities, Inc.

## ORCID iDs

M. Marongiu  <https://orcid.org/0000-0002-5817-4009>  
 C. Guidorzi  <https://orcid.org/0000-0001-6869-0835>  
 R. Margutti  <https://orcid.org/0000-0003-4768-7586>  
 D. L. Coppejans  <https://orcid.org/0000-0001-5126-6237>  
 R. Martone  <https://orcid.org/0000-0002-0335-319X>  
 A. Kamble  <https://orcid.org/0000-0003-0861-5168>

## References

- Berger, E., Kulkarni, S. R., & Chevalier, R. A. 2002, *ApJL*, 577, L5  
 Bietenholz, M. F. 2014, *PASA*, 31, e002  
 Björnsson, C.-I., & Fransson, C. 2004, *ApJ*, 605, 823  
 Blandford, R. D., & McKee, C. F. 1976, *PhFl*, 19, 1130  
 Bromberg, O., Nakar, E., Piran, T., & Sari, R. 2011, *ApJ*, 740, 100  
 Burrows, D. N., Hill, J. E., Nousek, J. A., et al. 2005, *SSRv*, 120, 165  
 Cano, Z. 2013, *MNRAS*, 434, 1098  
 Cano, Z., Wang, S.-Q., Dai, Z.-G., & Wu, X.-F. 2017, *AdAst*, 2017, 8929054  
 Chakraborti, S., Soderberg, A., Chomiuk, L., et al. 2015, *ApJ*, 805, 187  
 Chevalier, R. A. 1982, *ApJ*, 258, 790  
 Chevalier, R. A. 1996, in ASP Conf. Ser. 93, Radio Emission from the Stars and the Sun, ed. A. R. Taylor & J. M. Paredes (San Francisco, CA: ASP), 125  
 Chevalier, R. A. 1998, *ApJ*, 499, 810  
 Chevalier, R. A., & Fransson, C. 2006, *ApJ*, 651, 381  
 Chevalier, R. A., & Li, Z.-Y. 2000, *ApJ*, 536, 195  
 Coppejans, D. L., Margutti, R., Guidorzi, C., et al. 2018, *ApJ*, 856, 56  
 Corsi, A., Gal-Yam, A., Kulkarni, S. R., et al. 2016, *ApJ*, 830, 42  
 Corsi, A., Ofek, E. O., Gal-Yam, A., et al. 2014, *ApJ*, 782, 42  
 Cucchiara, A., Levan, A. J., Fox, D. B., et al. 2011, *ApJ*, 736, 7  
 Curran, P. A., Evans, P. A., de Pasquale, M., Page, M. J., & van der Horst, A. J. 2010, *ApJL*, 716, L135  
 De Colle, F., Kumar, P., & Aguilera-Dena, D. R. 2018a, *ApJ*, 863, 32  
 De Colle, F., Lu, W., Kumar, P., Ramirez-Ruiz, E., & Smoot, G. 2018b, *MNRAS*, 478, 4553  
 Dessart, L. 2015, in Wolf-Rayet Stars: Proc. an Int. Workshop held in Potsdam, ed. W.-R. Hamann, A. Sander, & H. Todt (Potsdam: Universitätsverlag Potsdam), 245  
 Dessart, L., Hillier, D. J., Woosley, S., et al. 2015, *MNRAS*, 453, 2189  
 Dessart, L., John Hillier, D., Yoon, S.-C., Waldman, R., & Livne, E. 2017, *A&A*, 603, A51  
 Djorgovski, S. G., Drake, A. J., Mahabal, A. A., et al. 2011, arXiv:1102.5004  
 Eichler, D., & Levinson, A. 1999, *ApJL*, 521, L117  
 Eldridge, J. J., Fraser, M., Smartt, S. J., Maund, J. R., & Crockett, R. M. 2013, *MNRAS*, 436, 774  
 Ensman, L. M., & Woosley, S. E. 1988, *ApJ*, 333, 754  
 Filippenko, A. V. 1997, *ARA&A*, 35, 309  
 Fransson, C., & Björnsson, C.-I. 1998, *ApJ*, 509, 861  
 Gal-Yam, A. 2017, in Handbook of Supernovae, ed. A. Alsabti & P. Murdin (Berlin: Springer), 195  
 Gehrels, N., Chincarini, G., Giommi, P., et al. 2004, *ApJ*, 611, 1005  
 Högbom, J. A. 1974, *A&AS*, 15, 417  
 Howerton, S., Drake, A. J., Djorgovski, S. G., et al. 2014, *CBET*, 3831, 1  
 Izzo, L., de Ugarte Postigo, A., Maeda, K., et al. 2019, *Natur*, 565, 324  
 Kalberla, P. M. W., Burton, W. B., Hartmann, D., et al. 2005, *A&A*, 440, 775  
 Kellermann, K. I., & Pauliny-Toth, I. I. K. 1981, *ARA&A*, 19, 373  
 Kilpatrick, C. D., Takaro, T., Foley, R. J., et al. 2018, *MNRAS*, 480, 2072  
 Kulkarni, S. R., Frail, D. A., Wieringa, M. H., et al. 1998, *Natur*, 395, 663  
 Laskar, T., Berger, E., Margutti, R., et al. 2015, *ApJ*, 814, 1  
 Laskar, T., Berger, E., Tanvir, N., et al. 2014, *ApJ*, 781, 1  
 Laskar, T., Berger, E., Zauderer, B. A., et al. 2013, *ApJ*, 776, 119  
 Laskar, T., Alexander, K. D., Berger, E., et al. 2016, *ApJ*, 833, 88  
 Laskar, T., Alexander, K. D., Berger, E., et al. 2018, *ApJ*, 862, 94  
 Lazzati, D., Morsony, B. J., Blackwell, C. H., & Begelman, M. C. 2012, *ApJ*, 750, 68  
 Li, Z.-Y., & Chevalier, R. A. 1999, *ApJ*, 526, 716  
 Liang, E., Zhang, B., Virgili, F., & Dai, Z. G. 2007, *ApJ*, 662, 1111  
 Margutti, R., Chornock, R., Metzger, B. D., et al. 2018, *ApJ*, 864, 45  
 Margutti, R., Milisavljevic, D., Soderberg, A. M., et al. 2014, *ApJ*, 797, 107  
 Margutti, R., Soderberg, A. M., Chomiuk, L., et al. 2012, *ApJ*, 751, 134  
 Margutti, R., Soderberg, A. M., Wieringa, M. H., et al. 2013, *ApJ*, 778, 18  
 Matzner, C. D., & McKee, C. F. 1999, *ApJ*, 510, 379  
 Mazzali, P. A., Deng, J., Maeda, K., et al. 2002, *ApJL*, 572, L61  
 McMullin, J. P., Waters, B., Schiebel, D., Young, W., & Golap, K. 2007, in ASP Conf. Ser. 376, Astronomical Data Analysis Software and Systems XVI, ed. R. A. Shaw, F. Hill, & D. J. Bell (San Francisco, CA: ASP), 127  
 Modjaz, M., Liu, Y. Q., Bianco, F. B., & Graur, O. 2016, *ApJ*, 832, 108  
 Perley, D. A., Cenko, S. B., Corsi, A., et al. 2014, *ApJ*, 781, 37  
 Piran, T. 2004, *RvMP*, 76, 1143  
 Podsiadlowski, P., Joss, P. C., & Hsu, J. J. L. 1992, *ApJ*, 391, 246  
 Rhoads, J. E. 1999, *ApJ*, 525, 737  
 Rybicki, G. B., & Lightman, A. P. 1979, Radiative Processes in Astrophysics (New York et al: Wiley)  
 Sahu, D. K., Anupama, G. C., Chakraborti, N. K., et al. 2018, *MNRAS*, 475, 2591  
 Salas, P., Bauer, F. E., Stockdale, C., & Prieto, J. L. 2013, *MNRAS*, 428, 1207  
 Sanders, N. E., Soderberg, A. M., Valenti, S., et al. 2012, *ApJ*, 756, 184  
 Schulze, S., Klose, S., Björnsson, G., et al. 2011, *A&A*, 526, A23  
 Shivvers, I., Modjaz, M., Zheng, W., et al. 2017, *PASP*, 129, 054201  
 Smartt, S. J. 2009, *ARA&A*, 47, 63  
 Smartt, S. J. 2015, *PASA*, 32, e016  
 Smith, N. 2014, *ARA&A*, 52, 487  
 Soderberg, A. M., Chakraborti, S., Pignata, G., et al. 2010, *Natur*, 463, 513  
 Soderberg, A. M., Kulkarni, S. R., Berger, E., et al. 2005, *ApJ*, 621, 908  
 Soderberg, A. M., Kulkarni, S. R., Nakar, E., et al. 2006b, *Natur*, 442, 1014  
 Soderberg, A. M., Nakar, E., Berger, E., & Kulkarni, S. R. 2006a, *ApJ*, 638, 930  
 Stevance, H. F., Maund, J. R., Baade, D., et al. 2017, *MNRAS*, 469, 1897  
 Taddia, F., Sollerman, J., Fremling, C., et al. 2019, *A&A*, 621, A71  
 Tan, J. C., Matzner, C. D., & McKee, C. F. 2001, *ApJ*, 551, 946  
 Terreran, G., Margutti, R., Bersier, D., et al. 2019, arXiv:1905.02226  
 Van Dyk, S. D., Zheng, W., Brink, T. G., et al. 2018, *ApJ*, 860, 90  
 van Eerten, H., van der Horst, A., & MacFadyen, A. 2012, *ApJ*, 749, 44  
 Wang, F. Y., Dai, Z. G., Yi, S. X., & Xi, S. Q. 2015, *ApJS*, 216, 8  
 Weiler, K. W., Sramek, R. A., Panagia, N., van der Hulst, J. M., & Salvati, M. 1986, *ApJ*, 301, 790  
 Yamazaki, R., Yonetoku, D., & Nakamura, T. 2003, *ApJL*, 594, L79  
 Yoon, S.-C. 2010, in ASP Conf. Ser. 425, Hot and Cool: Bridging Gaps in Massive Star Evolution, ed. C. Leitherer et al. (San Francisco, CA: ASP), 89

## **Appendix B**

### **Methods for detection and analysis of weak radio sources with single-dish radiotelescopes**

<b>Noname manuscript No.</b> (will be inserted by the editor)
--

## Methods for detection and analysis of weak radio sources with single-dish radiotelescopes

M. Marongiu · A. Pellizzoni · E. Egron ·  
T. Laskar · M. Giroletti · S. Loru · A. Melis ·  
G. Carboni · C. Guidorzi · S. Kobayashi ·  
N. Jordana-Mitjans · A. Rossi · C. G. Mundell ·  
R. Concu · R. Martone · L. Nicaastro

Received: date / Accepted: date

**Abstract** The detection of faint radio sources (mJy/sub-mJy events) is an open issue in single-dish radio astronomy. To date, observations of undetected radio sources in single-dish mode often result in a rough upper limit based on the root mean square (RMS) of the image.

Using Sardinia Radio Telescope (SRT), we compare the sensitivity and robustness of three methods applied to the detection of faint radio sources: the smart quick-look method, the source extraction method (typical of high-energy astronomy), and the fit with a 2-D Gaussian. The targets of interest are the faint radio afterglow emission (due to synchrotron

---

M. Marongiu · R. Martone  
Department of Physics and Earth Science, University of Ferrara, via Saragat 1, I-44122 Ferrara, Italy  
ICRANet, Piazzale della Repubblica 10, I-65122 Pescara, Italy  
E-mail: marco.marongiu@unife.it

A. Pellizzoni · E. Egron · A. Melis · G. Carboni · R. Concu  
INAF, Osservatorio Astronomico di Cagliari, Via della Scienza 5, I-09047 Selargius, Italy

M. Giroletti  
INAF, Istituto di Radioastronomia, Via Piero Gobetti 101, I-40129 Bologna, Italy

S. Loru  
INAF-Osservatorio Astrofisico di Catania, Via Santa Sofia 78, I-95123 Catania, Italy

T. Laskar · N. Jordana-Mitjans · C. G. Mundell  
Department of Physics, University of Bath, Claverton Down, Bath, BA2 7AY, UK

C. Guidorzi  
Department of Physics and Earth Science, University of Ferrara, via Saragat 1, I-44122 Ferrara, Italy

S. Kobayashi  
Astrophysics Research Institute, Liverpool John Moores University, Liverpool, L3 5RF, UK

A. Rossi · L. Nicaastro  
INAF-Osservatorio di Astrofisica e Scienza dello Spazio di Bologna, Via Piero Gobetti 93/3, I-40129 Bologna, Italy



radiation) from gamma-ray bursts (GRBs), flashes of high-energy radiation of cosmological origin. To this aim, we developed a Python code specific for the analysis of point-like radio sources applied to the SRT C-band (6.9 GHz) observations of both undetected sources (GRB afterglows of 181201A and 190114C) and the detected Galactic binary GRS 1915+105.

Our comparative analysis of the different detection methods made extensive use of simulations as a useful complement of actual radio observations. The best method for the SRT data analysis is the fit with a 2-D Gaussian, as it pushes down the sensitivity limits of single-dish observations –with respect to more traditional techniques– to  $\sim 1.8$  mJy, improving by  $\sim 40\%$  compared with the initial value. This analysis shows that –especially for faint sources– an accurate knowledge of the radio background is essential.

**Keywords** Radio astronomy · Faint sources · Single-dish · Gamma-Ray Bursts · Sardinia Radio Telescope

## 1 Introduction

Observations with single-dish radiotelescopes require (1) an accurate knowledge of the background (both instrumental and astronomical), (2) good sky opacity conditions to ensure an accurate calibration, and (3) a reliable and well-defined source detection method. Whenever the source is not detected, it is common practice to estimate an upper limit based on the flux density root mean square (RMS) calculated over the image<sup>1</sup>.

To this aim, among several detection methods for the analysis of sources in single-dish mode (e.g., [1,2]), we examine three of them through the network of radiotelescopes of the National Institute for Astrophysics (INAF), which includes the Sardinia Radio Telescope (SRT), the Medicina Radio Astronomical Station, and Noto Radio Observatory<sup>2</sup>: ‘quick-look’ (Method A, a smart but rough approach), ‘source extraction’ (Method B, typically adopted in X-ray/gamma-ray astronomy), and fitting procedure with a 2-D Gaussian (Method C, a more sophisticated approach accounting for the instrument point spread function).

The science case of study is GRB radio afterglows, a phenomenon associated with very faint sources (with flux densities  $\leq 1$  mJy), and hence, very suitable to our analysis (e.g. [3,4]). GRBs are detected through their bright and characteristic gamma-ray prompt emission and more recently, as the counterparts of gravitational waves (GWs; e.g. [5,6,7]). GRB ejecta produce a relativistic blast wave shock as they expand into their ambient environment. This shock accelerates electrons and produces synchrotron radiation, which is visible as long-lasting X-ray to radio “afterglow” emission. Observations of GRB afterglows at radio frequencies provide a wealth of information: (1) constrain the self-absorption frequency of the underlying synchrotron radiation [8], and thus break parameter degeneracies in conjunction with optical and X-ray observations, (2) track the presence and evolution of reverse shocks in the ejecta and hence derive the ejecta magnetization and initial Lorentz factor [9,10,11], (3) constrain the degree of ejecta collimation and hence the released energy corrected for relativistic beaming [12,13], and (4) derive the size of the afterglow using scintillation methods [14,15]. Overall, they contribute remarkably to our understanding of the hydrodynamics of relativistic outflows.

<sup>1</sup> The root mean square (RMS) of the image is the standard deviation of pixels flux densities taken in image regions not affected by the source flux.

<sup>2</sup> <http://www.radiotelesopes.inaf.it/>

We analyzed these detection methods through dedicated radio followup campaigns of two GRB afterglows (GRB 181201A and GRB 190114C) in C-band (6.9 GHz) with SRT, resulting in upper limits. The information on the position of these sources comes from the detection of afterglow counterparts both at X-ray and optical wavelengths. We make extensive use of simulations of point-like sources, injected in simulated images/fields.

This paper is organized as follows. We describe our targets in Section 2, our radio observations in Section 3, whereas Section 3.1 explains the imaging data analysis and the calibration procedure in single-dish mode. Following the description of the three detection methods for point-like sources (Section 4), in Section 5 we apply them to a simulated case (background and source). These simulations are crucial to analyze the real cases of undetected GRBs, and the faint source GRS 1915+105 (Sect. 6). We present our results in Section 7 and our conclusions in Section 8.

## 2 Our targets

We observed two long GRBs (181201A and 190114C) and GRS1,1915+105 with SRT in C-band (6.9 GHz). Even hours after the burst, GRB 181201A and GRB 190114C optical afterglow remained bright (magnitude < 18 in R-filter; e.g. [16] for GRB 181201A and [17] for GRB 190114C).

GRB 181201A was discovered by the INTEGRAL Burst Alert System (IBAS) in the IBIS/ISGRI data on 2018 December 1 at 02:38 UT [18]; it was also detected by the Fermi Large Area Telescope (LAT; [19]), the X-Ray Telescope (XRT) on Swift [20] and the High-Energy (HE) instrument aboard Insight-HXMT [21]. The afterglow was observed in optical (e.g. [22]), and mm/radio frequencies [23], with possible evidence for an associated supernova [24]. It has a redshift of 0.450 [25]. For our observations of GRB 181201A, we used the Karl G. Jansky Very Large Array (VLA) coordinates  $\alpha = 21^{\text{h}}17^{\text{m}}11^{\text{s}}.185$ ,  $\delta = -12^{\circ}37'51.37''$  [26].

GRB 190114C was discovered by the Burst Alert Telescope (BAT; [27]) on the Neil Gehrels Swift Observatory [28] on 2019 January 14 at 20:57:03 UT [29]. With a redshift  $z = 0.4245$  [30], it was also detected by Konus-Wind [31], the Fermi Gamma-ray Burst Monitor (GBM; [32]), the Fermi/LAT ([33, 34]), and radio facilities (e.g. ALMA, [11]; ATCA, [35]). GRB 190114C is the first GRB detected in the TeV band ( $\geq 300$  GeV) by the twin Major Atmospheric Gamma Imaging Cherenkov (MAGIC) telescopes, with observations starting 50 s after the BAT trigger [36, 37, 38]. For our observations of GRB 190114C, we used the VLA coordinates  $\alpha = 3^{\text{h}}38^{\text{m}}01^{\text{s}}.191$ ,  $\delta = -26^{\circ}56'46.73''$  [15].

GRS 1915+105 is a highly variable accreting black hole in our Galaxy. In the radio it shows relativistic superluminal jets of flux density  $\sim 1$  Jy [39, 40] and compact jets with flux density of 20–200 mJy [41, 42]. In the framework of the monitoring of GRS 1915+105 with SRT (PI: Egron, proposal 28-18), we performed observations on 22 May 2019 at 6.9 GHz when the source was slightly active. We carried out the data analysis with our software in order to test our methods of detection on a quite weak but clearly detected source with SRT and compare the result of the flux density with another software dedicated to single dish imager observations (SDI, [43]).

**Table 1** Observation campaign for our analysis with SRT.  $At_i$  and  $At_f$  indicate respectively the start and final observing epoch after the GRB explosion (in units of days).

Epoch	GRB	Receiver	$At_i$ (d)	$At_f$ (d)
2018/12/11	181201A	SRT-C	10.36	10.52
2019/01/30	181201A	SRT-C	60.27	60.49
2019/03/22	181201A	SRT-C	111.12	111.32
2019/01/17	190114C	SRT-C	2.77	2.99
2019/01/23	190114C	SRT-C	8.74	8.94
2019/03/05	190114C	SRT-C	49.66	49.84

### 3 Observations with SRT

We observed GRB 181201A, GRB 190114C and GRB 1915+105 with SRT<sup>3</sup>, which is part of the INAF radiotelescope network; it is the largest among them with a 64-m diameter parabolic reflector. SRT is located in San Basilio (near Cagliari, Sardinia, Italy) and operates in the 0.3 – 100 GHz nominal frequency range with a Gregorian configuration [44]. At present, SRT is equipped with three receivers: a coaxial dual-feed L–P-band (1.3 – 1.8 GHz; 305 – 410 MHz) receiver, a mono-feed C-band receiver (5.7 – 7.7 GHz), and a 7-beam K-band receiver (18 – 26.5 GHz) [45,46]. An active surface (composed of 1008 panels and 1116 electro-mechanical actuators) implemented on the primary mirror allow us to (1) compensate for gravitational deformations and (2) re-shape the primary mirror from a shaped configuration to a parabolic profile [47,48,49,50].

The targets were observed with SRT at 6.9 GHz (bandwidth = 1200 MHz) between 2018 December 11 and 2019 March 22 under the project 23-18 for GRB 181201A (PI: M. Marongiu) and the ToO request 02-19 for GRB 190114C (PI: M. Marongiu). We observed in “shared-risk mode” through a new-generation and flexible ROACH2-based backend called SARDARA (SARDinia Roach2-based Digital Architecture for Radio Astronomy [51]).

During SARDARA operations, the total bandwidth of each polarization (LCP and RCP<sup>4</sup>) is divided into 1024 channels. For continuum observations, this allows us to dynamically remove radio frequency interference (RFI) and thus maximize our point-source sensitivity. We performed the mapping of our targets through On-the-Fly (OTF) scans. Within this technique data are continuously stored while the antenna performs constant-speed orthogonal scans across the sky, alternately producing maps along the Right Ascension (RA) and Declination (Dec) directions. Unlike raster maps (where separated on-source/target and off-source/background pointing are performed), in OTF mapping the target signal is measured together with the background/baseline level (continuously spanning a sky region larger than the target). This allows for a more precise background/baseline subtraction. Observations were carried out through the repetition for  $\sim 15$  RA/Dec maps of  $0.2^\circ \times 0.2^\circ$  with 4 arcmin/s scan speed, 4.5 scan/beam, and a sampling time of 20 ms during the observations. The dimensions of the maps were chosen based on the beam size in C-band at the observing frequency  $\nu_{obs} = 6.9$  GHz ( $HPBW = 2.71 \pm 0.02$  arcmin [49]). This configuration allows us to reach an exposure of  $\sim 1$  minute/beam for a total mapping time of  $\sim 6$  hours including overheads and slew time, in order to have the chance to detect a counterpart at  $\sim$ mJy level

<sup>3</sup> <http://www.srt.inaf.it/>

<sup>4</sup> Radio waves interact with the antenna (the parabolic reflector) where they are carried to a focus. At the focus the radio waves in free space are coupled to an antenna through a device called feed, that probes the electric field of incoming radiation rotating counterclockwise (right-hand circular polarization, RCP) and clockwise (left-hand circular polarization, LCP), respectively, with time (e.g. [52]).

or below. This observing strategy provides a direct image of the sources close to the target as well as a better estimate of the flux density.

An accurate evaluation of flux density errors is possible thanks to the acquisition of  $> 10 - 20$  samples/beam for each scan passage; this generates a large beam oversampling (with respect to Nyquist sampling), that allows us to efficiently remove outlier measurements ascribed to RFI. The length of the scans is chosen based on the source size; the scan-dependent baseline (i.e. background emission and system-related signal) must be correctly subtracted, to properly reconstruct the morphology of the observed source and its associated flux density [50]. Ideally, each scan should be free of significant source contribution (and RFI contamination) for 40 – 60 per cent of its length/duration, to properly identify and subtract the baseline component; usually this requirement is satisfied for extragalactic targets (i.e. GRBs), but not trivially satisfied for targets located in crowded regions of the Galactic plane.

Two consecutive scans were separated by an offset of  $0.01^\circ$ , which implies that –assuming a beam size of 2.7 arcmin in C-band– (1) 4.5 passages were carried out per beam on average, and (2)  $\sim 17$  samples beam<sup>-1</sup> scan<sup>-1</sup> were taken. The total duration of an observation (defined as a complete map along both RA and Dec directions) at 6.9 GHz was about 6 h. Stable weather conditions (possibly a clear sky) result in the production of high-quality maps; in only two epochs (2019 January 17 and 2019 March 5) weather conditions were excellent during the observation (Tab. 1), while in the other epochs high cloud coverage and rainy conditions provided poor and changeable opacity.

The spectral flux density of the target was reconstructed by observing a set of OTF cross-scans on standard point-like calibrators at the considered frequencies (3C286, 3C295, 3C123, 3C48, 3C147 and NGC7027) before and after each target map, assuming calibrator fluxes as obtained by [53], using the VLA data [54].

### 3.1 Imaging data analysis and calibration

The imaging procedure is performed through SRT Single-Dish Imager (SDI), a tool optimized for OTF scan mapping; SDI performs automated baseline subtraction, RFI rejection and calibration, generating standard SAOImage DS9<sup>5</sup> output FITS images suitable for further analysis [54,50].

The conversion factor Jy/counts ( $K_{conv}$ ) for the calibration is defined as the ratio between the peak flux density  $S_{cal}$  (at that specific observing frequency) and the maximum value of the observed instrumental counts in the calibrator image  $C_{max}$ . This factor is roughly independent of the elevation since C-band SRT gain curve is approximately flat (within a few percent) thanks to optimized settings of the active surface (shaped mode) [49,54,44,50]. We considered calibrators and target observations in the elevation range  $\sim 30-80^\circ$  since the antenna beam has proved to be very stable in that interval. A Gaussian shape provides a very good fit to OTF scans on calibrators, thus we assumed a beam solid angle for image calibration (in units of steradians) as [50]:

$$\Omega_{beam} = \pi \left( 1.2 \times \frac{HPBW}{2} \right)^2, \quad (1)$$

where  $HPBW$  is in units of arcmin.

<sup>5</sup> <http://ds9.si.edu>

Calibrated data were binned through ARC-tangent projection using pixel sizes  $\sim 1/4$  of the HPBW, corresponding to the effective resolution of the images [50], and the DS9 FITS images were produced in units of Jy/beam and Jy/sr. The statistical errors on flux density measurements are calculated through the flux density standard deviation for each pixel; moreover, the integrated statistical flux errors (typically  $< 0.5\%$ ) are well below systematic errors, estimated to be  $\lesssim 3\%$  [50].

#### 4 Detection methods for point sources

Our study tackles the question "How is optimally detected a weak source surrounded by other sources and affected by background?" To answer it, we need a robust, reliable and sensitive detection method.

We analyze three detection methods according to sensitivity and robustness: 'quick-look' (Method A, Sect. 4.1), 'source extraction' (Method B, Sect. 4.2), and fitting procedure with a 2-Dimensional Gaussian (Method C, Sect. 4.3). These methods are applicable to radio detection, such as the case of highly variable sources, which can have a very weak radio flux density during periods of quiescent states, and/or in a crowded regions of the sky. This is the case for instance of the microquasar GRS 1915+105. Regarding undetected (or very faint) sources, in the radio domain the upper limit for the flux density is usually estimated through 2-times the minimum RMS of a region in the image not significantly affected by other sources ( $RMS_{min}$ ). Such upper limits can be overestimated if the target is surrounded by other sources (crowded field), and in any case it does not represent the actual sensitivity at the source position.

For this analysis we developed a specific Python code, where the input is the calibrated FITS image (suited for INAF network) produced by SDI, and the output consists of the flux density  $A_m$  and its uncertainty  $\Delta A_m$ . This code will be directly implemented in the SDI package soon. We define the significance as the signal-to-noise ratio  $S = A_m/\Delta A_m$ , using each technique (in turn characterized by different uncertainties). Tab. 2 reports the upper limits obtained with each method. It is worth noting that our analysis does not consider the systematic errors of the antenna, as they are negligible compared with the statistical ones for very weak sources (Section 3.1).

##### 4.1 Method A - Quick-look detection method

Method A consists of an estimation of the flux density of the target  $S_{source}$ , corresponding to the pixel of the source position (peak flux of the point-like target taken in Jy/beam units); the uncertainty is defined as  $RMS_{min}$ , the minimum RMS of a fixed region (a rectangle of size 1.5 beam for this work) in the image. In case the source is not detected, this is a suitable method to get a rough upper limit; we assume  $2 \times RMS_{min}$  as upper limit.

##### 4.2 Method B - Source extraction method

Method B is typical of X-/gamma-ray and optical imaging. At the beginning, the procedure extracts the sum of the Jy/pixel values corresponding to two regions:

**Table 2** Flux densities for Methods A, B and C (fixed position and position criterion) with SRT in C-band. In case of non-detection (numbers in bold font), we injected a fake sources in the image, and the target is detected at  $3\sigma$ -level; therefore we assumed the upper limit as  $2\sigma$ -level of the  $3\sigma$ -level detection.

Epoch (aaaa/mm/dd)	Source	Method A (mJy)	Method B (mJy)	Method C (fixed) (mJy)	Method C (free) (mJy)
2018/12/11	GRB 181201A	<b>3.9</b>	<b>2.2</b>	<b>7.4</b>	<b>4.6</b>
2019/01/17	GRB 190114C	<b>3.4</b>	<b>2.5</b>	<b>1.8</b>	<b>2.7</b>
2019/01/23	GRB 190114C	<b>6.5</b>	<b>5.1</b>	<b>3.0</b>	<b>6.5</b>
2019/01/30	GRB 181201A	<b>11.0</b>	<b>8.5</b>	<b>7.5</b>	<b>7.6</b>
2019/03/05	GRB 190114C	<b>5.2</b>	<b>2.4</b>	<b>2.5</b>	<b>3.5</b>
2019/03/22	GRB 181201A	<b>36.4</b>	<b>25.9</b>	<b>18.2</b>	<b>24.0</b>
2019/05/22	GRS 1915+105	159.0 ± 14.7	177.0 ± 11.7	187.0 ± 8.9	-

1. the region –centered on the source– with a radius of  $n$  HPBW<sup>6</sup>, depending on the maximum  $S/N$  ratio in the range  $1.5 - 5$  HPBW ( $T_{s,sum}$ ); the  $n$  value depends on the source and local background flux densities.
2. a background area taken from an image region free of sources ( $T_{b,sum}$ ).

After normalizing  $T_{s,sum}$  and  $T_{b,sum}$  with respect to the same extraction area, the contribution of residual background from the image is calculated through the difference  $D = T_{s,sum} - T_{b,sum}$ . The flux density of our target (in units of Jy) is calculated as  $S = D \times K_{conv} \times P$ , where  $K_{conv}$  is the calibration factor (Sect. 3.1) and  $P = \Omega_{pix}/\Omega_{beam}$  (where  $\Omega_{pix}$  is the solid angle of a single pixel of the image). The uncertainty on  $S$  is calculated as  $\Delta S = \Delta T_{s,sum} + \Delta T_{b,sum}$ ; the uncertainties  $\Delta T$  correspond to  $\sqrt{N_{pix}} \times RMS_{min}$ , where  $N_{pix}$  is the total number of pixels of the extraction region.

#### 4.3 Method C - 2-Dimensional Gaussian fitting procedure detection method

In Method C we fit the image using a 2-D Gaussian plus a constant, defined as:

$$G = N_0 + A \times e^{-u(x,y,x_0,y_0,\theta,a,b)/2}, \quad (2)$$

where  $N_0$  is the residual background,  $A$  is the amplitude and  $u$  is the ellipse equation, dependent on the position  $(x_0, y_0)$ , the semimajor and semiminor axes  $(a, b)$  and the position angle  $\theta$ <sup>7</sup>.

Our Python code adopts a non-linear least squares method through the Python package CURVEFIT. The parameter uncertainties are described by the square root of the diagonal elements of the covariance matrix.

### 5 Setting up of the code: simulations of point-like sources

To test the robustness of our fitting procedure, we inject a fake point-like source in image convolved with a 2-D Gaussian (Eq. 2) with fixed HPBW ( $a = b = 2.7$  arcmin, corresponding to the SRT C-band beam). We then create a sample of images, each of which composed by one fake point-like source with increasing Gaussian peak  $A$  in order to understand when the target becomes distinguishable from the background. In this way we tested the robustness

<sup>6</sup> The half power beamwidth (HPBW) is the angular separation in which the magnitude of the radiation pattern decrease by 50% (or 3 dB) from the peak of the main beam.

<sup>7</sup> For our purpose, we fixed  $a = b$  (circular beam) and  $\theta = 0$ .

of our fitting procedure by injecting fake point sources (one per image per trial) of varying amplitudes. We implemented two kinds of simulations: (1) full simulation of the source and the background (Sect. 5.1), and (2) simulation of the source in a real background/image (Sect. 6.1). Finally, for each image of this sample we apply these detection methods, comparing them in terms of sensitivity and robustness. For Method C, we assume  $A_m$  as free parameter, and we apply two combinations to localize the target in the image during the fitting procedure: (1) we fix the target position parameters  $(x_{0,m}, y_{0,m})$  to their true values, which are known in the simulation (fixed position case), and (2) we assume  $x_{0,m}$  and  $y_{0,m}$  as free parameters (free position case). Regarding the free position case, we assume two additional detection criteria: (1) the positional uncertainty  $\Delta x$  and  $\Delta y$  (obtained by fitting procedure) must be  $\leq 10\%$  of the actual source position, and (2)  $x_{0,m}$  and  $y_{0,m}$  must to be inside the 4% region of the true position. If these conditions are not satisfied, we consider it a non-detection.

We assume that –for each detection method– the source is detected at  $3\sigma$ -level, whereas upper limits are reported at  $2\sigma$ -level.

### 5.1 Full simulation

This procedure, consisting in the simulation both of the background and the source, is crucial to set up our Python code for the analysis. We simulated an image of  $46 \times 46$  pixels, corresponding to 27.6 arcmin (the pixel size is 36 arcsec), with a fake source at  $x_0 = y_0 = 23$  with  $A$  increasing from 0.1 mJy with step 0.1 mJy; we assume five cases of the background  $N_0$  ( $10^{-3}$ , 1, 2, 5 and 10 mJy).

The results shown in Figs. 1, 2, 3, 4, suggest that the Method C provides an excellent accordance with the original flux density injected in the 2D-Gaussian fake source, implying a good significance  $\mathcal{S}$ ; on the other hand, method A shows high uncertainties and we recommended it only for a rapid and preliminary estimation of the flux density and/or when the instrument beam is poorly known. According to the best case (Method C), in the fixed position case the  $3\sigma$ -level detection is reached for flux densities ranging between  $\geq 2$  mJy ( $N_0 = 1$  mJy, Fig. 1) and  $\geq 15$  mJy ( $N_0 = 10$  mJy, Fig. 4); in the free position case, this detection ranges between  $\geq 2.3$  mJy ( $N_0 = 1$  mJy, Fig. 1) and  $\geq 20.8$  mJy ( $N_0 = 10$  mJy, Fig. 4); moreover, the ideal case  $N_0 = 10^{-3} \sim 0$  mJy corresponds to a source  $3\sigma$ -level detection at the limiting sensitivity of  $\geq 0.1$  mJy.

For Method B, simulations suggest an optimal extraction region (providing the maximum  $S/N$  ratio) of  $\sim 2$  HPBW; this corresponds to 93.75% of the Gaussian beam solid angle, and hence for real observations we apply a corrective factor of 1.07 to the flux densities obtained with this method.

## 6 Detection methods applied to real observations

The analysis of these detection methods in the case of real radio observations shows very interesting aspects about the imaging of faint sources and the upper limit estimation in case of undetected targets. Fig. 5 (left) shows the image of the detected source GRS 1915+105; our detection methods produce similar values of flux densities (Tab. 2). In particular, Method C is able to detect a single source in the field also in free position case, despite the region being characterized by variable background and strong RFI. The analysis on this source (Tab. 2) shows that Method C provides an uncertainty on the flux density measurement of



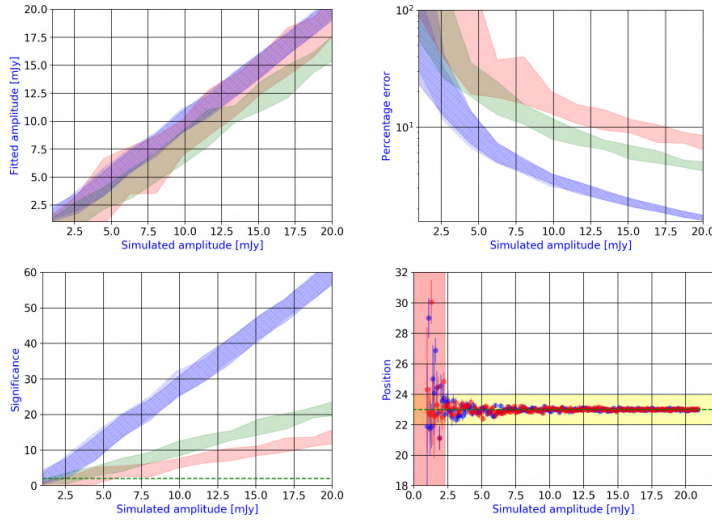


**Fig. 1** Results of full simulation procedure for the case  $N_0 = 1$  mJy. Color shaded area in the panels are bounded by the maximum and the minimum values computed in 20 bins of flux densities. Red, green and blue regions are Method A, B and C, respectively; for Method C, uniform region indicates fix position case, and hatched region indicates free position case. Top left: plot of the fitted amplitude  $A_m$  as a function of the simulated amplitude  $A_0$  (fixed position in blue, free position in red). Top right: plot of the relative error on the fitted peak as a function of the simulated amplitude  $A_0$  (fixed position in blue, free position in red). Bottom left: plot of the simulated amplitude  $A_0$  as a function of the significance  $S$  (fixed position in blue, free position in red); green dotted line indicates the  $2\sigma$ -level for upper limits. Bottom right: plot of the fitted position  $x_0$  (in red) and  $y_0$  (in blue), for the case of free position, as a function of the simulated amplitude  $A_0$ ; green line indicates the true position of the fake source; yellow area indicates the 4% region of good positional detection of the source, and red area indicates the excluded regions from the positional criteria.

$\sim 5\%$  ( $\sim 7\%$  for Method B, and  $\sim 9\%$  for Method A), suggesting that this method is the most accurate and robust for flux densities measurements.

The image on the right in Fig. 5 shows an example of a field characterized by an undetected source (GRB 190114C); we discuss this part in the following Section. Tab. 2 shows in detail the results of our Python code for real observations.

### 6.1 Real images of undetected sources

In single-dish mode, often faint radio sources could be non-detectable. In this context we wonder "What is the minimum significance level needed for source detection?". To answer this question, we need to inject fake sources in the real radio image (Eq. 2) in order to understand when the target becomes distinguishable from the background. These fake sources are located in the position detected by other facilities (from radio to high-energy frequencies); we simulated increasing values of  $A$  from 0.1 mJy to the maximum value of flux density in each image, with step 0.1 mJy. A detection of the fake injected source at  $2\sigma$ -level sets the precise upper limit in the real image at the actual source position.

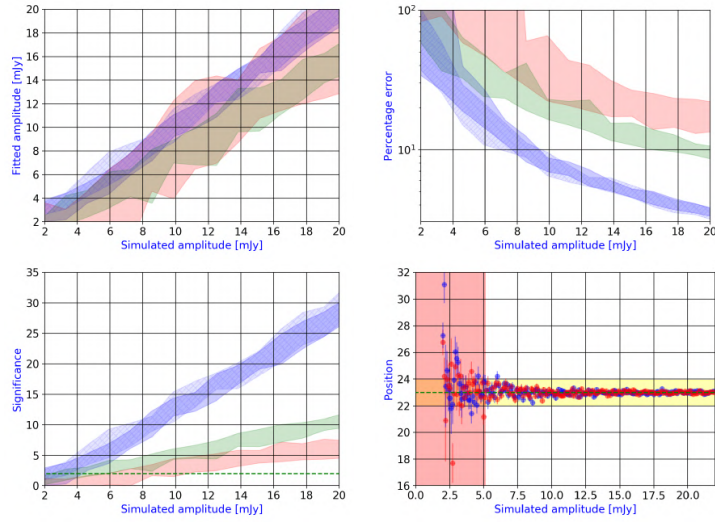


**Fig. 2** Results of full simulation procedure for the case  $N_0 = 2$  mJy. See the caption of Fig. 1 for a full description of the symbols and plots.

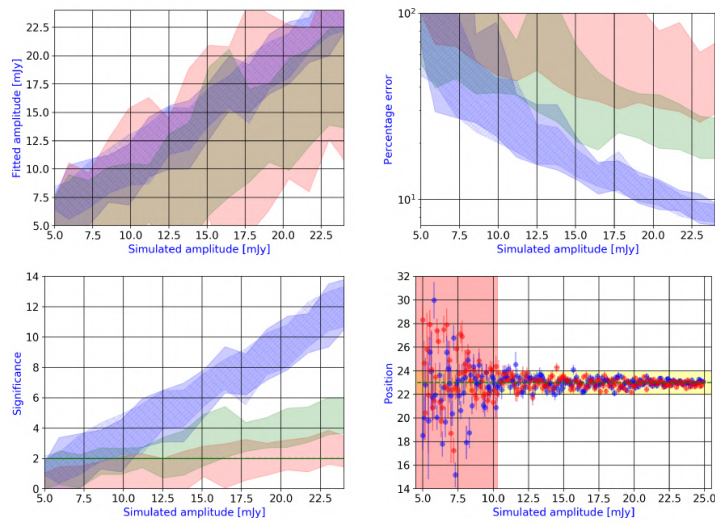


**Fig. 3** Results of full simulation procedure for the case  $N_0 = 5$  mJy. See the caption of Fig. 1 for a full description of the symbols and plots.

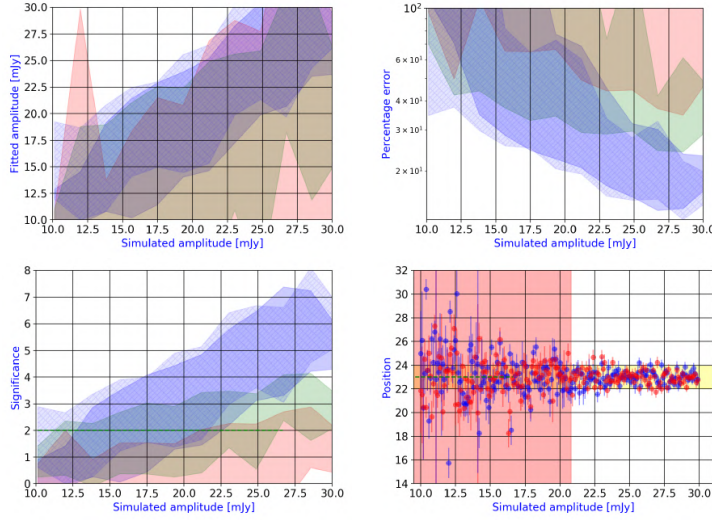


**Fig. 4** Results of full simulation procedure for the case  $N_0 = 10$  mJy. See the caption of Fig. 1 for a full description of the symbols and plots.

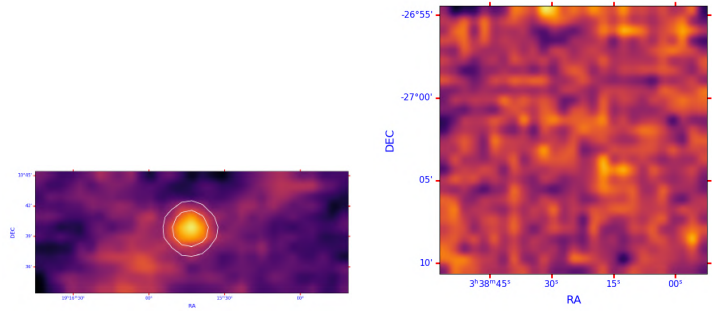


**Fig. 5** Gaussian smoothed images of GRS 1915+105 (left) and GRB 190114C (right). White circles indicate contours with respect to 2 (outer) and 5 (inner) times the value of  $RMS_{min}$ .

The first epoch at 2018 December 11 shows  $RMS_{min} \sim 1.9$  mJy (Tab. 3), resulting in a standard upper limit estimation of 3.8 mJy ( $2\sigma$ -level). The injection of fake source in this field shows that the  $2\sigma$ -level upper limit of the source is  $\sim 3.9$  mJy for Method A,  $\sim 2.2$  mJy for Method B and  $\sim 7.4$  mJy for Method C (Fig. 6). The additional criterion for the free position case (with a fake source) of Method C shows a detection at  $\sim 4.6$  mJy where, for the Method C, the significance  $\mathcal{S}$  is  $\sim 5$  ( $\sim 5$  for Method A, and  $\sim 7$  for method B). This is the only case where Method C is characterized by  $2\sigma$ -level upper limit higher than Method A and B estimations: this high value originates probably by an inaccurate baseline subtraction.

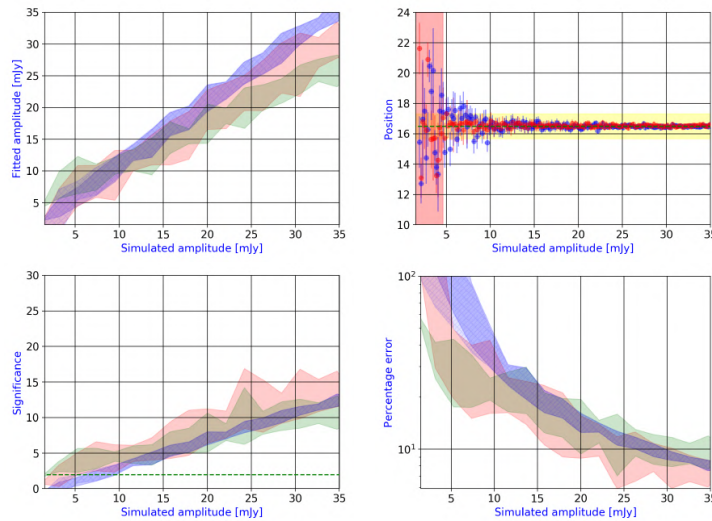


**Fig. 6** Overview of fitting procedure for a fake source (suited by a 2D-Gaussian) about SRT observation of GRB 181201A at 2018 December 11. See the caption of Fig. 1 for a full description of the symbols and plots.

The second epoch at 2019 January 17 shows a very low  $RMS_{min}$  ( $\sim 1.5$  mJy, Tab. 3), caused probably by the optimal weather conditions at that epoch, resulting in an high image quality. As we can see in Fig. 7, we confirm the results for the full simulation procedure: the most accurate method is the method C, and the worst method is the method A (Fig. 7). The injection of fake source in this field suggests a  $2\sigma$ -level upper limit at  $\sim 3.4$  mJy for Method A,  $\sim 2.5$  mJy for Method B and  $\sim 1.8$  mJy for Method C (Fig. 7); the additional criterion for the free position case for Method C shows a detection at  $\sim 2.7$  mJy, where the significance  $\mathcal{S}$  is  $\sim 4$  ( $\sim 2.5$  for both Method A and B; Fig. 7).

The third epoch at 2019 January 23 (Fig. 8) is characterized by  $RMS_{min} \sim 2.7$  mJy; Tab. 3), resulting in a standard upper limit estimation of 5.4 mJy ( $2\sigma$ -level). The analysis on this epoch seems to confirm the results for the full simulation procedure. The most accurate method is the method C, and the worst method is the method A (Fig. 8); moreover, methods A overestimates the flux densities, whereas method B underestimates these flux densities (Fig. 8). The injection of fake source in this field shows suggests a  $2\sigma$ -level upper limit at  $\sim 6.5$  mJy for Method A,  $\sim 5.1$  mJy for Method B and  $\sim 3.0$  mJy for Method C (Fig. 8); the additional criterion for the free position case for Method C shows a detection at  $\sim 6.5$  mJy, where the significance  $\mathcal{S}$  is  $\sim 4$  ( $\sim 2$  for Method A and  $\sim 2.5$  for Method B; Fig. 8).

The fourth epoch at 2019 January 30 shows  $RMS_{min} \sim 3.3$  mJy (Tab. 3). As we can see in Fig. 9, the most accurate method is the method C, and the worst method is the method A. The injection of fake source in this field suggests a  $2\sigma$  upper limit at  $\sim 11$  mJy for Method A,  $\sim 8.5$  mJy for Method B and  $\sim 7.5$  mJy for Method C (Fig. 9); the additional criterion for Method C (free position case with a fake source) shows a detection at  $\sim 7.6$  mJy, where the significance  $\mathcal{S}$  is  $\sim 3$  ( $\sim 2$  and  $\sim 1.5$  for Method B and A, respectively; Fig. 9).

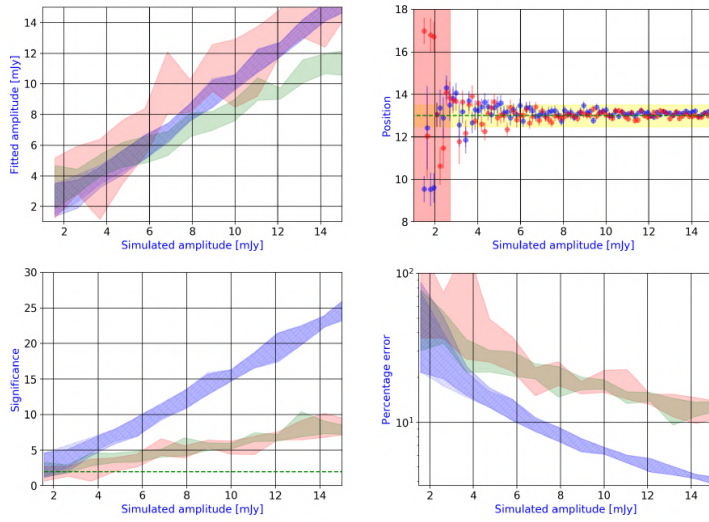


**Fig. 7** Overview of fitting procedure for a fake source (suited by a 2D-Gaussian) about SRT observation of GRB 190114C at 2019 January 17. See the caption of Fig. 1 for a full description of the symbols and plots.

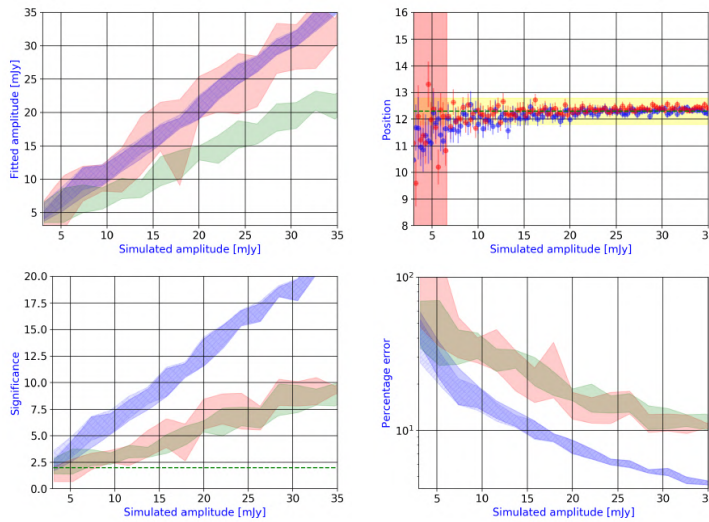


**Fig. 8** Overview of fitting procedure for a fake source (suited by a 2D-Gaussian) about SRT observation of GRB 190114C at 2019 January 23. See the caption of Fig. 1 for a full description of the symbols and plots.

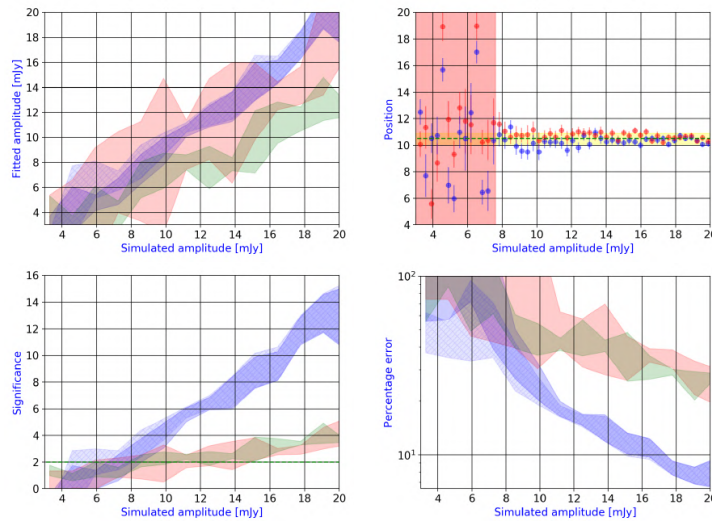


**Fig. 9** Overview of fitting procedure for a fake source (suited by a 2D-Gaussian) about SRT observation of GRB 181201A at 2019 January 30. See the caption of Fig. 1 for a full description of the symbols and plots.

The fifth epoch at 2019 March 5 shows the lowest value of  $RMS_{min}$  in our analysis ( $\sim 1.3$  mJy, Tab. 3). The analysis, as in the previous cases, confirms the results for the full simulation procedure (Sect. 5.1), where the most accurate method is the method C, and the worst method is the method A (Fig. 10). The injection of fake source in this field suggests a  $2\sigma$ -level upper limit at  $\sim 5.2$  mJy for Method A,  $\sim 2.4$  mJy for Method B and  $\sim 2.5$  mJy for Method C (Fig. 10); the additional criterion for the free position case for Method C shows a detection at  $\sim 3.5$  mJy, where the significance  $\mathcal{S}$  is  $\sim 4$  ( $\sim 3$  and  $\sim 1$  for Method B and A, respectively; Fig. 10). This epoch shows the power of the Method C in terms of accuracy and robustness: at the same conditions we are able to detect a source where Method A fails (Fig. 10, bottom right).

On the other hand, the last epoch at 2019 March 22 is the worst image in our followup campaign, characterized by a very bad weather at SRT site (rain and wind) and  $RMS_{min} \sim 9.6$  mJy (Tab. 3). The injection of fake source in this field suggests a  $2\sigma$ -level upper limit at  $\sim 36.4$  mJy for Method A,  $\sim 25.9$  mJy for Method B and  $\sim 18.2$  mJy for Method C (Fig. 11). The additional criterion for the free position case for Method C shows a detection at  $\sim 24$  mJy, where the significance  $\mathcal{S}$  is  $\sim 4$  ( $\sim 2$  for Method A and B; Fig. 11).

## 7 Discussion

Radio observations of real fields are intrinsically characterized by several features (such as the background, systematic errors of the radio devices or weather conditions) which directly impact on the detection and flux estimation of –especially faint– sources. The analysis of real images obtained with SDI confirms the results of the full simulation procedure (Sect. 5.1), showing that –especially for faint sources (mJy or sub-mJy events)– a refined knowledge of



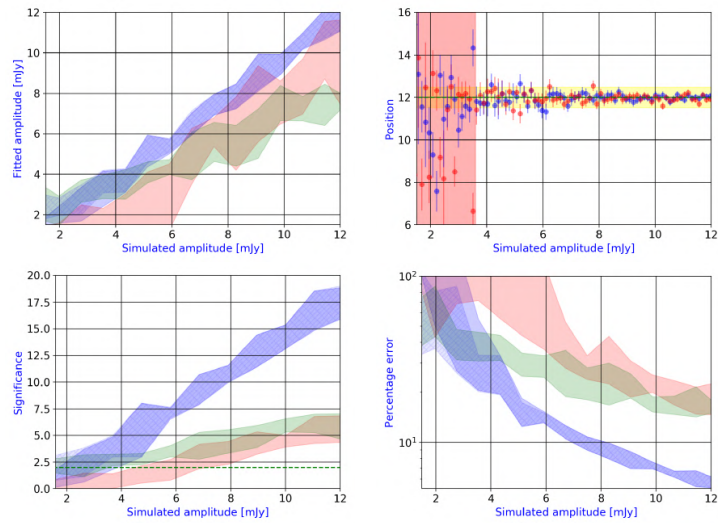


**Fig. 10** Overview of fitting procedure for a fake source (suited by a 2D-Gaussian) about SRT observation of GRB 190114C at 2019 March 5. See the caption of Fig. 1 for a full description of the symbols and plots.

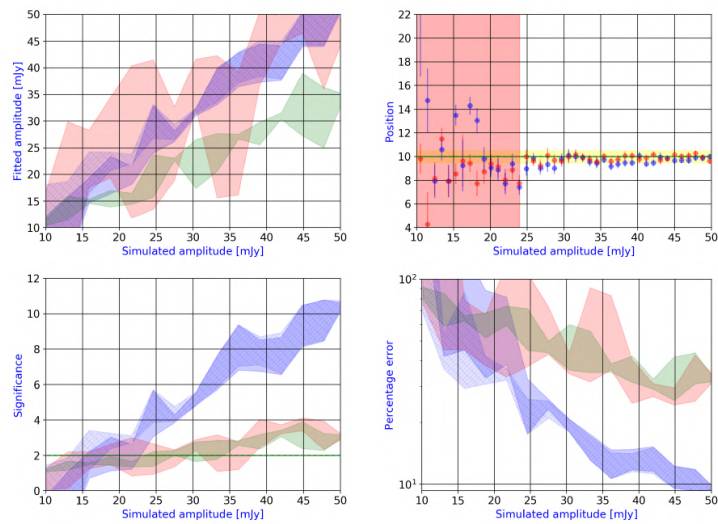


**Fig. 11** Overview of fitting procedure for a fake source (suited by a 2D-Gaussian) about SRT observation of GRB 181201A at 2019 March 22. See the caption of Fig. 1 for a full description of the symbols and plots.

the baseline (such as the background, other sources, RFI, weather, and the systematic errors of the antenna) is crucial. These images show that Method C is the most accurate, whereas the least accurate one is Method A, which either under- or overestimates flux densities, possibly due to the approximation of the 2D-Gaussian peak with respect to the corresponding pixel peak.

Method B tends to underestimate flux densities, possibly due to inaccurate baseline subtraction in SDI package, considering that this method does not consider RFI or other sources near the target. The baseline subtraction in SDI package is crucial especially for faint sources. In this respect, Method C is also particularly sensitive to the baseline subtraction.

In Section 6.1 we estimated  $2\sigma$  upper limits and set strong positional constraints, emphasizing how the knowledge of background is essential. These limits strongly depend on the weather conditions (e.g. rain, humidity, and cloud cover), especially for observations of very faint sources, as is our case. From the analysis of real images, we do not detect the afterglows of either 181201A or 190114C in any images at  $S \gtrsim 5$ . Our upper limits lie above the VLA and ATCA flux densities [23,35] and East Asia VLBI upper limits [55] obtained almost at the same epoch. In particular, our upper limit of 17 January 2019 for 190114C (1.8 mJy), estimated with Method C in fixed position case (Tab. 2), lies just above the interpolated ATCA flux density ( $\sim 1.6$  mJy) calculated in C-band (6.9 GHz) at the time of SRT observation (2.9 d after the GRB trigger). This value is affected by scintillation for about 35% of the observed flux density [35], and hence –even more so– is compatible with our upper limit.

In the literature there is an upper limit (0.6 mJy at  $3\sigma$ ) with SRT in C-band for an old GRB afterglow (GRB 151027A, [56]), significantly lower than our values. It is not straightforward to compare results obtained under very different observing conditions, so the discrepancy should not necessarily be alarming. In particular, [56] did not carry out a mapping, but limited their observations to cross-scans centered on source, following an approach designed for blazar observations [1]. While such a technique benefits from a higher efficiency (through a larger fraction of time spent on-source), it is on the other hand more limited in the presence of a complex background. Mapping thus represents a more reliable and general approach, particularly in the Galactic plane and/or at high frequency.

The success of the observations of faint sources (or the quality of the image) for SRT is described by the limiting sensitivity of a radio astronomical receiver, calculated with the radiometer equation  $S = \phi \Delta t^{-1/2}$ , where  $S = RMS_{min}$  (in units of mJy) and  $\delta t$  is the total observing time of the source (in units of hours). Therefore we calculate the parameter  $\phi = S \Delta t^{1/2}$  (in units of mJy h<sup>1/2</sup>) that provides a rough estimation of all the contamination factors of the image, such as the background, other sources beyond our target, RFI phenomenon, weather conditions, and systematic errors of the single-dish facility. Our radio campaign shows that (1)  $\phi \leq 3.5$  mJy h<sup>1/2</sup> indicates a high-quality image (with a good upper limit), (2)  $\phi$  between 3.5 and 8 mJy h<sup>1/2</sup> indicates a medium-quality image, and (3)  $\phi > 8$  mJy h<sup>1/2</sup> indicates a low-quality image (Tab. 3).

## 8 Conclusions

We analyzed three detection methods having different degrees of sensitivity and robustness ('quick-look' or Method A, 'source extraction' or Method B, fitting procedure with a 2-D Gaussian or Method C). Their performances were assessed in the case of weak sources in single-dish mode through the INAF network of radiotelescopes. To this aim, we developed



**Table 3** Minimum value of  $RMS_{min}$  (estimated with Method A) for the undetected sources observed in SRT maps (in units of mJy), based on 1.5 beams of SRT receiver.  $\delta t$  indicates the integration time (in units of hours), and  $\phi = RMS_{min}/\delta t$  (in units of mJy h<sup>1/2</sup>).

Epoch (aaaa/mm/dd)	GRB	Receiver	$\delta t$ (h)	$RMS_{min}$ (mJy)	$\phi$ (mJy h <sup>1/2</sup> )
2018/12/11	181201A	SRT-C	3.84	1.93	3.78
2019/01/17	190114C	SRT-C	4.80	1.49	3.26
2019/01/23	190114C	SRT-C	4.80	2.70	5.92
2019/01/30	181201A	SRT-C	5.28	3.26	7.49
2019/03/05	190114C	SRT-C	3.60	1.30	2.47
2019/03/22	181201A	SRT-C	4.08	9.57	19.33

a specific Python code, where the input data are the calibrated FITS images (suited for INAF network) produced by SDI, and the output consists in flux densities and corresponding uncertainties.

This new approach for the SRT data analysis enhances the capabilities of this radiotelescope, especially optimizing the detection of faint sources, as is the case for GRB afterglows or GW radio counterparts. We observed two GRB afterglows (181201A and 190114C) and the Galactic binary GRS 1915+105 with SRT in C-band (6.9 GHz).

Our comparative analysis of the different detection methods made extensive use of simulations as a useful complement of actual radio observations. In the regime of faint/undetected sources, simulations of injected point-like sources are used for the assessment; in particular, the estimated flux densities (or upper limits in case of undetected sources) strongly depend on the weather conditions (e.g. rain, humidity, and cloud cover). Simulations of both background and source are essential to characterize the detection of point-like sources in images/fields, and as such they were used to calibrate our software for the analysis of real targets. This analysis shows that the Method C provides an excellent agreement between fitted and real injected flux density. Source detection at  $3\sigma$  confidence (for  $N_0 \gtrsim 1$  mJy) is feasible for flux densities  $\gtrsim 2$  mJy; on the other hand, Method A shows high uncertainties and we recommended it only for a rapid and preliminary estimation of the flux density and/or when the instrument beam is poorly known.

These results are further corroborated by the analysis of real radio observations. For GRS 1915+105, Method C (in free position case) is able to detect it, although the region is characterized by a variable background. Images with undetected sources offer the possibility to study the conditions required for a detection through the injection of a fake source in the real radio image, located at the position previously found by other facilities. Our results show that –especially for faint sources (mJy or sub-mJy events)– a deep knowledge of the radio background is crucial for accurate flux density measures. These images show that Method C pushes down the sensitivity limits of this radiotelescope –with respect to more traditional techniques– to  $\sim 1.8$  mJy, improving by  $\sim 40\%$  compared with the initial value.

The image quality for faint sources is described by  $\phi$ , that provides a rough estimation of all the contamination factors affecting the image; our campaigns show that the range  $\phi \leq 3.5$  mJy h<sup>1/2</sup> corresponds to a high-quality image,  $3.5 \leq \phi/(\text{mJy h}^{1/2}) \leq 8$  corresponds to a medium-quality image, whereas  $\phi > 8$  mJy h<sup>1/2</sup> characterizes a low-quality image.

The code developed for this analysis will be further improved adopting a Bayesian approach in the fitting procedure that incorporates the likelihood analysis for crowded images. In the multi-messenger era, it can be employed to analyze (1) not only faint sources such as

the radio counterparts of GRBs or GWs, but also other sources such as solar flares<sup>8</sup>, and (2) images obtained through interferometric radiotelescopes, such as the Very Large Baseline Array (VLBA<sup>9</sup>), the European Very Large Baseline Interferometry Network (EVLBI<sup>10</sup>, of which SRT is part), LOw Frequency ARray (LOFAR, [57]) or the next generation Square Kilometer Array facility (SKA, [58]).

**Acknowledgements** The Sardinia Radio Telescope is funded by the Department of University and Research (MIUR), the Italian Space Agency (ASI), and the Autonomous Region of Sardinia (RAS), and is operated as a National Facility by the National Institute for Astrophysics (INAF). M. Marongiu gratefully acknowledges the University of Ferrara for the financial support of his PhD scholarship. M. Marongiu thanks P. Bergamini and G. Angora for the useful discussion about Python programming language and data analysis; moreover, M. Marongiu is very grateful to K. D. Alexander for useful conversations. We acknowledge the TAC, the scheduler and the SRT staff for approving and executing these followup campaigns.

### ORCID iDs

M. Marongiu: <https://orcid.org/0000-0002-5817-4009>  
 A. Pellizzoni: <https://orcid.org/0000-0002-4590-0040>  
 E. Egron: <https://orcid.org/0000-0002-1532-4142>  
 T. Laskar: <https://orcid.org/0000-0003-1792-2338>  
 M. Giroletti: <https://orcid.org/0000-0002-8657-8852>  
 S. Loru: <https://orcid.org/0000-0001-5126-1719>  
 A. Melis: <https://orcid.org/0000-0002-6558-1315>  
 G. Carboni: <https://orcid.org/0000-0002-2056-7501>  
 C. Guidorzi: <https://orcid.org/0000-0001-6869-0835>  
 S. Kobayashi: <https://orcid.org/0000-0001-7946-4200>  
 N. Jordana-Mitjans: <https://orcid.org/0000-0002-5467-8277>  
 A. Rossi: <https://orcid.org/0000-0002-8860-6538>  
 C. G. Mundell: <https://orcid.org/0000-0003-2809-8743>  
 R. Concu: <https://orcid.org/0000-0003-3621-349X>  
 R. Martone: <https://orcid.org/0000-0002-0335-319X>  
 L. Nicastro: <https://orcid.org/0000-0001-8534-6788>

### Conflict of interest

The authors declare that they have no conflict of interest.

### References

1. M. Giroletti, S. Righini, MNRAS(MNRAS submitted)
2. R.J. Maddalena, *Reduction and Analysis Techniques* (2002), *Astronomical Society of the Pacific Conference Series*, vol. 278, pp. 329–352
3. P. Chandra, D.A. Frail, *Astrophysical Journal* **746**, 156 (2012). DOI 10.1088/0004-637X/746/2/156

<sup>8</sup> <https://sites.google.com/inaf.it/sundish/home>

<sup>9</sup> <https://science.nrao.edu/facilities/vlba>

<sup>10</sup> [www.evlbi.org](http://www.evlbi.org)

4. P. Chandra, *Advances in Astronomy* **2016**, 296781 (2016). DOI 10.1155/2016/296781
5. B.P. Abbott, R. Abbott, T.D. Abbott, F. Acernese, K. Ackley, C. Adams, T. Adams, P. Addesso, R.X. Adhikari, V.B. Adya, et al., *Astrophysical Journal, Letters* **848**, L12 (2017). DOI 10.3847/2041-8213/aa91c9
6. K.D. Alexander, E. Berger, W. Fong, P.K.G. Williams, C. Guidorzi, R. Margutti, B.D. Metzger, J. Annis, P.K. Blanchard, D. Brout, D.A. Brown, H.Y. Chen, R. Chornock, P.S. Cowperthwaite, M. Drout, T. Eftekhari, J. Frieman, D.E. Holz, M. Nicholl, A. Rest, M. Sako, M. Soares-Santos, V.A. Villar, *Astrophysical Journal, Letters* **848**, L21 (2017). DOI 10.3847/2041-8213/aa905d
7. R. Margutti, K.D. Alexander, X. Xie, L. Sironi, B.D. Metzger, A. Kathirgamaraju, W. Fong, P.K. Blanchard, E. Berger, A. MacFadyen, D. Giannios, C. Guidorzi, A. Hajela, R. Chornock, P.S. Cowperthwaite, T. Eftekhari, M. Nicholl, V.A. Villar, P.K.G. Williams, J. Zrake, *Astrophysical Journal, Letters* **856**, L18 (2018). DOI 10.3847/2041-8213/aab2ad
8. J. Granot, R. Sari, *Astrophysical Journal* **568**(2), 820 (2002). DOI 10.1086/338966
9. S.R. Kulkarni, S.G. Djorgovski, S.C. Odewahn, J.S. Bloom, R.R. Gal, C.D. Koresko, F.A. Harrison, L.M. Lubin, L. Armus, R. Sari, G.D. Illingworth, D.D. Kelson, D.K. Magee, P.G. van Dokkum, D.A. Frail, J.S. Mulchaey, M.A. Malkan, I.S. McClean, H.I. Teplitz, D. Koerner, D. Kirkpatrick, N. Kobayashi, I.A. Yadigaroglu, J. Halpern, T. Piran, R.W. Goodrich, F.H. Chaffee, M. Feroci, E. Costa, *Nature* **398**, 389 (1999). DOI 10.1038/18821
10. T. Laskar, E. Berger, B.A. Zauderer, R. Margutti, A.M. Soderberg, S. Chakraborti, R. Lunnan, R. Chornock, P. Chandra, A. Ray, *ApJ* **776**, 119 (2013). DOI 10.1088/0004-637X/776/2/119
11. T. Laskar, K.D. Alexander, R. Gill, J. Granot, E. Berger, C.G. Mundell, R. Barniol Duran, J. Bolmer, P. Duffell, H. van Eerten, W.f. Fong, S. Kobayashi, R. Margutti, P. Schady, *Astrophysical Journal, Letters* **878**(1), L26 (2019). DOI 10.3847/2041-8213/ab2247
12. J.E. Rhoads, *Astrophysical Journal* **525**, 737 (1999). DOI 10.1086/307907
13. R. Sari, T. Piran, J.P. Halpern, *ApJ* **519**, L17 (1999). DOI 10.1086/312109
14. D.A. Frail, E. Waxman, S.R. Kulkarni, *Astrophysical Journal* **537**(1), 191 (2000). DOI 10.1086/309024
15. K.D. Alexander, T. Laskar, E. Berger, C.G. Mundell, R. Margutti, *GRB Coordinates Network* **23726**, 1 (2019)
16. A. Volnova, E. Mazaeva, D. Buckley, A. Pozanenko, *GRB Coordinates Network* **23477**, 1 (2018)
17. L. Izzo, A. Noschese, L. D'Avino, M. Mollica, *GRB Coordinates Network* **23699**, 1 (2019)
18. S. Mereghetti, D. Gotz, C. Ferrigno, E. Bozzo, V. Savchenko, L. Ducci, J. Borkowski, *GRB Coordinates Network* **23469**, 1 (2018)
19. M. Arimoto, M. Axelsson, M. Ohno, *GRB Coordinates Network* **23480**, 1 (2018)
20. F. Pintore, S. Mereghetti, D. Gotz, C. Ferrigno, E. Bozzo, V. Savchenko, L. Ducci, J. Borkowski, *GRB Coordinates Network* **23472**, 1 (2018)
21. C. Cai, C.K. Li, X.B. Li, G. Li, J.Y. Liao, S.L. Xiong, C.Z. Liu, X.F. Li, Z.W. Li, Z. Chang, X.F. Lu, J.L. Zhao, A.M. Zhang, Y.F. Zhang, C.L. Zou, Y.J. Jin, Z. Zhang, T.P. Li, F.J. Lu, L.M. Song, H.Y. Wang, M. Wu, Y.P. Xu, S.N. Zhang, *GRB Coordinates Network* **23491**, 1 (2018)
22. A.M. Watson, M. Pereyra, N. Butler, R.L. Becerra, W.H. Lee, C. Roman-Zuniga, A. Kutuyev, E. Troja, *GRB Coordinates Network* **23481**, 1 (2018)
23. T. Laskar, H. van Eerten, P. Schady, C.G. Mundell, K.D. Alexander, R. Barniol Duran, E. Berger, J. Bolmer, R. Chornock, D.L. Coppejans, W.f. Fong, A. Gomboc, N. Jordana-Mitjans, S. Kobayashi, R. Margutti, K.M. Menten, R. Sari, R. Yamazaki, V.M. Lipunov, E. Gorbovskoy, V.G. Kornilov, N. Tyurina, D. Zimnukhov, R. Podesta, H. Levato, D.A.H. Buckley, A. Tlatov, R. Rebolo, M. Serra-Ricart, *Astrophysical Journal* **884**(2), 121 (2019). DOI 10.3847/1538-4357/ab40ce
24. S. Belkin, E. Mazaeva, A. Pozanenko, P. Minaev, A. Volnova, N. Tominaga, S. Blinnikov, D. Chestnov, E. Klunko, I. Reva, V. Romyantsev, D. Buckley, R.Y. Inasaridze, *GRB Coordinates Network* **23601**, 1 (2019)
25. L. Izzo, A. de Ugarte Postigo, D.A. Kann, D.B. Malesani, K.E. Heintz, N.R. Tanvir, V. D'Elia, K. Wiersema, C. Kouveliotou, A.J. Levan, *GRB Coordinates Network* **23488**, 1 (2018)
26. T. Laskar, E. Berger, R. Chornock, W. Fong, R. Margutti, C.G. Mundell, P. Schady, *GRB Coordinates Network* **23519**, 1 (2018)
27. S.D. Barthelmy, L.M. Barbier, J.R. Cummings, E.E. Fenimore, N. Gehrels, D. Hullinger, H.A. Krimm, C.B. Markwardt, D.M. Palmer, A. Parsons, G. Sato, M. Suzuki, T. Takahashi, M. Tashiro, J. Tueller, *Space Sci. Rev.* **120**, 143 (2005). DOI 10.1007/s11214-005-5096-3
28. N. Gehrels, G. Chincarini, P. Giommi, K.O. Mason, J.A. Nousek, A.A. Wells, N.E. White, S.D. Barthelmy, D.N. Burrows, L.R. Cominsky, K.C. Hurley, F.E. Marshall, P. Mészáros, P.W.A. Roming, L. Angelini, L.M. Barbier, T. Belloni, S. Campana, P.A. Caraveo, M.M. Chester, O. Citterio, T.L. Cline, M.S. Cropper, J.R. Cummings, A.J. Dean, E.D. Feigelson, E.E. Fenimore, D.A. Frail, A.S. Fruchter, G.P. Garmire, K. Gendreau, G. Ghisellini, J. Greiner, J.E. Hill, S.D. Hunsberger, H.A. Krimm, S.R. Kulkarni, P. Kumar, F. Lebrun, N.M. Lloyd-Ronning, C.B. Markwardt, B.J. Mattson, R.F. Mushotzky, J.P. Norris,

- J. Osborne, B. Paczynski, D.M. Palmer, H.S. Park, A.M. Parsons, J. Paul, M.J. Rees, C.S. Reynolds, J.E. Rhoads, T.P. Sasseen, B.E. Schaefer, A.T. Short, A.P. Smale, I.A. Smith, L. Stella, G. Tagliaferri, T. Takahashi, M. Tashiro, L.K. Townsley, J. Tueller, M.J.L. Turner, M. Vietri, W. Voges, M.J. Ward, R. Willingale, F.M. Zerbi, W.W. Zhang, *ApJ* **611**, 1005 (2004). DOI 10.1086/422091
29. J.D. Gropp, S.D. Barthelmy, M.J. Moss, D.M. Palmer, A. Tohuvavohu, *GRB Coordinates Network* **23642**, 1 (2019)
  30. A.J. Castro-Tirado, Y. Hu, E. Fernández-García, A. Valeev, V. Sokolov, S. Guziy, S. Oates, S. Jeong, S.B. Pandey, I. Carrasco, D. Reverte-Paya, *GRB Coordinates Network* **23708**, 1 (2019)
  31. D. Frederiks, S. Golenetskii, R. Aptekar, A. Kozlova, A. Lysenko, D. Svinikin, A. Tsvetkova, M. Ulanov, T. Cline, *GRB Coordinates Network* **23737**, 1 (2019)
  32. C. Meegan, G. Lichti, P.N. Bhat, E. Bissaldi, M.S. Briggs, V. Connaughton, R. Diehl, G. Fishman, J. Greiner, A.S. Hoover, A.J. van der Horst, A. von Kienlin, R.M. Kippen, C. Kouveliotou, S. McBreen, W.S. Paciesas, R. Preece, H. Steinle, M.S. Wallace, R.B. Wilson, C. Wilson-Hodge, *ApJ* **702**, 791 (2009). DOI 10.1088/0004-637X/702/1/791
  33. R. Hamburg, P. Veres, C. Meegan, E. Burns, V. Connaughton, A. Goldstein, D. Kocevski, O.J. Roberts, *GRB Coordinates Network* **23707**, 1 (2019)
  34. D. Kocevski, N. Omodei, M. Axelsson, E. Burns, G. Vianello, E. Bissaldi, F. Longo, *GRB Coordinates Network* **23709**, 1 (2019)
  35. K. Misra, L. Resmi, D.A. Kann, M. Marongiu, A. Moin, S. Klose, A. de Ugarte Postigo, V.K. Jaiswal, D.A. Perley, A. Ghosh, G. Bernardi, S. Schulze, M.J. Michałowski, S. Martin, A. Cockeram, H. Kumar, S.V. Cherukuri, V. Bhalerao, G.E. Anderson, G.C. Anupama, C.C. Thöne, S. Barway, M.H. Wieringa, J.P.U. Fynbo, N. Habeeb, arXiv e-prints arXiv:1911.09719 (2019)
  36. R. Mirzoyan, K. Noda, E. Moretti, A. Berti, C. Nigro, J. Hoang, S. Micanovic, M. Takahashi, Y. Chai, A. Moralejo, *MAGIC Collaboration, GRB Coordinates Network* **23701**, 1 (2019)
  37. R. Mirzoyan, *The Astronomer's Telegram* **12390**, 1 (2019)
  38. *MAGIC Collaboration*, V.A. Acciari, S. Ansoldi, L.A. Antonelli, A.A. Engels, D. Baack, A. Babić, B. Banerjee, U. Barres de Almeida, J.A. Barrio, J.B. González, W. Bednarek, L. Bellizzi, E. Bernardini, A. Berti, J. Besenrieder, W. Bhattacharyya, C. Bigongiari, A. Biland, O. Blanch, G. Bonoli, Ž. Bošnjak, G. Busetto, R. Carosi, G. Ceribella, Y. Chai, A. Chilingaryan, S. Cikota, S.M. Colak, U. Colin, E. Colombo, J.L. Contreras, J. Cortina, S. Covino, V. D'Elia, P. da Vela, F. Dazzi, A. de Angelis, B. de Lotto, M. Delfino, J. Delgado, D. Depaoli, F. di Piero, L. di Venere, E.D.S. Espiñeira, D.D. Prester, A. Donini, D. Dorner, M. Doro, D. Elsaesser, V.F. Ramazani, A. Fattorini, G. Ferrara, D. Fidalgo, L. Foffano, M.V. Fonseca, L. Font, C. Fruck, S. Fukami, R.J.G. López, M. Garczarezyk, S. Gasparyan, M. Gaug, N. Giglietto, N. Giordano, F. and Godinović, D. Green, D. Guberman, D. Hadasch, A. Hahn, J. Herrera, J. Hoang, D. Hrupec, M. Hütten, T. Inada, S. Inoue, K. Ishio, Y. Iwamura, L. Jouvin, D. Kerszberg, H. Kubo, J. Kushida, A. Lamastra, F. Las, D. and Leone, E. Lindfors, S. Lombardi, F. Longo, M. López, R. López-Coto, A. López-Oramas, S. Loporchio, B.M. de Oliveira Fraga, C. Maggio, P. Majumdar, M. Makariev, M. Mallamaci, G. Maneva, M. Manganaro, K. Mannheim, L. Maraschi, M. Mariotti, M. Martínez, D. Mazin, S. Mićanović, D. Miceli, M. Mineev, J.M. Miranda, R. Mirzoyan, E. Molina, A. Moralejo, D. Morcuende, V. Moreno, E. Moretti, P. Munar-Adrover, V. Neustroev, C. Nigro, K. Nilsson, D. Ninci, K. Nishijima, K. Noda, L. Nogués, S. Nozaki, S. Paiano, M. Palatiello, D. Paneque, R. Paoletti, J.M. Paredes, P. Peñil, M. Peresano, M. Persic, P.G.P. Moroni, E. Prandini, I. Puljak, W. Rhode, M. Ribó, J. Rico, C. Righi, A. Rugliancich, L. Saha, N. Sahakyan, T. Saito, S. Sakurai, K. Satalecka, T. Schmidt, K. and Schweizer, J. Sitarek, I. Šnidarić, D. Sobczynska, A. Somero, A. Stamerra, D. Strom, M. Strzys, Y. Suda, T. Surić, M. Takahashi, F. Tavecchio, P. Temnikov, T. Terzić, M. Teshima, N. Torres-Albà, L. Tosti, V. Vagelli, J. van Scherpenberg, G. Vanzo, M.V. Acosta, C.F. Vigorito, V. Vitale, I. Vovk, M. Will, D. Zarić, L. Nava, P. Veres, P.N. Bhat, M.S. Briggs, W.H. Cleveland, R. Hamburg, C.M. Hui, B. Mailyan, R.D. Preece, O.J. Roberts, A. von Kienlin, C.A. Wilson-Hodge, D. Kocevski, M. Arimoto, D. Tak, K. Asano, M. Axelsson, G. Barbiellini, E. Bissaldi, F.F. Dirirsa, R. Gill, J. Granot, J. McEnery, N. Omodei, S. Razzaque, F. Piron, J.L. Racusin, D.J. Thompson, S. Campana, M.G. Bernardini, N.P.M. Kuin, M.H. Siegel, S.B. Cenko, P. O'Brien, M. Capalbi, A. Dai, M. de Pasquale, J. Gropp, N. Klingler, J.P. Osborne, M. Perri, R.L.C. Starling, G. Tagliaferri, A. Tohuvavohu, A. Ursi, M. Tavani, M. Cardillo, C. Casentini, G. Piano, Y. Evangelista, F. Verrecchia, C. Pittori, F. Lucarelli, A. Bulgarelli, N. Parmiggiani, G.E. Anderson, J.P. Anderson, G. Bernardi, J. Bolmer, M.D. Caballero-García, I.M. Carrasco, A. Castellón, N.C. Segura, A.J. Castro-Tirado, S.V. Cherukuri, A.M. Cockeram, P. D'Avanzo, A. di Dato, R. Diretse, R.P. Fender, E. Fernández-García, J.P.U. Fynbo, A.S. Fruchter, J. Greiner, M. Gromadzki, K.E. Heintz, I. Heywood, A.J. van der Horst, Y.D. Hu, C. Inerra, L. Izzo, V. Jaiswal, P. Jakobsson, J. Japelj, E. Kankare, D.A. Kann, C. Kouveliotou, S. Klose, A.J. Levan, X.Y. Li, S. Lotti, K. Maguire, D.B. Malesani, I. Manulis, M. Marongiu, S. Martin, A. Melandri, M.J. Michałowski, J.C.A. Miller-Jones, K. Misra, A. Moin, K.P. Mooley, S. Nasri, M. Nicholl, A. Noschese, G. Novara, S.B. Pandey, E. Peretti, C.J.P. Del Pulgar, M.A. Pérez-Torres, D.A.

- Perley, L. Piro, F. Ragosta, L. Resmi, R. Ricci, A. Rossi, R. Sánchez-Ramírez, J. Selsing, S. Schulze, S.J. Smartt, I.A. Smith, V.V. Sokolov, J. Stevens, N.R. Tanvir, C.C. Thöne, A. Tiengo, E. Tremou, E. Troja, A. de Ugarte Postigo, A.F. Valeev, S.D. Vergani, M. Wieringa, P.A. Woudt, D. Xu, O. Yaron, D.R. Young, *Nature* **575**(7783), 459 (2019). DOI 10.1038/s41586-019-1754-6
39. I.F. Mirabel, L.F. Rodríguez, *Nature* **371**(6492), 46 (1994). DOI 10.1038/371046a0
  40. R.P. Fender, S.T. Garrington, D.J. McKay, T.W.B. Muxlow, G.G. Pooley, R.E. Spencer, A.M. Stirling, E.B. Waltman, *MNRAS* **304**(4), 865 (1999). DOI 10.1046/j.1365-8711.1999.02364.x
  41. G.G. Pooley, R.P. Fender, *MNRAS* **292**(4), 925 (1997). DOI 10.1093/mnras/292.4.925
  42. S.S. Eikenberry, K. Matthews, E.H. Morgan, R.A. Remillard, R.W. Nelson, *Astrophysical Journal, Letters* **494**(1), L61 (1998). DOI 10.1086/311158
  43. E. Egron, A. Pellizzoni, M. Giroletti, S. Righini, M. Stagni, A. Orlati, C. Migoni, A. Melis, R. Concu, L. Barbas, S. Buttaccio, P. Cassaro, P. De Vicente, M.P. Gawroński, M. Lindqvist, G. Maccaferri, C. Stanghellini, P. Wolak, J. Yang, A. Navarrini, S. Loru, M. Pilia, M. Bachetti, M.N. Iacolina, M. Buttu, S. Corbel, J. Rodriguez, S. Markoff, J. Wilms, K. Pottschmidt, M. Cadolle Bel, E. Kalemci, T. Belloni, V. Grinberg, M. Marongiu, G.P. Vargiu, A. Trois, *MNRAS* **471**(3), 2703 (2017). DOI 10.1093/mnras/stx1730
  44. I. Prandoni, M. Murgia, A. Tarchi, M. Burgay, P. Castangia, E. Egron, F. Govoni, A. Pellizzoni, R. Ricci, S. Righini, M. Bartolini, S. Casu, A. Corongiu, M.N. Iacolina, A. Melis, F.T. Nasir, A. Orlati, D. Perrodin, S. Poppi, A. Trois, V. Vacca, A. Zanichelli, M. Bachetti, M. Buttu, G. Comoretto, R. Concu, A. Fara, F. Gaudiomonte, F. Loi, C. Migoni, A. Orfei, M. Pilia, P. Bolli, E. Carretti, N. D'Amico, D. Guidetti, S. Loru, F. Massi, T. Pisanu, I. Porceddu, A. Ridolfi, G. Serra, C. Stanghellini, C. Tiburzi, S. Tingay, G. Valente, *A&A* **608**, A40 (2017). DOI 10.1051/0004-6361/201630243
  45. G. Valente, T. Pisanu, P. Bolli, S. Mariotti, P. Marongiu, A. Navarrini, R. Nesti, A. Orfei, J. Roda, *The dual-band LP feed system for the Sardinia Radio Telescope prime focus* (2010), *Society of Photo-Optical Instrumentation Engineers (SPIE) Conference Series*, vol. 7741, p. 774126. DOI 10.1117/12.857306
  46. G. Valente, A. Orfei, R. Nesti, A. Navarrini, S. Mariotti, P. Bolli, T. Pisanu, J. Roda, L. Cresci, P. Marongiu, A. Scalambra, D. Panella, A. Ladu, A. Cattani, L. Carbonaro, E. Urru, A. Cremonini, F. Fiocchi, A. Maccaferri, M. Morsiani, M. Poloni, *Status of the radio receiver system of the Sardinia Radio Telescope* (2016), *Society of Photo-Optical Instrumentation Engineers (SPIE) Conference Series*, vol. 9914, p. 991425. DOI 10.1117/12.2232880
  47. A. Orfei, M. Morsiani, G. Zacchiroli, G. Maccaferri, J. Roda, F. Fiocchi, *Active surface system for the new Sardinia Radiotelescope* (2004), *Society of Photo-Optical Instrumentation Engineers (SPIE) Conference Series*, vol. 5495, pp. 116–125. DOI 10.1117/12.548944
  48. M. Buttu, A. Orlati, G. Zacchiroli, M. Morsiani, F. Fiocchi, F. Buffa, G. Maccaferri, G.P. Vargiu, C. Migoni, S. Poppi, S. Righini, A. Melis, *Diving into the Sardinia Radio Telescope minor servo system* (2012), *Society of Photo-Optical Instrumentation Engineers (SPIE) Conference Series*, vol. 8451, p. 84512L. DOI 10.1117/12.925387
  49. P. Bolli, A. Orlati, L. Stringhetti, A. Orfei, S. Righini, R. Ambrosini, M. Bartolini, C. Bortolotti, F. Buffa, M. Buttu, A. Cattani, N. D'Amico, G. Deiana, A. Fara, F. Fiocchi, F. Gaudiomonte, A. Maccaferri, S. Mariotti, P. Marongiu, A. Melis, C. Migoni, M. Morsiani, M. Nanni, F. Nasyr, A. Pellizzoni, T. Pisanu, M. Poloni, S. Poppi, I. Porceddu, I. Prandoni, J. Roda, M. Roma, A. Scalambra, G. Serra, A. Trois, G. Valente, G.P. Vargiu, G. Zacchiroli, *Journal of Astronomical Instrumentation* **4**, 1550008-880 (2015). DOI 10.1142/S2251171715500087
  50. E. Egron, A. Pellizzoni, M.N. Iacolina, S. Loru, M. Marongiu, S. Righini, M. Cardillo, A. Giuliani, S. Mulas, G. Murtas, D. Simeone, R. Concu, A. Melis, A. Trois, M. Pilia, A. Navarrini, V. Vacca, R. Ricci, G. Serra, M. Bachetti, M. Buttu, D. Perrodin, F. Buffa, G.L. Deiana, F. Gaudiomonte, A. Fara, A. Ladu, F. Loi, P. Marongiu, C. Migoni, T. Pisanu, S. Poppi, A. Saba, E. Urru, G. Valente, G.P. Vargiu, *MNRAS* **470**(2), 1329 (2017). DOI 10.1093/mnras/stx1240
  51. A. Melis, R. Concu, A. Trois, A. Possenti, A. Bocchinu, P. Bolli, M. Burgay, E. Carretti, P. Castangia, S. Casu, C.C. Pestellini, A. Corongiu, N. D'Amico, E. Egron, F. Govoni, M.N. Iacolina, M. Murgia, A. Pellizzoni, D. Perrodin, M. Pilia, T. Pisanu, A. Poddighe, S. Poppi, I. Porceddu, A. Tarchi, V. Vacca, G. Aresu, M. Bachetti, M. Barbaro, A. Casula, A. Ladu, S. Leurini, F. Loi, S. Loru, P. Marongiu, P. Maxia, G. Mazzarella, C. Migoni, G. Montisci, G. Valente, G. Vargiu, *Journal of Astronomical Instrumentation* **7**(1), 1850004 (2018). DOI 10.1142/S2251171718500046
  52. T. Robishaw, C. Heiles, arXiv e-prints arXiv:1806.07391 (2018)
  53. R.A. Perley, B.J. Butler, *ApJS* **204**(2), 19 (2013). DOI 10.1088/0067-0049/204/2/19
  54. E. Egron, A. Pellizzoni, M.N. Iacolina, et al., *INAF/OAC Internal Report* **59** (2016)
  55. T. An, O. Sharan Salafia, Y. Zhang, G. Ghirlanda, G. Giovannini, M. Giroletti, K. Hada, G. Migliori, M. Orienti, B.W. Sohn, arXiv e-prints arXiv:1911.03646 (2019)
  56. F. Nappo, A. Pescalli, G. Oganessyan, G. Ghirlanda, M. Giroletti, A. Melandri, S. Campana, G. Ghisellini, O.S. Salafia, P. D'Avanzo, M.G. Bernardini, S. Covino, E. Carretti, A. Celotti, V. D'Elia, L. Nava,

- E. Palazzi, S. Poppi, I. Prandoni, S. Righini, A. Rossi, R. Salvaterra, G. Tagliaferri, V. Testa, T. Venturi, S.D. Vergani, *A&A* **598**, A23 (2017). DOI 10.1051/0004-6361/201628801
57. M.P. van Haarlem, M.W. Wise, A.W. Gunst, G. Heald, J.P. McKean, J.W.T. Hessels, A.G. de Bruyn, R. Nijboer, J. Swinbank, R. Fallows, M. Brentjens, A. Nelles, R. Beck, H. Falcke, R. Fender, J. Hörandel, L.V.E. Koopmans, G. Mann, G. Miley, H. Röttgering, B.W. Stappers, R.A.M.J. Wijers, S. Zaroubi, M. van den Akker, A. Alexov, J. Anderson, K. Anderson, A. van Ardenne, M. Arts, A. Asgekar, I.M. Avruch, F. Batejat, L. Bähren, M.E. Bell, M.R. Bell, I. van Bemmel, P. Bennema, M.J. Bentum, G. Bernardi, P. Best, L. Birzan, A. Bonafede, A.J. Boonstra, R. Braun, J. Bregman, F. Breitling, R.H. van de Brink, J. Broderick, P.C. Broekema, W.N. Brouw, M. Brüggén, H.R. Butcher, W. van Cappellen, B. Ciardi, T. Coenen, J. Conway, A. Coolen, A. Corstanje, S. Damstra, O. Davies, A.T. Deller, R.J. Dettmar, G. van Diepen, K. Dijkstra, P. Donker, A. Doorduyn, J. Dromer, M. Drost, A. van Duin, J. Eislöffel, J. van Enst, C. Ferrari, W. Frieswijk, H. Gankema, M.A. Garrett, F. de Gasperin, M. Gerbers, E. de Geus, J.M. Grießmeier, T. Grit, P. Gruppen, J.P. Hamaker, T. Hassall, M. Hoeft, H.A. Holties, A. Hornegger, A. van der Horst, A. van Houwelingen, A. Huijgen, M. Iacobelli, H. Intema, N. Jackson, V. Jelic, A. de Jong, E. Juette, D. Kant, A. Karastergiou, A. Koers, H. Kollen, V.I. Kondratiev, E. Kooistra, Y. Koopman, A. Koster, M. Kuniyoshi, M. Kramer, G. Kuper, P. Lambropoulos, C. Law, J. van Leeuwen, J. Lemaître, M. Loose, P. Maat, G. Macario, S. Markoff, J. Masters, R.A. McFadden, D. McKay-Bukowski, H. Meijering, H. Meulman, M. Mevius, E. Middelberg, R. Millenaar, J.C.A. Miller-Jones, R.N. Mohan, J.D. Mol, J. Morawietz, R. Morganti, D.D. Mulcahy, E. Mulder, H. Munk, L. Nieuwenhuis, R. van Nieuwpoort, J.E. Noordam, M. Norden, A. Noutsos, A.R. Offringa, H. Olofsson, A. Omar, E. Orrù, R. Overeem, H. Paas, M. Pandey-Pommier, V.N. Pandey, R. Pizzo, A. Polatidis, D. Rafferty, S. Rawlings, W. Reich, J.P. de Reijer, J. Reitsma, G.A. Renting, P. Riemers, E. Rol, J.W. Romein, J. Roosjen, M. Ruiter, A. Scaife, K. van der Schaaf, B. Scheers, P. Schellart, A. Schoenmakers, G. Schoonderbeek, M. Serylak, A. Shulevski, J. Sluman, O. Smirnov, C. Sobey, H. Spreeuw, M. Steinmetz, C.G.M. Sterks, H.J. Stiepel, K. Stuurwold, M. Tagger, Y. Tang, C. Tasse, I. Thomas, S. Thoudam, M.C. Toribio, B. van der Tol, O. Usov, M. van Veelen, A.J. van der Veen, S. ter Veen, J.P.W. Verbiest, R. Vermeulen, N. Vermaas, C. Vocks, C. Vogt, M. de Vos, E. van der Wal, R. van Weeren, H. Weggemans, P. Weltevrede, S. White, S.J. Wijnholds, T. Wilhelmsson, O. Wucknitz, S. Yatawatta, P. Zarka, A. Zensus, J. van Zwieten, *A&A* **556**, A2 (2013). DOI 10.1051/0004-6361/201220873
58. S. Johnston, R. Taylor, M. Bailes, N. Bartel, C. Baugh, M. Bietenholz, C. Blake, R. Braun, J. Brown, S. Chatterjee, J. Darling, A. Deller, R. Dodson, P. Edwards, R. Ekers, S. Ellingsen, I. Feain, B. Gaensler, M. Haverkorn, G. Hobbs, A. Hopkins, C. Jackson, C. James, G. Joncas, V. Kaspi, V. Kilborn, B. Koribalski, R. Kothes, T. Landecker, E. Lenc, J. Lovell, J.P. Macquart, R. Manchester, D. Matthews, N. McClure-Griffiths, R. Norris, U.L. Pen, C. Phillips, C. Power, R. Protheroe, E. Sadler, B. Schmidt, I. Stairs, L. Staveley-Smith, J. Stil, S. Tingay, A. Tzioumis, M. Walker, J. Wall, M. Wollaben, *Experimental Astronomy* **22**(3), 151 (2008). DOI 10.1007/s10686-008-9124-7



Università  
degli Studi  
di Ferrara

Sezioni

## Dottorati di ricerca

**Il tuo indirizzo e-mail**

*mrnmrc@unife.it*

**Oggetto:**

*Dichiarazione di conformità della tesi di Dottorato*

**Io sottoscritto Dott.**

*Marongiu Marco*

**Nato a:**

*Iglesias*

**Provincia:**

*Sud Sardegna*

**Il giorno:**

*26 Gennaio 1984*

**Avendo frequentato il Dottorato di Ricerca in:**

*Fisica*

**Ciclo di Dottorato**

*32*

**Titolo della tesi:**

*Broadband modelling of relativistic explosions*

**Titolo della tesi (traduzione):**

*Modellizzazione multi-frequenza di esplosioni relativistiche*

**Tutore: Prof.**

*Guidorzi Cristiano*

**Settore Scientifico Disciplinare (S.S.D.)**

*FIS/05*

**Parole chiave della tesi (max 10):**

*Gamma-ray bursts, Afterglows, Modelling, Radioastronomy*

**Consapevole, dichiara**

*CONSAPEVOLE: (1) del fatto che in caso di dichiarazioni mendaci, oltre alle sanzioni previste dal codice penale e dalle Leggi speciali per l'ipotesi di falsità in atti ed uso di atti falsi, decade fin dall'inizio e senza necessità di alcuna formalità dai benefici conseguenti al provvedimento emanato sulla base di tali dichiarazioni; (2) dell'obbligo per l'Università di provvedere al deposito di legge delle tesi di dottorato al fine di assicurarne la conservazione e la consultabilità da parte di terzi; (3) della procedura adottata dall'Università di Ferrara ove si richiede che la tesi sia consegnata dal dottorando in 2 copie di cui una in formato*

---

cartaceo e una in formato pdf non modificabile su idonei supporti (CD-ROM, DVD) secondo le istruzioni pubblicate sul sito: <http://www.unife.it/studenti/dottorato> alla voce ESAME FINALE –disposizioni e modulistica; (4) del fatto che l'Università, sulla base dei dati forniti, archiverà e renderà consultabile in rete il testo completo della tesi di dottorato di cui alla presente dichiarazione attraverso l'Archivio istituzionale ad accesso aperto "EPRINTS.unife.it" oltre che attraverso i Cataloghi delle Biblioteche Nazionali Centrali di Roma e Firenze; DICHIARO SOTTO LA MIA RESPONSABILITÀ: (1) che la copia della tesi depositata presso l'Università di Ferrara in formato cartaceo è del tutto identica a quella presentata in formato elettronico (CDROM, DVD), a quelle da inviare ai Commissari di esame finale e alla copia che produrrò in seduta d'esame finale. Di conseguenza va esclusa qualsiasi responsabilità dell'Ateneo stesso per quanto riguarda eventuali errori, imprecisioni o omissioni nei contenuti della tesi; (2) di prendere atto che la tesi in formato cartaceo è l'unica alla quale farà riferimento l'Università per rilasciare, a mia richiesta, la dichiarazione di conformità di eventuali copie; (3) che il contenuto e l'organizzazione della tesi è opera originale da me realizzata e non compromette in alcun modo i diritti di terzi, ivi compresi quelli relativi alla sicurezza dei dati personali; che pertanto l'Università è in ogni caso esente da responsabilità di qualsivoglia natura civile, amministrativa o penale e sarà da me tenuta indenne da qualsiasi richiesta o rivendicazione da parte di terzi; (4) che la tesi di dottorato non è il risultato di attività rientranti nella normativa sulla proprietà industriale, non è stata prodotta nell'ambito di progetti finanziati da soggetti pubblici o privati con vincoli alla divulgazione dei risultati, non è oggetto di eventuali registrazioni di tipo brevettale o di tutela. PER ACCETTAZIONE DI QUANTO SOPRA RIPORTATO

**Firma del dottorando**

Ferrara, li 24/02/2020 Firma del Dottorando \_\_\_\_\_

**Firma del Tutore**

Visto: Il Tutore Si approva Firma del Tutore \_\_\_\_\_